Direct and Indirect Searches for New Physics beyond Standard Model

DIRECT AND INDIRECT SEARCHES FOR NEW PHYSICS BEYOND STANDARD MODEL

by

Huanian Zhang

A Dissertation Submitted to the Faculty of the

DEPARTMENT OF PHYSICS

In Partial Fulfillment of the Requirements
For the Degree of

DOCTOR OF PHILOSOPHY

In the Graduate College

THE UNIVERSITY OF ARIZONA

2016

THE UNIVERSITY OF ARIZONA
GRADUATE COLLEGE

As members of the Dissertation Committee, we certify that we have read the dissertation prepared by Huanian Zhang
entitled Direct and indirect searches for new physics beyond Standard Model
and recommend that it be accepted as fulfilling the dissertation requirement for the Degree of Doctor of Philosophy.

Date: May 25th, 2016

Doug Toussaint

Date: May 25th, 2016

John Rutherfoord

Date: May 25th, 2016

Stefan Meinel

Date: May 25th, 2016

Koen Visscher

Final approval and acceptance of this dissertation is contingent upon the candidate's submission of the final copies of the dissertation to the Graduate College.
I hereby certify that I have read this dissertation prepared under my direction and recommend that it be accepted as fulfilling the dissertation requirement.

Date: May 25th, 2016

Dissertation Director: Shufang Su

STATEMENT BY AUTHOR

This dissertation has been submitted in partial fulfillment of requirements for an advanced degree at the University of Arizona and is deposited in the University Library to be made available to borrowers under rules of the Library.

Brief quotations from this dissertation are allowable without special permission, provided that accurate acknowledgment of source is made. Requests for permission for extended quotation from or reproduction of this manuscript in whole or in part may be granted by the head of the major department or the Dean of the Graduate College when in his or her judgment the proposed use of the material is in the interests of scholarship. In all other instances, however, permission must be obtained from the author.

SIGNED: Huanian Zhang

ACKNOWLEDGEMENTS

This dissertation would not have been possible without the help from my kind supervisors and trusted friends. Pursuing a PhD is a wonderful journey with exploration to the unknown nature, happiness, and also struggle, sorrow. I've grown as a person who can tackle difficulties, a physicist who keeps passion and enthusiasm for the beauty of physics, a teacher who is willing to share and patient to help.

I owe my deepest gratitue to my supervisor Professor Shufang Su for her guidance, support and patience in the research on fundamental physics. I can still remember the moment we discussed the problems on the projects, and exchanged ideas to approach the difficulties on the projects. Her analysis and support for my future career always encourages me to do the best. It is a pity I wasted some good ideas of the physics projects. I thank Dr. Jonathan Eckel for his patience to work with me on the project, to teach me various skills and to help me with job hunting.

I would like to thank my first advisor Professor Elliott Cheu. I spent a year in his group to do experiment research work, from when I learned so much about experiment physics and technique. I would like to thank Dr. Caleb Lampen and Matt Leone in Professor Cheu's group. It was a wonderful experience to work with them. They taught me coding, helped me to prepare the ATLAS data and instructed me the data analysis. I thank Dr. Brokk Toggerson for helping me a lot about the data analysis and ATLAS experimentalists down the hall for helpful discussion.

I thank Professor Dennis Zaritsky to let me work with him on side projects. I learned a lot about astronomy from him, and he is open for discussion at any time and always can come up with ideas to resolve difficult problems. It is pleasant to work with him and exchange ideas. This experience also provides me more opportunities for my future career.

I would like to thank my collaborators Professor Tao Han and Yongcheng Wu. The join of both of you greatly speed up our projects. I would also like to thank professors, peer colleagues and staffs at the Department of the Physics, especially Professor John Rutherfoord, Professor Douglas Toussaint, Professor Stefan Meinel and Professor Koen Visscher, who kindly accepted to serve on my committee. I thank my friends Lei Xu, Shulei Zhang, You Zhou, Fei Huang, Meng Xu. It was a lot of fun to discuss questions and play soccer with you guys. I thank Carole Capen and Bob Capen for careful editting of the dissertation.

I thank my family for their continuous support and unconditional love. Lastly, I thank my wonderful girlfriend Lanlan Tan for her support and love.

DEDICATION

To My Family

TABLE OF CONTENTS

TABLE OF CONTENTS – *Continued*

LIST OF FIGURES

LIST OF FIGURES – *Continued*

LIST OF FIGURES – *Continued*

LIST OF TABLES

LIST OF TABLES – *Continued*

ABSTRACT

The search for new physics beyond the Standard Model can follow one of two tracks: direct searches for new particles at the collider or indirect probes for new physics from precision measurements. In the direct searches for third generation squarks in SUSY at the LHC, the common practice has been to assume a 100% decay branching fraction for a given search channel. In realistic MSSM scenarios, there is often more than one significant decay mode present, which significantly weakens the current search limits on third generation squarks at the LHC. On the other hand, the combination of multiple decay modes as well as the new open decay modes offer alternative discovery channels for third generation squarks searches. In this work, we present the third generation squarks decay and the collider signatures in a few representative mass parameter scenarios. We then analyze the reach of the stop/sbottom signal for the pair production in QCD at the 14 TeV LHC with 300 fb^{-1} integrated luminosity and of the 100 TeV future collider with 3000 fb^{-1} integrated luminosity in a few representative scenarios.

In the scenario of Bino LSP with Wino NLSP, we investigate stop/sbottom pair production at the LHC with one stop/sbottom decaying via $\tilde{t} \to t\chi_1^0,\ t\chi_2^0/\tilde{b} \to b\chi_1^0,\ b\chi_2^0$, and the other one decaying via $\tilde{t} \to b\chi_1^\pm/\tilde{b} \to t\chi_1^\pm$. With the gaugino subsequent decaying to gauge bosons or a Higgs boson $\chi_2^0 \to Z\chi_1^0,\ h\chi_1^0$ and $\chi_1^\pm \to W^\pm\chi_1^0$, leading to $bbbbjj\ell\not{E}_T$ final states for the Higgs channel and $bbjjjj\ell\ell\not{E}_T$ final states for the Z channel, we study the reach of those signals at the 14 TeV LHC with 300 fb^{-1} integrated luminosity. Because the sbottom and stop signals in the same SUSY parameter scenario have undistinguishable final states, they are combined to obtain optimal sensitivity, which is about 150 GeV better than the individual reaches of the sbottom or stop.

In the scenario of Bino LSP with Higgsino NLSP. The light stop pair production at

the 14 TeV LHC, with stops decaying via $\tilde{t}_1 \to t\chi_2^0/\chi_3^0$ and the neutralino subsequently decaying to a gauge boson or a Higgs boson $\chi_2^0/\chi_3^0 \to \chi_1^0 h/Z$, leads to $t\bar{t}hh\not{E}_T$, $t\bar{t}hZ\not{E}_T$ or $t\bar{t}ZZ\not{E}_T$ final states. The above decay channels give rise to final states containing one or more leptons, therefore our search strategy is to divide the signal regions based on the multiplicity of leptons. We find that the one lepton signal region of channel $t\bar{t}hZ\not{E}_T$ has the best reach sensitivity of light stop searches at the 14 TeV LHC with 300 fb^{-1} integrated luminosity. We then combine all the signal regions for a given decay channel or combine all the decay channels for a given signal region to maximize the reach sensitivity of the stop search. For the light stop pair production at the $\sqrt{s} = 100$ TeV future machine with 3000 fb^{-1} integrated luminosity, we find that a stop with a mass up to 6 TeV can be discovered at 5σ significance, while a mass up to 6.8 TeV can be excluded at 95% C.L. for the combined results of all three channels.

In the indirect probes for new physics, we utilize the Z-pole Oblique Parameters S, T, U and Higgs precision measurements complementarily in the framework of the Two Higgs Doublet Model at current and future colliders. The S, T , U is not that sensitive to the rotation angle $\beta - \alpha$, while the Higgs precision measurements set strong constrains on $\beta - \alpha$. Also the T is very sensitive to the mass difference of Higgs bosons, leading to the mass of charged Higgs ($H^{\pm}$) aligning either along with the mass of neutral Higgs H or A. As for the Higgs precision measurements, we consider the tree level corrections to Higgs coupling constants as well as the radiative corrections to Higgs coupling constants at one loop level for the future collider. The combination of Z-pole precision measurements and Higgs precision measurements complementarily set strong constraints on the parameter space of the 2HDM, especially in the future e^+e^- circular collider compared to the current collider due to much cleaner backgrounds and higher luminosity.

CHAPTER 1

Introduction

The breakthrough discovery of a Standard Model (SM) like Higgs boson completed the last missing piece of fundamental particles [1, 2]. The SM has evolved into a spectacularly successful theoretical framework to describe the strong, the weak and the electromagnetic (EM) interactions of all the elementary particles, which is governed by the $SU(3)_C \times SU(2)_L \times U(1)_Y$ gauge symmetry.

After a few decades, the Standard Model has become an incredibly successful theory, of which the Quantum Chromodynamics (QCD), Quantum Electrodynamics (QED), and Glashow-Weinberg-Salam (GWS) theory are robust theoretical frameworks describing the strong, the electromagnetic and the weak interactions of fundamental fields, respectively. Rigorous tests have found these theories to give correct predictions with astounding accuracy. The electroweak sector of the Standard Model has been extensively studied at the Large Electron-Positron (LEP) [3, 4], with measurements of the W, Z bosons masses and width, and the effective weak mixing angle $\sin^2\theta^{lep}_{eff}$ with high precision. The top quark mass is now measured with uncertainties below 0.76 GeV by the ATLAS, CDF, CMS and D0 groups [5]. The QED prediction of the anomalous magnetic moment of the electron (g - 2) matches experiment to 10 significant figures and is the most precisely known quantity in all of physics [6]. The Higgs mass and coupling strengths are measured by the ATLAS and CMS groups [7–9] and will be discussed in Chapter 2.

Despite the great success of the Standard Model theory, it is still not complete. It is now widely argued that while the SM is an effective low energy description of nature, a more fundamental theory of physics which will incorporate the gravitational force is yet to be established. There are still a few puzzles that are beyond the explanation in the framework of the Standard Model. The first puzzle is the quadratic divergency of the

Higgs mass. A light Higgs at the weak scale receives unstable quadratic corrections to its mass, and requires a cancellation of 17 orders of magnitude to recover the physical Higgs mass measured at 125.36 GeV. This is referred to as the "hierarchy problem" [10]. Another puzzle concerns the matter content of the Universe, where observations indicate that the majority of matter in the Universe is composed of an unknown component, so-called Dark Matter (DM). However, no SM particles can be the DM candidate, indicating that we need new physics beyond the SM to explain the existence of the DM particle. The third puzzle is the neutrino mass. Disappearance of the solor ν_e and atmospheric ν_μ due to the oscillations have been observed respectively, in the solor neutrino [11–19], KamLAND [20, 21] and Super-Kamokande [22, 23] experiments, indicating that the neutrino has mass. However, the SM can not provide a mechanism for neutrino to acquire mass.

All puzzles indicate the need of new physics beyond the SM to explain the observed phenomena. Indeed, there are a variety of interesting extensions to the SM, among which Supersymmetry (SUSY) is a well motivated model beyond the SM. SUSY postulates a new symmetry relating fermions to bosons, with their intrinsic spin differing by 1/2. Therefore, the quadratic divergence to the Higgs mass induced by the SM fermions is cancelled out by that of the corresponding superpartners, effectively solving the hierarchy problem. In addition, the SUSY model accommodates a light Higgs, with properties close to that of the Standard Model Higgs. Finally, the SUSY model also provides a mechanism for approaching the grand unified theory (GUT), which can naturally accommodate gauge coupling unification below the Plank scale. Another feature of the SUSY model is that it can provide a good dark matter candidate - the lightest supersymmetric particle (LSP).

In the Minimal Supersymmetric Standard Model (MSSM), the third generation squark sector might be the most relevant supersymmetric partner in connection to the Higgs physics given the large top and bottom Yukawa couplings. The top squark (stop) loops provide the dominant radiative corrections to the Higgs mass, which sets strong constraints on the stop sector and favors heavily mixed stops and at least one light stop [24]. The left-handed squark $(\tilde{t}_L, \tilde{b}_L)$ is grouped as $SU(2)_L$ doublets, with masses controlled by the same soft SUSY breaking mass parameter [25, 26], therefore the bottom squark (sbottom) is also of interest. In the region of higher ratios of the Higgs vacuum expectation values:

$\tan\beta = v_2/v_1$, the bottom Yukawa coupling is large and could allow large corrections to the Higgs physics from the sbottom sector as well [27].

Although the LHC program has been carrying out a rather broad and impressive SUSY search plan, many searches are still limited by strong assumptions for the sake of simplicity. Most of the current searches for the third generation squarks carried out by the ATLAS and CMS groups focus on the decay $\tilde{t}_1 \to t\chi_1^0$ ($\tilde{b}_1 \to b\chi_1^0$) or $\tilde{t}_1 \to b\chi_1^\pm \to bW\chi_1^0$ ($\tilde{b}_1 \to t\chi_1^\pm \to bWW\chi_1^0$), with χ_1^0 being the stable LSP appearing as missing energy ($\not{E}_T$) at colliders. For stop/sbottom pair production at the LHC, such processes lead to $tt+\not{E}_T$ or $bbWW+\not{E}_T$ final states. However, due to the lhuge SM backgrounds from $t\bar{t}$, searches for the stop/sbottom can be very challenging. Unfortunately, until now still no SUSY signal over Standard Model backgrounds has been found.

In realistic MSSM scenarios, there is often more than one significant decay mode present because of the different mass hierarchies between stop/sbottom, gauginos and Higgsinos. The decays of the light stop or sbottom highly depend on the low-lying neutralino/chargino spectrum, as well as the composition of the light stop and sbottom. Therefore, third generation squarks posses very rich decay patterns. A few prominent scenarios stand out: A left-handed stop (sbottom) in the Bino LSP with Wino NLSP scenario has a decay of $\tilde{t} \to t\chi_2^0 \to th/Z$ ($\tilde{b} \to b\chi_2^0 \to bh/Z$) with a branching fraction as high as $20\% - 40\%$, along with the leading decay $\tilde{t} \to b\chi_1^\pm$ ($\tilde{b} \to t\chi_1^\pm$), leading to $t\bar{t}h/Z$ final states; a left-handed stop in the Bino LSP with Higgsino NLSP scenario has two almost equal decays $\tilde{t} \to t\chi_2^0 \to th/Z\chi_1^0$ and $\tilde{t} \to t\chi_3^0 \to th/Z\chi_1^0$ with a branching fractions as high as 45%, leading to $t\bar{t}hh$, $t\bar{t}hZ$ and $t\bar{t}ZZ$ final states. Similarly, a right-handed sbottom in the Bino LSP with Higgsino NLSP scenario may have the leading decay mode $\tilde{b} \to b\chi_1^0$ with a branching fraction of only $40\% - 60\%$, along with a sub-leading decay of $\tilde{b} \to t\chi_1^\pm$ of $20\% - 30\%$. Those additional channels dilute the leading signals currently being searched for at the LHC and significantly weaken the stop/sbottom search limits when assuming a 100% branching fraction for a given search channel. On the other hand, the new decay modes and a combination of the multiple decay modes offer alternative discovery channels for stop/sbottom searches, that must be taken into account.

In this work, we present the stop/sbottom decay patterns in three representative sce-

narios with different mass hierarchies between stop/sbottom, gauginos and Higgsinos. We then analyze the possible collider signatures for the stop/sbottom pair production with the stop/sbottom decay channels. We study the reach of those signals at the 14 TeV LHC with 300 fb^{-1} integrated luminosity and those of the 100 TeV future collider with 3000 fb^{-1} integrated luminosity. Because the final states may contain 1 or 2 Z bosons and the Z boson has clean lepton channels, our analysis is divided in to a few signal regions based on the multiplicity of leptons. Because of the similarity of the final state signatures and the potential correlation of the left-handed soft mass, the sbottom and stop signals are combined to obtain the optimal sensitivity for the same SUSY parameter region. The combined discovery reach of the stop/sbottom can be greatly improved by a factor of 2 at the 14 TeV LHC or by a factor of 10 at the 100 TeV future collider.

Another extension to the SM is the Two Higgs Doublet Model (2HDM). In the Standard Model, the fermion structure contains more than one family and allows family mixing, while the scalar structure only contains one $SU(2)$ doublet. So it is natural to explore the possibility of introducing another scalar doublet. The 2HDM incorporates two $SU(2)$ doublets, which can fit in the SUSY model with Higgs quartic couplings governed by the gauge couplings. The 2HDM can generate a baryon asymmetry of the universe of sufficient size, due to the flexibility of its scalar mass spectrum and the existence of additional sources of CP violation. With two complex scalar $SU(2)$ doublets, there are eight degrees of freedom, three of which are eaten as the longitudinal components of the $W^{\pm}$ and Z bosons. The remaining five degrees of freedom are the physical Higgs bosons, with one CP-even Higgs (h), two CP-odd Higgs bosons (H, A) and two charged Higgs bosons ($H^{\pm}$). The tree level corrections as well as the radiative corrections, (at one loop level due to the additional Higgs bosons,) to hff, hVV ($VV = ZZ,\ WW$) coupling constants will introduce deviations on the Standard Model observables, which can be probed from the precision measurements at the current LHC or the future e^+e^- collider.

In this work, our goal is to explore the detectability of new physics in the framework of the 2HDM in aspects of Z-pole and Higgs precision measurements. The potential new physics in the radiative corrections to electroweak sectors can be parameterized by the Oblique Parameters S, T, U [28–32]. We do a global fit of the S, T, U parameters

from the current precision measurements and those of the future e^+e^- collider, to obtain constraints on the parameter space of the 2HDM. The Higgs physics in the framework of the 2HDM is very rich because of the extra Higgs bosons and tree level corrections to hff, hVV coupling constants. For instance, the hZZ coupling constant of the 2HDM at tree level, given by the multiplication of the factor $\sin(\beta - \alpha)$ to the SM coupling constant, can deviate from the Standard Model values due to the Higgs mixing effect. The radiative corrections to the hZZ coupling constant from extra Higgs bosons in the loop can also be significant. In the future e^+e^- collider, the Higgs signal strengths can be measured at precision of one percent or less, which sets strong constraints on the parameter space of the 2HDM. We then combine the Z-pole and Higgs precision measurements to do a complementary probe of the 2HDM.

The rest of the dissertation is organized as follows. In Chapter 2, I review the significant structure of the Standard Model, especially the gauge structure and the electroweak symmetry breaking mechanism, and point out the unsolved puzzles. In Chapter 3, I review the formalism and the gauge structure of the Supersymmetry model. I highlight the general MSSM soft breaking Lagrangian, Higgs sectors, electroweak gaugino sectors and the third generation sectors. In the last section of Chapter 3, I have a brief review of the general 2HDM, including the physical Higgs masses, the couplings of the Higgses to the fermions and gauge bosons. In Chapter 4, the decay channels and possible collider signatures of third generation squarks are investigated in detail for a few representative scenarios. In Chapter 5, I present detailed collider analysis of direct searches for third generation squarks in the scenario of Bino LSP with Wino NLSP and Bino LSP with Higgsino NLSP. In Chapter 6, an indirect probe for the Two Higgs Double Model is presented with both Z-pole and Higgs precision measurements. In Chapter 7, I give my conclusions.

CHAPTER 2

Standard Model

The core of the Standard Model is symmetry. In QED, QCD and the Glashow-Weinberg-Salam weak theory, local gauge symmetry provides the interactions between the gauge fields and fermion fields. Any attempts to extend the SM almost exclusively seek new symmetry embedded in the SM. For instance, the SUSY introduces another space time symmetry relating fermions to bosons. Below we briefly review the gauge symmetry in the SM as well as the spontaneous symmetry breaking and the Higgs mechanism. For a complete and comprehensive review of the SM, refer to Ref. [33].

2.1 Gauge symmetry and Lagrangian of the SM

The SM gauge symmetry is expressed in terms of groups. The gauge symmetry of strong interaction follows the group $SU(3)_c$, where the subscript c stands for color, describing the interaction between quarks and gluons with color charge. The electroweak gauge symmetry is governed by the group $SU(2)_L \otimes U(1)_Y$, corresponding to weak isospin and hypercharge. The charges of the fundamental particles in the SM under the symmetry groups are shown in Table 2.1. The fermions are split into two chiral states: the left-handed (LH) state and the right-handed (RH) state: $\psi = \binom{\psi_L}{\psi_R}$. The LH fields are grouped as an $SU(2)_L$ doublet,

$$Q_L = \begin{pmatrix} u_L \\ d_L \end{pmatrix}, \quad E_L = \begin{pmatrix} \nu_L \\ e_L \end{pmatrix} \tag{2.1}$$

while the RH ones u_R, d_R and e_R are $SU(2)_L$ singlets. In the current SM theory, we assume there is no RH neutrino, therefore we do not list it in Table 2.1. There exist three generations for each fermion. The gauge bosons sit in the adjoint representation of the corresponding symmetry groups. There are 8 gluons with color charge for $SU(3)_c$ QCD, 3

weak bosons for $SU(2)_L$ and one for the hypercharge. The only scalar field in the SM is represented as an $SU(2)_L$ doublet:

$$\Phi = \begin{pmatrix} \phi^+ \\ \phi^0 \end{pmatrix} \tag{2.2}$$

Field	$SU(3)_c, SU(2)_L, U(1)_Y$	Q
$Q_L = \binom{u_L}{d_L}$	$\left(\mathbf{3}, \mathbf{2}, \frac{1}{6}\right)$	$\binom{\frac{2}{3}}{-\frac{1}{3}}$
u_R	$\left(\mathbf{3}, \mathbf{1}, \frac{2}{3}\right)$	$\frac{2}{3}$
d_R	$\left(\mathbf{3}, \mathbf{1}, -\frac{1}{3}\right)$	$-\frac{1}{3}$
$E_L = \binom{\nu_L}{e_L}$	$\left(\mathbf{1}, \mathbf{2}, -\frac{1}{2}\right)$	$\binom{0}{-1}$
e_R	$(\mathbf{1}, \mathbf{1}, -1)$	-1
g_μ	$(\mathbf{8}, \mathbf{1}, 0)$	0
$(W^\pm_\mu, W^0_\mu)$	$(\mathbf{1}, \mathbf{3}, 0)$	($\pm$1,0)
B_μ	$(\mathbf{1}, \mathbf{1}, 0)$	0
$\Phi = \binom{\phi^+}{\phi^0}$	$\left(\mathbf{1}, \mathbf{2}, \frac{1}{2}\right)$	$\binom{1}{0}$

Table 2.1: Charges of the SM fields in the gauge representation. Particles listed include the fermions, gauge bosons and the Higgs.

The gauge invariant Standard Model Lagrangian consists of several pieces, can be written down concisely as:

$$\mathcal{L}_{\text{SM}} = \mathcal{L}_{\text{gauge}} + \mathcal{L}_{\text{fermion}} + \mathcal{L}_{\text{Higgs}} + \mathcal{L}_{\text{Yukawa}} \tag{2.3}$$

The meaning of each part is quite clear by the subscripts. Each individual part is reviewed in detail below.

The Lagrangian of the three gauge fields is expressed as:

$$\mathcal{L}_{\text{gauge}} = -(\frac{1}{4}G^a_{\mu\nu}G^a_{\mu\nu} + \frac{1}{4}W^i_{\mu\nu}W^i_{\mu\nu} + \frac{1}{4}B_{\mu\nu}B_{\mu\nu}) \tag{2.4}$$

containing the $SU(3)_c$, $SU(2)_L$ and $U(1)_Y$ field strength $G^a_{\mu\nu}$, $W^i_{\mu\nu}$ and $B_{\mu\nu}$, respectively:

$$\begin{aligned} G^a_{\mu\nu} &= \partial_\mu A^a_\nu - \partial_\nu A^a_\mu + g_s f^{abc} A^b_\mu A^c_\nu \\ W^i_{\mu\nu} &= \partial_\mu W^i_\nu - \partial_\nu W^i_\mu + g\epsilon^{ijk} W^i_\mu W^j_\nu \\ B_{\mu\nu} &= \partial_\mu B_\nu - \partial_\nu B_\mu \end{aligned} \tag{2.5}$$

where $a, b, c \subset 1 \ldots 8$, is the color index, $i, j, k \subset 1 \ldots 3$, is the weak index, g_s and g are the strong and weak coupling constants, respectively. f^{abc} and ϵ^{ijk} are the $SU(3)_c$ and $SU(2)_L$ structure constants, respectively, defined as:

$$[T^a, T^b] = i f^{abc} T^c \tag{2.6}$$

for the generators of $SU(3)_c$, and a similar relation holds for $SU(2)_L$.

The fermion gauge interactions are represented in the Lagragian as:

$$\mathcal{L}_{\text{fermion}} = \bar{Q}_{Li} \not{\mathcal{D}} Q_{Li} + \bar{u}_{Ri} \not{\mathcal{D}} u_{Ri} + \bar{d}_{Ri} \not{\mathcal{D}} d_{Ri} + \bar{e}_{Li} \not{\mathcal{D}} e_{Li} + \bar{e}_{Ri} \not{\mathcal{D}} e_{Ri} \tag{2.7}$$

where we sum over the index $i \subset 1 \ldots 3$, representing the family index. The "slash" notation is short for a contraction with a γ^μ matrix, like $\not{\mathcal{D}} \equiv \gamma^\mu \mathcal{D}_\mu$. The covariant derivative $\mathcal{D}_\mu$ is defined as:

$$\begin{aligned} \mathcal{D}_\mu &= \partial_\mu - i g_s T^a G^a_\mu - i g \frac{\tau^i}{2} W^i_\mu - i g' Y B_\mu, \quad \text{for LH quarks} \\ \mathcal{D}_\mu &= \partial_\mu - i g_s T^a G^a_\mu - i g' Y B_\mu, \quad \text{for RH quarks} \\ \mathcal{D}_\mu &= \partial_\mu - i g \frac{\tau^i}{2} W^i_\mu - i g' Y B_\mu, \quad \text{for LH leptons} \\ \mathcal{D}_\mu &= \partial_\mu - i g' Y B_\mu, \quad \text{for RH leptons} \end{aligned} \tag{2.8}$$

which provides the kinetic term and the gauge interaction term for the $SU(3)_c$, $SU(2)_L$ and $U(1)_Y$ gauge groups with coupling strengths g_s, g and g', respectively. Because the leptons have no $SU(3)_c$ interactions, therefore there is no $i g_s T^a G^a_\mu$ term in the leptons' covariant derivative. τ^a is the $SU(2)_L$ generator, corresponding to the Pauli matrices. T^a is the $SU(3)_c$ generator, corresponding to the Gell-Mann matrices.

So far all fermions and gauge bosons are massless, we do not write any mass term like $\frac{m_A^2}{2} A_\mu A^\mu$ or $m_\psi \bar{\psi}\psi = m_\psi(\psi_L^\dagger \psi_R + \psi_R^\dagger \psi_L)$. Those terms are not allowed for the sake

of gauge symmetry. In the Standard Model, the LH fermions and RH fermions carry different gauge charges, therefore any term such as $m_\psi \bar{\psi}\psi$ will break the gauge symmetry. For the gauge boson, even in the simplest case of $U(1)_Y$ under a gauge transformation: $A_\mu \to A_\mu + \frac{1}{e}\partial_\mu \alpha(x)$, the mass term is not gauge invariant under the gauge transformations as:

$$A_\mu A^\mu \to A_\mu A^\mu + \frac{2}{e} A^\mu \partial_\mu \alpha + \frac{1}{e^2} \partial_\mu \alpha \partial^\mu \alpha \tag{2.9}$$

But all particles are massive from the experimental measurements. What is the origin of the particle masses? We will reveal the mystery in the following section.

2.2 Electroweak symmetry breaking and the Higgs Mechanism

The Higgs field is the only scalar field in the Standard Model. It is responsible for Spontaneous Symmetry Breaking [34–37], giving mass to weak gauge bosons as described in the GWS theory of weak interactions [38–40], and giving mass to the fermions through the Yukawa interactions. The Lagrangian for the Higgs sector is:

$$\mathcal{L}_{\text{Higgs}} = |\mathcal{D}_\mu \Phi|^2 + \mu^2 \Phi^\dagger \Phi - \frac{\lambda}{2}(\Phi^\dagger \Phi)^2, \quad \Phi = \begin{pmatrix} \phi^+ \\ \phi^0 \end{pmatrix} \tag{2.10}$$

which consists of a kinetic term and potential terms with $\mu^2 > 0$ and self-coupling strength $\lambda > 0$. The Higgs field is an $SU(2)_L$ complex doublet with the $U(1)_Y$ hypercharge $Y = +1$ as defined in Eq. 2.10. The covariant derivative of Φ is defined as:

$$\mathcal{D}_\mu \Phi = (\partial_\mu - ig\frac{\tau^i}{2} W_\mu^i - ig' Y B_\mu)\Phi \tag{2.11}$$

The minimum of the potential occurs at:

$$\Phi = \begin{pmatrix} 0 \\ v \end{pmatrix} \tag{2.12}$$

with a vacuum expectation value (VEV) $v = \sqrt{\frac{\mu^2}{\lambda}}$. After the spontaneous symmetry breaking, the Higgs potential contains a mass term with mass $m = \sqrt{2}\mu$ and ϕ^3, ϕ^4 interaction terms. The spontaneous symmetry breaking also leads to the original $SU(2)_L \times U(1)_Y$ symmetry breaking down to $U(1)_{EM}$. Three massless scalar particles are created

according to Goldstone's theorem [41], and are absorbed by the gauge bosons, becoming the longitudinal degrees of freedom of the gauge bosons. Therefore the gauge bosons become massive. The masses and mass eigenstates of the gauge bosons can be calculated from the first term in Eq. 2.10 with Φ replaced with the VEV.

$$\begin{aligned}\Delta\mathcal{L} &= \frac{1}{2}\begin{pmatrix}0 & v\end{pmatrix}(gW_\mu^a\tau^a + \frac{1}{2}g'B_\mu)(gW^{b\mu}\tau^b + \frac{1}{2}g'B_\mu)\begin{pmatrix}0\\ v\end{pmatrix} \\ &= \frac{1}{2}\frac{v^2}{4}[g^2(W^1\mu)^2 + g^2(W^2\mu)^2 + (-gW_\mu^3 + g'B^\mu)^2]\end{aligned} \tag{2.13}$$

The gauge eigenstates W^1 and W^2 mix together to form mass eigenstates $W^\pm$, with mass $m_{W^\pm} = g\frac{v}{2}$; whereas the W^3 and B fields mix to form the neutral Z^0 boson, with mass $m_Z = \sqrt{g^2 + g'^2}\frac{v}{2}$ and massless photon A_μ:

$$\begin{aligned}W_\mu^\pm &= \frac{1}{\sqrt{2}}(W_\mu^1 \mp W_\mu^2), \quad \text{with mass} \quad m_{W^\pm} = g\frac{v}{2} \\ Z_\mu^0 &= \frac{1}{\sqrt{g^2 + g'^2}}(gW_\mu^3 - g'B_\mu), \quad \text{with mass} \quad m_Z = \sqrt{g^2 + g'^2}\frac{v}{2} \\ A_\mu &= \frac{1}{\sqrt{g^2 + g'^2}}(g'W_\mu^3 + gB_\mu), \quad \text{massless}\end{aligned} \tag{2.14}$$

We define the weak mixing angle θ_w to be the angle that appears in the change of basis from (W^3, B) to (Z^0,A):

$$\begin{aligned}\begin{pmatrix}Z^0\\ A\end{pmatrix} &= \begin{pmatrix}\cos\theta_w & -\sin\theta_w\\ \sin\theta_w & \cos\theta_w\end{pmatrix}\begin{pmatrix}W^3\\ B\end{pmatrix} \\ \cos\theta_w &= \frac{g}{\sqrt{g^2 + g'^2}}, \quad \sin\theta_w = \frac{g'}{\sqrt{g^2 + g'^2}}\end{aligned} \tag{2.15}$$

The masses of $W^\pm$ and Z^0 are not independent, since it follows the Eq.2.15:

$$m_W = m_Z\cos\theta_w \tag{2.16}$$

The covariant derivative (Eq. 2.11) uniquely determines the couplings of Higgs to gauge bosons and the masses of gauge bosons. Similarly, fermion masses are also generated through the Higgs boson VEV in the Standard Model. The Lagragian of Higgs-fermion Yukawa interactions can be written as:

$$\mathcal{L}_{\text{Yukawa}} = y_u\bar{Q}\Phi^c u_R + y_d\bar{Q}\Phi d_R + y_e\bar{L}\Phi e_R \tag{2.17}$$

where $\Phi^c = -i\tau_2\Phi$ is the charge conjugate of the Higgs field, $y_{u,d,e}$ are 3×3 complex matrices, and the generation indices are hidden. After electroweak symmetry breaking, the Yukawa interaction term for an electron, as an example, is:

$$\Delta\mathcal{L}_e = -\frac{1}{\sqrt{2}} y_e v \bar{e}_L e_R + \text{h.c.}, \qquad \text{with mass} \quad m_e = \frac{1}{\sqrt{2}} y_e v \tag{2.18}$$

similar relations hold for other fermions with masses proportional to the corresponding Yukawa coupling constants. One feature of the above Lagrangian is that it causes mixing between the generations of quarks when transfering from the gauge basis to the physical basis. The physical states are obtained by diagonalizing $y^{u,d}$ by four unitary matrices, $V_{L,R}^{u,d}$, as $m^f = V_L^f y^f v V_R^{f\dagger}$, $f = u, d$. As a result, the W boson couples to the physical u_{Lj} and d_{Lj} quarks with couplings given by:

$$\frac{-g}{2}(\bar{u}_L, \bar{c}_L, \bar{t}_L)\gamma^\mu W_\mu^+ V_{\text{CKM}} \begin{pmatrix} d_L \\ s_L \\ b_L \end{pmatrix} + \text{h.c.} \tag{2.19}$$

where $V_{\text{CKM}} = V_L^u V_L^{d\dagger}$ is Cabibbo-Kobayashi-Maskawa (CKM) 3×3 unitary matrix [42, 43], defined as:

$$V_{\text{CKM}} = V_L^u V_L^{d\dagger} = \begin{pmatrix} V_{ud} & V_{us} & V_{ub} \\ V_{cd} & V_{cs} & V_{cb} \\ V_{td} & V_{ts} & V_{tb} \end{pmatrix} \tag{2.20}$$

The V_{CKM} can be parameterized by three mixing angles and one CP-violating phase δ [43]. The SM very successfully generates all interactions and masses to gauge bosons and fermions, and they are consistent with the experimental measurements with astonishing accuracy.

2.3 Precision tests

Precision experiments have been essential in establishing the Standard Model. With the observation of weak neutral/charge currents [44], and the discovery of the W and Z bosons in CERN [45, 46], these key features of the Standard Model of electroweak interactions as well as the gauge structure are well established. By combining experimental inputs and

the EW theory, the existence of the top quark was predicted and later confirmed by the CDF and D0 Collaboration at Tevatron [47]. The Higgs boson was predicted theoretically a half-century ago, and was finally discovered by the ATLAS and CMS groups [1, 2]. As the tests match the SM theory with higher and higher accuracy in the current experiments at the LEP and the LHC, the SM is becoming more and more powerful in correlating experimental observables to predictions. However, as people now firmly believe that the SM is not the end of the story, it is reasonable to probe new physics from those precision tests from current experiments and future experiments. Here we briefly review the precision tests from the LEP and the LHC.

The mass and width of the Z boson, m_Z and Γ_Z, the mass of W boson, m_W and the weak mixing angle are precisely measured at LEP [4]:

$$\begin{aligned} m_Z &= 91.1875 \pm 0.0021 \quad \text{GeV} \\ \Gamma_Z &= 2.4952 \pm 0.0023 \quad \text{GeV} \\ m_W &= 80.363 \pm 0.032 \quad \text{GeV} \\ \sin^2\theta_w &= 0.23153 \pm 0.00016 \end{aligned} \tag{2.21}$$

The sensitivity of the SM observables to the mass of the top quark from LEP is shown in the left panel of Fig 2.1. The LEP experiment measured the SM observables at Z-pole, while the Tevatron and the LHC can measure the properties of the top quark and Higgs boson more accurately. The top quark mass is measured accurately by combining the measurements of the CDF and D0 experiments at the Tevatron collider and the ATLAS and CMS experiments at the LHC [5], which reads $m_t = 173.34 \pm 0.27$ (stat) ± 0.71 (syst) GeV. An improved measurement of the mass of the Higgs boson is made by both the ATLAS and CMS group. From the high-resolution $\gamma\gamma$ and ZZ channel with about 25 fb^{-1} data collected at the $\sqrt{s} = 7$ and 8 TeV LHC, the Higgs mass is measured at $m_h = 125.36 \pm$ 0.37 (stat)$\pm$0.18 (syst) GeV by the ATLAS group [7] and $m_h = 125.02^{+0.26}_{-0.27}$ (stat)$^{+0.14}_{-0.15}$ (syst) GeV by the CMS group [9]. Combined analyses of the Higgs boson production and decay rates as well as its coupling strengths to vector bosons and fermions are presented by both the ATLAS and CMS group. Combining all production modes and decay channels ($h \to \gamma\gamma, ZZ, W^+W^-, Z\gamma, b\bar{b}, \tau\tau, \mu\mu$), the measured signal yield, normalised to the Standard

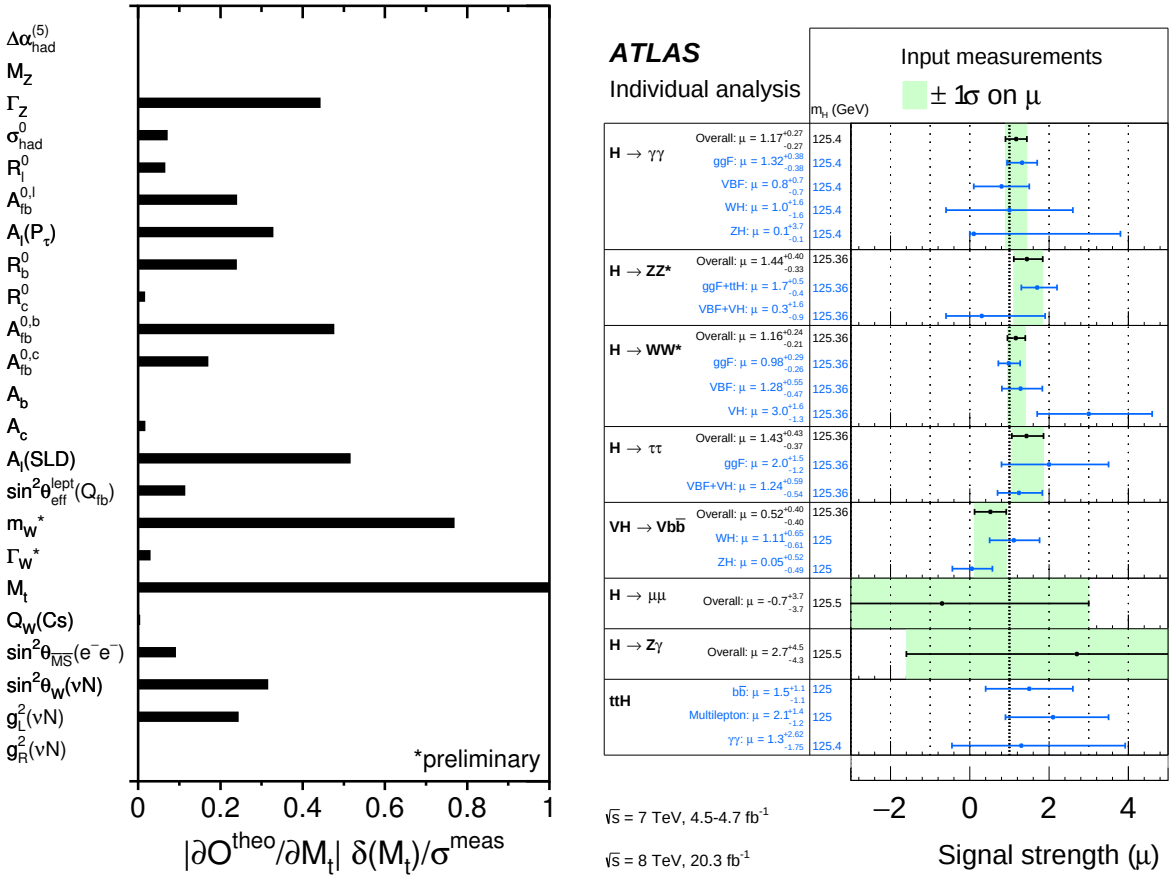

Figure 2.1: Left panel shows the sensitivity of each pseudo-observable to the mass of the top quark, defined as the partial derivative of the SM calculation of the observable with respect to m_t, figure extracted from Ref.[4]. A summary of the signal-strength measurements of the Higgs boson is in the right panel, figure extracted from Ref.[8]

Model expectation is $1.18^{+0.15}_{-0.14}$ [8]. The summary of the signal-strength measurements of the Higgs boson is shown in the right panel of Fig 2.1.

2.4 Unsolved puzzles

Even though the SM has achieved great success, it is still incomplete. There are some puzzles beyond the explaination of the Standard Model, including the "hierarchy problem", the dark matter issue, gauge coupling unification and baryon asymmetry. In this section, we will investigate those puzzles in detail.

2.4.1 The Hierarchy Problem

The Higgs boson was discovered by the ATLAS and CMS group [1, 2], with mass m_h = 125.36 GeV. This is a great success completing the last missing piece of the Standard Model, however, there is still an unsatisfactory feature in the model. The problem lies in the radiative corrections to Higgs mass from loops of higher order, which is quadratically divergent. The contribution from the top quark is dominant because of the large top Yukawa coupling, as shown in Fig 2.2, yielding a correction as [25]:

$$\Delta m_h^2 = -\frac{y_t^2}{8\pi^2}\left(\Lambda^2 - 2m_t^2 \log \Lambda/m_t + ...\right) \tag{2.22}$$

where y_t is the top Yukawa coupling and Λ is an ultraviolet momentum cutoff used to regulate the loop integral. It should be interpreted as the energy scale at which new physics enters to alter the high-energy behavior of the theory. A natural scale for new physics is the Plank scale $M_P = \frac{1}{\sqrt{8\pi G}} \sim 10^{19}$ GeV, at which the quantum gravity effect starts to be manifest. The problem is that the quadratically divergent quantum correction Λ^2 is about 34 orders of magnitude larger than the Higgs mass squared, measured at $(125.36 \text{ GeV})^2$. To mitigate this problem, the counter terms need to be precisely tuned to 1 part in 10^{34} to recover the physical Higgs mass of 125.36 GeV. This disparity between the weak and gravitational scale is, in essence, the "Hierarchy Problem" [10]. SUSY proposes a new space time symmetry relating the fermions to bosons. The bosonic one-loop corrections to the Higgs mass square is the same magnitude as that of fermions but with opposite sign, resolving the "Hierarchy Problem" elegantly. The SUSY will be discussed in detail in Chapter 3.

2.4.2 Dark matter puzzle

The observed expansion of the Universe is a natural (almost inevitable) result of any homogeneous and isotropic cosmological model based on Einstein's general relativity. The Robertson-Walker metric and Friedmann equations of motion incorporating a Λ term which is known as vacuum energy, describe the Universe with a high correlation to observations. The "Standard Model" of cosmology states that the Universe is spatially flat and is expanding at an increasing rate [48, 49]. And it is made up of radiation, baryonic matter,

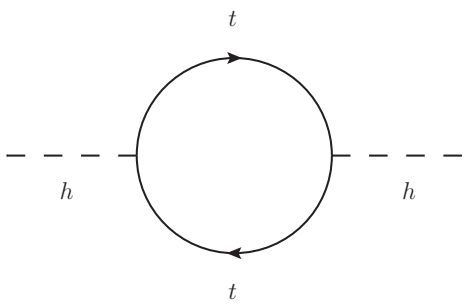

Figure 2.2: One-loop quantum corrections to the Higgs mass squared from the top quark.

some unknown matter which is referred to as Dark Matter, and a dark energy component which is the Λ term in the Friedmann equations. Moreover, the Universe is dominated by the unknown Cold Dark Matter (CMD) and energy components; thus the model is referred to as ΛCDM. As the Universe expanded and cooled, the density of particles became too low to support frequent interactions and conditions for thermal equilibrium were violated. Then particles are said to "freeze out" and the number density remained constant. The density of a specific particle at the time of freeze out is known as the relic density of that particle. Observations including galaxy rotation curve [50], weak gravitational lensing of distant galaxies by foreground structure [51], and the velocity dispersions of dwarf spheroidal galaxies [52] all indicate the existence of dark matter. From the analysis of the Wilkinson Microwave Anisotropy Probe (WMAP) data, Planck data, Cosmic Microwave Background (CMB) data and Baryon Acoustic Oscillations (BAO) data, the relic densities can be extracted [53]:

$$\begin{aligned} \Omega_b h^2 &= 0.02211 \pm 0.00034, \quad \Omega_c h^2 = 0.1162 \pm 0.0020 \\ \Omega_\Lambda h^2 &= 0.33465 \pm 0.0128, \quad h = 0.688 \pm 0.008 \end{aligned} \tag{2.23}$$

where h is the Hubble constant in units of 100 km/(sMpc).

The composition of the dark matter component of our Universe is relatively unknown. From observations, we have the following constraints on dark matter [54]: It is

- Massive, otherwise the relic density of dark matter does not match the observations. This criterion excludes the SM neutrinos because the relic density of the neutrino is

too small ($\Omega_\nu h^2 < 0.07$) given the upper limit on the neutrino mass $m_\nu < 2.05$ eV (95% C.L.) [54], while the observation value in Eq. 2.23 shows the relic density of DM is about 0.1162.

- Stable, that is its lifetime should be at a scale comparable to the age of the Universe, otherwise the current shape of the Universe can not be formed.
- "Weakly" interacting.
- Cold, that is it propagates non-relativistically, for the same reasoning as item 2.

These constraints rule out all particles of the Standard Model, so the existence of dark matter implies new physics beyond the Standard Model. A common type of dark matter falls in the category of a weakly interacting massive particle (WIMP) with a mass roughly between 10 GeV and a few TeV [53]. After the WIMPs freeze out when the rate of reactions that change SM particles into WIMPs or vice versa becomes smaller than the Hubble expansion rate of the Universe, the co-moving WIMP density remains essentially constant, is given by [53]:

$$\Omega_{DM} h^2 \simeq \frac{0.1\text{pb} \times c}{\langle \sigma_A v \rangle} \tag{2.24}$$

where σ_A is the total annihilation cross section of a pair of WIMPs into SM particles, v is the relative velocity and $\langle ... \rangle$ denotes thermal averaging. Given the WIMP mass region and couplings, the calculated relic density falls in the observed range. Many extensions of the Standard Model have WIMP candidates. One well motivated WIMP candidate is the LSP in the supersymmetric model with exact R-parity. This will be discussed in detail in Chapter 3. Other WIMP candidates include the "Little Higgs" model [55–58] which contains possible dark matter candidates [59], Kaluza-Klein excitation states of the Standard Model fields which appear in models of universal extra dimensions [60], and light scalar dark matter [61, 62].

2.4.3 Gauge coupling unification

The SM is a renormalized theory of gauge group $SU(3)_c \times SU(2)_L \times U(1)_Y$. It can be described by the Renormalization Group Equation (RGE, also called β function), giving

the rate at which the renormalized coupling constant changes as the renormalization scale Q is increased. The β function of the non-Abelian gauge group is significantly different from that of the Abelian gauge group. In a non-Abelian gauge group like QCD with a strong coupling constant, it obeys the Asymptotic freedom [63, 64], which states that the gauge coupling constant becomes progressively larger as the renormalization scale Q is decreased. The 1-loop RGE for the Standard Model gauge couplings g_1, g_2 and g_3 are [25, 65, 66]:

$$\beta_{g_a} \equiv \frac{d}{dt} g_a = \frac{1}{16\pi^2} b_a g_a^3, \quad (b_1, b_2, b_3) = \begin{cases} (41/10, -19/6, -7) & \text{Standard Model} \\ (33/5, 1, -3) & \text{MSSM} \end{cases} \tag{2.25}$$

where $t = \ln(Q/Q_0)$, with Q the RG scale. The MSSM coefficients are larger because of the extra MSSM particles in the loops. Thus, in terms of the conventional electroweak gauge couplings g and g', one has $g_1 = \sqrt{\frac{5}{3}} g'$, $g_2 = g$. The quantities $\alpha_a = g_a^2/4\pi$ have the nice property that their reciprocals run linearly with the logarithmic RG scale at one-loop order:

$$\frac{d}{dt} \alpha_a^{-1} = -\frac{b_a}{2\pi} \tag{2.26}$$

Figure 2.3 compares the RG evolution of the quantities α_a^{-1} including two-loop radiative corrections in the Standard Model (dashed lines) and MSSM (solid lines). Unlike the Standard Model, the MSSM includes just the exact particle content to ensure that the gauge couplings can unify, at a scale of $Q \sim 1.5 \times 10^{16}$ GeV.

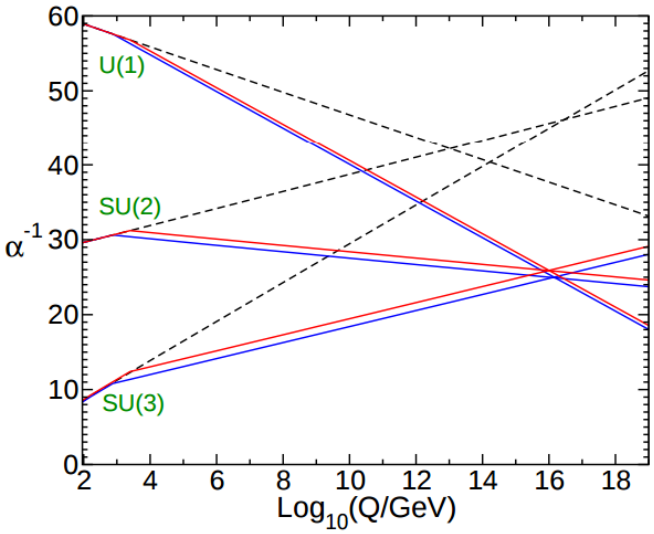

Figure 2.3: Two-loop renormalization group evolution of α_a^{-1} in the Standard Model (dashed lines) and MSSM (solid lines), figure credited to Ref.[25].

CHAPTER 3

Minimal Supersymmetric Standard Model and Two Higgs Doublet Model

The Standard Model provides a remarkably successful description of presently known phenomena. However, the unknown theoretical dilemma, experimental measurements and cosmological observations are beyond the explanations of the Standard Model, all of which imply new physics beyond the Standard Model. There are many extensions of the Standard Model, of which I will focus on one supersymmetric extension of the Standard Model - Minimum Supersymmetric Standard Model (MSSM) and the Two Higgs Doublet Model (2HDM). There are many motivations of MSSM, including: the MSSM provides a solution to the hierarchy problem by postulating a new symmetry relating fermions to bosons; the MSSM can provide a potential candidate for dark matter assuming R-parity conservation and the MSSM can also provide a solution to the unification of gauge couplings at two-loop radiative corrections. In this chapter, I will review the MSSM and 2HDM including the theoretical structure, particle contents and interactions in detail. For a more complete review, please read Ref. [25, 67].

3.1 Motivation for SUSY

The "Hierarchy Problem" in the Standard Model can be solved by assuming that there exists a heavy scalar particle S with mass m_S that couples to the Higgs with a ϕ^4 interaction term as $-\lambda_S |H|^2 |S|^2$. Then the one-loop Feymann diagram in Figure 3.1 gives a correction to Higgs mass square:

$$\Delta m_h^2 = \frac{\lambda_S}{16\pi^2} \left(\Lambda^2 - 2m_S^2 \log \Lambda / m_S + ... \right) \tag{3.1}$$

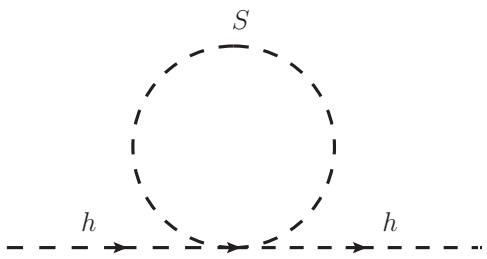

Figure 3.1: One-loop quantum corrections to the Higgs mass square from a scalar with ϕ^4 interaction to Higgs boson.

where Λ is the momentum cutoff where new physics enters. The radiative correction at one loop level by fermions is given in Eq. 2.22. Fortunately, SUSY postulates that the couplings of corresponding fermions and bosons are equal, such that the Λ^2 contributions from fermions and bosons are neatly cancelled out. The remaining corrections to the Higgs are only logarithmically divergent. Such symmetry relating fermions to bosons, is called a **Supersymmetry**.

A supersymmetric transformation with generators Q_S, turns a fermionic state into a bosonic state, and vice versa, therefore the operator Q_S must be an anti-commuting spinor:

$$Q_S|\text{Boson}\rangle = |\text{Fermion}\rangle, \qquad Q_S|\text{Fermion}\rangle = |\text{Boson}\rangle \tag{3.2}$$

The corresponding fermionic and bosonic states, which are superpartners of each other, fall into irreducible representations of the supersymmetry algebra, called supermultiplets. Importantly, the generators Q_S, $Q_S^\dagger$ commute with the generators of gauge transformations, therefore particles in the same supermultiplet must also be in the same representation of the gauge group, and so must have the same electric charges, weak and color degrees of freedom. The superpartners of quark and lepton are called *squark* and *slepton*, short for "scalar quark" and "scalar lepton", or sometimes $sfermion$. The superpartners of gauge bosons (B, W and gluon) are called *gaugino* ($Bino$, $Wino$, $gluino$). The particle states fall into two irreducible representations of the supersymmetry algebra: a chiral supermultiplet with a two-component Weyl fermion and a complex scalar field, and a gauge supermultiplet with spin-1/2 gauginos and spin-1 gauge bosons. It turns out that one Higgs doublet is not suffcient in the SUSY model, so an extra Higgs doublet is added for two reasons. First,

spin 0	spin 1/2	$SU(3)_c, SU(2)_L, U(1)_Y$	Q
$\tilde{Q}_L = \binom{\tilde{u}_L}{\tilde{d}_L}$	$Q_L = \binom{u_L}{d_L}$	$\left(\mathbf{3}, \mathbf{2}, \frac{1}{6}\right)$	$\binom{\frac{2}{3}}{-\frac{1}{3}}$
$\tilde{u}_R$	u_R	$\left(\mathbf{3}, \mathbf{1}, \frac{2}{3}\right)$	$\frac{2}{3}$
$\tilde{d}_R$	d_R	$\left(\mathbf{3}, \mathbf{1}, -\frac{1}{3}\right)$	$-\frac{1}{3}$
$\tilde{E}_L = \binom{\tilde{\nu}_L}{\tilde{e}_L}$	$E_L = \binom{\nu_L}{e_L}$	$\left(\mathbf{1}, \mathbf{2}, -\frac{1}{2}\right)$	$\binom{0}{-1}$
$\tilde{e}_R$	e_R	$(\mathbf{1}, \mathbf{1}, -1)$	-1
$H_u = \binom{H_u^+}{H_u^0}$	$\tilde{H}_u = \binom{\tilde{H}_u^+}{\tilde{H}_u^0}$	$\left(\mathbf{1}, \mathbf{2}, \frac{1}{2}\right)$	$\binom{1}{0}$
$H_d = \binom{H_d^0}{H_d^-}$	$\tilde{H}_d = \binom{\tilde{H}_d^0}{\tilde{H}_d^-}$	$\left(\mathbf{1}, \mathbf{2}, -\frac{1}{2}\right)$	$\binom{0}{-1}$

Table 3.1: Charges of Chiral supermultiplets in the gauge representation in the MSSM.

the extra Higgs doublet cancels the gauge anomalies from the two fermionic members of the Higgs chiral supermultiplets, which satisfies the gauge anomalies cancellation. Second, because of the structure of supersymmetric theories, a $Y = \frac{1}{2}$ Higgs doublet can only have the necessary Yukawa couplings to give masses to the up-type quarks (up, charm, top), and a $Y = -\frac{1}{2}$ Higgs doublet can only have the necessary Yukawa couplings to give masses to the down-type quarks (down, strange, bottom) and the charged leptons. The particle contents in MSSM are shown in Table 3.1 and Table 3.2.

The particle contents within a supermultiplet have exactly same quantum numbers and coupling constants, therefore the particles and corresponding superpartners are expected to have exactly the same masses if supersymmetry is an exact symmetry. In fact, all Standard Model particles are already discovered while none of their corresponding superpartners have been discovered. This interesting feature of the theory indicates clearly that the supersymmetry must be a broken symmetry, incorporating other mass sources for the superpartners.

spin 1/2	spin 1	$SU(3)_c, SU(2)_L, U(1)_Y$	Q
$\tilde{g}_\mu$	g	$(\mathbf{8},\mathbf{1},0)$	0
$(\tilde{W}^\pm_\mu, \tilde{W}^0_\mu)$	$(W^\pm_\mu, W^0_\mu)$	$(\mathbf{1},\mathbf{3},0)$	$(\pm1,0)$
$\tilde{B}_\mu$	B_μ	$(\mathbf{1},\mathbf{1},0)$	0

Table 3.2: Charges of gauge supermultiplets in the gauge representation in the MSSM.

3.2 The Minimal Supersymmetric Standard Model and Soft Supersymmetry Breaking

The superpotential for the MSSM is:

$$W_{MSSM} = \bar{u}\mathbf{y_u}QH_u - \bar{d}\mathbf{y_d}QH_d - \bar{e}\mathbf{y_e}QH_d + \mu H_u H_d \tag{3.3}$$

where all the gauge ($SU(3)_c$ and $SU(2)_L$) and family indices are suppressed. The dimensionless Yukawa coupling parameters $\mathbf{y_u}, \mathbf{y_d}, \mathbf{y_e}$ are 3×3 matrices in family space. The Lagrangian including all interaction terms can be written down from the MSSM superpotential as:

$$\mathcal{L} = -W^i W^*_i - \frac{1}{2}(W^{ij}\psi_i\psi_j + W^*_{ij}\psi^{\dagger i}\psi^{\dagger j}) \tag{3.4}$$

with definitions:

$$\begin{aligned} W^i &\equiv \frac{\delta W}{\delta \phi_i} = M^{ij}\phi_j + \frac{1}{2}y^{ijk}\phi_j\phi_k \\ W^{ij} &\equiv \frac{\delta^2}{\delta\phi_i\delta\phi_j}W = M^{ij} + y^{ijk}\phi_k \end{aligned} \tag{3.5}$$

where M^{ij} is the mass term for the chiral superfield and y^{ijk} is the Yukawa coupling corresponding to $\mathbf{y_u}, \mathbf{y_d}, \mathbf{y_e}$ in the above equation.

Since the third generation fermions have the largest Yukawa coupling and SUSY superpartners have the same Yukawa coupling as the corresponding Standard Model particles,

it is reasonable to make an approximation to the Yukawa 3×3 parameter matrices:

$$\mathbf{y_u} \approx \begin{pmatrix} 0 & 0 & 0 \\ 0 & 0 & 0 \\ 0 & 0 & y_t \end{pmatrix}, \qquad \mathbf{y_d} \approx \begin{pmatrix} 0 & 0 & 0 \\ 0 & 0 & 0 \\ 0 & 0 & y_b \end{pmatrix}, \qquad \mathbf{y_e} \approx \begin{pmatrix} 0 & 0 & 0 \\ 0 & 0 & 0 \\ 0 & 0 & y_\tau \end{pmatrix} \tag{3.6}$$

After the approximation, the superpotential for the MSSM is:

$$W_{MSSM} \approx y_t(\bar{t}tH_u^0 - \bar{t}bH_u^+) - y_b(\bar{b}tH_d^- - \bar{b}bH_d^0) - y_\tau(\bar{\tau}\nu_\tau H_d^- - \bar{\tau}\tau H_d^0) + \mu(H_u^+ H_d^- - H_u^0 H_d^0) \tag{3.7}$$

In the Standard Model, the Higgs boson couples to lepton-lepton or quark-quark through Yukawa interactions, while the Yukawa terms $\mathbf{y_u}, \mathbf{y_d}, \mathbf{y_e}$ in the MSSM superpotential implies the Higgsino-squark-quark and Higgsino-slepton-lepton interactions. The ϕ^3 and ϕ^4 interactions are quite rich in the MSSM: the ϕ^3 terms include Higgs-squark-squark, Higgs-slepton-slepton with a mass parameter μ, and $(Higgs)^3$; the ϕ^4 terms include $(squark)^4$, $(slepton)^4$, $(squark)^2(slepton)^2$, $(squark)^2(Higgs)^2$, $(slepton)^2(Higgs)^2$, and $(Higgs)^4$. Other than the normal gauge interactions in the Standard Model, there are squark-quark-gaugino, slepton-lepton-gaugino, and Higgs-Higgsino-gaugino interactions. Some of the Feymann diagrams are shown in Figure 3.2, Figure 3.3 and Figure 3.4.

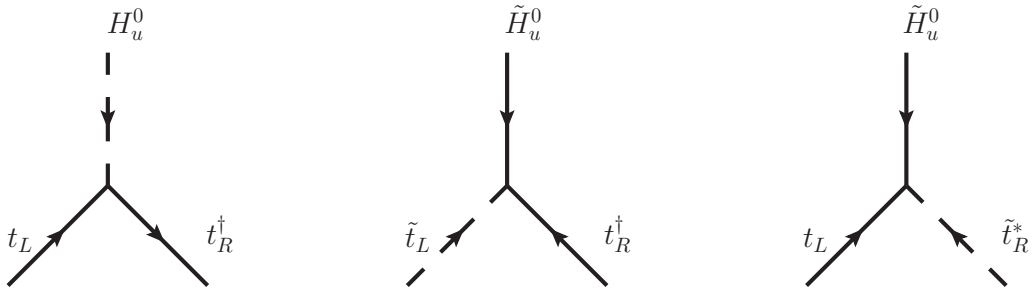

Figure 3.2: The Higgs-quark-quark and its supersymmetric version Higgsino-squark-quark interactions.

From the last term in the MSSM potential of Eq. 3.7, the mass term for the Higgsinos can be writen as:

$$\mathcal{L}_{\tilde{H}} = -\mu(\tilde{H}_u^+ \tilde{H}_d^- - \tilde{H}_u^0 \tilde{H}_d^0) + \text{c.c.} \tag{3.8}$$

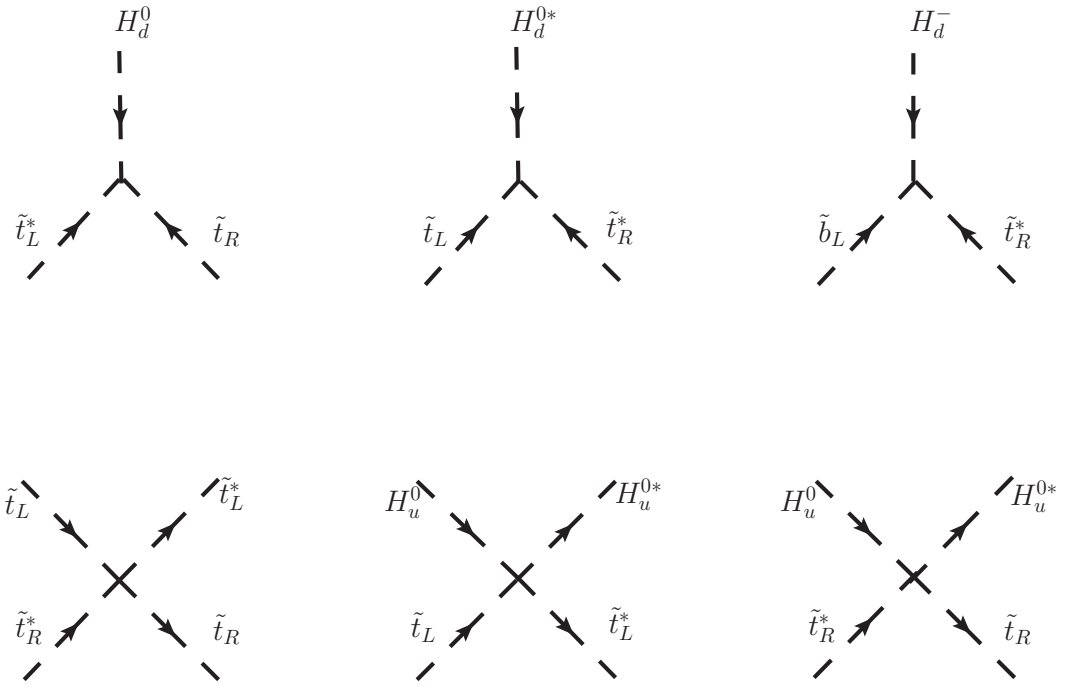

Figure 3.3: The ϕ^3 and ϕ^4 interactions are on the top panel and bottom panel, respectively.

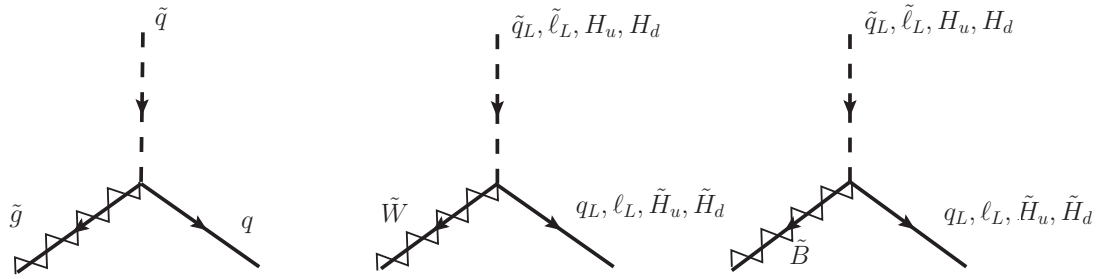

Figure 3.4: Interactions of the Gluino, Wino, and Bino to MSSM (scalar, fermion) pairs.

From a theoretical perspective, we expect supersymmetry to be an exact symmetry at a certain high energy scale, but to be spontaneously broken at low energy, in a manner analogous to the electroweak symmetry breaking in the Standard Model. The mechanism of SUSY breaking is still unknown, however, many models of spontaneous symmetry breaking have been proposed, including gravity mediated (MSUGRA), gauge mediated (GMSB), and a anomaly mediated (AMSB) symmetry breaking mechanism. Here we will not review the various conjectured mechanisms of spontaneous symmetry breaking, for a detailed review, refer to Ref. [68–72]. The soft supersymmetry breaking terms introduce the mass terms for the SUSY particles, leading to different masses for Standard Model particles and their corresponding superpartners. Therefore, the SUSY particles can be hidden at a certain high energy scale, which matches the null searching results from the ATLAS and CMS experimental searches. The most general form of the SUSY breaking term is:

$$\begin{aligned}\mathcal{L}_{\text{soft}} = &-\frac{1}{2}(M_3\tilde{g}\tilde{g} + M_2\tilde{W}\tilde{W} + M_1\tilde{B}\tilde{B} + \text{c.c.}) \\ &- (\tilde{\bar{u}}\ \mathbf{a_u}\tilde{Q}H_u - \tilde{\bar{d}}\ \mathbf{a_d}\tilde{Q}H_d - \tilde{\bar{e}}\ \mathbf{a_e}\tilde{L}H_d + \text{c.c.}) \\ &- \tilde{Q}^\dagger\mathbf{m_Q^2}\tilde{Q} - \tilde{\bar{u}}^\dagger\mathbf{m_u^2}\tilde{\bar{u}} - \tilde{\bar{d}}^\dagger\mathbf{m_d^2}\tilde{\bar{d}} - \tilde{L}^\dagger\mathbf{m_L^2}\tilde{L} - \tilde{\bar{e}}^\dagger\mathbf{m_e^2}\tilde{\bar{e}} \\ &- m_{H_u}^2 H_u^* H_u - m_{H_d}^2 H_d^* H_d - (bH_uH_d + \text{c.c.})\end{aligned} \tag{3.9}$$

where M_1, M_2 and M_3 are the Bino, Wino and Gluino mass terms. $\mathbf{a_u}$, $\mathbf{a_d}$ and $\mathbf{a_e}$ are the couplings for the ϕ^3 interaction terms; they are a 3×3 matrix in family space with dimensions of [mass]. The third line contains the squark and slepton mass terms, with a $\mathbf{m_Q^2}, \mathbf{m_u^2}, \mathbf{m_d^2}, \mathbf{m_L^2}, \mathbf{m_e^2}$ 3×3 matrix in family space. The last line consists of supersymmetry-breaking mass terms to the Higgs potential. The coupling and mass parameters are expected to be "soft" at a energy scale of TeV, to retain the cancellation of the quadratic divergence of the Higgs mass without large fine tuning. There are a total of 105 parameters [73] in the MSSM, including masses, phases, mixing angles which can not be rotated away by any symmetry, and CP violating phase angles. In fact, the soft breaking terms introduce a tremendous arbitrariness in the Lagrangian and have no counterparts in the Standard Model.

According to the structure of superpotential, we can write down some terms which are gauge invariant, supersymmetric invariant and renormalizable but violate the lepton

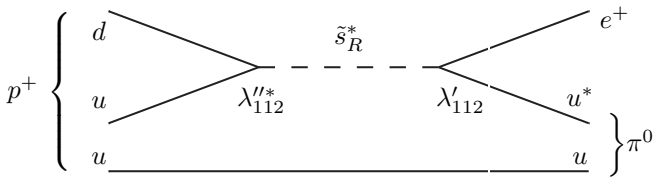

Figure 3.5: Feynman diagram of proton decay via B- and L-violating terms of the form shown in Eq. 3.10.

number and baryon number:

$$\begin{aligned} W_{\Delta \mathrm{L}=1} &= \frac{1}{2}\lambda^{ijk} L_i L_j \bar{e}_k + \lambda'^{ijk} L_i Q_j \bar{d}_k + \mu'^i L_i H_u \\ W_{\Delta \mathrm{B}=1} &= \frac{1}{2}\lambda''^{ijk} \bar{u}_i \bar{d}_j \bar{d}_k \end{aligned} \tag{3.10}$$

These terms cause severe problems because the Standard Model does not allow the lepton and baryon violating processes which have not been observed experimentally. If the couplings λ's and μ' were unsuppressed, the above two terms would cause proton decay, leading to an extremely short lifetime of the proton. However, the lifetime of the proton is strongly constrained by experiment [74]. The Feymann diagram in Figure 3.5 shows the proton decay $p^+ \to e^+\pi^0$ induced by the B- and L-violating terms. Therefore, to avoid the proton decay phenomenologically, we add a new symmetry in the MSSM, which has the effect of eliminating the possibility of B and L violating terms in the renormalizable superpotential, while keeping the allowed terms in Eq. 3.3. The new symmetry is called "R-parity" [75], which is defined as below:

$$P_R = (-1)^{3(B-L)+2s} \tag{3.11}$$

where B is the baryon number, L is the lepton number, and s is the spin of the particle. It can be seen that all of the Standard Model particles and the Higgs bosons have even R-parity ($P_R = 1$), while all of the squarks, sleptons, gauginos, and higgsinos have odd R-parity ($P_R = -1$). The R-parity conservation is very useful from the sense of phenomenology:

- The terms that violate the baryon and lepton numbers are now forbidden.

- There is no mixing between particles with positive R-parity and its superpartners with negative R-parity.
- The SUSY particles must be produced in even number in collider experiments.
- The lightest supersymmetric particle (LSP) must be absolutely stable, which makes it an attractive non-baryonic dark matter candidate.
- Other SUSY particles will eventually decay into Standard Model particles and an odd number of LSPs.

3.3 The Higgs sector and Electroweak Symmetry Breaking

In the MSSM, the Higgs sector contains two complex doublets $H_u = (H_u^+, H_u^0)$ and $H_d = (H_d^+, H_d^0)$, which makes the electroweak symmetry breaking more complicated. The scalar potential for the Higgs sector in the MSSM is described as:

$$\begin{aligned} V = &(|\mu|^2 + m_{H_u}^2)(\left|H_u^0\right|^2 + \left|H_u^+\right|^2) + (|\mu|^2 + m_{H_d}^2)(\left|H_d^0\right|^2 + \left|H_d^-\right|^2) \\ &+ [b(H_u^+ H_d^- - H_u^0 H_d^0) + \text{c.c.}] + \frac{1}{2} g^2 \left|H_u^+ H_d^{0*} + H_u^0 H_d^{-*}\right|^2 \\ &+ \frac{1}{8}(g^2 + g'^2)(\left|H_u^0\right|^2 + \left|H_u^+\right|^2 - \left|H_d^0\right|^2 - \left|H_d^-\right|^2)^2 \end{aligned} \tag{3.12}$$

where the $|\mu|^2$ terms come from the F-term which is introduced to balance the degrees of freedom when the chiral supermultiplet is off shell, the g^2 and g'^2 terms come from the D-term contribution which is introduced to balance the degrees of freedom when the gauge supermultiplet is off shell, the $m_{H_u}^2$, $m_{H_d}^2$ and b terms are the soft breaking mass terms, and the g and g' are the couplings of the $SU(2)_L$ and $U(1)_Y$ gauge groups, respectively. Similar to the Standard Model, the two Higgs doublets get VEVs to break the Electroweak symmetry, $SU(2)_L \times U(1)_Y \to U(1)_{EM}$. The VEVs can be writen as:

$$\frac{1}{\sqrt{2}} v_u = \left\langle H_u^0 \right\rangle, \qquad \frac{1}{\sqrt{2}} v_d = \left\langle H_d^0 \right\rangle, \tag{3.13}$$

satisfying the condition:

$$v^2 = v_u^2 + v_d^2 = (247 \text{ GeV})^2. \tag{3.14}$$

The ratio of the two VEVs is defined as:

$$\tan\beta = v_u/v_d. \tag{3.15}$$

where the β is chosen to be in the first quadrant ($0 < \beta < \pi/2$) by convention. The conditions of the potential minimum $\partial V/\partial H_u^0 = \partial V/\partial H_d^0 = 0$ can be expressed as:

$$\begin{aligned} m_{H_u}^2 + |\mu|^2 - b\cot\beta - \frac{1}{2}m_Z^2\cos(2\beta) = 0 \\ m_{H_d}^2 + |\mu|^2 - b\tan\beta + \frac{1}{2}m_Z^2\cos(2\beta) = 0 \end{aligned} \tag{3.16}$$

After spontaneous symmetry breaking, three bosons are the would-be Nambu-Goldstone bosons G^0, $G^\pm$, which become the longitudinal modes of the Z^0 and $W^\pm$ bosons, giving masses to the Z^0 and $W^\pm$ bosons as in the mechanism in the SM. The remaining five physical Higgs bosons consist of two CP-even neutral scalars h and H, one CP-odd neutral scalar A, and two charge scalars $H^\pm$. The gauge-eigenstate fields can be expressed in terms of the mass eigenstate fields as:

$$\begin{aligned} \begin{pmatrix} H_u^0 \\ H_u^+ \end{pmatrix} = \begin{pmatrix} \frac{1}{\sqrt{2}}(v_u + h + G^0) \\ G^+ \end{pmatrix} \\ \begin{pmatrix} H_d^- \\ H_d^0 \end{pmatrix} = \begin{pmatrix} H^- \\ \frac{1}{\sqrt{2}}(v_d + H + A) \end{pmatrix} \end{aligned} \tag{3.17}$$

Pluging Eq. 3.17 into the Higgs scalar potential, obtains the mass matrices for the mass eigenstates. The mass matrix of CP-odd neutral scalar can be written as:

$$\mathcal{M}_A^2 = \begin{pmatrix} |\mu|^2 + m_{H_d}^2 + \frac{1}{2}m_Z^2\cos(2\beta) & -b \\ -b & |\mu|^2 + m_{H_u}^2 - \frac{1}{2}m_Z^2\cos(2\beta) \end{pmatrix} = b\begin{pmatrix} \tan\beta & -1 \\ -1 & \cot\beta \end{pmatrix} \tag{3.18}$$

the second equation is derived from Eq. 3.16. Then the masses and the mass eigenstates are obtained after diagonalizing the mass matrix:

$$\begin{aligned} m_A^2 &= 2b/\sin(2\beta) = 2|\mu|^2 + m_{H_d}^2 + m_{H_u}^2 \\ m_{G^0}^2 &= 0 \\ \begin{pmatrix} G^0 \\ A \end{pmatrix} &= \begin{pmatrix} \sin\beta & -\cos\beta \\ \cos\beta & \sin\beta \end{pmatrix}\begin{pmatrix} H_u^0 \\ H_d^0 \end{pmatrix} \end{aligned} \tag{3.19}$$

The charged Higgs has the following mass matrix:

$$\mathcal{M}^2_{H^\pm} = \begin{pmatrix} |\mu|^2 + m^2_{H_d} + \frac{1}{2}m^2_Z\cos(2\beta) + m^2_W\cos^2\beta & b + m^2_W\sin\beta\cos\beta \\ b + m^2_W\sin\beta\cos\beta & |\mu|^2 + m^2_{H_u} - \frac{1}{2}m^2_Z\cos(2\beta) + m^2_Z\sin^2\beta \end{pmatrix} \tag{3.20}$$

with masses and mass eigenstates:

$$\begin{aligned} m^2_{H^\pm} &= 2|\mu|^2 + m^2_{H_d} + m^2_{H_u} + m^2_W = m^2_A + m^2_W \\ m^2_{G^\pm} &= 0 \\ \begin{pmatrix} G^+ \\ H^+ \end{pmatrix} &= \begin{pmatrix} \sin\beta & -\cos\beta \\ \cos\beta & \sin\beta \end{pmatrix} \begin{pmatrix} H^+_u \\ H^{-*}_d \end{pmatrix} \end{aligned} \tag{3.21}$$

For the CP-even neutral scalars:

$$\mathcal{M}^2_{h,H} = \begin{pmatrix} |\mu|^2 + m^2_{H_d} + \frac{1}{2}m^2_Z\cos(2\beta) + m^2_Z\cos^2\beta & -b - m^2_Z\sin\beta\cos\beta \\ -b - m^2_Z\sin\beta\cos\beta & |\mu|^2 + m^2_{H_u} - \frac{1}{2}m^2_Z\cos(2\beta) + m^2_Z\sin^2\beta \end{pmatrix} \tag{3.22}$$

the masses and mass eigenstates for h and H can be obtained to diagonalize its mass matrix:

$$\begin{aligned} m^2_h &= \frac{1}{2}\Big(m^2_A + m^2_Z - \sqrt{(m^2_A - m^2_Z)^2 + 4m^2_A m^2_Z\sin^2(2\beta)}\Big) \\ m^2_H &= \frac{1}{2}\Big(m^2_A + m^2_Z + \sqrt{(m^2_A - m^2_Z)^2 + 4m^2_A m^2_Z\sin^2(2\beta)}\Big) \\ \begin{pmatrix} h \\ H \end{pmatrix} &= \begin{pmatrix} \cos\alpha & -\sin\alpha \\ \sin\alpha & \cos\alpha \end{pmatrix} \begin{pmatrix} H^0_u \\ H^0_d \end{pmatrix} \end{aligned} \tag{3.23}$$

The mixing angle α is determined, at tree-level, by

$$\frac{\sin 2\alpha}{\sin 2\beta} = -\frac{m^2_H + m^2_h}{m^2_H - m^2_h}, \qquad \frac{\tan 2\alpha}{\tan 2\beta} = \frac{m^2_A + m^2_Z}{m^2_A - m^2_Z} \tag{3.24}$$

In the MSSM, the masses of quarks and leptons are determined not only by the Yukawa coupling, but also by the parameter $\tan\beta$. This is because the up-type quarks (top, charm and up) couple to H_u, with a mass proportional to $v_u = v\sin\beta$ and the down-type quarks (bottom, strange, and down) and the charged leptons couple to H_d, with a mass

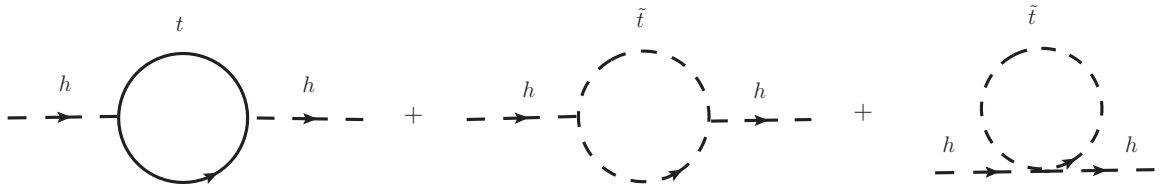

Figure 3.6: One loop quantum corrections to Higgs mass square from both top quark and top squark. The quadratic divergence of Higgs mass square is cancelled perfectly between the first and third Feymann diagrams. The left correction is only logarithm divergent.

proportional to $v_d = v\cos\beta$. In other words, the Yukawa couplings of the MSSM are scaled compared to the Standard Model, especially for the third generation. We have:

$$y_t = \frac{m_t}{v\sin\beta}, \qquad y_b = \frac{m_b}{v\cos\beta}, \qquad y_\tau = \frac{m_\tau}{v\cos\beta} \tag{3.25}$$

In principle, there is a constraint on both $\sin\beta$ and $\cos\beta$ in order to keep y_t and y_b, y_τ from becoming nonperturbatively large, giving us a rough bound on $\tan\beta$ of:

$$1.2 \lesssim \tan\beta \lesssim 65 \tag{3.26}$$

3.4 A constraint

The masses of Higgs H, A and $H^\pm$ can be arbitrarily large, while the mass of h is bounded above [76] from Eq. 3.23:

$$m_h \leq m_Z\,|\cos(2\beta)| \tag{3.27}$$

However, the observed value of the Higgs mass is 125.36 GeV [1, 2], which is way over the above limit. Fortunately, the Higgs mass is subject to significant quantum corrections at one-loop level. Given the large top Yukawa coupling, the dominant one loop quantum corrections to the Higgs mass square are from the top quark and top squark, as shown in Figure 3.6. This gives the following corrections in the limits of $m^2_{\tilde{t}_1} \sim m^2_{\tilde{t}_2} \gg m_t$ [25]:

$$\Delta m_h^2 = \frac{3}{4\pi^2}\cos^2\alpha y_t^2 m_t^2[\ln(m^2_{\tilde{t}_1} m^2_{\tilde{t}_2})/m_t^2 + ...] \tag{3.28}$$

Incorporating all the corrections, the Higgs mass is bounded above by:

$$m_h \lesssim 135 \text{ GeV} \tag{3.29}$$

a limit within which the discovery of 125 GeV Higgs lies.

Given the large top Yukawa coupling, the top squark couples to the Higgs boson most tightly. Therefore, the Higgs mass constraint plays a significant role in the top squark mass. It will be discussed in detail in the following sections.

3.5 Neutralinos and charginos

There is significant mixing between Higgsinos and electroweak gauginos after electroweak symmetry breaking due to the Higgs-Higgsino-gaugino interactions with Higgs replaced with VEVs. The neutral Higgsinos and neutral electroweak gauginos mix together to form mass eigenstates, called *neutralinos*, while the charged Higgsinos and charged electroweak gauginos mix together to form mass eigenstates, called *charginos*. The existence of neutralinos and charginos greatly enriches but also complicates the decay patterns in the MSSM. This will be discussed in Chapter 4. In the gauge-eigenstate basis $\psi^0 = (\tilde{B}, \tilde{W}^0, \tilde{H}_d^0, \tilde{H}_u^0)$, the mass matrix can be written:

$$\mathbf{M}_\chi = \begin{pmatrix} M_1 & 0 & -g'v_d/\sqrt{2} & g'v_u/\sqrt{2} \\ 0 & M_2 & gv_d/\sqrt{2} & -gv_u/\sqrt{2} \\ -g'v_d/\sqrt{2} & gv_d/\sqrt{2} & 0 & -\mu \\ g'v_u/\sqrt{2} & -gv_u/\sqrt{2} & -\mu & 0 \end{pmatrix} \tag{3.30}$$

where the M_1 and M_2 terms are the soft breaking mass terms for Bino and Wino, and the μ term is the Higgsino mass term expressed in Eq. 3.8. All the g and g' terms are the Higgs-Higgsino-gaugino interaction terms with Higgs replaced with VEVs. The masses and mass eigenstates, namely neutralinos (χ_1^0, χ_2^0, χ_3^0, χ_4^0), can be obtained by diagonalizing the mass matrix with a unitary matrix $\mathbf{N}$:

$$\mathbf{N}^*\mathbf{M}_\chi\mathbf{N}^{-1} = \begin{pmatrix} m_{\chi_1^0} & 0 & 0 & 0 \\ 0 & m_{\chi_2^0} & 0 & 0 \\ 0 & 0 & m_{\chi_3^0} & 0 \\ 0 & 0 & 0 & m_{\chi_4^0} \end{pmatrix} \tag{3.31}$$

If the off-diagonal terms (g and g' terms) are small, in other words if the m_Z meets:

$$m_Z \ll |\mu \pm M_1|, |\mu \pm M_2| \tag{3.32}$$

because m_Z can be expressed as $m_Z = \sqrt{g^2 + g'^2}v/2$, then we can do the following approximation:

- $\chi_1^0 \approx \tilde{B}$ is Bino-like , with mass $m_{\chi_1^0} \approx M_1 - \frac{m_Z^2 s_W^2 (M_1 + \mu \sin 2\beta)}{\mu^2 - M_1^2} + ...$
- $\chi_2^0 \approx \tilde{W}$ is Wino-like, with mass $m_{\chi_2^0} \approx M_2 - \frac{m_W^2 (M_2 + \mu \sin 2\beta)}{\mu^2 - M_2^2} + ...$
- $\chi_{3,4}^0 \approx (\tilde{H}_u^0 \pm \tilde{H}_d^0)/\sqrt{2}$ is Higgsino-like, with masses $m_{\chi_{3,4}^0} = |\mu| + ...$

where for simplicity we assume the mass hierarchy $M_1 < M_2 \ll |\mu|$, but in general the masses can be arbitrary.

The lightest neutralino χ_1^0 is usually assumed to be the LSP, unless there is a lighter gravitino or R-parity violation. Therefore, it is the only particle in the MSSM that is an attractive dark matter candidate.

The chargino sector is similar to the neutralino with neutral Higgsinos and electroweak gauginos replaced with charged ones. In the gauge basis $\psi^{\pm} = (\tilde{W}^+, \tilde{H}_u^+, \tilde{W}^-, \tilde{H}_d^-)$, the mass matrix can be written as:

$$\mathbf{M}_{\chi^{\pm}} = \begin{pmatrix} \mathbf{0} & \mathbf{X^T} \\ \mathbf{X} & \mathbf{0} \end{pmatrix} \tag{3.33}$$

with

$$\mathbf{X} = \begin{pmatrix} M_2 & g v_u \\ g v_d & \mu \end{pmatrix} = \begin{pmatrix} M_2 & \sqrt{2} s_\beta m_W \\ \sqrt{2} c_\beta m_W & \mu \end{pmatrix}. \tag{3.34}$$

the mass eigenstates, namely charginos ($\chi_1^{\pm}$, $\chi_2^{\pm}$), and masses can be obtained by diagonalizing the mass matrix with a unitary matrices $\mathbf{V}$ and and $\mathbf{U}$:

$$\mathbf{U^* X V^{-1}} = \begin{pmatrix} m_{\chi_1^{\pm}} & 0 \\ 0 & m_{\chi_2^{\pm}} \end{pmatrix} \tag{3.35}$$

In the same limit of Eq. 3.32, we can do the following approximation:

- $\chi_1^{\pm} \approx \tilde{W}^{\pm}$ is Wino-like, with mass $m_{\chi_1^{\pm}} \approx M_2 - \frac{m_W^2 (M_2 + \mu \sin 2\beta)}{\mu^2 - M_2^2} + ...$
- $\chi_2^{\pm} \approx (\tilde{H}_u^{\pm} \pm \tilde{H}_d^{\pm})/\sqrt{2}$ is Higgsino-like, with masses $m_{\chi_2^{\pm}} \approx |\mu| - \frac{S m_W^2 (M_2 + \mu \sin 2\beta)}{\mu^2 - M_2^2} + ...$, where S is the sign of μ, which can be either + or -.

where for simplicity we assume the mass hierarchy $M_2 \ll |\mu|$, but in general the masses can be arbitrary. The masses above are calculated at tree level, however, loop corrections to the masses can be significant, for a detail review please refer to Ref. [77–79].

3.6 Third generation squark

The third generation might be the most relevant SUSY partners in connection to Higgs because of its large Yukawa couplings. On one hand, it plays an important role in the recovery of the observed Higgs mass, on the other hand, the Higgs-squark-squark interactions contribute to the masses of third generation squarks. In the gauge basis $(\tilde{t}_L, \tilde{t}_R)$, the mass matrix for the stop can be written as:

$$\mathbf{m}^{\mathbf{2}}_{\tilde{\mathbf{t}}} = \begin{pmatrix} M^2_{3SQ} + m_t^2 + \Delta_{\tilde{u}_L} & m_t \tilde{A}_t \\ m_t \tilde{A}_t & M^2_{3SU} + m_t^2 + \Delta_{\tilde{u}_R} \end{pmatrix}. \tag{3.36}$$

Along the diagonal, the M^2_{3SQ} and M^2_{3SU} are the soft SUSY breaking mass terms, the m_t^2 term comes from the ϕ^4 F-term of the form $y_t^2 H_u^{0*} H_u^0 \tilde{t}_L^* \tilde{t}_L$ ($y_t^2 H_u^{0*} H_u^0 \tilde{t}_R^* \tilde{t}_R$) with Higgs fields replaced with the VEVs, and the Δ term is the D-term contribution which is expressed below. The off-diagonal terms consist of the ϕ^3 F-term of the form $-\mu^* y_t \tilde{t}_L \tilde{t}_R^* H_d^{0*}$ + c.c. and the ϕ^3 soft SUSY breaking mass term of the form $A_t \tilde{t}_L \tilde{t}_R^* H_u^0$ + c.c. with Higgs fields replaced with the respective VEVs.

$$\begin{aligned} \Delta_{\tilde{u}_L} &= \left(\frac{1}{2} - \frac{2}{3} \sin^2 \theta_W \right) m_Z^2 \cos 2\beta \\ \Delta_{\tilde{u}_R} &= \frac{2}{3} \sin^2 \theta_W \; m_Z^2 \cos 2\beta \\ \tilde{A}_t &= A_t - \mu \cot \beta \end{aligned} \tag{3.37}$$

The hermitian matrix can be diagonalized by a unitary matrix to give masses and mass eigenstates:

$$\begin{pmatrix} \tilde{t}_1 \\ \tilde{t}_2 \end{pmatrix} = \begin{pmatrix} \cos\theta_t & -\sin\theta_t \\ \sin\theta_t & \cos\theta_t \end{pmatrix} \begin{pmatrix} \tilde{t}_L \\ \tilde{t}_R \end{pmatrix} \tag{3.38}$$

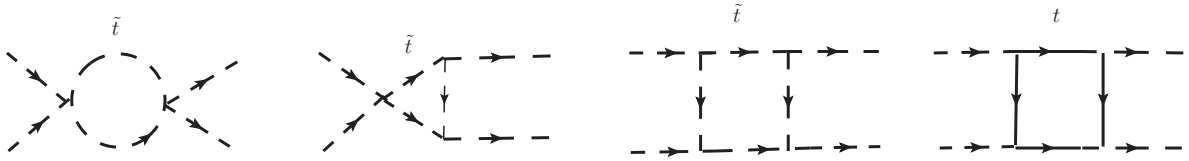

Figure 3.7: One loop quantum corrections to Higgs quartic coupling from both the top quark and the top squark.

with masses and mixing angle

$$\begin{aligned} m^2_{\tilde{t}} &= \frac{1}{2}\left(M^2_{3SQ} + M^2_{3SU} + 2m^2_t + \Delta_{\tilde{u}_L} + \Delta_{\tilde{u}_R}\right) \pm \frac{1}{2}\Delta m^2_{\tilde{t}} \\ \Delta m^2_{\tilde{t}} &= \sqrt{\left(M^2_{3SQ} - M^2_{3SU} + \Delta_{\tilde{u}_L} - \Delta_{\tilde{u}_R}\right)^2 + 4m^2_t \tilde{A}^2_t} \\ \tan 2\theta_t &= \frac{2m_t \tilde{A}_t}{M^2_{3SQ} - M^2_{3SU} + \Delta_{\tilde{u}_L} - \Delta_{\tilde{u}_R}} \end{aligned} \tag{3.39}$$

The off-diagonal term $\tilde{A}_t$ plays a significant role in the stop phenomenology since it controls the mass difference and mixing between the two stops. In certain cases, the mixing between $\tilde{t}_L$ and $\tilde{t}_R$ is large, resulting in a heavy stop and a light stop. Because the off-diagonal terms originate from the Higgs-stop-stop interactions, the $\tilde{A}_t$ is also important in the loop corrections to the Higgs mass. The Higgs mass corrections can be calculated from the quartic coupling corrections, as shown in Figure 3.7. For nearly degenerate soft SUSY breaking parameters in the stop sector, $M^2_{3SQ} \sim M^2_{3SU} \sim M^2_S$, the correction is [80, 81]:

$$\Delta m^2_h = \frac{3}{4\pi^2}\frac{m^4_t}{v^2}\left[\log\frac{M^2_S}{m^2_t} + \frac{\tilde{A}^2_t}{M^2_S}\left(1 - \frac{\tilde{A}^2_t}{12M^2_S}\right)\right] + ... \tag{3.40}$$

A very similar analysis can be performed for the bottom squarks in the gauge basis $(\tilde{b}_L, \tilde{b}_R)$, the mass matrix can be written:

$$\mathbf{m^2_{\tilde{b}}} = \begin{pmatrix} M^2_{3SQ} + m^2_b + \Delta_{\tilde{d}_L} & m_b\tilde{A}_b \\ m_b\tilde{A}_b & M^2_{3SD} + m^2_b + \Delta_{\tilde{d}_R} \end{pmatrix} \tag{3.41}$$

where,

$$\tilde{A}_b = A_b - \mu\tan\beta \tag{3.42}$$

Given the suppression of the off-diagonal terms by the small bottom mass, mixing among the sbottom mass eigenstates is typically small. For $\tilde{A}_b \sim$ TeV, the sbottom mixing angle is about one degree for $M_{3SQ} \sim M_{3SD} \sim$TeV.

3.7 Two Higgs Doublet Model

Among all the new physics models, one of the simplest possible extensions of the Standard Model is the Two Higgs Doublet Model (2HDM). 2HDM is a well motivated extension of the Standard Model. First, the Higgs sector in a few new physics models has the structure of 2HDM, like the Higgs sector in SUSY and the radiative seesaw models of neutrino masses [82–86]. Second, the mass hierarchy between the top quark and bottom quark can be naturally explained by the 2HDM [87]. Furthermore, the 2HDM can provide additional CP violation phases and a strong first order electroweak phase transition effect to explain the baryogenesis.

In general, the vacuum structure and mass spectrum of 2HDM is very rich. Let Φ_1 and Φ_2 denote the complex hypercharge $Y = \pm 1/2$, $SU(2)_L$ doublet scalar fields, then the most general form of the gauge invariant scalar potential is written as [88, 89]:

$$\begin{aligned} V(\Phi_1,\Phi_2) = {} & m_{11}^2\Phi_1^\dagger\Phi_1 + m_{22}^2\Phi_2^\dagger\Phi_2 - m_{12}^2(\Phi_1^\dagger\Phi_2 + \Phi_2^\dagger\Phi_1) \\ & + \frac{1}{2}\lambda_1(\Phi_1^\dagger\Phi_1)^2 + \frac{1}{2}\lambda_2(\Phi_2^\dagger\Phi_2)^2 + \lambda_3(\Phi_1^\dagger\Phi_1)(\Phi_2^\dagger\Phi_2) + \lambda_4(\Phi_1^\dagger\Phi_2)(\Phi_2^\dagger\Phi_1) \\ & + \left\{\frac{1}{2}\lambda_5(\Phi_1^\dagger\Phi_2)^2 + \left[\lambda_6(\Phi_1^\dagger\Phi_1) + \lambda_7(\Phi_2^\dagger\Phi_2)\right](\Phi_1^\dagger\Phi_2) + \text{h.c.}\right\} \end{aligned} \tag{3.43}$$

In principle, m_{12}^2, λ_5, λ_6, λ_7 can be complex while λ_{1-4}, m_{11}^2 and m_{22}^2 are real. The potential with real coefficients does not induce CP violation in the Higgs sector, but CP violation becomes possible due to the complex values of some coefficients [90]. The λ_6, λ_7 terms can cause severe flavor-changing neutral currents (FCNC) at tree-level, which is highly constrained in the Standard Model by the phenomenological dilemma of $K - \bar{K}$ mixing at tree-level [91, 92]. Those terms can be avoided by imposing a discrete symmetry $\Phi_1 \to -\Phi_1$ on the scalar potential. Such a symmetry would also require $m_{12}^2 = 0$, however, we will relax this constraint ($m_{12}^2 \neq 0$) to allow soft breaking of the discrete symmetry. After electroweak symmetry breaking, the two complex Higgs doublets acquire the vacuum

expectation value:

$$\langle \Phi_1 \rangle_0 = \frac{1}{\sqrt{2}} \begin{pmatrix} 0 \\ v_1 \end{pmatrix}, \qquad \langle \Phi_2 \rangle_0 = \frac{1}{\sqrt{2}} \begin{pmatrix} 0 \\ v_2 \end{pmatrix} \tag{3.44}$$

with

$$v^2 = v_1^2 + v_2^2 = (247 \text{ GeV})^2. \tag{3.45}$$

The ratio of the two VEVs is defined as:

$$t_\beta \equiv \tan\beta \equiv v_2/v_1. \tag{3.46}$$

The angle β is chosen to be in the first quadrant by convention. The minima conditions of the scalar potential can be expressed as:

$$\begin{aligned} m_{11}^2 - t_\beta m_{12}^2 + \frac{1}{2} v^2 c_\beta^2 (\lambda_1 + \lambda_{345} t_\beta^2) = 0 \\ m_{22}^2 - t_\beta^{-1} m_{12}^2 + \frac{1}{2} v^2 s_\beta^2 (\lambda_2 + \lambda_{345} t_\beta^{-2}) = 0 \end{aligned} \tag{3.47}$$

where we use the following abbreviations: $s_\beta = \sin\beta$, $c_\beta = \cos\beta$ and $\lambda_{345} = \lambda_3 + \lambda_4 + \lambda_5$. Of the original eight scalar degrees of freedom, the three Nambu-Goldstone bosons G^0, $G^\pm$ become the longitudinal modes of the Z^0 and $W^\pm$, giving them mass. The remaining five physical Higgs scalars are: two CP-even neutral scalars h and H, one CP-odd neutral scalar A, and two charge scalar $H^\pm$. The gauge-eigenstate Higgs fields can be written as:

$$\Phi_i = \begin{pmatrix} \phi_i^+ \\ (v_i + \phi_i^0 + i\eta_i)/\sqrt{2} \end{pmatrix}, \ i = 1, 2 \tag{3.48}$$

The mass matrix for the CP-odd scalar is:

$$\mathcal{M}_A = \left(m_{12}^2 - \lambda_5 v^2 s_\beta c_\beta\right) \begin{pmatrix} t_\beta & -1 \\ -1 & t_\beta^{-1} \end{pmatrix} \tag{3.49}$$

the masses and mass eigenstate can be obtained:

$$\begin{aligned} m_A^2 = \frac{m_{12}^2}{s_\beta c_\beta} - \lambda_5 v^2, \qquad m_G^2 = 0 \\ A = \eta_1 \sin\beta - \eta_2 \cos\beta \\ G = \eta_1 \cos\beta + \eta_2 \sin\beta \end{aligned} \tag{3.50}$$

There is a zero eigenvalue corresponding to the Goldstone boson which gets eaten by the neutral Z boson. The mass matrix for the charged scalar is:

$$\mathcal{M}_{H^\pm} = \left[m_{12}^2 - \frac{1}{2}v^2(\lambda_4 s_\beta c_\beta + \lambda_5 s_\beta c_\beta)\right] \begin{pmatrix} t_\beta & -1 \\ -1 & t_\beta^{-1} \end{pmatrix} \tag{3.51}$$

the masses and mass eigenstates of the charged Higgs are:

$$\begin{aligned} m_{H^\pm}^2 &= \frac{m_{12}^2}{s_\beta c_\beta} - \frac{1}{2}v^2(\lambda_4 + \lambda_5), \qquad m_{G^\pm}^2 = 0 \\ H^\pm &= \phi_1^\pm \sin\beta - \phi_2^\pm \cos\beta \\ G^\pm &= \phi_1^\pm \cos\beta + \phi_2^\pm \sin\beta \end{aligned} \tag{3.52}$$

Again there is a zero eigenvalue corresponding to the Goldstone boson which gets eaten by the charged $W^\pm$ boson. The mass matrix for the CP-even scalars is:

$$\begin{aligned} \mathcal{M}_H &= m_{12}^2 \begin{pmatrix} t_\beta & -1 \\ -1 & t_\beta^{-1} \end{pmatrix} + v^2 s_\beta c_\beta \begin{pmatrix} \lambda_1 t_\beta^{-1} & \lambda_{345} \\ \lambda_{345} & \lambda_2 t_\beta \end{pmatrix} \\ &= \begin{pmatrix} m_{12}^2 t_\beta + \lambda_1 v^2 c_\beta^2 & -m_{12}^2 + \lambda_{345} v^2 s_\beta c_\beta \\ -m_{12}^2 + \lambda_{345} v^2 s_\beta c_\beta & m_{12}^2 t_\beta^{-1} + \lambda_1 v^2 s_\beta^2 \end{pmatrix} \end{aligned} \tag{3.53}$$

The masses and mass eigenstates can be obtained by diagonalizing the mass matrix:

$$A = m_{12}^2 t_\beta + \lambda_1 v^2 c_\beta^2, \quad B = m_{12}^2 t_\beta^{-1} + \lambda_1 v^2 s_\beta^2, \quad C = -m_{12}^2 + \lambda_{345} v^2 s_\beta c_\beta \tag{3.54}$$

$$m_{h,H} = \frac{1}{2}\left[A + B \pm \sqrt{(A-B)^2 + 4C^2}\right] \tag{3.55}$$

$$h = \phi_1^0 \sin\alpha - \phi_2^0 \cos\alpha \tag{3.56}$$

$$H = -\phi_1^0 \cos\alpha + \phi_2^0 \sin\alpha \tag{3.57}$$

The charged Higgs mass can be expressed by the neutral CP-even Higgs mass:

$$m_{H^\pm}^2 = m_A^2 + \frac{1}{2}(\lambda_5 - \lambda_4) \tag{3.58}$$

The most general Yukawa interactions of quarks, charged leptons and Higgs can be (for example, for Q = -1/3 quarks):

$$\mathcal{L} = \mathbf{y}^1 \bar{Q} \Phi_1 d_R + \mathbf{y}^2 \bar{Q} \Phi_2 d_R \tag{3.59}$$

The mass matrix is then:

$$M_{ij} = y^1_{ij}\frac{v_1}{\sqrt{2}} + y^2_{ij}\frac{v_2}{\sqrt{2}} \tag{3.60}$$

where i, j are the family indices.

In general, the two matrices y^1 and y^2 can not be simultaneously diagonalizd, leading to the Yukawa coupling not being diagonal in flavor space. The non-diagonal Yukawa coupling will cause serious FCNC. However, if all the fermions with the same quantum number couple to the same Higgs multiplet, then FCNC will be absent. This was formalized by the Paschos- GlashowWeinberg theorem [93, 94]. According to the theorem, there are two ways for the quarks and charged leptons to couple to the Higgs fields. In the Type I 2HDM, all quarks and RH charged leptons couple to just one of the Higgs doublets (conventionally chosen to be Φ_2). In the Type II 2HDM, the $Q = 2/3$ RH quarks couple to one Higgs doublet (conventionally chosen to be Φ_2), and the $Q = 1/3$ RH quarks and all RH charged leptons couple to the other (Φ_1). There are two more models: lepton-specific 2HDM and flipped 2HDM. In the lepton-specific 2HDM, the RH quarks all couple to Φ_2 and the RH leptons couple to Φ_1. In the flipped 2HMD, the RH quarks couplings are the same as in the Type II 2HDM, but the RH charged leptons couple to Φ_2.

The couplings of the CP-even Higgs bosons and CP-odd Higgs to the SM gauge bosons and fermions are the same as the SM value except for one multiplicative factor for the four different types of 2HDM models, which is presented in Table 3.3. It can be seen that the Higgs h branching fractions receive tree level corrections by a multiplicative factor related to the rotation angle α and β.

In the MSSM, the Higgs sector is a Type II model in the 2HDM. Unlike the fact that the light CP-even Higgs mass is bounded above and the mass spectrum for heavy Higgs bosons is determined by the CP-odd Higgs mass in the MSSM, the spectrum in the general 2HDM is quite arbitrary. Therefore, the Higgs decay patterns in the general 2HDM is also richer. The relation between the Higgs self-coupling constants in the general 2HDM and

	Type I	Type II	Lepton-specific	Flipped
ξ_{hVV}	$\sin(\beta-\alpha)$	$\sin(\beta-\alpha)$	$\sin(\beta-\alpha)$	$\sin(\beta-\alpha)$
ξ_h^u	$\cos\alpha/\sin\beta$	$\cos\alpha/\sin\beta$	$\cos\alpha/\sin\beta$	$\cos\alpha/\sin\beta$
ξ_h^d	$\cos\alpha/\sin\beta$	$-\sin\alpha/\sin\beta$	$\cos\alpha/\sin\beta$	$-\sin\alpha/\sin\beta$
ξ_h^ℓ	$\cos\alpha/\sin\beta$	$-\sin\alpha/\sin\beta$	$-\sin\alpha/\sin\beta$	$\cos\alpha/\sin\beta$
ξ_{HVV}	$\cos(\beta-\alpha)$	$\cos(\beta-\alpha)$	$\cos(\beta-\alpha)$	$\cos(\beta-\alpha)$
ξ_H^u	$\sin\alpha/\sin\beta$	$\sin\alpha/\sin\beta$	$\sin\alpha/\sin\beta$	$\sin\alpha/\sin\beta$
ξ_H^d	$\sin\alpha/\sin\beta$	$\cos\alpha/\sin\beta$	$\sin\alpha/\sin\beta$	$\cos\alpha/\sin\beta$
ξ_H^ℓ	$\sin\alpha/\sin\beta$	$\cos\alpha/\sin\beta$	$\cos\alpha/\sin\beta$	$\sin\alpha/\sin\beta$
ξ_{AVV}	0	0	0	0
ξ_A^u	$\cot\beta$	$\cot\beta$	$\cot\beta$	$\cot\beta$
ξ_A^d	$-\cot\beta$	$\tan\beta$	$-\cot\beta$	$\tan\beta$
ξ_A^ℓ	$-\cot\beta$	$\tan\beta$	$\tan\beta$	$-\cot\beta$

Table 3.3: The multiplicative factor ξ of the SM Yukawa couplings of V, u, d, ℓ to the neutral Higgs bosons h, H, A in the four different models.

the gauge coupling constants in the MSSM can be expressed [88, 95]:

$$\begin{aligned}
\lambda_1 &= \lambda_2 = \frac{1}{4}(g^2 + g'^2) \\
\lambda_3 &= \frac{1}{4}(g^2 - g'^2) \\
\lambda_4 &= -\frac{1}{2}g^2 \\
\lambda_5 &= \lambda_6 = \lambda_7 = 0
\end{aligned} \tag{3.61}$$

3.7.1 Theoretical constraints

In order for the vacuum configuration to be positive, bounded from below and stable, the following conditions have to be fulfilled [96, 97]:

$$\begin{aligned}
&\lambda_1 > 0, \quad \lambda_2 > 0, \quad \lambda_3 > -\sqrt{\lambda_1\lambda_2} \\
&\lambda_3 + \lambda_4 + |\lambda_5| > -\sqrt{\lambda_1\lambda_2}
\end{aligned} \tag{3.62}$$

In addition to the constraints on the stability of the Higgs potential, its parameters can be further constrained by applying tree-level unitarity for the scattering of the Higgs bosons including the absorbed Goldstone boson's degree of freedom. It has been stated

that the eigenvalues of the tree level scattering matrix need to be less than $1/8\pi$ [98–102]:

$$
\begin{aligned}
8\pi S_{Y=2,\sigma=1} &= \begin{pmatrix} \lambda_1 & \lambda_5 & \sqrt{2}\lambda_6 \\ \lambda_5^* & \lambda_2 & \sqrt{2}\lambda_7^* \\ \sqrt{2}\lambda_6^* & \sqrt{2}\lambda_7 & \lambda_3+\lambda_4 \end{pmatrix} \\
8\pi S_{Y=2,\sigma=0} &= \lambda_3 - \lambda_4 \\
8\pi S_{Y=0,\sigma=1} &= \begin{pmatrix} \lambda_1 & \lambda_4 & \lambda_6 & \lambda_6^* \\ \lambda_4 & \lambda_2 & \lambda_7 & \lambda_7^* \\ \lambda_6^* & \lambda_7^* & \lambda_3 & \lambda_5^* \\ \lambda_6 & \lambda_7 & \lambda_5 & \lambda_3 \end{pmatrix} \\
8\pi S_{Y=0,\sigma=0} &= \begin{pmatrix} 3\lambda_1 & 2\lambda_3+\lambda_4 & 3\lambda_6 & 3\lambda_6^* \\ 2\lambda_3+\lambda_4 & 3\lambda_2 & 3\lambda_7 & 3\lambda_7^* \\ 3\lambda_6^* & 3\lambda_7^* & \lambda_3+2\lambda_4 & 3\lambda_5^* \\ 3\lambda_6 & 3\lambda_7 & 3\lambda_5 & \lambda_3+2\lambda_4 \end{pmatrix}
\end{aligned}
\tag{3.63}
$$

where Y is the total hypercharge and σ is the total weak isospin, both of which are conserved in the high energy Higgs Higgs scattering process. Remember we already set λ_6 and λ_7 to be zero to avoid the FCNC problem. The unitarity constraint requires that the eigenvalues Λ_i of the above matrices should meet:

$$
|\Lambda_i| < \frac{1}{8\pi} \tag{3.64}
$$

Now the eigenvalues Λ_i of the above scattering matrices can be obtained in the simple

case without λ_6 and λ_7:

$$\begin{aligned}
\Lambda_1 &= \lambda_3 + \lambda_4 \\
\Lambda_2 &= \lambda_3 - \lambda_4 \\
\Lambda_3 &= \lambda_3 \pm |\lambda_5| \\
\Lambda_4 &= \lambda_3 + 2\lambda_4 \pm 3\,|\lambda_5| \\
\Lambda_5 &= \frac{1}{2}\left(\lambda_1 + \lambda_2 \pm \sqrt{(\lambda_1 - \lambda_2)^2 + 4\,|\lambda_5|^2}\right) \\
\Lambda_6 &= \frac{1}{2}\left(\lambda_1 + \lambda_2 \pm \sqrt{(\lambda_1 - \lambda_2)^2 + 4\lambda_4^2}\right) \\
\Lambda_7 &= \frac{1}{2}\left(3(\lambda_1 + \lambda_2) \pm \sqrt{9(\lambda_1 - \lambda_2)^2 + 4(2\lambda_3 + \lambda_4)^2}\right)
\end{aligned} \tag{3.65}$$

Because the parameter m_{12} does not involve the Higgs quartic interactions, the unitarity constraints, in general, do not set any limits on the masses of the observable Higgs bosons, as stated in Ref. [100].

3.7.2 The LHC and LEP Constraints

The direct searches for new scalars are conducted at the LEP and the LHC. The LEP set mass bounds on a charged Higgs of $m_{H^\pm} > 80$ (72) GeV for the Type II (I) 2HDM [103]. The constaints on the sum of two neutral Higgs bosons $m_A + m_H$ from channel $e^+e^- \to AH$ ($H \to bb/\tau\tau, A \to bb/\tau\tau$) requires $m_A + m_H \gtrsim 209$ GeV [104]. At the LHC, direct searches for A/H in bb-associated production with a $\tau\tau$ channel by ATLAS and CMS set strong constraints on the high $\tan\beta$ region in the Type II 2HDM. Direct searches by ATLAS/CMS for H using channels $H \to W^+W^-, ZZ$ [105–107] and $H \to hh \to bb\gamma\gamma, bbbb$ [108–110], and for A using channel $A \to hZ$ ($h \to bb$) [111, 112] yield strong constaints on the rotation angle plane $\cos(\beta - \alpha)$ vs $\tan\beta$ in a few representative masses of m_H and m_A.

ATLAS/CMS also conduct searches for the charged scalar and impose constraints on it [113, 114] beyond those of the LEP. A light charged Higgs with a mass less than top quark is mostly excluded by the the null result of top pair production at the LHC with channel $t \to H^+b \to \tau\nu b$. For the charged Higgs with a higher mass $m_{H^\pm} > m_t$, current limits are not strong and impose constraints on the charged Higgs mass that are not much above the

top mass.

The flavour measurements can provide indirect constraints on the charged Higgs mass as a function of $\tan\beta$. The most stringent constraints come from the measurements of the b quark decay branching fraction $b \to s\gamma$ ($B_d^0 \to X_s\gamma$), which sets the mass bound on the charged Higgs mass of $m_{H^\pm} > 480$ GeV at 95% C.L. [115]. In the range of a large $\tan\beta \gtrsim 20$, the limits on $m_{H^\pm}$ from the branching fraction measurements of $B_d^+ \to \tau^+\nu$ is significantly stronger, for instance, $m_{H^\pm} > 700$ GeV is obtained for $\tan\beta = 30$. Note that the flavour constraints on the Higgs masses are typically very model dependent. Contributions from additional sectors in the model could relax the constraints significantly. Therefore, we will not consider flavour measurements as a hard constraint in the framework of 2HDM.

3.7.3 Oblique Parameters

The Z-pole precision observables, in particular, the Oblique Parameters S, T, U [28–32], parameterize potential new physics contributions to electroweak radiative corrections, providing an indirect probe of new physics beyond the Standard Model. The Oblique Parameters S, T, U receive contributions from either the coupling corrections at tree level shown in Table 3.3 or from the extra Higgs bosons that couple to the vector bosons in the framework of the 2HDM. The S and T parameters absorb possible new physics contributions to the neutral currents and the difference between the neutral and charged currants, respectively, while the U parameter is sensitive to the changes in masses and the W boson width. The potential new physics effects in gauge-boson self energies $\delta\Pi(q^2)_{ab}$ at scale q^2, where $a, b = W, Z, \gamma$, can be parameterized by the three parameters S, T and U, defined as:

$$\alpha T = \frac{\delta\Pi_{WW}(0)}{M_W^2} - \frac{\delta\Pi_{ZZ}(0)}{M_Z^2} \tag{3.66}$$

$$\frac{\alpha S}{4c_W^2 s_W^2} = [\frac{\delta\Pi_{ZZ}(M_Z^2) - \delta\Pi_{ZZ}(0)}{M_Z^2}] - \frac{c_W^2 - s_W^2}{c_W s_W}\delta\Pi'_{Z\gamma}(0) - \delta\Pi'_{\gamma\gamma}(0) \tag{3.67}$$

$$\frac{\alpha U}{4s_W^2} = [\frac{\delta\Pi_{WW}(M_W^2) - \delta\Pi_{WW}(0)}{M_W^2}] - c_W^2[\frac{\delta\Pi_{ZZ}(M_Z^2) - \delta\Pi_{ZZ}(0)}{M_Z^2}] \\ - s_W^2\delta\Pi'_{\gamma\gamma}(0) - 2c_W s_W \delta\Pi'_{Z\gamma}(0) \tag{3.68}$$

In the 2HDM, the one-loo contributions from the Higgs bosons (h, H, A, $H^\pm$) with masses (m_h, m_H, m_A, $m_{H^\pm}$) to the Oblique Parameters S, T, U, after subtracting the SM Higgs corrections can be expressed as [95, 116]:

$$S = \frac{1}{\pi m_Z^2}\{\sin^2(\beta-\alpha)\mathcal{B}_{22}(m_Z^2; m_H^2, m_A^2) - \mathcal{B}_{22}(m_Z^2; m_{H^\pm}^2, m_{H^\pm}^2) \\ + \cos^2(\beta-\alpha)[\mathcal{B}_{22}(m_Z^2; m_h^2, m_A^2) + \mathcal{B}_{22}(m_Z^2; m_Z^2, m_H^2) - \mathcal{B}_{22}(m_Z^2; m_Z^2, m_h^2) \\ - m_Z^2\mathcal{B}_{22}(m_Z^2; m_Z^2, m_H^2) + m_Z^2\mathcal{B}_{22}(m_Z^2; m_Z^2, m_h^2)]\} \tag{3.69}$$

$$T = \frac{1}{16\pi m_W^2 s_W^2}\{F(m_{H^\pm}^2, m_A^2) + \sin^2(\beta-\alpha)[F(m_{H^\pm}^2, m_H^2) - F(m_A^2, m_H^2)] \\ + \cos^2(\beta-\alpha)[F(m_{H^\pm}^2, m_h^2) - F(m_A^2, m_h^2) + F(m_W^2, m_H^2) - F(m_W^2, m_h^2)] \\ - F(m_Z^2, m_H^2) + F(m_Z^2, m_h^2) + 4m_Z^2\bar{B}_0(m_Z^2, m_H^2, m_h^2) - 4m_W^2\bar{B}_0(m_W^2, m_H^2, m_h^2)\} \tag{3.70}$$

$$U = -S + \frac{1}{\pi m_Z^2}\{\mathcal{B}_{22}(m_W^2; m_A^2, m_{H^\pm}^2) - 2\mathcal{B}_{22}(m_W^2; m_{H^\pm}^2, m_{H^\pm}^2) \\ + \sin^2(\beta-\alpha)\mathcal{B}_{22}(m_W^2; m_H^2, m_{H^\pm}^2) + \cos^2(\beta-\alpha)[\cos^2(\beta-\alpha)\mathcal{B}_{22}(m_W^2; m_h^2, m_{H^\pm}^2) \\ + \mathcal{B}_{22}(m_W^2; m_W^2, m_H^2) - \mathcal{B}_{22}(m_W^2; m_W^2, m_h^2) - m_W^2\mathcal{B}_0(m_W^2; m_W^2, m_H^2) + m_W^2\mathcal{B}_0(m_W^2; m_W^2, m_h^2)]\} \tag{3.71}$$

where the $\mathcal{B}$ and F functions can be found in Ref.[116].

In 2HDM with a general Higgs mass spectrum, significant contributions to S, T, U can arise in large regions of the parameter space. The contribution T can be either positive or negative depending on the Higgs boson's mass spectrum and the rotation angle $\alpha - \beta$. Therefore, an improvement of the precision measurements on S, T, U can help constrain the parameter space in 2HDM.

CHAPTER 4

Phenomenology of Third Generation Squarks

Given the large top Yukawa coupling, the top and top squark (stop) sectors of the Minimal Supersymmetric Standard Model (MSSM) provide the largest radiative corrections to the Higgs mass. However, stop masses can not be too heavy in order to avoid excessive fine tuning of the Higgs mass. A TeV scale stop typically leads to a fine tuning of about 1% [117]. Given the tight connection between the stop and the Higgs sectors, it is important to fully explore the discovery potential of the stop at the LHC; the bottom squark (sbottom) sector is also of great interest. The left-handed sbottom mass is related to the left-handed stop mass since they are controlled by the same soft SUSY breaking mass parameter. Although the LHC program has been carrying out a rather broad and impressive SUSY search plan, many searches are still limited by strong assumptions for the sake of simplicity. In preparing to exploit the large amount of the incoming data from the LHC experiments, it is thus of priority to embrace the SUSY searches in a comprehensive way. In realistic MSSM scenarios, there is often more than one significant decay mode present.

In this study, we work in the framework of the MSSM and focus primarily on the third generation squark sector. We decouple other SUSY particles: the gluino, sleptons, and the first two generations of squarks. We also decouple the non-SM Higgs particles by setting M_A large. Besides the third generation squarks, the other relevant SUSY states are a Bino (with a soft SUSY breaking mass M_1), Winos (with a soft SUSY breaking mass M_2), and Higgsinos (with bilinear Higgs mass parameter μ). After the mass diagonalization, they form neutralinos ($\chi^0_{1,2,3,4}$) and charginos ($\chi^\pm_{1,2}$).

We consider the neutralino/chargino spectrum with a Bino-like LSP and three representative SUSY mass hierarchy scenarios:

- Case I, Bino-like LSP with decoupled Winos and Higgsinos: $M_1 < m_{\tilde{t},\tilde{b}_1} \ll |\mu|, M_2$.
- Case IA, Bino-like LSP with Wino-like NLSPs: $M_1 < M_2 < m_{\tilde{t},\tilde{b}_1} \ll |\mu|$.
- Case IB, Bino-like LSP with Higgsino-like NLSPs: $M_1 < |\mu| < m_{\tilde{t},\tilde{b}_1} \ll M_2$.

The decays of the light stop or sbottom highly depend on the low-lying neutralino/chargino spectrum, as well as on the composition of the light stop and sbottom.

In each scenario, we consider two limiting cases with different stop left-right mixing. In the minimal mixing case, $\tilde{A}_t = A_t - \mu \cot\beta = 0$, the lightest stop mass eigenstate $\tilde{t}_1$ is either purely $\tilde{t}_L$ ($M_{3SQ} < M_{3SU}$) or purely $\tilde{t}_R$ ($M_{3SQ} > M_{3SU}$). We decouple $\tilde{t}_2$ for simplicity. In the maximal mixing case with $M_{3SQ} = M_{3SU} = M_{SUSY}$ and $|\tilde{A}_t| = \sqrt{6} M_{SUSY}$, both $\tilde{t}_{1,2}$ are a mixture of $\tilde{t}_L$ and $\tilde{t}_R$, with mass squared splitting $\Delta m^2_{\tilde{t}} \approx 2\sqrt{6} m_t M_{SUSY}$. In our analysis below, we use $\tilde{A}_t > 0$. Negative values of $\tilde{A}_t$ introduce little changes to the numerical results. Since M_{3SQ} also controls the mass for $\tilde{b}_L$, there is a light $\tilde{b}_1 \sim \tilde{b}_L$ for the light M_{3SQ} case, assuming small sbottom left-right mixing and a decoupled $\tilde{b}_R$.

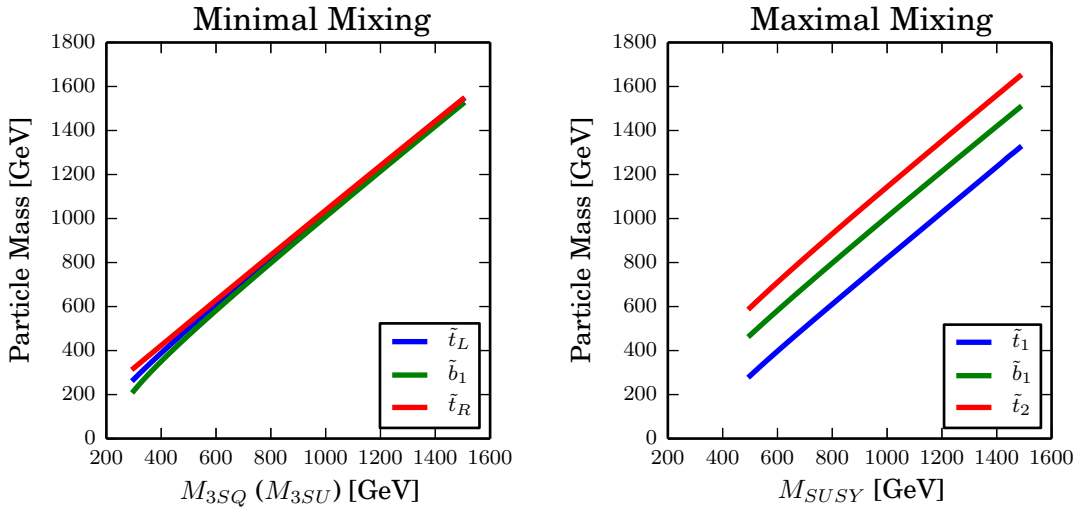

Figure 4.1: The mass spectra for stops and sbottom for the minimal mixing case (left panel) and the maximal mixing case with $M_{3SQ} = M_{3SU} = M_{SUSY}$ (right panel).

The mass spectra for stops and sbottom are shown in Fig. 4.1. In the minimal mixing case (left panel), $m_{\tilde{t}_L}$ ($m_{\tilde{t}_R}$), $m_{\tilde{b}_1} \sim M_{3SQ}(M_{3SU})$, especially for large M_{3SQ} (M_{3SU}). In

the maximal mixing case (right panel), the mass difference between $\tilde{b}_1$ and $\tilde{t}_1$ is typically about 250 GeV while the mass difference between $\tilde{t}_2$ and $\tilde{t}_1$ is about 350 GeV or larger.

We used SUSY-HIT [118] to calculate the supersymmetric particle spectrum and decay branching fractions. In this section, unless otherwise specified, we have set the Bino-like LSP mass parameter $M_1 = 150$ GeV, the intermediate gaugino mass parameters $M_2, \mu =$ 300 GeV in both Cases IA and IB, and $\tan\beta = 10$.

4.1 Case I: Bino-like LSP with decoupled Wino and Higgsino

The simplest case has a mass spectrum with stop(s), the left-handed sbottom, and only the low-lying neutralino being the Bino-like LSP.

In the minimal mixing case with the light stop $\tilde{t}_1$ as a pure left- or right-handed state, $\tilde{t}_1$ either directly decays to $t\chi_1^0$ when it is kinematically accessible or through $bW^*\chi_1^0$ with 100% branching fraction. Similarly, in the case of a small M_{3SQ}, $\tilde{b}_1$ decays directly through $b\chi_1^0$ with a 100% branching fraction.

In the maximal mixing case, $\tilde{t}_1$, $\tilde{t}_2$, and $\tilde{b}_1$ appear in the spectrum, with a typical mass order of $m_{\tilde{t}_1} < m_{\tilde{b}_1} < m_{\tilde{t}_2}$ and with a relatively large mass splitting of 150 GeV or larger. While the decay of $\tilde{t}_1$ is straightforward (100% into $bW^{(*)}\chi_1^0$), the decays of $\tilde{b}_1$ and $\tilde{t}_2$ could have multiple competing channels, as shown in Fig. 4.2. For $\tilde{b}_1$, it dominantly decays into $W\tilde{t}_1$ while the branching fraction of the $\tilde{b}_1 \to b\chi_1^0$ channel is only a few percent or less. For $\tilde{t}_2$, it dominantly decays into a light stop/sbottom with a gauge boson: $Z\tilde{t}_1$ about 75% and $W\tilde{b}_1$ about 20%. The direct decay down to $t\chi_1^0$ is less than 10%.

The pair production of stops and sbottoms at the LHC and their subsequent decays result in the appearance of various final states. In the left panel of Fig. 4.3, we show the $\sigma \times$ BR of final states $tt/bbWW+ \not{E}_T$ for $\tilde{t}_1$ in the minimal and maximal mixing scenarios, as well as $bb+ \not{E}_T$ for $\tilde{b}_1$ in the minimal mixing scenario at the 14 TeV LHC. All the cross sections shown in the plots are for stop and sbottom pair production at 14 TeV including NLO supersymmetric QCD correction as well as resummation of soft-gluon emission at next-to-leading logarithmic accuracy [119–121]. Since $\tilde{t}_1 \to t/bW\chi_1^0$ and $\tilde{b}_1 \to b\chi_1^0$ dominate in those channels, $\sigma \times$ BR is the same as the production cross sections

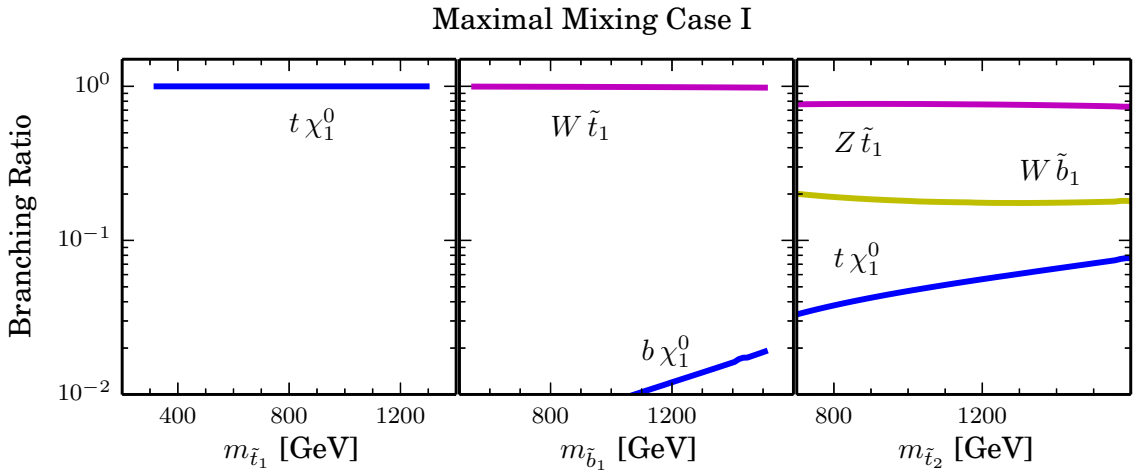

Figure 4.2: Branching fractions for $\tilde{t}_1$ (left), $\tilde{b}_1$ (middle) and $\tilde{t}_2$ (right) in the maximal mixing scenario with a Bino-like LSP (Case I). We set $M_1 = 150$ GeV, $M_2 = 2$ TeV, $\mu = 2$ TeV, and $\tan\beta = 10$, which corresponds to $m_{\chi_1^0} = 151$ GeV.

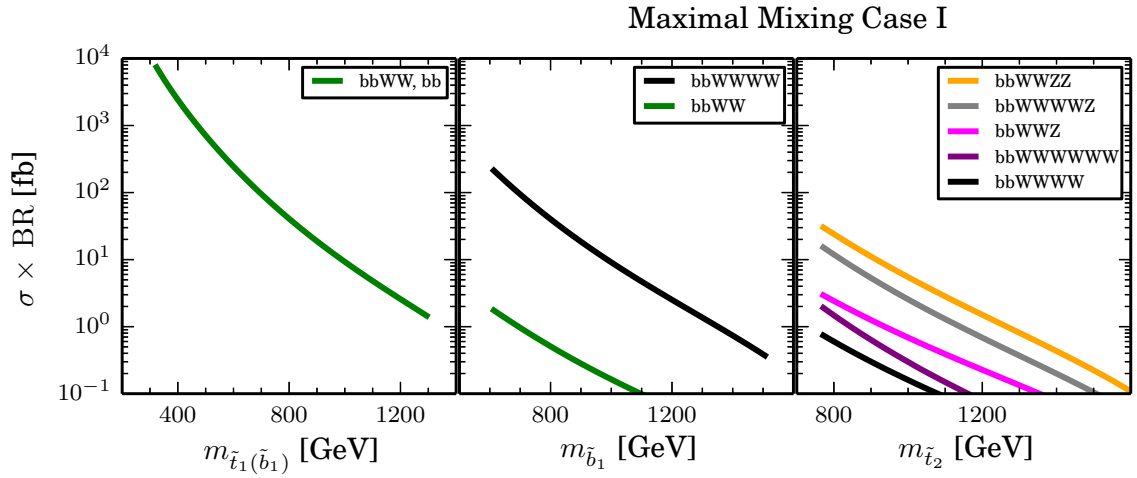

Figure 4.3: Case I: left panel shows $\sigma \times$ BR of final states for $\tilde{t}_1$ pair production in both the minimal and maximal mixing scenarios, as well as $\tilde{b}_1$ pair production in the minimal mixing scenario. The middle and right panel show $\sigma \times$ BR for various final states of $\tilde{b}_1$ and $\tilde{t}_2$ pair production, respectively, in the maximal mixing scenario. All channels include $\not{E}_T$ in the final states. All the cross sections are for the 14 TeV LHC stop and sbottom pair production, calculated including NLO + NLL corrections [119–121]. The choice of neutralino and chargino mass parameters is the same as in Fig. 4.2.

for the stop pair and sbottom pair. The middle panel of Fig. 4.3 shows the $\sigma \times \mathrm{BR}$ for $\tilde{b}_1\tilde{b}_1$ pair production in the maximal mixing scenario. The $bb+\not{E}_T$ channel is highly suppressed, while $bbWWWW+\not{E}_T$ becomes dominant. The right panel of Fig. 4.3 shows the $\sigma \times \mathrm{BR}$ for $\tilde{t}_2\tilde{t}_2$ pair production in the maximal mixing scenario. The dominant channel is $ttZZ+\not{E}_T$, with $ttWWZ$ being the second dominant channel. The cross section, however, is relatively small, less than about 10 fb for $m_{\tilde{t}_2} \gtrsim 800$ GeV, given the heaviness of the second stop. Note that the range of the stop and sbottom masses are controlled by the choice of parameter $M_{3SQ} = M_{3SU} = M_{SUSY} = 600 \ldots 1500$ GeV in the maximal mixing case(see Fig. 4.1).

4.2 Case IA: Bino LSP with Wino NLSP

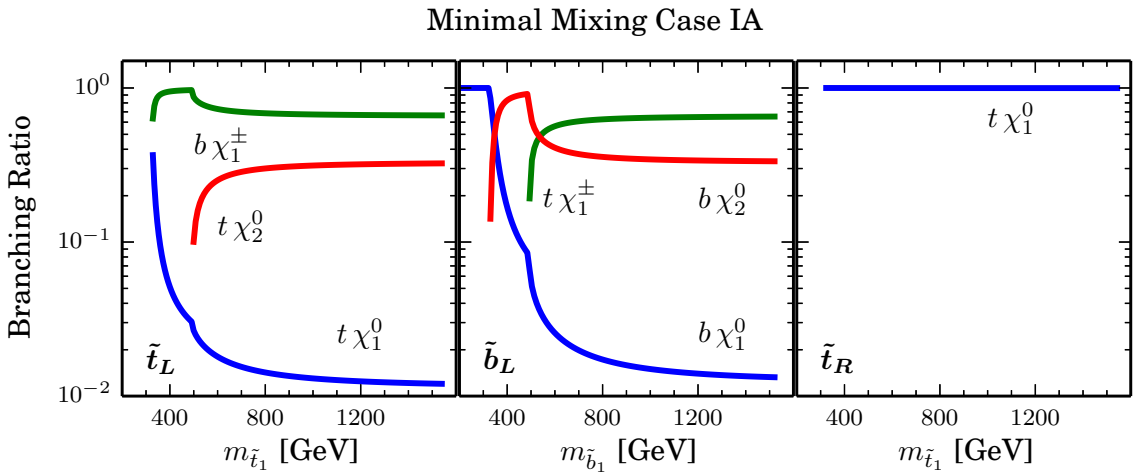

Figure 4.4: Case IA: branching fractions for left-handed $\tilde{t}_1$ (left), $\tilde{b}_1$ (middle), right-handed $\tilde{t}_1$ (right) in the minimal mixing scenario. We set $M_1 = 150$ GeV, $M_2 = 300$ GeV, $\mu = 2$ TeV, and $\tan\beta = 10$, which corresponds to $m_{\chi_1^0} = 151$ GeV, $m_{\chi_2^0} = 319$ GeV and $m_{\chi_1^\pm} = 319$ GeV.

The low lying neutralino/chargino spectrum in Case IA comprises of a Bino-like LSP, as well as a pair of Wino-like states: χ_2^0 and $\chi_1^\pm$ with nearly degenerate masses. In the minimal mixing scenario, the decay branching fractions are shown in Fig. 4.4 for left-handed $\tilde{t}_1$ (left), $\tilde{b}_1$ (middle), and right-handed $\tilde{t}_1$ (right). For the left-handed $\tilde{t}_1$, decays to $b\chi_1^\pm$ ($\sim 70\%$ for large $m_{\tilde{t}_1}$) and $t\chi_2^0$ ($\sim 30\%$ for large $m_{\tilde{t}_1}$) dominate over $t\chi_1^0$ once

kinematically accessible, due to the stronger $SU(2)_L$ coupling compared to the relatively weaker $U(1)_Y$ coupling. Similarly, $\tilde{b}_1 \to t\chi_1^{\pm}$ ($\sim 65\%$) and $\tilde{b}_1 \to b\chi_2^0$ ($\sim 30\%$) dominate over the $b\chi_1^0$ channel for sbottom. Given the dominant decay channels of the Wino-like neutralino/chargino[1]: $\chi_1^{\pm} \to W\chi_1^0$, $\chi_2^0 \to Z/h\chi_1^0$, the dominant decay modes for $\tilde{t}_1$ and $\tilde{b}_1$ are: $\tilde{t}_1 \to bW\chi_1^0,\ tZ/h\chi_1^0$, $\tilde{b}_1 \to tW\chi_1^0,\ bZ/h\chi_1^0$. When $\tilde{t}_1$ is mostly right-handed, it decays to $t\chi_1^0$ almost 100%, since its couplings to the Wino-like neutralino/charginos are highly suppressed.

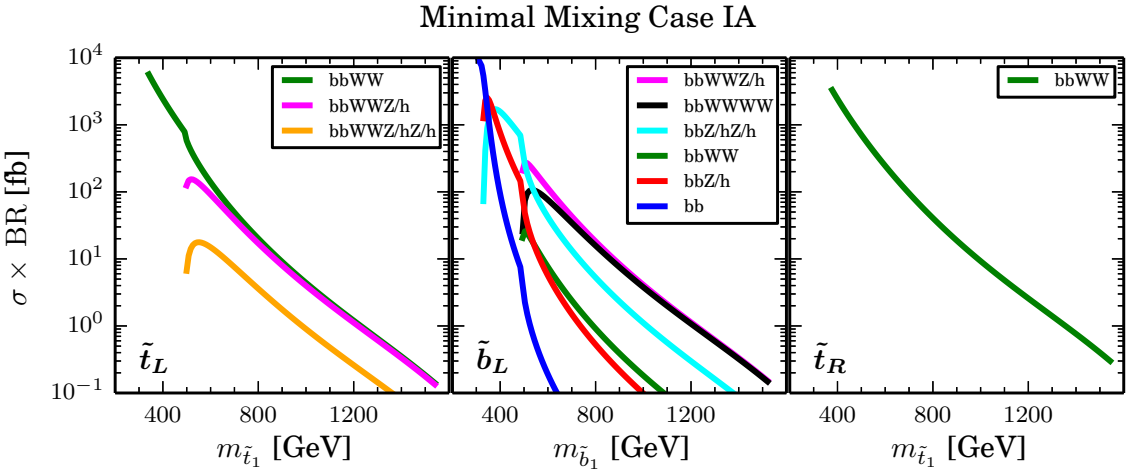

Figure 4.5: Case IA: $\sigma \times$ BR of various final states for pair production of left-handed $\tilde{t}_1$ (left), $\tilde{b}_1$ (middle), and right-handed $\tilde{t}_1$ (right) in the minimal mixing scenario at the 14 TeV LHC. The choice of neutralino and chargino mass parameters is the same as in Fig. 4.4.

The left, middle and right panels of Fig. 4.5 show the $\sigma \times$ BR for pure left-handed $\tilde{t}_1\tilde{t}_1$, $\tilde{b}_1\tilde{b}_1$ and pure right-handed $\tilde{t}_1\tilde{t}_1$ pair production, respectively, in the minimal mixing scenario of Case IA. For pure left-handed $\tilde{t}_1$, $bbWWZ/h + \not{E}_T$ is as abundant as the $bbWW + \not{E}_T$ channel, which could be an important new search channel for the stop. For pure left-handed $\tilde{b}_1$, the $bb + \not{E}_T$ channel is highly suppressed. New final states of $bbWWZ/h$ and $bbWWWW$ are dominant and comparable in size, with $bbZ/hZ/h$ being subdominant, opening up new channels for sbottom searches. The final state for the pure right-handed

[1]For χ_2^0, whether it decays preferably to $Z\chi_1^0$ or $h\chi_1^0$ depends on the sign of μ, as explained in detail in Ref. [122].

$\tilde{t}_1$ is still $bbWW+\not{E}_T$, despite the existence of light Wino NLSPs in the spectrum.

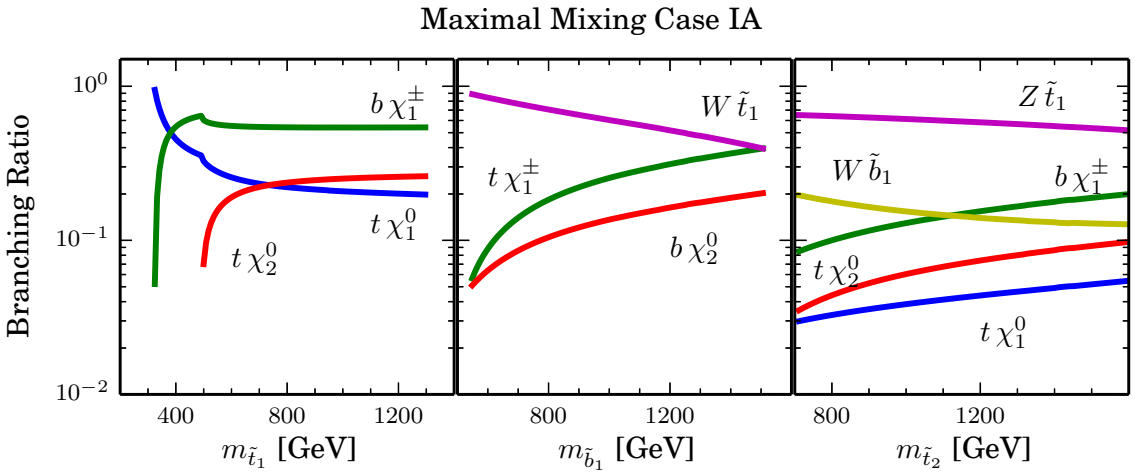

Figure 4.6: Case IA: Branching fractions for $\tilde{t}_1$ (left), $\tilde{b}_1$ (middle) and $\tilde{t}_2$ (right) in the maximal mixing scenario. The choice of neutralino and chargino mass parameters is the same as in Fig. 4.4.

For the maximally mixed scenario, the decay of $\tilde{t}_1$, $\tilde{b}_1$ and $\tilde{t}_2$ are shown in the left, middle and right panels of Fig. 4.6, respectively. For $\tilde{t}_1$ with a large mass, the decay to $b\chi_1^\pm$, $t\chi_2^0$ still dominates over $t\chi_1^0$, but the corresponding branching fractions are smaller compared to the pure left-handed case (Fig. 4.4) due to the decrease of the coupling to the Wino-like state caused by the right-handed stop component. For $\tilde{b}_1$, while the $t\chi_1^\pm$ and $b\chi_2^0$ modes still dominate the $b\chi_1^0$ mode, the new decay channel of $W\tilde{t}_1$ opens up and even dominates most of the mass range. Its branching fraction varies between 100% to about 40% for $m_{\tilde{b}_1}$ between 600 GeV to 1500 GeV. For $\tilde{t}_2$, in addition to $b\chi_1^\pm$ and $t\chi_{1,2}^0$ (from a few percent to 20%), the decays to a light stop/sbottom plus a gauge boson [123] become comparable or even dominant: about $50\% - 70\%$ for $Z\tilde{t}_1$ and about $20\% - 15\%$ for $W\tilde{b}_1$.

The left, middle and right panels of Fig. 4.7 show the $\sigma \times$ BR for $\tilde{t}_1\tilde{t}_1$, $\tilde{b}_1\tilde{b}_1$, and $\tilde{t}_2\tilde{t}_2$ respectively for the maximal mixing scenario of Case IA at the 14 TeV LHC. For the light stop, while the dominant channel is still $bbWW+\not{E}_T$, the subdominant channel $bbWWZ/h+\not{E}_T$ could still have a sizable cross section. For the light sbottom, $bbWWWW+\not{E}_T$ becomes dominant. For the heavy stop, multiple channels open, with

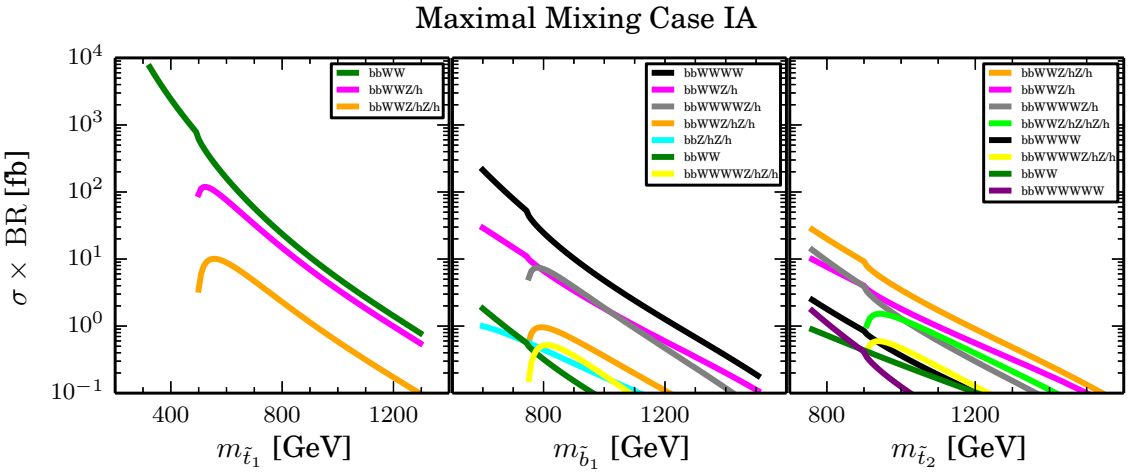

Figure 4.7: Case IA: $\sigma \times$ BR of various final states for pair production of $\tilde{t}_1$ (left), $\tilde{b}_1$ (middle), and $\tilde{t}_1$ (right) in the maximal mixing scenario at the 14 TeV LHC. The choice of neutralino and chargino mass parameters is the same as in Fig. 4.4.

$bbWWZ/hZ/h+\not{E}_T$ being dominant, followed by $bbWWZ/h+\not{E}_T$, $bbWWWWZ/h+\not{E}_T$, and $bbWWZ/hZ/hZ/h+\not{E}_T$.

4.3 Case IB: Bino-LSP with Higgsino-NLSP

The low lying neutralino/chargino spectrum in Case IB is comprised of a Bino-like LSP, as well a pair of Higgsino-like neutralino states $\chi^0_{2,3}$ and chargino states $\chi^\pm_1$ with nearly degenerate masses. Fig. 4.8 shows the branching fractions of left-handed $\tilde{t}_1$ and $\tilde{b}_1$ and right-handed $\tilde{t}_1$ in the left, middle and right panels for the minimal mixing scenario. For $\tilde{t}_1$, decays to $t\chi^0_{2,3}$ dominate over $b\chi^\pm_1$ and $t\chi^0_1$ since the former are controlled by the large top Yukawa coupling, compared to the small bottom Yukawa coupling and $\mathrm{U}(1)_Y$ couplings for the latter two. However, for $\tilde{b}_1$, the decay of $t\chi^\pm_1$ becomes dominant since the $\tilde{b}_L\bar{t}_R\tilde{H}^+_u$ coupling is proportional to the top Yukawa while its couplings to $\chi^0_{2,3}$ and χ^0_1 are suppressed by the bottom Yukawa coupling and $\mathrm{U}(1)_Y$ couplings. The right-handed $\tilde{t}_1$ case dominantly decays to $b\chi^\pm_1$, reaching almost 50%, while decays to $t\chi^0_2+t\chi^0_3$ are about 20%. All channels are controlled by the top Yukawa coupling while the latter ones have extra phase space suppression. Given the near degeneracy of the two Higgsino states $\chi^0_{2,3}$, contributions from

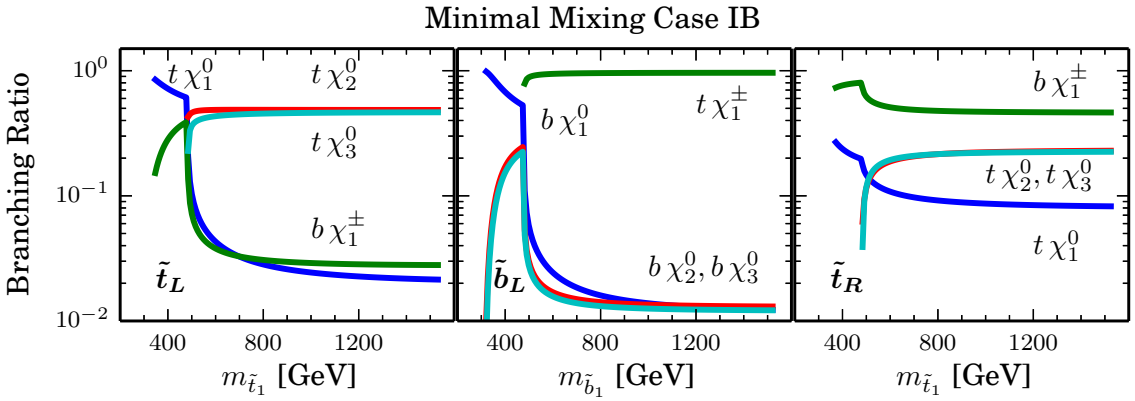

Figure 4.8: Case IB: branching fractions for left-handed $\tilde{t}_1$ (left), $\tilde{b}_1$ (middle), right-handed $\tilde{t}_1$ (right) in the minimal mixing scenario. We set $M_1 = 150$ GeV, $\mu = 300$ GeV, $M_2 = 2$ TeV, and $\tan\beta = 10$, which corresponds to $m_{\chi_1^0} = 145$ GeV, $m_{\chi_2^0} = 308$ GeV, $m_{\chi_3^0} = 310$ GeV and $m_{\chi_1^\pm} = 304$ GeV.

final states involving $\chi^0_{2,3}$ are usually summed over in collider analyses.

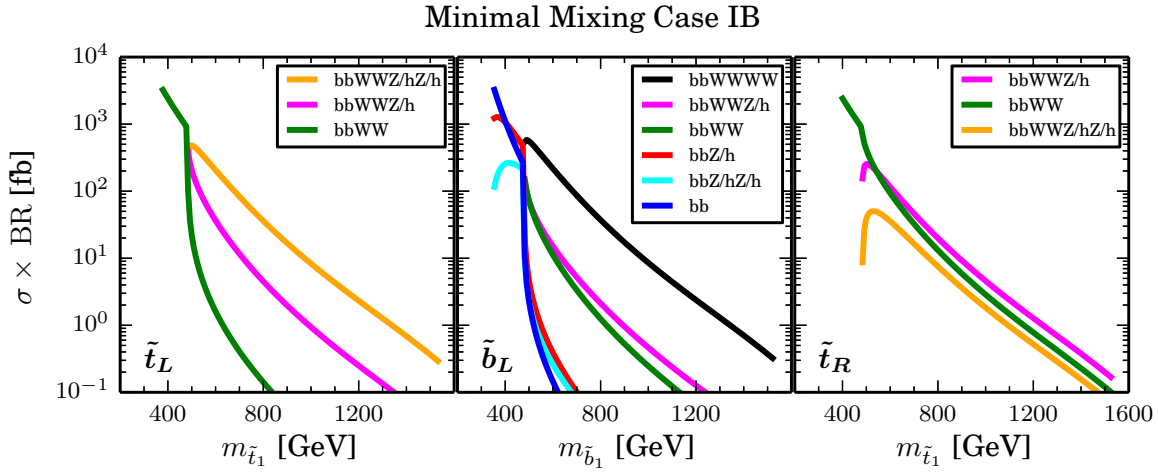

Figure 4.9: Case IB: $\sigma \times$ BR of various final states for pair production of left-handed $\tilde{t}_1$ (left), $\tilde{b}_1$ (middle), and right-handed $\tilde{t}_1$ (right) in the minimal mixing scenario at the 14 TeV LHC. The choice of neutralino and chargino mass parameters is the same as in Fig. 4.8.

Given the further decays of $\chi_1^\pm \to W\chi_1^0$, $\chi^0_{2,3} \to Z\chi_1^0/h\chi_1^0$ as discussed in detail in [122], the pair production of stops and sbottoms lead to complicated final states at the collider.

The left, middle and right panels of Fig. 4.9 show the $\sigma \times \mathrm{BR}$ for pure left-handed $\tilde{t}_1\tilde{t}_1$, $\tilde{b}_1\tilde{b}_1$ and pure right-handed $\tilde{t}_1\tilde{t}_1$ pair production in the minimal mixing scenarios of Case IB. For pure left-handed $\tilde{t}_1$, $bbWWZ/hZ/h+\not{E}_T$ is the dominant final state with the stop search channel $bbWW+\not{E}_T$ being highly suppressed. For pure left-handed $\tilde{b}_1$, $bbWWWW+\not{E}_T$ is the dominant channel. The dominant final states for pure right-handed $\tilde{t}_1$ are $bbWWZ/h+\not{E}_T$ as well as $bbWW+\not{E}_T$.

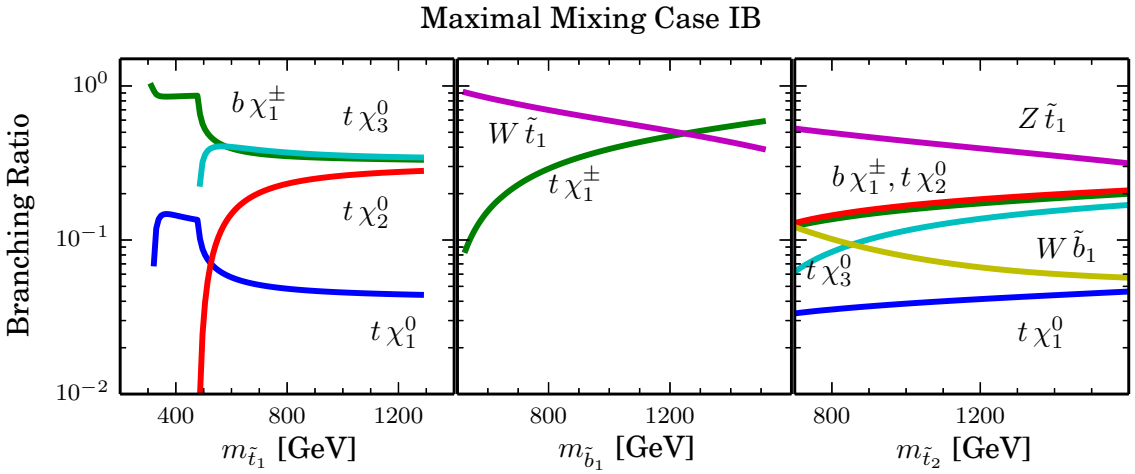

Figure 4.10: Case IB: Branching fractions for $\tilde{t}_1$ (left), $\tilde{b}_1$ (middle) and $\tilde{t}_2$ (right) in the maximal mixing scenario. The choice of neutralino and chargino mass parameters is the same as in Fig. 4.8.

For the maximal mixing scenario, the decay branching fractions for $\tilde{t}_1$, $\tilde{b}_1$, and $\tilde{t}_2$ are shown in the left, middle and right panels of Fig. 4.10, respectively. Since $\tilde{t}_1$ is an equal mixture of left- and right-handed components, the decays to $t\chi^0_{2,3}$ (dominant for $\tilde{t}_L$) and $b\chi_1^\pm$ (dominant for $\tilde{t}_R$) (see the left and right panel of Fig. 4.8) have roughly the same decay branching fraction, around 30% each. Decay to the final state of $t\chi_1^0$ is typically a few percent, unless other decay modes are kinematically unaccessible at small $m_{\tilde{t}_1}$.

For $\tilde{b}_1$, the relative strength of $t\chi_1^\pm$ and $b\chi^0_{2,3}$ is similar to that of the $\tilde{b}_1$ in the minimal mixing scenario, but the opening of the $W\tilde{t}_1$ mode dominates the decay for most of the mass range, leading to the suppression of the $t\chi_1^\pm$ and $b\chi^0_{2,3}$ modes. With increasing $m_{\tilde{b}_1}$, $t\chi_1^\pm$ becomes more and more important, which dominates over $W\tilde{t}_1$ when $m_{\tilde{b}_1} \gtrsim 1200$ GeV.

For $\tilde{t}_2$, decay to $Z\tilde{t}_1$ is dominant, about 60% − 30% for $m_{\tilde{t}_2}$ in the range of 700 − 1600 GeV. Decays to $b\chi_1^{\pm}$, $t\chi_{2,3}^0$ are sub-dominant, around 10% − 20% for each channel. $\tilde{t}_2 \to W\tilde{b}_1$ is typically around 10% to only a few percent, while $\tilde{t}_2 \to t\chi_1^0$ is only at a few percent level.

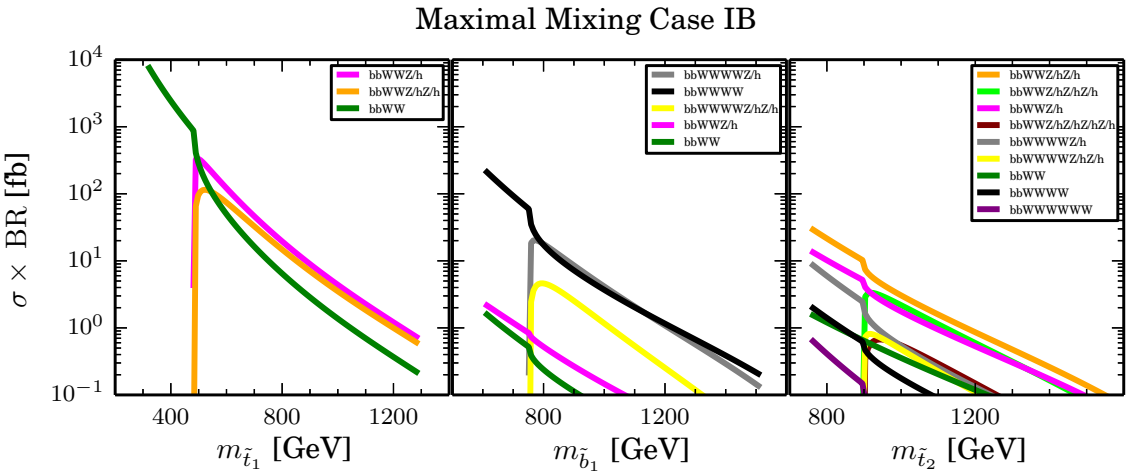

Figure 4.11: Case IB: $\sigma \times$ BR of various final states for pair production of $\tilde{t}_1$ (left), $\tilde{b}_1$ (middle), and $\tilde{t}_2$ (right) in the maximal mixing scenario at the 14 TeV LHC. The choice of neutralino and chargino mass parameters is the same as in Fig. 4.8.

The left, middle and right panel of Fig. 4.11 show the $\sigma \times$ BR for $\tilde{t}_1\tilde{t}_1$, $\tilde{b}_1\tilde{b}_1$, and $\tilde{t}_2\tilde{t}_2$ for the maximal mixing scenario of Case IB at the 14 TeV LHC. For the light stop, the dominant channel is $bbWWZ/h+\not{E}_T$, followed by $bbWWZ/hZ/h+\not{E}_T$. The $bbWW+\not{E}_T$ channel is suppressed by about a factor of 5. For the light sbottom, $bbWWWW+\not{E}_T$ and $bbWWWWZ/h+\not{E}_T$ are dominant. For the heavy stop, multiple channels open, with $bbWWZ/hZ/h+\not{E}_T$ being dominant, followed by $bbWWZ/hZ/hZ/h+\not{E}_T$ and $bbWWZ/h+\not{E}_T$.

4.4 More on Sbottom Decays

The most commonly studied channel in experimental searches is the case $\tilde{b}_1 \to b\chi_1^0$ with a branching fraction of 100%. This is true for the case with the Bino-LSP and the sbottom-NLSP, or for the case with the stop-NLSP but $m_{\tilde{b}} < m_{\tilde{t}} + M_W$, or for the case with the

Wino-NLSP for a right-handed sbottom. In a more general ground, sbottom decays lead to a much richer pattern.

4.4.1 The decay of $\tilde{b}_L$

For a more general electroweakino spectrum, other decay channels may appear or even dominate, as analyzed in detail in Ref. [124]. Here we first consider the case of the lighter sbottom being mainly left-handed $\tilde{b}_1 \sim \tilde{b}_L$. The mass spectrum of sbottom and gaugino would severely influence the decay modes of sbottom. We discuss the (mainly left-handed) sbottom decay in detail in two general situations with a Bino-LSP:

$$m_{\tilde{b}_1} > M_2 > M_1 \quad (\text{Wino} - \text{NLSP}), \tag{4.1}$$

$$m_{\tilde{b}_1} > |\mu| > M_1 \quad (\text{Higgsino} - \text{NLSP}). \tag{4.2}$$

The more complex cases where both Winos and Higgsinos are below the sbottom mass threshold

$$m_{\tilde{b}_1} > |\mu| > M_2 > M_1 \quad (\text{Wino} - \text{NLSP/Higgsino} - \text{NNLSP}), \tag{4.3}$$

$$m_{\tilde{b}_1} > M_2 > |\mu| > M_1 \quad (\text{Higgsino} - \text{NLSP/Wino} - \text{NNLSP}), \tag{4.4}$$

are also included when distinct features are present (sometimes referred as mixed NLSP's). We illustrate the sbottom decay in Fig. 4.12 for these four different situations. Each corresponds to a different mass spectrum of gaugino and sbottom for a Bino-LSP. The usually considered channel $b\chi_1^0$ is suppressed, if other channels are open, since the bino $\mathrm{U}(1)_Y$ coupling is smaller than the wino $\mathrm{SU}(2)_L$ coupling or top Yukawa coupling. In Fig. 4.12(a), where $\tilde{b}_1 \to t\chi_1^\pm$ and $\tilde{b}_1 \to b\chi_2^0$ are open while the Higgsinos-like neutralinos/charginos are decoupling ($|\mu| > M_{\tilde{b}_1} > M_2 > M_1$), sbottom decays dominantly into $t\chi_1^\pm$ and $b\chi_2^0$. Contrarily, in Fig. 4.12(b), we decouple Wino-like gaugino while leaving the channel containing Higgsino-like gaugino opening ($M_2 > M_{\tilde{b}_1} > |\mu| > M_1$), $\tilde{b}_1 \to t\chi_1^\pm$ will soon dominant other possible channels when the phase space is open due to the large top Yukawa coupling. $\tilde{b}_1 \to b\chi_{2,3}^0$ are suppressed due to the relatively small bottom Yukawa coupling. Here we have adopted $\tan\beta = 10$. For a larger value of $\tan\beta$, $b\chi_2^0, b\chi_3^0$ channels will be relatively more important. For more complicated situation, in the lower two panels,

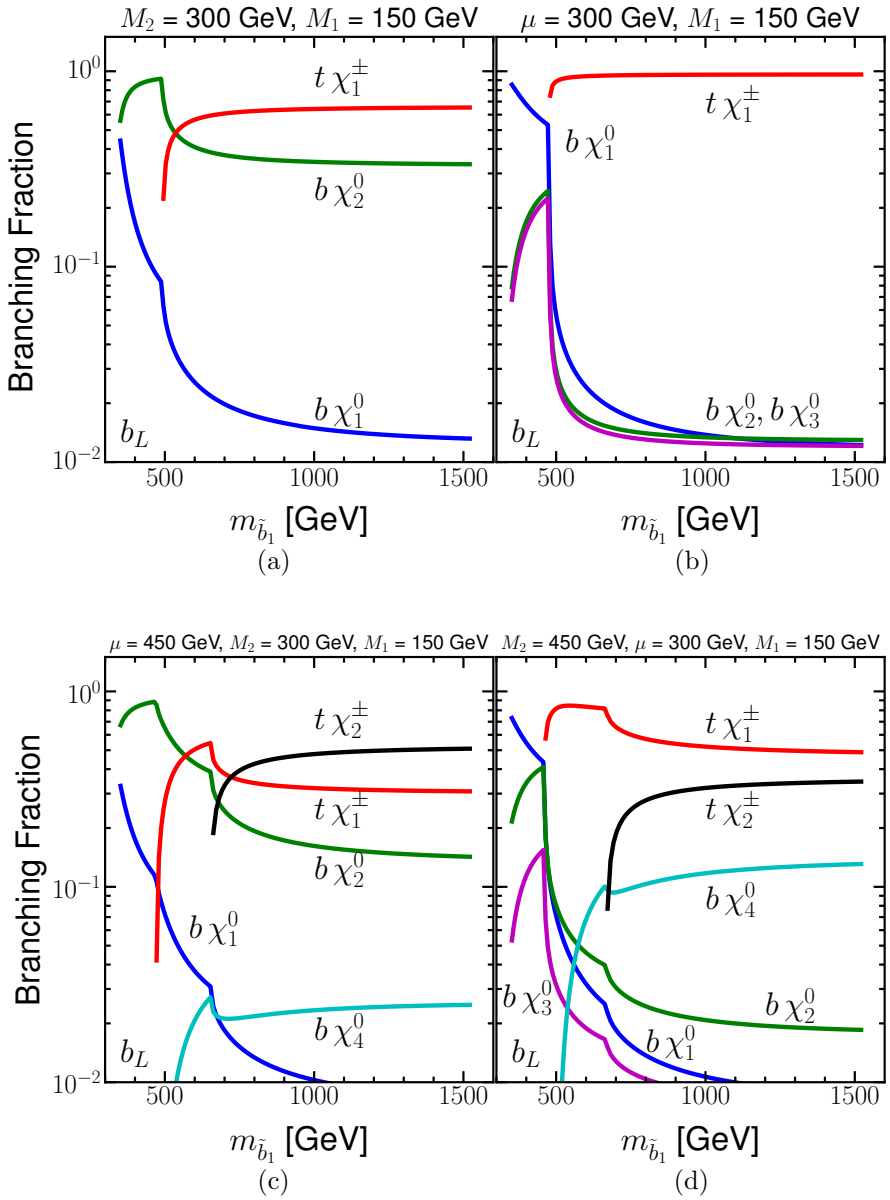

Figure 4.12: Branch fractions of the left-handed sbottom decay versus its mass in four different cases: (a) $m_{\tilde{b}_1} > M_2 > M_1$, Wino-NLSP; (b) $m_{\tilde{b}_1} > |\mu| > M_1$, Higgsino-NLSP; (c) $m_{\tilde{b}_1} > |\mu| > M_2 > M_1$, Wino-NLSP/Higgsino-NNLSP, and (d) $m_{\tilde{b}_1} > M_2 > |\mu| > M_1$, Higgsino-NLSP/Wino-NNLSP. Here we have adopted $\tan\beta = 10$.

we consider the cases of $M_{\tilde{b}_1} > |\mu| > M_2 > M_1$ (Fig. 4.12(c)) and $M_{\tilde{b}_1} > M_2 > |\mu| > M_1$ (Fig. 4.12(d)). In both cases, sbottom decays dominantly into Higgsino-like chargino, then Wino-like chargino and finally Wino-like neutralino. Other channels are highly suppressed since the $U(1)_Y$ coupling and bottom Yukawa coupling are much smaller.

A special remark is in order. Although $\tilde{b}_L$ and $\tilde{t}_L$ share the same soft mass parameter M_{3SQ}, the large mixing between $\tilde{t}_L - \tilde{t}_R$ due to the large trilinear soft SUSY breaking A_t often drags the mass of the (mixed) stop below that of the (mainly left-handed) sbottom. The decay $\tilde{b}_1 \to W\tilde{t}_1$ usually dominates once it is kinematically open. However, the above decay patterns still hold as long as $M_{\tilde{b}_1} < M_{\tilde{t}_1} + m_W$.

4.4.2 The decay of $\tilde{b}_R$

For the $\tilde{b}_R$, the usually considered channel $b\chi_1^0$ is the dominant mode. We present the branching fractions of $\tilde{b}_R$ in Fig. 4.13, for (a) the Wino-NLSP and (b) the Higgsino-NLSP. We see that the channel $\tilde{b}_1 \to b\chi_1^0$ in the Wino-NLSP scenario is almost 100%, since the right-handed squark has no $SU(2)_L$ coupling. However, this channel in the Higgsino-NLSP scenario presents a branching fraction of about $40\% - 60\%$, followed by the channel of $\tilde{b}_1 \to t\chi_1^\pm$ about $20\% - 30\%$, since the coupling effects of the right-handed squark to Bino and Higgsino is $U(1)_Y$ and bottom Yukawa, respectively.

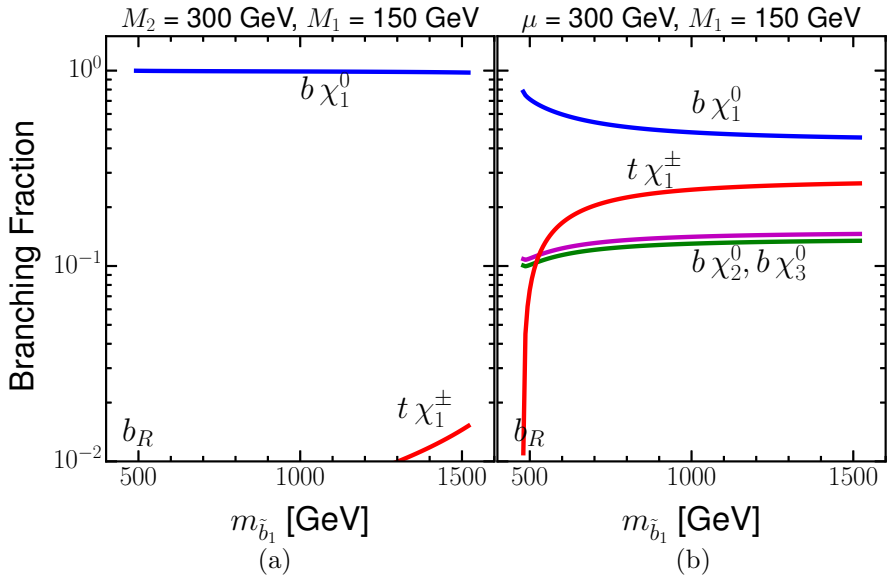

Figure 4.13: Branch fractions of the right-handed sbottom decay versus its mass for (a) $m_{\tilde{b}_1} > M_2 > M_1$, Wino-NLSP and (b) $m_{\tilde{b}_1} > |\mu| > M_1$, Higgsino-NLSP. Here we have adopted $\tan\beta = 10$.

CHAPTER 5

Collider Analysis

5.1 Collider physics

High energy experiments played a critical role in the development of the Standard Model, including the discovery of vector bosons, the top quark and the Higgs boson. These discoveries promote the establishment of the Electroweak theory and the Higgs Mechanism. In this section, I will introduce (1) the QCD and parton model to understand the proton at high speed, (2) the detectors at the current LHC to understand the collision processes, and (3) the detection of particles. Since various tools are used for Monte Carlo simulation for phenomenology studies, it is necessary to introduce those simulation tools.

5.1.1 QCD

As discussed in Chapter 2, the gauge symmetry of QCD follows the group $SU(3)_c$. The gauge theory of $SU(3)_c$ is non-Abelian, leading to two peculiar properties: asymptotic freedom and color confinement. Asymptotic freedom states that the interaction strength decreases as the transferred momentum in the interaction increases. After careful calculations of gauge-invariant one-loop radiative corrections to the quarks, gluons as well as ghosts, one can obtain the β function [125, 126] for QCD:

$$\beta(g_s) \equiv \frac{\partial g_s}{\partial \log Q} = -\frac{g_s^3}{(4\pi)^2}(11 - \frac{2n_f}{3}) \tag{5.1}$$

where Q is the energy scale, n_f is the number of quark flavors, and g_s is the coupling constant of strong interaction. In the Standard Model $n_f = 6$, then the coefficient of the β function is -7, which means the coupling strength becomes weaker at a higher energy scale.

The quantity $\alpha_s = g_s^2/(4\pi)^2$, being similar to the fine structure, has the following feature:

$$\frac{\partial \alpha_s^{-1}}{\partial \log(Q/M)} = -\frac{b_0}{2\pi} \tag{5.2}$$

with $b_0 \equiv 11 - \frac{2n_f}{3}$ and initial condition $\alpha_s(M) = \alpha_s$. The solution to the above renormalization group equation is:

$$\alpha_s(Q) = \frac{\alpha_s}{1 + (b_0\alpha_s/2\pi)\log(Q/M)} \tag{5.3}$$

We define a mass scale called Λ_{QCD} satisfying:

$$1 = \frac{g^2 b_0}{8\pi^2}\log(M/\Lambda_{\mathrm{QCD}}) \tag{5.4}$$

For "massless" quarks, Λ_{QCD} is typically 200 MeV. At an energy scale less than Λ_{QCD}, the perturbative approach is not valid any more.

The evolution of α_s has been confirmed by various experiments, shown in Figure 5.1. In contrast to the electromagnetic screening at large distance, the coupling constant of strong interaction is amplified at large distance, instead. This can be explained by the behavior of gluons. In QED, virtual particle and anti-particle pairs act as electric dipoles and align themselves along with the electric field produced by the electric charge in the vacuum. Therefore the net effect is to partially cancel out the field, leading to screening of the electric charge. However, there are gluons in QCD in addition to quark-antiquark pairs, and these gluons carry color charges and can interact with themselves, contributing to augmenting the field instead of screening the field. So the net effect of quark-antiquark and gluons is anti-screening of the field. This phenomenon , called "$asympotic\ freedom$", was discovered by Gross and Wilczek [63], and Politzer [64].

The proton is a bound state of light quarks uud, called "Valence quarks". Inside a proton, the light quarks are not static. Instead, enormous virtual processes of gluons self interaction, quarks creation and annihilation happen inside proton, especially when the proton is accelerated nearly to the speed of light. The internal structure of the proton can be well described by the parton distribution functions (PDF). The PDF denoted as $f_q(x)$ states the probability of finding a certain flavor quark q with momentum fraction x. The

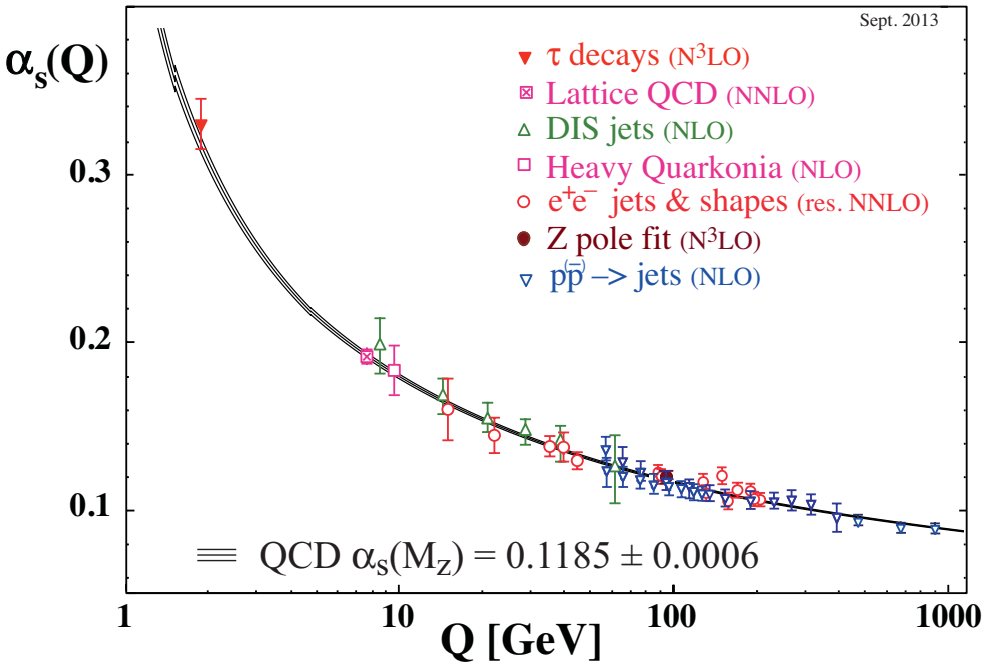

Figure 5.1: Running of α_s as a function of energy scale, figure taken from Ref [33].

proton should contain an excess of two u quarks and one d quark, from which we can get the following constraints,

$$\int_0^1 dx\,[f_u(x) - f_{\bar{u}}(x)] = 2 \qquad \int_0^1 dx\,[f_d(x) - f_{\bar{d}}(x)] = 1 \tag{5.5}$$

Calculations of PDF are non-perturbative and challenging. Therefore, the PDF is usually determined by the data-driven method. Figure 5.2 shows the proton PDF at energy scale $Q^2 = 10$ (10000) GeV^2. At a high momentum fraction regime, the PDF is dominated by the valence quarks as expected, with a 2:1 ratio of u to d quarks. We also find a large contribution of gluons (scaled by a factor of 10), which is the dominant contributor to the Higgs boson production through gluon gluon fusion at the LHC. Comparing the left and right panels, we find that the gluons and sea quarks PDF shift to a higher momentum fraction regime, at a higher energy scale Q. In high center of mass energy colliders like the current LHC and the future 100 TeV collider, heavy quarks such as charm quarks and bottom quarks have non-trivial contributions to the proton PDF.

Due to the Asymptotic freedom, any non-Abelian gauge structure will exhibit the

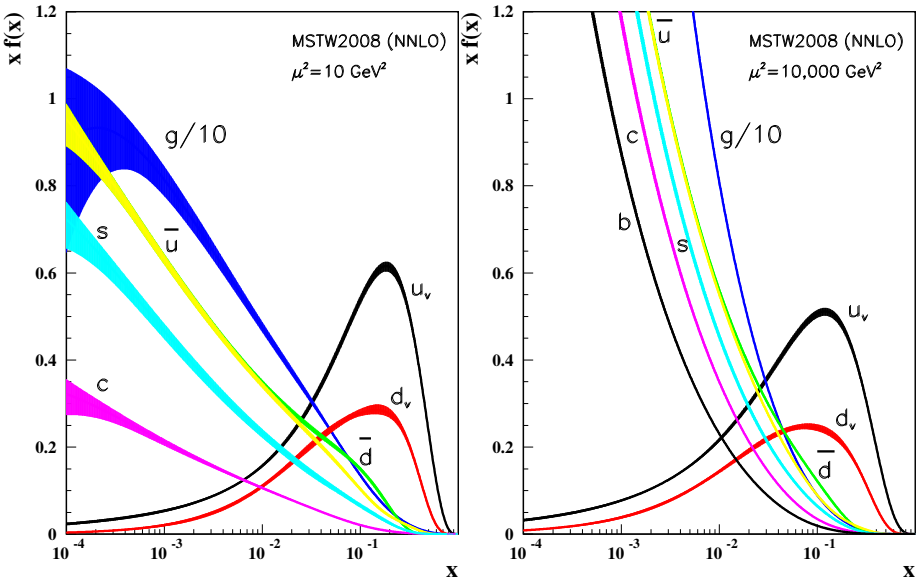

Figure 5.2: Proton PDF at energy scale $Q^2 = 10$ GeV^2 (left) and $Q^2 = 10000$ GeV^2 (right) compiled by the MSTW collaboration and taken from Ref [33].

"*confinement of color*" for sufficiently strong coupling, leading to the phenomena of hadronization. So the only asymptotic states are those that are singlets of $SU(3)$ color. If one attempts to separate a color-singlet state into colored components, for instance, to dissociate a meson into a quark and an antiquark state, then a tube of gauge field forms between the two sources. The potential between the two sources increases with the distance $V(r) \sim r$, contrary to the potential decreasing with distance $V(r) \sim \frac{1}{r}$ in QED. When free quarks are created, they will soon be captured by other quarks or gluons to form color-singlet state, and this process will continue to form a bunch of hardons and mesons, called "*jet*" in experimental high energy physics.

5.1.2 Detectors

The Large Hadron Collider (LHC) at CERN in Geneva, Switzerland, is designed to have proton proton collision at $\sqrt{s} = 14$ TeV. The LHC has not reached its full design. During 2015, the LHC began to run at the center-of-mass energy of 13 TeV. Later upgrades will

increase the center-of-mass energy to 14 TeV in the near future. At center-of-mass energy of 14 TeV, the LHC is expected to collect 300 fb^{-1} of data. Future high luminosity upgrades are planned to run at the High Luminosity LHC (HL-LHC) to collect about 3000 fb^{-1} of data [127]. The two important detectors in connection to this work, ATLAS and CMS, are similar in the structure [128, 129]. The ATLAS and CMS detectors consist of four parts: the tracker, electromagnetic calorimeter, hadronic calorimeter, and muon spectrometer. There exists a strong magnetic field inside the detector which is used to deflect charged particles. Here I give a brief introduction to the detectors, using ATLAS as the example.

Tracker

The tracker is the innermost part of the detector, near the interaction point. The Tracker is composed of pixel silicon microstrip (SCT) and the straw tubes of the Transition Radiation Tracker (TRT), used to capture the the tracks of charged particles. From this the charge and vertex locations of the tracks can be extracted to help identify particles. The inner detector (Tracker) is contained in a solenoid magnet of 2 Tesla, and the strong magnetic field bends the trajectory of charge particles thus allowing it to measure the momentum of the particle from the curvature of the tracks. The secondary vertex measurement is also conducted in the innermost layer of pixels. Therefore, the tracker is particularly critical in the identification of jets originating from bottom quarks, called b-jets. Hadrons containing b quarks are relatively long lived before they decay, leaving a secondary interaction vertex. The process containing one or more b jet in the final state is very important to reduce huge QCD backgrounds.

Calorimeters

Outside the Tracker live LAr electromagnetic (EM) calorimeters and hadronic calorimeters. The main function of the calorimeters is to contain the electromagnetic and hadronic showers produced in pp collisions. The EM calorimeter is divided into a barrel part ($|\eta| < 1.475$) and two end-cap components ($1.375 < |\eta| < 3.2$), to achieve the desired calorimeter performance. The EM calorimeter uses lead as the absorbption material to fully absorb incident particles, uses a scintillator for light output and uses liquid argon for ionization information. The hadronic calorimeters are directly placed outside the EM calorimeter envelope. The hadronic calorimeters are divided into three parts: the tile calorimeter, LAr

hadronic end-cap calorimeter and LAr forward calorimeter. The hadronic calorimeters are the same as the EM calorimeters in principle except that the hadronic calorimeters are deeper and denser, due to the larger interaction length of the hadronic processes.

Muon spectrometer

The muon spectrometer is the outermost and largest detector of ATLAS and CMS, and is designed to measure high-p_T muons with high resolution. The muon is approximately 200 times as massive as the electron and has a long half life time. As a result, muons do not deposit all of their energy in the electromagnetic calorimeters and can travel all the way to the outermost muon spectrometer before they decay. The spectrometer can measure trajectories of muons to determine their direction, their electric charge and their momentum due to the strong magnetic field induced by toroid magnets. Because the muon spectrometer sits outermost from the process interaction point, very few particles can reach or leave signals in the muon spectrometer.

Although all the above detectors can collect information of the particles, it is a difficult task to reconstruct particles especially jets from detector readouts, due to the huge QCD backgrounds.

5.1.3 Monte Carlo Simulation

The Monte Carlo simulation is essential in both experimental study and phenomenology research to understand how physics processes work and present themselves in data. Specifically, the Monte Carlo simulation is critical for new physics beyond the Standard Model like SUSY, since it helps phenomenology researchers to visualize the feasibility of a new physics model and provides hints to improve it. The simulations fall into two categories: numerical calculations to obtain the matrix elements as well as the cross sections up to next leading order (NLO) for a process, and stochastic process generation to simulate the stochastic processes of event generation, hadronization, and detector simulation. The CalcHEP [130] is used to calculate the cross sections of physical processes.

The software package Madgraph [131] is a framework which can provide the computations of cross sections, the generation of hard processes, their shower matching and merging with event generators, and a variety of tools relevant to event analysis. It has been up-

graded to include calculations of NLO cross sections. It implements models of the Standard Model, SUSY, 2HDM and other new physics models. The stage at which processes are generated by Madgraph is referred to as the parton level, which can help to calibrate the performance of the simulation in the comparison to the detector reconstructions. The next step incorporates particle showers, fragmentation and hadronization. In our Monte Carlo studies, Pythia [132] is used for this purpose. Pythia is a framework containing theory and models for a variety of aspects in physics, including hard and soft processes, parton distributions, initial state and final state parton showers, fragmentation, hadronization and decay. Lastly, the whole process will go through PGS [133] or Delphes [134] for the detector simulation. The simulation includes the track system, a magnetic field, calorimeters and a muon spectrometer. The goal of the detector simulation is to turn the Pythia outputs into detector objects: electrons, photons, muons, jets, and missing energy.

5.2 Current bounds on third generation squarks

Most of the current searches for the light stop focus on the decay $\tilde{t}_1 \to t\chi_1^0$ or $\tilde{t}_1 \to b\chi_1^\pm \to bW\chi_1^0$. For stop pair production at the LHC, such processes lead to $tt+\not{E}_T$ or $bbWW+\not{E}_T$ final states. However, due to the large SM backgrounds from $t\bar{t}$, searches for the stop can be very challenging. Searches for direct stop and sbottom pair production have been performed at both ATLAS and CMS, with about 20 fb^{-1} data at $\sqrt{s} = 8$ TeV, and about 5 fb^{-1} data at $\sqrt{s} = 7$ TeV [135–153]. Here we summarize the current experimental search channels and exclusion bounds assuming a stable neutralino LSP. Stop searches in scenarios with a Gravitino LSP have been analyzed in Refs. [143, 146].

- $\tilde{t}_1 \to t^{(*)}\chi_1^0$ and $\tilde{t}_1 \to b\chi_1^\pm \to bW^{(*)}\chi_1^0$ [135–140]

  ATLAS results on fully hadronic final states [135] exclude stops in the regions of 270 $< m_{\tilde{t}_1} <$ 645 GeV for $m_{\tilde{\chi}_1^0} < 30$ GeV, assuming both stops decay 100% via $\tilde{t}_1 \to t\chi_1^0$. Regions of $245 < m_{\tilde{t}_1} < 400$ GeV for $m_{\tilde{\chi}_1^0} < 60$ GeV, $m_{\chi_1^\pm} = 2m_{\chi_1^0}$ are excluded when both stops decay 100% via $\tilde{t}_1 \to bW^{(*)}\chi_1^0$. For BR$(\tilde{t}_1 \to bW^{(*)}\chi_1^0)$ = BR$(\tilde{t}_1 \to t\chi_1^0)$ = 50%, stop masses in the range of $250 - 550$ GeV are excluded for $m_{\tilde{\chi}_1^0} < 60$ GeV, $m_{\chi_1^\pm} = 2m_{\chi_1^0}$.

For semileptonic channels, stop masses between 210 GeV and 640 GeV are excluded at 95% C.L. for a massless LSP, and stop masses around 550 GeV are excluded for LSP mass below 230 GeV [136], assuming BR($\tilde{t}_1 \to t\chi_1^0$) =100%. For BR($\tilde{t}_1 \to b\chi_1^\pm \to bW^{(*)}\chi_1^0$) =100%, the excluded stop and LSP masses depend strongly on the mass of the $\chi_1^\pm$. For $m_{\chi_1^\pm} = 2m_{\chi_1^0}$, stop masses up to 500 GeV are excluded for LSP masses in the range of 100 and 150 GeV. For the compressed spectrum case when $m_{\chi_1^\pm} - m_{\chi_1^0}$ is small with soft leptons from $\chi_1^\pm$ decay, stop masses between 265 (240) GeV and 600 GeV are excluded for $m_{\chi_1^\pm} - m_{\chi_1^0} = 5(20)$ GeV with an LSP mass of 100 GeV. For small mass splitting between $\tilde{t}_1$ and $\chi_1^\pm$ (for example, 10 GeV) with soft b jets, stop masses below 390 GeV are excluded for a massless LSP. When both decay modes $\tilde{t}_1 \to t\chi_1^0$ and $\tilde{t}_1 \to b\chi_1^\pm$ are open, the excluded stop masses increase from 530 GeV to 660 GeV for an LSP mass of 100 GeV when BR($\tilde{t}_1 \to t\chi_1^0$) is increased from 0% to 100% and $m_{\chi_1^\pm} = 2m_{\chi_1^0}$. The limits get weaker with an increased branching ratio to decays other than $\tilde{t}_1 \to t\chi_1^0$ and $\tilde{t}_1 \to b\chi_1^\pm$.

Limits from the pure leptonic channels are weaker [137]. Stops with masses between 215 GeV and 530 GeV decaying to an on-shell t-quark and a neutralino are excluded at 95% C. L. for a 1 GeV neutralino. For $m_b + m_W + m_{\chi_1^0} < m_{\tilde{t}_1} < m_t + m_{\chi_1^0}$ with an off-shell top and a neutralino LSP, the stop masses are excluded between 90 GeV and 170 GeV. For BR($\tilde{t}_1 \to b\chi_1^\pm$) = 100%, the limits on the stop mass depend on both the LSP mass and $m_{\chi_1^\pm}$. $m_{\tilde{t}_1}$ between 150 GeV and 445 GeV is excluded at 95% C. L. for $m_{\tilde{t}_1} = m_{\chi_1^\pm} + 10$ GeV, in the case of a 1 GeV neutralino LSP. For $m_{\tilde{t}_1} = 2m_{\chi_1^\pm}$, stop masses between 210 GeV and 340 GeV are excluded for an LSP mass of 100 GeV. For a fixed $m_{\chi_1^\pm} = 106$ GeV, stop masses between 240 GeV to 325 GeV are excluded with an LSP mass of 1 GeV.

Limits from CMS are very similar [138–140]. Note that limits on the stop exclusion depend on the branching fractions of $\tilde{t}_1 \to t^{(*)}\chi_1^0$ and $\tilde{t}_1 \to b\chi_1^\pm$. For $\tilde{t}_1 \to b\chi_1^\pm$, the limits also depend on the mass of the intermediate chargino.

- $\tilde{t}_1 \to c\chi_1^0$ or $\tilde{t}_1 \to bff'\chi_1^0$ [141, 142]

  For small mass splitting between $m_{\tilde{t}_1}$ and $m_{\chi_1^0}$, stop decays via $\tilde{t}_1 \to c\chi_1^0$ or $\tilde{t}_1 \to$

$bff'\chi_1^0$ [141, 142]. For 100% branching fraction of $\tilde{t}_1 \to c\chi_1^0$, searches on charm tagged events and monojet-like events exclude stop masses around 240 GeV for $\Delta m = m_{\tilde{t}_1} - m_{\chi_1^0} < 85$ GeV. Stop masses up to 270 GeV are excluded for an LSP mass of 200 GeV. For nearly degenerate stop and LSP, stop masses up to about 260 GeV are excluded. For 100% branching fraction of $\tilde{t}_1 \to bff'\chi_1^0$, searches based on monojet plus $\not{E}_T$ exclude stop masses up to about 255 GeV for $\Delta m \sim m_b$ and about 150 (200) GeV for $m_b < \Delta m < 50(35)$ GeV.

For small mass splitting between $m_{\chi_1^\pm}$ and $m_{\chi_1^0}$ with undetectable decay products of $\chi_1^\pm$, pair production of stop with $\tilde{t}_1 \to b\chi_1^\pm$ leads to two b jets plus $\not{E}_T$ events. Results from ATLAS [147] exclude stop masses up to 580 (440) GeV for $m_{\chi_1^\pm} - m_{\chi_1^0} = 5(20)$ GeV and $m_{\chi_1^0} = 100$ GeV.

- $\tilde{t}_2 \to \tilde{t}_1 Z/h$ [143–145]

  Searches for the second stop utilize the decay of $\tilde{t}_2 \to \tilde{t}_1 Z/h$, looking for signals including b-jets and large $\not{E}_T$ with either same flavor leptons reconstruction of the Z boson [143] and/or high p_T jet and b-jet multiplicities with additional leptons [144, 145]. The interpretation is performed in the region $m_{\tilde{t}_1} - m_{\chi_1^0} \sim m_t$, which is hard to probe by the $\tilde{t}_1 \to t\chi_1^0$ channel given the relative small $\not{E}_T$. For BR($\tilde{t}_2 \to \tilde{t}_1 Z$) = 100%, the second stop mass is excluded up to about 600 GeV for a light LSP mass. For BR($\tilde{t}_2 \to \tilde{t}_1 h$) = 100%, the second stop mass exclusion limit is about 540 GeV. When the decay branching fraction to $\tilde{t}_1 Z$ and $\tilde{t}_1 h$ is 50% each, the exclusion limit is about 580 GeV for a light LSP mass.

- $\tilde{b}_1 \to b\chi_1^0$ [141, 147, 148]

  Sbottom pair production with $\tilde{b}_1 \to b\chi_1^0$ leads to signals with two b jets and large $\not{E}_T$. The null results from ATLAS [147] exclude sbottom masses up to 620 GeV for $m_{\chi_1^0}$ <120 GeV. $m_{\tilde{b}_1} - m_{\chi_1^0}$ is excluded up to 50 GeV for sbottom masses up to 300 GeV. The exclusion limits depend largely on the branching fraction of $\tilde{b}_1 \to b\chi_1^0$. For 60% branching fractions, the sbottom exclusion limit is reduced to 520 GeV. The CMS exclusion limits are about 70 GeV stronger [148]. For small mass splitting

between sbottom and the LSP: $m_{\tilde{b}_1} - m_{\chi_1^0} \sim m_b$, monojet plus $\not{E}_T$ search excludes sbottom masses up to about 255 GeV [141].

- $\tilde{b}_1 \to b\chi_2^0$ [149, 150]

  Sbottom searches on direct sbottom pair production with $\tilde{b}_1 \to b\chi_2^0$ with 100% decay branching fraction of $\chi_2^0 \to \chi_1^0 h$ have been performed at ATLAS [149], searching for signals with zero lepton, large $\not{E}_T$, high jet multiplicity and at least three b-tagged jets. Null search results exclude the sbottom masses between 340 and 600 GeV for $m_{\chi_2^0} = 300$ GeV and $m_{\chi_1^0} = 60$ GeV. No sensitivity is obtained for $m_{\chi_2^0} < 240$ GeV due to the soft $\not{E}_T$ in the signal events. For $\tilde{b}_1 \to b\chi_2^0$ with 100% decay branching fraction of $\chi_2^0 \to \chi_1^0 Z$, three leptons plus one b jet plus $\not{E}_T$ search at the CMS excludes sbottom masses up to 450 GeV for LSP masses between 100 to 125 GeV and $m_{\chi_1^\pm} - m_{\chi_1^0} = 110$ GeV [150].

- $\tilde{b}_1 \to t\chi_1^\pm$ [150–153]

  Sbottom searches on direct sbottom pair production with $\tilde{b}_1 \to t\chi_1^\pm$ with 100% decay branching fraction of $\chi_1^\pm \to W\chi_1^0$ have been performed at both ATLAS and CMS [151, 152], looking for signals with two same charge leptons or three leptons plus multiple jets. The interpretation was done for fixed $m_{\chi_1^0} = 60$ GeV as well as varying $m_{\chi_1^0}$ with $m_{\chi_1^\pm} = 2m_{\chi_1^0}$. The sbottom mass limit is about 440 GeV in both cases for $m_{\chi_1^\pm} < m_{\tilde{b}_1} - m_t$ [151]. The CMS limits are about 50 to 100 GeV stronger [150, 152, 153].

At the 14 TeV LHC, with the dominant decay channel of $\tilde{t}_1 \to t\chi_1^0$, studies using semileptonic channel and fully hadronic channel show that for LSP masses below 200 GeV, a 5σ reach of stop discovery is possible for stop masses up to about 1 TeV with 300 fb^{-1} integrated luminosity [154]. For the high luminosity option of LHC (HL-LHC) with 3000 fb^{-1} integrated luminosity, the discovery reach is extended by about 200 GeV. The 95% exclusion limit is about 1.2 TeV (1.45 TeV) with 300 (3000) fb^{-1} integrated luminosity. For sbottom searches with $\tilde{b}_1 \to b\chi_1^0$, the discovery reach is about 1.1 (1.3) TeV and the exclusion reach is about 1.4 (1.55) TeV with 300 (3000) fb^{-1} integrated luminosity [155]. CMS analyses using specific full spectrum benchmark points show similar sensitivities [156].

Decay channels	Mass bounds $m_{\tilde{b}}$	BR	Assumptions
$\tilde{b}_1 \to b\chi_1^0$ (ATLAS [147])	620	100%	$m_{\chi_1^0} < 120$
	520	60%	$m_{\chi_1^0} < 150$
$\tilde{b}_1 \to b\chi_1^0$ (ATLAS [141])	255	100%	$m_{\tilde{b}} - m_{\chi_1^0} \sim m_b$
$\tilde{b}_1 \to b\chi_1^0$ (CMS [148])	700	100%	Small $m_{\chi_1^0}$
$\tilde{b}_1 \to b\chi_2^0 \to bh\chi_1^0$ (ATLAS [149])	340 - 600	100%	$m_{\chi_2^0} = 300$ $m_{\chi_1^0} = 60$
$\tilde{b}_1 \to b\chi_2^0 \to bZ\chi_1^0$ (CMS [150])	450	100%	$100 < m_{\chi_1^0} < 125$ $m_{\chi_2^0} - m_{\chi_1^0} = 110$
$\tilde{b}_1 \to t\chi_1^-$ (ATLAS [151])	440	100%	$m_{\chi_1^\pm} < m_{\tilde{b}} - m_t$
$\tilde{b}_1 \to t\chi_1^-$ (CMS [150])	575	100%	$150 < m_{\chi_1^\pm} < 375$ $m_{\chi_1^0} = 50$
	575	100%	$25 < m_{\chi_1^0} < 150$ $\frac{m_{\chi_1^0}}{m_{\chi_1^\pm}} = 0.5$
	525	100%	$25 < m_{\chi_1^0} < 200$ $\frac{m_{\chi_1^0}}{m_{\chi_1^\pm}} = 0.8$
$\tilde{b}_1 \to t\chi_1^-$ (CMS [152])	500	100%	$\frac{m_{\chi_1^0}}{m_{\chi_1^\pm}} = 0.5$ (0.8)
$\tilde{b}_1 \to t\chi_1^-$ (CMS [153])	550	100%	$m_{\chi_1^0} = 50$

Table 5.1: Current mass bounds on the sbottom from the direct searches at the LHC. All units are in GeV for mass.

Other theoretical studies in the literature on the stop searches at the LHC mostly focus on the light stop decaying to light generation quarks [157–161] with little missing energy, which mimics the WW signal at the LHC [162–166] or on multi-b jets final states from a light stop [167]. For the sbottom, in a parameter space with a highly degenerate sbottom and LSP masses, a strategy has been proposed to search for sbottom based on boosting bottoms through an energetic initial radiation jet [168].

We summarize the current search bounds in Table 5.1 and Table 5.2.

Decay channels	Mass bounds $m_{\tilde{t}_1}$	BR	Assumptions
$\tilde{t}_1 \to t\chi_1^0$ (ATLAS 0ℓ [135])	270 - 645	100%	$m_{\chi_1^0} < 30$
	250 - 550	50%	$m_{\chi_1^0} < 60$, $m_{\chi_1^\pm} = 2m_{\chi_1^0}$
$\tilde{t}_1 \to t\chi_1^0$ (ATLAS 1ℓ [136])	210 - 640	100%	$m_{\chi_1^0} = 0$
	550	100%	$m_{\chi_1^0} < 230$
$\tilde{t}_1 \to t\chi_1^0$ (ATLAS 2ℓ [137])	215 - 530	100%	$m_{\chi_1^0} = 1$
$\tilde{t}_1 \to t\chi_1^0$ (CMS 0ℓ [138])	535	100%	$m_{\chi_1^0} < 10$
$\tilde{t}_1 \to t\chi_1^0$ (CMS 1ℓ [139])	750	100%	$m_{\chi_1^0} = 100$
	680	50%	$m_{\chi_1^0} = 100$
$\tilde{t}_1 \to t\chi_1^0$ (CMS 1ℓ [140])	150 - 650	100%	$m_{\chi_1^0} < 250$
$\tilde{t}_1 \to b\chi_1^\pm$ (ATLAS 0ℓ [135])	245 - 400	100%	$m_{\chi_1^0} < 60$
$\tilde{t}_1 \to b\chi_1^\pm$ (ATLAS 1ℓ [136])	500	100%	$100 < m_{\chi_1^0} < 150$, $m_{\chi_1^\pm} = 2m_{\chi_1^0}$
$\tilde{t}_1 \to b\chi_1^\pm$ (ATLAS 2ℓ [137])	150 - 445	100%	$m_{\chi_1^0} = 1$, $m_{\chi_1^\pm} \sim m_{\tilde{t}_1}$
$\tilde{t}_1 \to b\chi_1^\pm$ (CMS 1ℓ [139])	700	100%	$m_{\chi_1^\pm} - m_{\chi_1^0} = 5$, $m_{\chi_1^0} = 100$
	670	50%	$m_{\chi_1^\pm} - m_{\chi_1^0} = 5$, $m_{\chi_1^0} = 100$
$\tilde{t}_1 \to b\chi_1^\pm$ (CMS 1ℓ [140])	620	100%	$m_{\chi_1^\pm} = 0.25\ m_{\chi_1^0} + 0.75\ m_{\tilde{t}_1}$, $m_{\chi_1^0} = 130$
	680	100%	$m_{\chi_1^\pm} = 0.75\ m_{\chi_1^0} + 0.25\ m_{\tilde{t}_1}$, $m_{\chi_1^0} = 0$
$\tilde{t}_1 \to c\chi_1^0$ (ATLAS [141])	240	100%	$m_{\tilde{t}_1} - m_{\chi_1^\pm} < 85$
	270	100%	$m_{\chi_1^0} = 200$
	260	100%	$m_{\chi_1^0} \sim m_{\tilde{t}_1}$
$\tilde{t}_1 \to c\chi_1^0$ (CMS [142])	250	100%	$m_{\tilde{t}_1} - m_{\chi_1^0} < 10$
$\tilde{t}_1 \to bff'\chi_1^0$ (ATLAS [141])	255	100%	$m_{\tilde{t}_1} - m_{\chi_1^0} \sim m_b$

Table 5.2: Current mass bounds on the stop from the direct searches at the LHC. The 0ℓ, 1ℓ and 2ℓ mean the all-hadronic, semileptonic and dileptonic final states. All units are for GeV for mass.

5.3 Searches for third generation squarks in Bino LSP with Wino NLSP

In this section, we study the collider phenomenology of the light third generation squarks at the 14 TeV LHC. The key point in this work is to explore the mixed decay channels according to the mass hierarchies beyond the common assumption of 100% branching fraction of a given channel.

Including those channels listed in Table 5.1 and Table 5.2 with realistic branching fractions would help increase the overall sensitivity, but we did not repeat the analyses. We note that Ref. [169] also exploited mixed decays to search for stop. They introduced a new variable "topness" for the top-rich signal events to help efficiently reduce the top pair

backgrounds.

Given a different neutralino/chargino mass spectrum, many new decay channels for stop and sbottom appear, while the channels of $\tilde{t}_1 \to t\chi_1^0, b\chi_1^\pm$ and $\tilde{b}_1 \to b\chi_1^0$ cand be highly suppressed. This leads to the relaxation of current collider search limits based on those above mentioned channels. At the same time, those new channels provide new discovery opportunities. We do a complete collider analyses to demonstrate the new discovery potential for a few representative SUSY scenarios.

We study the detectability of the light stop/sbottom in Case IA with a mass hierarchy of $M_1 < M_2 < M_{3SQ} \ll |\mu|, M_{3SU}$, resulting in a mass spectrum including a mostly left-handed stop and a mostly left-handed sbottom, Wino-like NLSPs, and a Bino-like LSP. Other soft SUSY breaking parameters are decoupled to be 2 TeV, and $\tilde{A}_t$ is set to be large such that the SM-like Higgs is around 125 GeV. Note that even though $\tilde{A}_t$ is set to a large value, the large mass splitting between M_{3SQ} and M_{3SU} results in a mostly left-handed $\tilde{t}_1$ and mostly right-handed $\tilde{t}_2$. Therefore, the decay patterns of $\tilde{t}_1$ and $\tilde{b}_1$ follow those of the Case IA: purely left-handed stop/sbottom in the minimal mixing scenario. In our analyses, we consider the kinematic region of $m_{\tilde{t}_1} - m_{\chi_2^0} > m_t$ and $m_{\chi_2^0} - m_{\chi_1^0} > m_h$ such that $\tilde{t}_1 \to t\chi_2^0$ ($\tilde{b}_1 \to b\chi_2^0$) and $\chi_2^0 \to h\chi_1^0$ are kinematically open. The collider analyses of the current event topology can not be applied for the more compressed scenarios when either M_{3SQ} is close to M_2 or M_2 is close to M_1. The value of μ is chosen such that χ_2^0 dominantly decays to $h\chi_1^0$ for $\mu > 0$ and to $Z\chi_1^0$ for $\mu < 0$[1]. The decay channels and the corresponding decay branching fractions for $\tilde{b}_1$, $\tilde{t}_1$, as well as χ_2^0 and $\chi_1^\pm$ are listed in Table. 5.4. The conventional channels $\tilde{t}_1 \to t\chi_1^0$ and $\tilde{b}_1 \to b\chi_1^0$ are highly suppressed, having only about 2% branching fraction, which dramatically weakens the current experimental search limit. Instead, the decay channels of $\tilde{t}_1 \to t\chi_2^0$ ($\tilde{b}_1 \to b\chi_2^0$) and $\tilde{t}_1 \to b\chi_1^+$ ($\tilde{b}_1 \to t\chi_1^-$) are comparable and dominant instead. In particular, with one stop (sbottom) decaying to χ_2^0 and one stop (sbottom) decaying to $\chi_1^\pm$, $\tilde{t}_1\tilde{t}_1^*$ ($\tilde{b}_1\tilde{b}_1^*$) pair production leads to interesting final states of $bbWW + h/Z + \not{E}_T$. Note that unmixed decays of $\tilde{b}_1\tilde{b}_1^* \to bbhh + \not{E}_T$, $bbZZ + \not{E}_T$, $ttWW + \not{E}_T$ have been studied at the LHC [149–153], assuming 100% decay branching fractions. Given

[1]Note that $\chi_2^0 \to Z\chi_1^0$ is not always dominated for $\mu < 0$, as pointed out in Refs. [170, 171]. We have chosen the value of μ in the $\mu < 0$ case to guarantee the Z channel dominance.

	M_1	M_2	M_{3SQ}	A_t	μ	$\tan\beta$	$m_{\chi_1^0}$	$m_{\chi_2^0}$	$m_{\chi_1^\pm}$	$m_{\tilde{b}_1}$	$m_{\tilde{t}_1}$	m_h
BP1	150	300	650	2950	+2000	10	152	320	320	640	650	125
BP2	150	300	650	2950	−1300	10	150	320	320	640	630	125

Table 5.3: MSSM parameters and mass spectrum of SUSY particles for the two benchmark points. All masses are in units of GeV.

	Decay Channel	BR	Decay Channel	BR	Decay Channel	BR
BP1 ($\mu > 0$)	$\tilde{b}_1 \to b\chi_1^0$	2%	$\tilde{t}_1 \to t\chi_1^0$	2%	$\chi_2^0 \to h\chi_1^0$	97%
	$\tilde{b}_1 \to b\chi_2^0$	39%	$\tilde{t}_1 \to t\chi_2^0$	27%	$\chi_2^0 \to Z\chi_1^0$	3%
	$\tilde{b}_1 \to t\chi_1^-$	59%	$\tilde{t}_1 \to b\chi_1^\pm$	71%	$\chi_1^\pm \to W^\pm\chi_1^0$	100%
BP2 ($\mu < 0$)	$\tilde{b}_1 \to b\chi_1^0$	2%	$\tilde{t}_1 \to t\chi_1^0$	2%	$\chi_2^0 \to h\chi_1^0$	6%
	$\tilde{b}_1 \to b\chi_2^0$	39%	$\tilde{t}_1 \to t\chi_2^0$	27 %	$\chi_2^0 \to Z\chi_1^0$	94%
	$\tilde{b}_1 \to t\chi_1^-$	59%	$\tilde{t}_1 \to b\chi_1^\pm$	71%	$\chi_1^\pm \to W^\pm\chi_1^0$	100%

Table 5.4: Decay channels and the corresponding branching fractions of $\tilde{b}_1$, $\tilde{t}_1$, χ_2^0 and $\chi_1^\pm$ for the two benchmark points, which correspond to the cases of $\mu > 0$ and $\mu < 0$.

the more realistic branching fractions of about 40% (27%) for $\tilde{b}_1 \to b\chi_2^0$ ($\tilde{t}_1 \to t\chi_2^0$) and about 60% (71%) for $\tilde{b}_1 \to t\chi_1^-$ ($\tilde{t}_1 \to b\chi_1^+$), the collider limits for those channels will be relaxed. Including all the mixed and unmixed channels further increases the collider reach for the stop/sbottom.

The branching fraction for such decay is about 38% (48%) for stop (sbottom) in our benchmark points and varies between 25% and 50% for a stop (sbottom) mass larger than 500 GeV with $M_2 = M_1 + 150$ GeV. Since we choose the CP-odd Higgs mass m_A to be 2000 GeV, we are in the decoupling region of the Higgs sector with the light CP-even Higgs being SM-like. Given that we are in the Bino-LSP scenario with $M_2 = M_1 + 150$ GeV, additional possible decay modes of h into neutralino/charginos are either highly suppressed or kinematically forbidden. Therefore, the light CP-even Higgs is consistent with the observed signal of a 125 GeV SM-like Higgs boson. In our analyses, we have taken the branching fraction of $h \to b\bar{b}$ to be the SM value of 57.7%.

The two benchmark points listed in Table. 5.3 are only for illustration whenever instructive. In our following analyses, we perform a broad scan over the mass parameter space.

• M_{3SQ} from 400 to 1075 GeV with a step size of 25 GeV, corresponding to $m_{\tilde{b}_1}$ from about 350 GeV to about 1085 GeV and $m_{\tilde{t}_1}$ from about 367 GeV to about 1090 GeV.

• M_1 is scanned from 3 GeV to 700 GeV, in the step of 25 GeV.

• M_2 is fixed to be $M_2 = M_1 + 150$ GeV.

• We further require $m_{\tilde{t}_1} - m_{\chi_2^0} > m_t$ and $m_{\tilde{b}_1} > m_{\chi_1^\pm} + m_t$ such that $\tilde{t}_1 \to t\chi_2^0$ and $\tilde{b}_1 \to t\chi_1^\pm$ can be open.

Event samples are generated using Madgraph MG5_aMC_V2_2_1 [131], processed through Pythia 6.420 [132] for fragmentation and hadronization and then through Delphes-3.1.2 [134] with the Snowmass combined LHC No-Pile-up detector card [172] for detector simulation. Both the SM backgrounds and the stop pair production signals are normalized to theoretical cross sections, calculated including higher-order QCD corrections [119–121, 173–177]. For event generation, we have set m_t to be 173 GeV, and the Higgs mass m_h to be 125 GeV. The renormalization scale and factorization scale are taken to be $\sqrt{M^2 + p_T^2}$ for a single heavy particle. For pair production of heavy particles, the geometric mean of $\sqrt{M^2 + p_T^2}$ for each particle is used.

5.3.1 The Case of $\mu > 0$: final states with a Higgs

In the case of $\mu > 0$, the leading signal under consideration for the pair production of sbottom (stop), with $\tilde{b}_1 \to b\chi_2^0 \to bh\chi_1^0$ ($\tilde{t}_1 \to t\chi_2^0 \to th\chi_1^0 \to bW^+h\chi_1^0$) and $\tilde{b}_1^* \to t\chi_1^- \to bW^+\, W^-\chi_1^0$ ($\tilde{t}_1^* \to b\chi_1^+ \to bW^+\chi_1^0$), is

$$\tilde{b}_1\tilde{b}_1^* \to bb\; WW\; h\; \not{E}_T \to \ell\; bbbb\; jj\not{E}_T$$

$$\tilde{t}_1\tilde{t}_1^* \to bb\; WW\; h\; \not{E}_T \to \ell\; bbbb\; jj\not{E}_T$$

The signal contains four b-jets, two light flavor jets, one isolated lepton (e or μ), and large missing energy. The dominant backgrounds will be from $t\bar{t}$+jets and $t\bar{t}b\bar{b}$ with large cross sections and similar final states. While $t\bar{t}h$ is an irreducible background, the production cross section is relatively small. Other SM backgrounds include $t\bar{t}W$, $t\bar{t}Z$ and $b\bar{b}WW$, with typically smaller cross sections.

We apply the following basic event selection cuts:

- Events are required to have at least four isolated jets[2] with

$$p_T^{j1,j2,j3} > 40 \text{ GeV}, \; p_T^{j4} > 25 \text{ GeV}, \; |\eta^j| < 2.5. \tag{5.6}$$

  All isolated jets satisfying $p_T^j > 25$ GeV, $|\eta^j| < 2.5$ are counted in N_j.

- Among the jets, at least two are b-tagged jets. The b-tagging efficiency depends on the p_T and η of the jets, which is 0 for $p_T < 15$ GeV or $|\eta| > 2.5$, about 70% for $|\eta^j| < 1.2$ and about 60% for $1.2 < |\eta^j| < 2.5$ with $p_T^j \gtrsim 200$ GeV. The mistag rate depends on the quark species, as well as p_T and η of the jets. It is about 15% for c-quark and a constant 2% for light jets.

- One isolated lepton[3] (e or μ) is required to have

$$p_T^\ell > 20 \text{ GeV with } |\eta^\ell| < 2.5. \tag{5.7}$$

Beside these basic cuts, we further optimize the cuts and divide the events into signal regions on the following variables:

- Missing energy $\not{E}_T$, which is the magnitude of the the missing transverse momentum, to be above 100, 120, 140, 160 180, and 200 GeV.

- H_T, the scalar sum of the jet transverse momentum of all surviving isolated jets: $H_T = \sum_{\text{jets}} |p_T^j|$, to be above 400, 450, 500, 550, 600 GeV.

- M_T, the transverse mass, defined as the invariant mass of the lepton and missing energy:

$$M_T(\mathbf{p}_T^\ell, \mathbf{p}_T^{\text{miss}}) = \sqrt{2p_T^\ell p_T^{\text{miss}}(1 - \cos\phi_{\ell,\not{E}_T})}, \tag{5.8}$$

  to be above 100, 120, 140, 160, 180, 200 GeV.

- N_j, the multiplicity of all surviving isolated jets, being at least 4, 5 and 6.

[2] The anti-k_t jet algorithm is used in the reconstruction of jets, with the jet radius being 0.5. For isolated jets, we require any jet within $\Delta R = 0.2$ of a lepton be discarded. An event is discarded if the distance between $\not{E}_T$ and all jets, $\Delta\Phi(\not{E}_T, j)$, is less than 0.8.

[3] For an isolated lepton, we require $\Delta R(\ell, j) > 0.4$.

- N_b, the multiplicity of tagged b-jets, being at least 2, 3 and 4.

The normalized distributions of $\not{E}_T$ and H_T are shown in Fig. 5.3. As expected, the signal process has larger $\not{E}_T$ from the missing neutralino-LSP than the background processes, which is typically bounded by $m_W/2$ due to the primary contribution $W \to \ell\nu$. Given the relatively large stop/sbottom mass, the signal process typically has larger H_T than the SM backgrounds as well.

In Table. 5.5, we list the cumulative cut efficiencies after different levels of cuts, as well as cross sections before and after cuts for both the sbottom and stop signals as well as the SM backgrounds for the benchmark point listed in Table 5.3 for $\mu > 0$. The cross section for each process is normalized to their theoretical values including NLO QCD corrections [178–184]. The background processes are significantly suppressed after strong $\not{E}_T$, H_T, M_T cuts. The leading background left is $t\bar{t}$, followed by $t\bar{t}b\bar{b}$. We scan over the combinations of the signal regions, to select the optimal combination which gives the best significance for each mass grid point, including 10% systematic uncertainty. At $\sqrt{s} = 14$ TeV with 300 fb^{-1} integrated luminosity, the significance could reach about 17σ (14σ) for $\tilde{b}_1$ ($\tilde{t}_1$) of about 640 GeV.

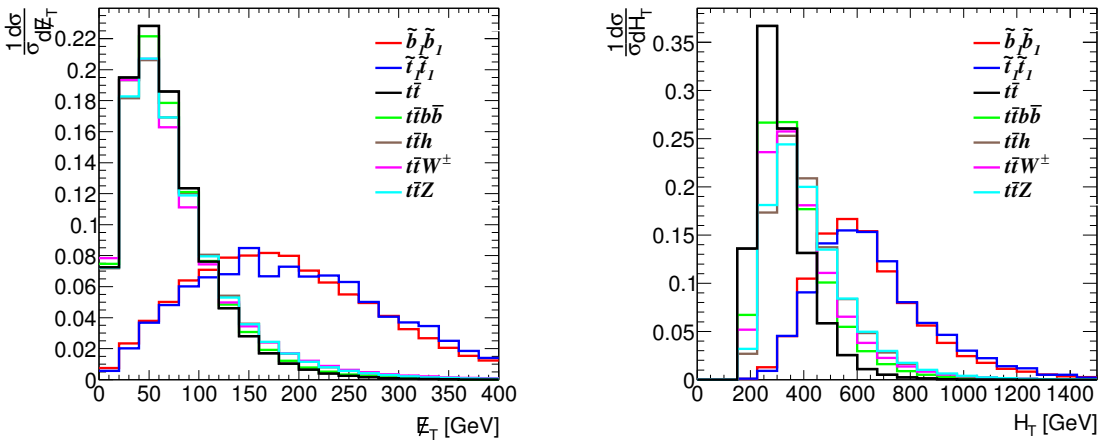

Figure 5.3: Normalized distributions of $\not{E}_T$ (left panel) and H_T (right panel) for the signal $\tilde{b}_1\tilde{b}_1^*$ (red curves), $\tilde{t}_1\tilde{t}_1^*$ (blue curves) $\to bbWWh\,\not{E}_T \to \ell\ bbbb\ jj\ \not{E}_T$ after basic cuts with $m_{\tilde{b}_1} = 637$ GeV, $m_{\tilde{t}_1} = 646$ GeV, as well as SM backgrounds at the 14 TeV LHC.

Signal significance contours are shown in Fig. 5.4 with the 5σ discovery reach (black

Process	σ (fb)	Basic cuts	$\not{E}_T >$ 200 GeV	$H_T >$ 500 GeV	$M_T >$ 160 GeV	$N_j \geq$ 5	$N_b \geq$ 2	σ (fb) after cuts
$\tilde{b}_1\tilde{b}_1$	13	39%	17%	14%	5.8%	4.3%	2.7%	3.4×10^{-1}
$\tilde{t}_1\tilde{t}_1$	10	39%	18%	16%	5.9%	4.4%	2.9%	2.9×10^{-1}
$t\bar{t}$	260,000	14%	0.24%	7.4×10^{-4}	1.7×10^{-6}	9.3×10^{-7}	2.4×10^{-7}	6.3×10^{-2}
$t\bar{t}bb$	2,300	24%	0.6%	0.3%	3.5×10^{-5}	2.3×10^{-5}	1.2×10^{-5}	2.8×10^{-2}
$t\bar{t}h$	100	31%	1.2%	0.8%	5.8×10^{-5}	3.4×10^{-5}	1.9×10^{-5}	2.0×10^{-3}
$t\bar{t}Z$	230	30%	1.2%	0.8%	6.6×10^{-5}	3.9×10^{-5}	9.8×10^{-6}	2.2×10^{-3}
$t\bar{t}W^{\pm}$	224	25%	1.2%	0.7%	4.8×10^{-5}	2.3×10^{-5}	6.3×10^{-6}	1.4×10^{-3}
		$\sqrt{s} = 14$ TeV $\int L\,dt = 300$ fb^{-1} $\frac{S}{\sqrt{B+(10\%B)^2}} = 17$ (14) for $\tilde{b}_1$ ($\tilde{t}_1$)						

Table 5.5: Cut efficiencies and cross sections before and after cuts for the signal $\tilde{b}_1\tilde{b}_1^*, \tilde{t}_1\tilde{t}_1^* \to bbWWh\not{E}_T \to \ell\, bbbb\, jj\, \not{E}_T$ for BP1 listed in Table 5.3 for $\mu > 0$, as well as SM backgrounds at the 14 TeV LHC. The significance is obtained for $\int Ldt = 300$ fb^{-1} with 10% systematic error combining both sbottom and stop signals.

curve) and 95% C.L. exclusion limit (red curve) for 14 TeV LHC with 300 fb^{-1} integrated luminosity. Fig. 5.4 (a) shows the $m_{\tilde{b}_1} - m_{\chi_1^0}$ plane and Fig. 5.4 (b) shows the $m_{\tilde{t}_1} - m_{\chi_1^0}$ plane. We find that 5σ discovery can reach approximately 750 GeV for $\tilde{b}_1$ ($\tilde{t}_1$) when χ_1^0 is almost massless and reach about 920 GeV (900 GeV) when χ_1^0 is roughly 200 GeV to 300 GeV. The 95% C.L. exclusion reach is about 100 GeV better.

Since the (mostly left-handed) sbottom and stop have the same undistinguishable final states with their masses controlled by the same parameter M_{3SQ}, we present the combined reach of stop and sbottom in Fig. 5.4 (c) in $M_{3SQ} - m_{\chi_1^0}$ plane[4]. The 5σ discovery reach in M_{3SQ} increases to 820 GeV for a massless LSP and 1080 GeV for $m_{\chi_1^0} \sim 300$ GeV. The masses up to 980 GeV can be excluded for a massless LSP, and the masses up to 1180 GeV can be excluded for $m_{\chi_1^0} \sim 300$ GeV at 95% C.L.

We would like to reiterate that the mixing in sbottom and stop sectors governs the mass spectrum of the sbottom and stop. Small mixing in the sbottom sector is always a good approximation given the small bottom Yukawa coupling, while the mixing in the stop sector may be large enough to suppress the mass of the lighter stop further. In our cases (including the $\mu < 0$ case discussed below), the right-handed stop is assumed to be

[4]The mass difference between the stop and sbottom does not affect the combination of the stop and sbottom signals, since the same cuts are used for both the stop and sbottom events.

very heavy (decoupled to be 2 TeV), which will result in a smaller mixing for a large range of $A_t \in [-4000, 4000]$ GeV. Furthermore, even if a large mixing in the stop sector gives a much lighter stop compared with the sbottom, this would potentially lead to a better signal in the stop sector. The combination of the stop and sbottom signals, however, does not depend on the mass difference between the stop and sbottom. In the parameter space that we are considering with a relatively small stop and sbottom mass difference, both channels contribute significantly to the combined reach. In cases when the mass difference between the stop and sbottom is large, only one channel will contribute dominantly to the combined significance.

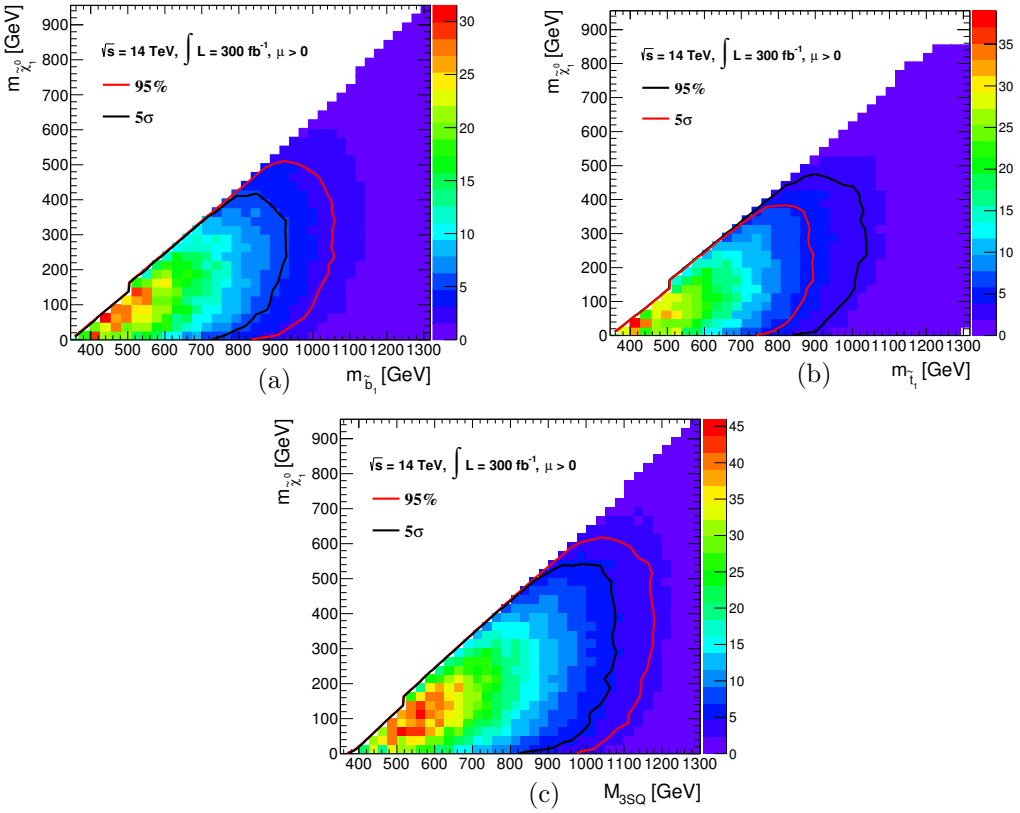

Figure 5.4: Signal significance contours for $\tilde{b}_1\tilde{b}^*, \tilde{t}_1\tilde{t}_1^* \to bbWWh \not{E}_T \to \ell\ bbbb\ jj\ \not{E}_T$ final states for 14 TeV LHC with $\int L\, dt = 300$ fb^{-1} luminosity. The 5σ discovery reach (black curves) and 95% C.L exclusion limit (red curves) for the sbottom only are shown in the (a) $m_{\tilde{b}_1} - m_{\chi_1^0}$ plane, (b) $m_{\tilde{t}_1} - m_{\chi_1^0}$ plane and in the (c) $M_{3SQ} - m_{\chi_1^0}$ plane for the combined reach for sbottom and stop.

5.3.2 The Case of $\mu < 0$: final states with a Z-boson

For the case of $\mu < 0$, the dominant decay channel of χ_2^0 is $\chi_2^0 \to Z\chi_1^0$ instead [122]. The leading signal under consideration for the pair production of sbottom and stop with $\tilde{b}_1 \to b\chi_2^0 \to bZ\chi_1^0$, $\tilde{b}_1^* \to t\chi_1^- \to bW^+\ W^-\chi_1^0$ and $\tilde{t}_1 \to t\chi_2^0 \to bW^+Z\chi_1^0$, $\tilde{t}_1^* \to b\chi_1^- \to bW^-\chi_1^0$, is then

$$\tilde{b}_1\tilde{b}_1^* \to bb\ WW\ Z\ \not{E}_T \to \ell^+\ell^-\ bb\ jjjj\ \not{E}_T$$

$$\tilde{t}_1\tilde{t}_1^* \to bb\ WW\ Z\ \not{E}_T \to \ell^+\ell^-\ bb\ jjjj\ \not{E}_T$$

The signal contains two b-jets, four light flavor jets, two same flavor but opposite sign leptons, and large missing energy. The two leptons are used to reconstruct the Z boson, which will significantly reduce the SM backgrounds. The dominant background is $t\bar{t}$ plus one or two additional QCD jets.

We impose the basic event selection cuts as the previous case. We again optimize the cuts and divide the events into signal regions:

- $\not{E}_T$ to be above 100, 120, 140, 160 180, and 200 GeV.
- H_T to be above 400, 450, 500, 550, 600 GeV.
- M_{T2}, the lepton-bashed transverse mass [185–187]:

$$M_{T2}(\mathbf{p}_T^{\ell_1}, \mathbf{p}_T^{\ell_2}, \mathbf{p}_T^{\rm miss}) = \min_{\mathbf{p}_{T,1}^{\rm miss}+\mathbf{p}_{T,2}^{\rm miss}=\mathbf{p}_T^{\rm miss}} \{\max\{M_T(\mathbf{p}_T^{\ell_1}, \mathbf{p}_{T,1}^{\rm miss}), M_T(\mathbf{p}_T^{\ell_2}, \mathbf{p}_{T,2}^{\rm miss})\}\} \quad (5.9)$$

  to be above 75, 80, 85, 90 GeV.

- $\Delta M_{\ell\ell} = |M_{\ell\ell} - m_Z|$, being less than 10 GeV.
- N_j being at least 4, 5 and 6.
- N_b being at least 1 to suppress the enormous QCD backgrounds with light flavor jets.

The normalized distributions of $\not{E}_T$ and M_{T2} for both the sbottom and stop signal, as well as the SM backgrounds are presented in Fig. 5.5. The $\not{E}_T$ distributions for the signal typically extends to larger values. The $M_{T2}(\mathbf{p}_T^{\ell_1}, \mathbf{p}_T^{\ell_2}, \mathbf{p}_T^{\rm miss})$ distributions for SM

backgrounds with the lepton pair coming from leptonic W decay are cut off at m_W, while the signal as well as the $bbZZ$ background have much flatter M_{T2} distributions. Note that while the distribution of the $bbZZ$ background is similar to that of the signal, the overall cross section for $bbZZ$ is negligibly small.

Another interesting variable for the sbottom case is $M_{\ell\ell b}$, which is related to $m_{\tilde{b}_1}$ if the b jet and the lepton pair from the same sbottom cascade decay chain $\tilde{b}_1 \to b\chi_2^0 \to bZ\chi_1^0$ can be identified. While we will not use it for event selection in our analyses, $M_{\ell\ell b}$ distribution could provide information on $m_{\tilde{b}_1}$ as well as $m_{\chi_2^0}$ if a sbottom signal is discovered.

The advanced cuts and the corresponding cumulative cut efficiencies as well as the cross sections for sbottom and stop signal for BP2 with $\mu < 0$ and SM backgrounds before and after cuts are given in Table 5.6. The dominant SM background is $t\bar{t}$ plus jets. A significance of about 12σ (8.7σ) can be reached for $\tilde{b}_1$ ($\tilde{t}_1$) for the benchmark point at the 14 TeV LHC with 300 fb^{-1} luminosity, including 10% systematic error.

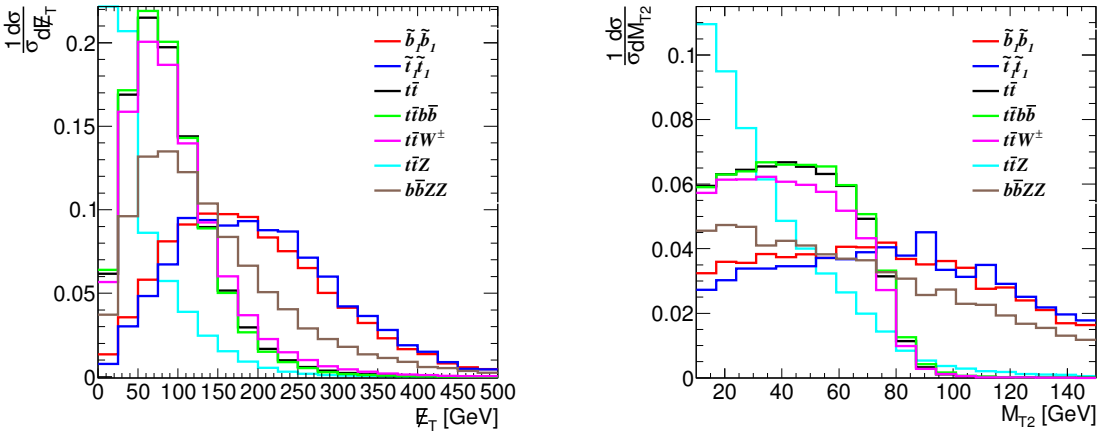

Figure 5.5: Normalized distributions $\not{E}_T$ (left panel) and M_{T2} (right panel) for the signal $\tilde{b}_1\tilde{b}^*$ (red curve), $\tilde{t}_1\tilde{t}_1^*$ (blue curves) $\to bbWWZ\not{E}_T \to \ell^+\ell^-$ bb $jjjj$ $\not{E}_T$ after basic cuts with $m_{\tilde{b}_1} = 637$ GeV, $m_{\tilde{t}_1} = 634$ GeV, as well as SM backgrounds at the 14 TeV LHC.

Signal significance contours are shown in Fig. 5.6 with the 5σ discovery reach (black curve) and 95% C.L. exclusion limit (red curve) for 14 TeV LHC with 300 fb^{-1} integrated luminosity, in the (a) $m_{\tilde{b}_1} - m_{\chi_1^0}$ plane, (b) $m_{\tilde{t}_1} - m_{\chi_1^0}$ plane, and (c) $M_{3SQ} - m_{\chi_1^0}$ plane. For massless χ_1^0, sbottom (stop) masses up to 650 (680) GeV can be discovered and 720 (760)

Process	σ (fb)	Basic cuts	$\not{E}_T >$ 175 GeV	$H_T >$ 400 GeV	$M_{T2} >$ 90 GeV	$\Delta M_{ll} <$ 10 GeV	$N_j \geq$ 4	$N_b \geq$ 1	σ (fb) after cuts
$\tilde{b}_1\tilde{b}_1$	2.1	32%	17%	16%	5.8%	5.3%	5.3%	4.2%	8.8×10^{-2}
$\tilde{t}_1\tilde{t}_1$	1.8	27%	16%	11.2%	4.9%	4.4%	4.4%	3.6%	6.5×10^{-2}
$t\bar{t}$	33,000	1.3%	0.09%	0.06%	5.0×10^{-6}	4.9×10^{-7}	4.9×10^{-7}	3.7×10^{-7}	1.2×10^{-2}
$t\bar{t}Z$	71	11%	0.25%	0.16%	5.8×10^{-5}	4.2×10^{-5}	4.2×10^{-5}	2.7×10^{-5}	1.9×10^{-3}
$t\bar{t}b\bar{b}$	400	3.2%	0.20%	0.12%	1.4×10^{-5}	2.0×10^{-6}	2.0×10^{-6}	1.8×10^{-6}	6.9×10^{-4}
$t\bar{t}ZZ$	0.16	16%	0.86%	0.64%	0.31%	0.27%	0.27%	0.18%	3.0×10^{-4}
$b\bar{b}ZZ$	2.3	0.39%	0.11%	0.06%	2.9×10^{-4}	2.6×10^{-4}	2.6×10^{-4}	2.1×10^{-4}	4.8×10^{-4}
		$\sqrt{s} = 14$ TeV $\int L\,dt = 300$ fb^{-1} $\frac{S}{\sqrt{B+(10\%B)^2}} = 12$ (8.7) for $\tilde{b}_1$ ($\tilde{t}_1$)							

Table 5.6: Cut efficiencies and cross sections before and after cuts for the signal $\tilde{b}_1\tilde{b}_1^*, \tilde{t}_1\tilde{t}_1^* \to bbWWZ\not{E}_T \to \ell^+\ell^-\ bb\ jjjj\ \not{E}_T$, for BP2 in Table 5.3 for $\mu < 0$, as well as dominant SM backgrounds at the 14 TeV LHC. The significance is obtained for $\int L\,dt = 300$ fb^{-1} with 10% systematic error combining both sbottom and stop signals.

will be excluded at 95% C.L. if there is found over SM backgrounds. For moderate mass of χ_1^0 around 200 $\sim$ 300 GeV, the 5σ discovery can reach up to 820 (840) GeV, and the 95% exclusion limit can go up to 890 (900) GeV for sbottom (stop). The combined reach of the stop and sbottom is shown in Fig. 5.6 (c) in the M_{3SQ} versus $m_{\chi_1^0}$ plane. About 980 GeV can be achieved in M_{3SQ} for the 5σ discovery reach and about 1025 GeV for the 95% C.L. exclusion. The experimental reach for the case of $\mu < 0$ is lower than that for the case of $\mu > 0$.

5.3.3 Signature of $\tilde{b}_1 \sim \tilde{b}_R$

To complete our exploration for the sbottom signal, we consider another scenario with the low energy mass spectrum containing a light mostly right-handed sbottom, a Bino-like LSP and Higgsino-like NLSPs. Here, the sign of μ does not affect the decay modes of sbottom and neutralinos. The typical benchmark point is listed in Table 5.7, and the corresponding branching fractions are listed in Table 5.8. Other soft SUSY breaking parameters are decoupled by setting them to be 2 TeV. In this scenario, the right-handed sbottom couples to the Bino and Higgsino through the $\mathrm{U}(1)_Y$ or the bottom Yukawa couplings, which results in the sbottom dominantly decaying to $b\chi_1^0$ due to the large phase space, followed by the channel $t\chi_1^\pm$ when it is kinematically open. We will focus on the signal reach of the sbottom

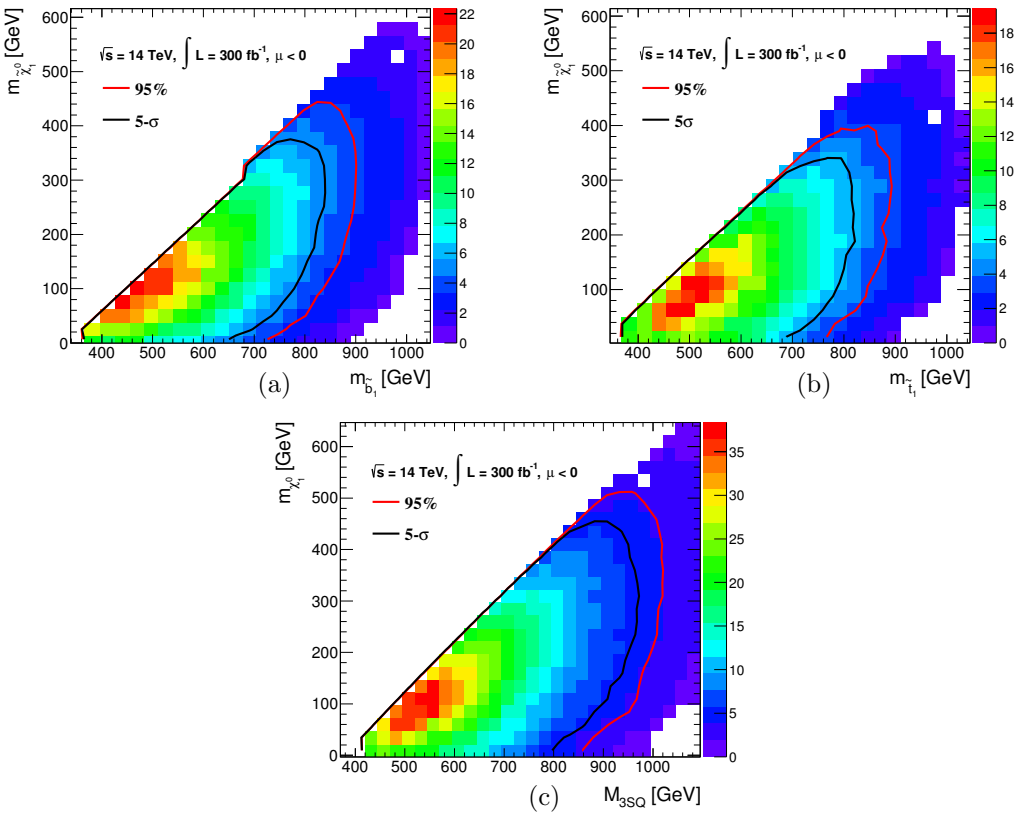

Figure 5.6: Signal significance contours for $\tilde{b}_1\tilde{b}^*, \tilde{t}_1\tilde{t}_1^* \to bbWWZ\not{E}_T \to \ell^+\ell^- bbjjjj\not{E}_T$ final states for 14 TeV LHC with $\int L\, dt = 300$ fb^{-1} luminosity. The 5σ discovery reach (black curves) and 95% C.L. exclusion limit (red curves) are show in the (a) $m_{\tilde{b}_1} - m_{\chi_1^0}$ plane, in the (b) $m_{\tilde{t}_1} - m_{\chi_1^0}$ plane, and the combined reach in the (c) $M_{3SQ} - m_{\chi_1^0}$ plane.

	M_1	M_2	M_{3SD}	A_t	μ	$\tan\beta$	$m_{\chi_1^0}$	$m_{\chi_1^\pm}$	$m_{\tilde{b}_1}$	m_h
BP3	150	2000	650	2895	300	10	145	307	635	125

Table 5.7: MSSM parameters and mass spectrum of SUSY particles for the the benchmark point in the case of Right-handed sbottom. All masses are in units of GeV.

	Decay Channel	BR	Decay Channel	BR
BP3	$\tilde{b}_1 \to b\chi_1^0$	58%	$\chi_1^\pm \to \chi_1^0 W^\pm$	100%
	$\tilde{b}_1 \to t\chi_1^-$	18%		

Table 5.8: Decay channels and the corresponding branching fractions of $\tilde{b}_1$ and $\chi_1^\pm$ for the benchmark point, which corresponds to the case of Right-handed sbottom.

pair production

$$\tilde{b}_1\tilde{b}_1^* \to b\chi_1^0\ t\chi_1^\pm \to b\chi_1^0\ tW^\pm\chi_1^0 \to \ell\ bb\ jj\ \not{E}_T.$$

The SM backgrounds are somewhat similar to that of the $\mu > 0$ case of left-handed sbottom with fewer jets. We also include vector bosons plus additional jets as another background [188].

We scan over a broad mass parameter space: M_1 from 3 GeV to 800 GeV in steps of 30 GeV, M_{3SD} from 400 GeV to 1180 GeV in step of 30 GeV, μ is fixed to be $\mu = M_1 + 150$ GeV. We further require that $m_{\tilde{b}_1} > m_{\chi_1^\pm} + m_t$ so that the decay channel $\tilde{b}_1 \to t\chi_1^\pm$ is kinematically accessible. Since the final state particles are stiffer than the previous cases with cascade decays, we apply stronger basic cuts than before. The basic event selection cuts are

- Jet:
$$|\eta_j| < 2.5, \quad p_T^j > 40 \text{ GeV}, \quad \Delta\phi_{j\not{E}_T} > 0.8. \tag{5.10}$$
- Lepton:
$$|\eta_\ell| < 2.5, \quad p_T^\ell > 30 \text{ GeV}, \quad \Delta R_{\ell j} > 0.4. \tag{5.11}$$
- at least three jets satisfying the requirement of Eq. (5.10), within which at least one b-tagged, and exactly one lepton satisfying requirement Eq. (5.11).

Process	σ (fb)	Basic Cuts	$\not{E}_T >$ 200 GeV	$H_T >$ 500 GeV	$M_T >$ 160 GeV	$N_j \geq$ 4	$N_b \geq$ 1	σ (fb) after Cuts
$\tilde{b}_1\tilde{b}_1$	9.7	30%	20%	14%	8.1%	5.6%	5.6%	5.4×10^{-1}
$t\bar{t}$	260,000	5.3%	0.14%	4.7×10^{-4}	1.6×10^{-6}	8.1×10^{-7}	8.1×10^{-7}	2.1×10^{-1}
$t\bar{t}b\bar{b}$	2,300	13%	0.4%	0.2%	3.7×10^{-5}	2.6×10^{-5}	2.6×10^{-5}	6.1×10^{-2}
$t\bar{t}h$	100	20%	1%	0.7%	7.8×10^{-5}	5.2×10^{-5}	5.2×10^{-5}	5.3×10^{-3}
$t\bar{t}Z$	230	14%	0.7%	0.5%	8.1×10^{-5}	4.5×10^{-5}	4.5×10^{-5}	1×10^{-2}
$t\bar{t}W^{\pm}$	224	11%	0.7%	0.5%	6.6×10^{-5}	3.4×10^{-5}	3.4×10^{-5}	7.6×10^{-3}
Vjj	3.7×10^7	4.8×10^{-5}	2.9×10^{-6}	1.8×10^{-6}	2.9×10^{-9}	1×10^{-9}	1×10^{-9}	3.8×10^{-2}
		$\sqrt{s} = 14$ TeV		$L = 300\text{fb}^{-1}$		$S/\sqrt{B + (10\%B)^2}$		11.4

Table 5.9: Cut efficiencies and cross sections before and after cuts for the signal $\tilde{b}_1\tilde{b}_1^* \to bbWW\not{E}_T \to \ell\, bb\, jj\, \not{E}_T$, for BP3 in Table 5.7, as well as SM backgrounds at the 14 TeV LHC. The significance is obtained for $\int Ldt = 300$ fb^{-1} with 10% systematic error.

- the leading b-jet p_T is required to be larger than 100 GeV since one b-jet originates directly from a heavy sbottom decay.

Besides the basic event selection cuts, we apply the same advanced event selection cuts in the signal regions (H_T, $\not{E}_T$, M_T, N_j and N_b) as in Sec. 5.3.1, and optimize them for different mass parameters. In Table 5.9, we list the cross section before and after the above cuts and also the resultant efficiency after every cut for the benchmark point listed in Table 5.7.

Signal significance contours are shown in Fig. 5.7 with the 5σ discovery reach (black curve) and 95% C.L. exclusion limit (red curve) for 14 TeV LHC with 300 fb^{-1} integrated luminosity, in the $m_{\tilde{b}_1} - m_{\chi_1^0}$ plane. For a large range of mass of χ_1^0 (from massless to about 300 GeV), sbottom masses up to approximately 880 GeV can be discovered or 1050 GeV will be excluded at 95% C.L. if there is no SUSY signal found over SM backgrounds. The reach at the lower mass of χ_1^0 is better than that of the left-handed case, since lowering the mass of χ_1^0 will increase the p_T of the b-jet produced together with χ_1^0. This effect is suppressed in the left-handed case where the leading b-jets are produced together with χ_2^0 or $\chi_1^{\pm}$ which are always heavier than χ_1^0.

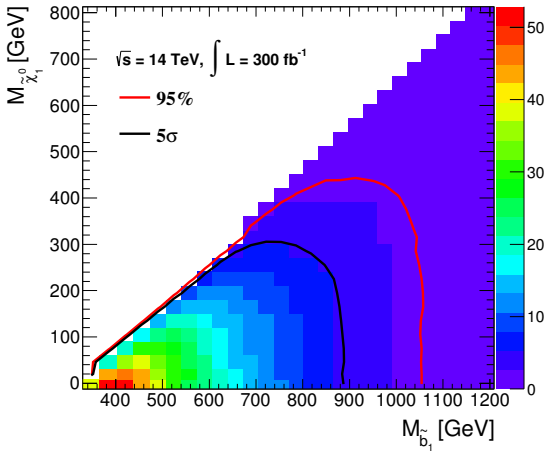

Figure 5.7: Signal significance contours for $\tilde{b}_1\tilde{b}_1^* \to bbWW\not{E}_T \to \ell^{\pm}\, bb\, jj\, \not{E}_T$ final state for the right-handed sbottom in the $m_{\tilde{b}_1} - m_{\chi_1^0}$ plane for 14 TeV LHC with $\int L\, dt = 300$ fb^{-1} luminosity. The 5σ discovery reach (black curves) and 95% C.L. exclusion limit (red curves) are shown.

5.4 Third generation squarks search in Bino LSP with Higgsino NLSP

In the scenario of a Higgiso-like NLSP and a Bino-like LSP, in addition to the third generation squark sector, the relevant SUSY parameters are the Bino LSP with mass parameter M_1 and the Higgsino NLSP with mass parameter μ. After mass diagonalization, the SUSY particles in the model are the lighter stop ($\tilde{t}_1$), the neutralinos (χ_1^0, χ_2^0 and χ_3^0) and charginos ($\chi_1^{\pm}$). Other SUSY particles, the wino, gluino, sleptons, and the first and second generation squarks, are decoupled to be 2 TeV. We also decouple the non-SM Higgs particles by setting M_A to be 2 TeV.

The two neutralinos χ_2^0, χ_3^0 and chargino $\chi_1^{\pm}$ are almost degenerate, leading to undistinguished collider signals due to the resolution of the detector, so we will not distinguish the intermediate states χ_2^0 and χ_3^0 hereafter. The light stop dominantly decays to $t\chi_2^0/\chi_3^0$ over $t\chi_1^0$ and $b\chi_1^{\pm}$ given the large SU(2)$_L$ and the top Yukawa coupling. The neutralinos χ_2^0/χ_3^0 further decay to either a Z boson or a Higgs boson, which is discussed in detail in Ref.[122], leading to $t\bar{t}hh\,\not{E}_T$, $t\bar{t}hZ\,\not{E}_T$ and $t\bar{t}ZZ\,\not{E}_T$ final states. Figure 5.8 shows the

branching fractions of the three channels $t\bar{t}hh\not{E}_T$, $t\bar{t}hZ\not{E}_T$ and $t\bar{t}ZZ\not{E}_T$ for three different M_1 values, with $\mu = 150$ GeV + M_1. When M_1 is small, the phase space of Higgs channel is suppressed compared to the Z boson channel, resulting in a small branching fraction of the channel $\chi_2^0/\chi_3^0 \to h\chi_1^0$, which leads to a suppressed channel $t\bar{t}hh\not{E}_T$ of approximately 4%. As the M_1 increases, the phase space has little impact on the decay branching fraction, then $\mathscr{B}(\chi_2^0/\chi_3^0 \to h\chi_1^0) \approx \mathscr{B}(\chi_2^0/\chi_3^0 \to Z\chi_1^0) \approx 50\%$, making the branching fraction of $\tilde{t}_1 \to t\chi_2^0/\chi_3^0 \to th\chi_1^0$ and $\tilde{t}_1 \to t\chi_2^0/\chi_3^0 \to tZ\chi_1^0$ almost equal, about 45% each.

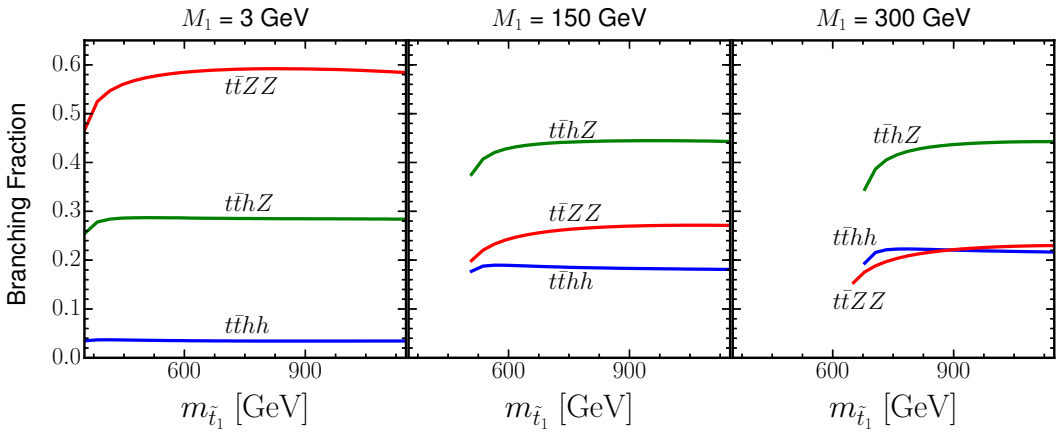

Figure 5.8: Branching fractions of three different channels $t\bar{t}hh\not{E}_T$, $t\bar{t}hZ\not{E}_T$ and $t\bar{t}ZZ\not{E}_T$ as a function of light stop mass for the stop pair production. From left to right, three different cases $M_1 = 3$, 150, 300 GeV are considered, with μ fixed to be M_1 + 150 GeV.

5.4.1 Recasting the CMS search results

The CMS group performed a search for the heavier stop ($\tilde{t}_2$) [144] utilizing the same searching final states. The channels for their search were: $\tilde{t}_2 \to \tilde{t}_1 h$ and $\tilde{t}_2 \to \tilde{t}_1 Z$ with $\tilde{t}_1$ further decaying via $\tilde{t}_1 \to t\chi_1^0$ assuming the mass relation $m_{\tilde{t}_1} - m_{\chi_1^0} = m_t$. This leads to the finals states of $tthh\not{E}_T$, $tthZ\not{E}_T$ and $ttZZ\not{E}_T$ for the pair production of $\tilde{t}_2$ at the $\sqrt{s} = 8$ TeV LHC. The analysis by the CMS group is based on the multiplicities of the leptons, multiplicities of jets, multiplicities of b-jets, missing energy $\not{E}_T$, transverse mass m_T and H_T, as demonstrated in Table I in Ref. [144]. We recast the experimental results

of the CMS group using exactly the same event selections to obtain our own simulated signal event yields as well as background predictions and observed data yields. Because the reach of the two same-sign (SS) signal region is very low, we neglect it in this analysis.

The background predictions and observed data yields for the various signal regions are listed in Tables II, III and IV in Ref. [144]. The root package TLimit [189] is used to calculate the 95% confidence level upper limits. Figure 5.9 shows the comparison of the contour plots of the CMS work [144] and our recast for 95% C.L. upper limits in the plane of the $m_{\tilde{t}_2}$ vs $m_{\tilde{t}_1}$ for $\tilde{t}_2 \to \tilde{t}_1 h$ (left) and $\tilde{t}_2 \to \tilde{t}_1 Z$ (right) decay channel assuming a 100% branching fraction, in which the NLO + NLL cross section [120] of the signal process at $\sqrt{s} = 8$ TeV is taken to calculate the signal yields. As can be seen from the figure, our recast results match the CMS results quite well except for the edge region, validating the procedures which were used to recast the results to the plane $m_{\tilde{t}_1}$ vs $m_{\chi_1^0}$. The discrepancy between the CMS results and our simulations are due to the different detector simulations of the signal process and the different methods used to calculate the 95% C.L. upper limits. The 95% upper limits in the plane of $m_{\tilde{t}_2}$ vs $m_{\tilde{t}_1}$ for the three choices of the branching fraction $\mathscr{B}(\tilde{t}_2 \to \tilde{t}_1 Z)$ is shown in left panel of Figure 5.10.

We also translated the CMS heavier stop $\tilde{t}_2$ search exclusion limits at $\sqrt{s} = 8$ TeV to that of the lighter stop $m_{\tilde{t}_1}$ vs $m_{\chi_1^0}$ in the scenario of Higgsino NLSP and Bino LSP, since those two processes lead to the same final states (pp $\to \tilde{t}_1\tilde{t}_1 \to tt\chi_2^0/\chi_3^0 \to tth/Z\ h/Z$). We use exactly the same event selections to obtain our own simulated signal event yields as well as the background predictions and observed data yields to get the lighter stop search reach. As can be seen in Figure 5.8, the $t\bar{t}hh\not{E}_T$ channel is highly suppressed in the low χ_1^0 mass region, leading to no reach in the current situation; there is a suppression of about 1/3 for the branching fractions of the channels $t\bar{t}hZ$ and $t\bar{t}ZZ$, leading to lower exclusion limits (less than 500 GeV) as shown in right panel of Figure 5.10.

5.4.2 Collider analysis at $\sqrt{s} = 14$ TeV

In the large parameter regions of the MSSM with light neutralinos and charginos, many new decay channels of stop will open and even dominate in certain scenarios. Thus the current searching channels of $\tilde{t}_1 \to t\chi_1^0/b\chi_1^+$ will be highly suppressed, leading to large

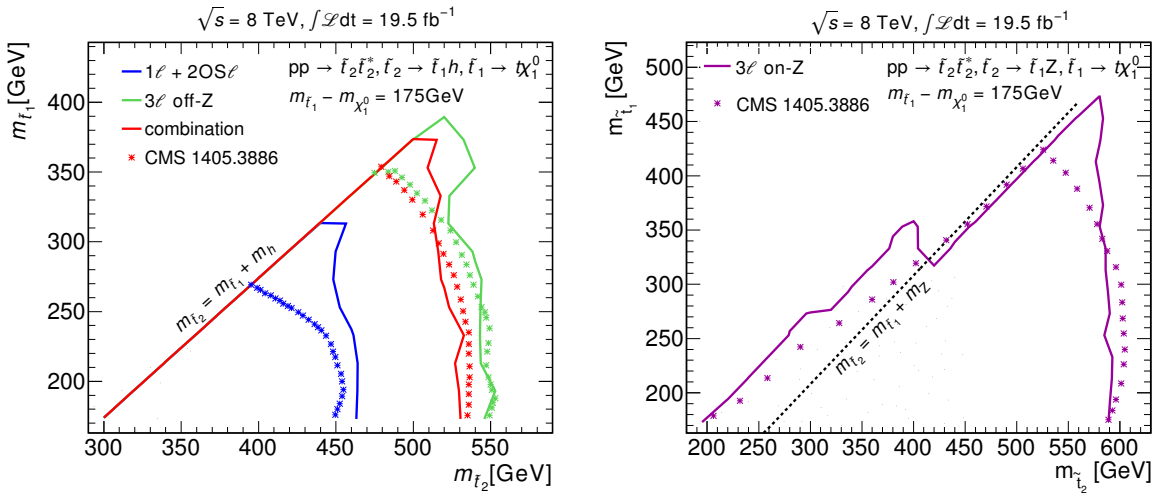

Figure 5.9: The comparison of 95% C.L. upper limits between CMS results and our simulations are shown in the plane of MSSM parameter space $m_{\tilde{t}_2}$ vs $m_{\tilde{t}_1}$, with the LSP mass fixed to be $m_{\tilde{t}_1} - m_{\chi_1^0} = 175$ GeV. The left panel is the 95% C.L. upper limit for the process $\tilde{t}_2 \to \tilde{t}_1 h$ assuming 100% branching fraction for 1ℓ signal region plus 2 OS ℓ signal region, at least 3 ℓ signal region, and the combination of those two signal regions. The right panel is the 95% C.L. upper limit for the process $\tilde{t}_2 \to \tilde{t}_1 Z$ assuming 100% branching ratio for the "on-Z" signal region. The CMS results are digitized and shown in asterisk. Our results match with the CMS results quite well except the region near the edge.

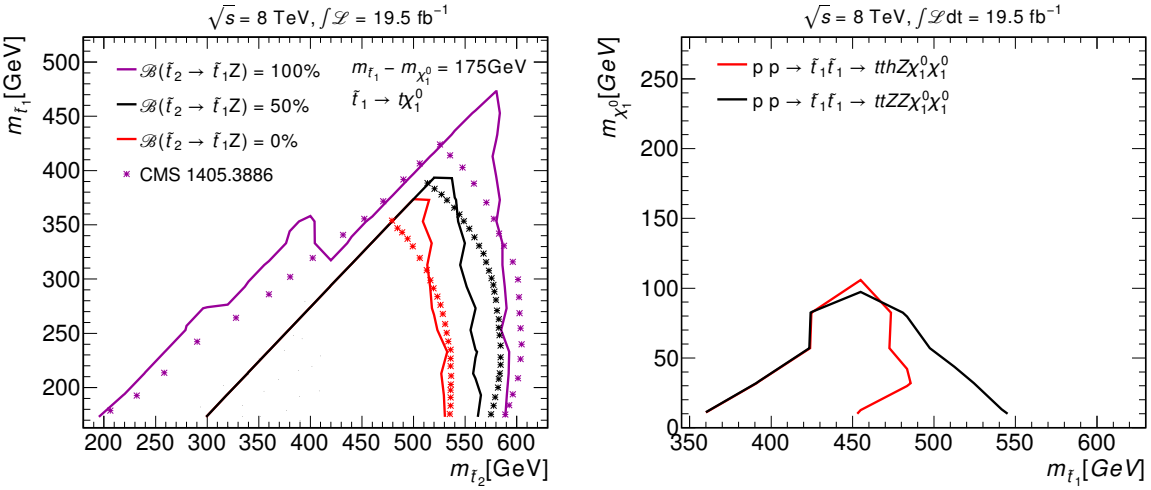

Figure 5.10: The left panel shows comparison of 95% C.L. upper limits between CMS results and our simulations in the plane of MSSM parameter space $m_{\tilde{t}_2}$ vs $m_{\tilde{t}_1}$ for the three typical choices of $\mathscr{B}(\tilde{t}_2 \to \tilde{t}_1 Z)$ (assuming $\mathscr{B}(\tilde{t}_2 \to \tilde{t}_1 Z) + \mathscr{B}(\tilde{t}_2 \to \tilde{t}_1 h) = 100\%$). The decay channel of $\tilde{t}_2 \to \tilde{t}_1 h$ is only consider when the Higgs boson production is kinematically open. The signal regions of 1ℓ, 2 OS ℓ and 3ℓ "off-Z" are combined for the $\mathscr{B}(\tilde{t}_2 \to \tilde{t}_1 Z) = 0\%$ case. For the mixed decay mode, both "off-Z" and "on-Z" signal regions are used to set the 95% upper limit. Only "on-Z" signal regions are considered for the $\mathscr{B}(\tilde{t}_2 \to \tilde{t}_1 Z) = 100\%$ case. The right panel shows the reach contour plot for the recast light stop case in the plane $m_{\tilde{t}_1}$ vs $m_{\chi_1^0}$ for the decay pp $\to \tilde{t}_1\tilde{t}_1 \to tt\chi_2^0/\chi_3^0 \to tthZ, ttZZ$. The light stop mass up to 550 GeV are excluded at 95% C.L. upper limits.

relaxation of the current searching limits using the above channels. In this analysis, we consider the scenario with a Bino LSP and a Higgsino NLSP assuming the mass hierarchy of $M_1 < \mu < M_{3SQ} \ll M_2$, which is studied phenomenologically in detail in Ref. [124]. The mass spectrum of the benchmark point is shown in Table 5.10. It consists of a mostly left-handed stop and mostly left-handed sbottom, almost degenerate Higgsino-like NLSPs (χ_2^0, χ_3^0 and $\chi_1^\pm$), and a Bino-like LSP (χ_1^0). The off diagonal term $\tilde{A}_t$ in the stop mass matrix plays an important role in the mass of the SM-like Higgs, accordingly the value of $\tilde{A}_t$ is chosen such that the SM-like Higgs mass is around $125 \sim 126$ GeV. Even though the $\tilde{A}_t$ term is large, the mixing between $\tilde{t}_L$ and $\tilde{t}_R$ is small because of the large mass difference between those two components, leading to a most left-handed stop. The branching fraction of sbottom decay modes $\tilde{b}_1 \to b\chi_2^0/\chi_3^0$ is highly suppressed due to the small bottom Yukawa couplings, while $\tilde{b}_1 \to t\chi_1^\pm$ is the dominant channel with a branching fraction as high as 98%. Therefore the sbottom signals will not contaminate the stop signals.

M_1	μ	M_2	$\tilde{A}_t$	M_{3SQ}	M_{3SU}	χ_1^0	χ_2^0	χ_3^0	χ_1^+	$\tilde{t}_1$	h
150	300	2000	2890	650	2000	145	308	311	305	620	125

Table 5.10: Mass parameters and mass spectrum of SUSY particles and the SM-like Higgs for the benchmark point. There are two almost degenerate neutral NLSPs and one charged NLSP. All masses are in units of GeV.

The existence of two degenerate neutralinos introduces complexity into the stop decay which is shown in Table 5.11. The decay channels of $\tilde{t}_1 \to t\chi_2^0$ and $\tilde{t}_1 \to t\chi_3^0$ are dominant with a branching fraction of about 50% each, with subsequent decay of neutralinos χ_2^0/χ_3^0 to either a Higgs boson or a Z boson, while the decay channels of $\tilde{t}_1 \to t\chi_1^0/b\chi_1^+$ are highly suppressed, about only $3 \sim 4\%$, leading to large relaxation of the current search limits. In the case of positive μ, the χ_2^0 (χ_3^0) dominantly decays to $Z\chi_1^0$ ($h\chi_1^0$), while the negative μ leads to the opposite case, so changing the sign of μ has a negligible impact on the collider analysis. Given the degeneracy of χ_2^0 and χ_3^0, the stop dominantly decays to $th\chi_1^0$ and $tZ\chi_1^0$, respectively, with a branching fraction of about 45%. In LHC, the $\tilde{t}_1\tilde{t}_1^*$ pair production leads to interesting final states of $bbWWhh\not{E}_T$, $bbWWhZ\not{E}_T$ and $bbWWZZ\not{E}_T$.

The benchmark points listed in Table 5.10 and 5.11 are only for illustration whenever instructive. In the following analysis, we perform a broad scan over the mass parameter

Decay channel	Branching ratio	Decay channel	Branching ratio
$\tilde{t}_1 \to t\chi_1^0$	3%	$\chi_2^0 \to Z\chi_1^0$	96%
$\tilde{t}_1 \to t\chi_2^0$	44%	$\chi_2^0 \to h\chi_1^0$	4%
$\tilde{t}_1 \to t\chi_3^0$	49%	$\chi_3^0 \to Z\chi_1^0$	16%
$\tilde{t}_1 \to b\chi_1^+$	4%	$\chi_3^0 \to h\chi_1^0$	84%

Table 5.11: The decay branching fractions of $\tilde{t}_1$, χ_2^0 and χ_3^0 for the benchmark point listed in Table5.10, and χ_1^+ is 100% decaying to $W^+\chi_1^0$.

space.

- M_{3SQ} from 400 to 1250 GeV with a step of 25 GeV, corresponding to $m_{\tilde{t}_1}$ from about 352 GeV to about 1256 GeV.
- M_1 is scanned from 3 GeV to 750 GeV, in the step of 25 GeV.
- μ is fixed to be $\mu = M_1 + 150$ GeV.
- We further require $m_{\tilde{t}_1} > m_{\chi_2^0}/m_{\chi_3^0} + m_t$ such that $\tilde{t}_1 \to t\chi_2^0/\chi_3^0$ is kinematically open.

Event samples, including all SM backgrounds and signals, are generated using Madgraph 5 [131], processed through Pythia 6 [132] for fragmentation and hadronization and then through Delphes 3 [134] with the Snowmass combined LHC No-Pile-up detector card [172] for the detector simulation. Both the SM backgrounds and the stop pair production signal are normalized to theoretical cross sections, calculated including higher-order QCD corrections [119–121, 173–177]. For the event generation, the top quark mass m_t is set to be 175 GeV and the Higgs mass m_h to be 125 GeV.

Events Selection

In the phenomenological studies, we divide the signal regions into three primary categories: 1) the one lepton signal region (1ℓ), 2) the two opposite-sign leptons signal region (2OS ℓ), 3) and the at-least-three leptons signal region ($\geq 3\ell$) for the three dominant channels $t\bar{t}hh\ \not{E}_T$, $t\bar{t}hZ\ \not{E}_T$ and $t\bar{t}ZZ\ \not{E}_T$. The signal region of the two same-sign leptons is not considered in this analysis since the reach of this signal region is small.

The jets are reconstructed using the anti-k_t algorithm with a cone radius of 0.5. All jets

	1ℓ	2OS ℓ	$\geq 3\ell$
Basic cuts	Leading three jets $p_T > 40$ $N_j \geq 4$, $N_b \geq 2$ Exact one lepton with $p_T > 25$ $\Delta R(j,l) > 0.4$ $\Delta\Phi(j, \mathbf{p}_T^{miss}) > 0.8$ -	Leading two jets $p_T > 40$ $N_j \geq 4$, $N_b \geq 2$ Exact two leptons with $p_T > 25$ $\Delta R(j,l) > 0.4$, $\Delta R(l,l) > 0.4$ same -	- $N_j \geq 2$, $N_b \geq 1$ ≥ 3 leptons with $p_T > 10$ same same "off-Z", "on-Z"
Advanced cuts	$\not{E}_T > 100$, 125, 150, 175, 200 $H_T > 400$, 450, 500, 550, 600 $m_T > 100$, 125, 150, 175, 200 - $N_j \geq 4$, 5, 6, 7 $N_b \geq 2$, 3, 4, 5	$\not{E}_T > ...$, 225, 250 same $M_{T2} > 60$, 70, 80, 90 $\lvert m_{\ell\ell} - m_Z \rvert < 5$, 10, 15 $N_j \geq 4$, 5, 6 $N_b \geq 2$, 3, 4	same same - same $N_j \geq 2$, 3, 4, 5 $N_b \geq 1$, 2, 3

Table 5.12: All units are in GeV. The basic cuts and the finer signal regions on the variables for the three primary signal regions 1ℓ, 2 OS ℓ and $\geq 3\ell$. All combinations of the advanced cuts are examined, the specific one that gives the best significance will be used.

are required to meet $p_T > 30$ GeV and $\eta < 2.5$, all leptons (e or μ) are required to meet $\eta < 2.5$. For the at-least-three leptons signal region, the events are divided into two categories: the "on-Z" region, if there are pairs such that the invariant mass of two opposite sign same flavor leptons is within 15 GeV of a Z boson mass, and the "off-Z" region, if there is no such pair or the invariant mass is outside the mass window of the Z boson mass. All the cuts are summarized in Table 5.12, and the cut variables are defined below:

- $\not{E}_T$, defined as the magnitude of the missing transpose momentum $\mathbf{p}_T^{miss}$.
- H_T, defined as the scalar sum of the p_T of all the jets which meet the basic selection cuts: $H_T = \sum_{jet} p_T^{jet}$.
- m_T, defined as the invariant mass of the lepton and the missing transpose momentum:

$$m_T = \sqrt{2 p_T^{\ell} \not{E}_T (1 - \cos\phi(\mathbf{p}_T^{\ell}, \mathbf{p}_T^{miss}))}, \tag{5.12}$$

- M_{T2} [185–187], defined as the lower bound on the transverse mass resulting from the two missing energies.

$$M_{T2}(\mathbf{p}_T^{\ell_1}, \mathbf{p}_T^{\ell_2}, \mathbf{p}_T^{\text{miss}}) = \min_{\mathbf{p}_{T,1}^{\text{miss}} + \mathbf{p}_{T,2}^{\text{miss}} = \mathbf{p}_T^{\text{miss}}} \{\max\{m_T(\mathbf{p}_T^{\ell_1}, \mathbf{p}_{T,1}^{\text{miss}}), m_T(\mathbf{p}_T^{\ell_2}, \mathbf{p}_{T,2}^{\text{miss}})\}\} \tag{5.13}$$

Process	σ (fb)	Basic cuts	$\not{E}_T >$ 175 GeV	$H_T >$ 500 GeV	$m_T >$ 150 GeV	$N_j \geq$ 7	$N_b \geq$ 2	σ (fb) after cuts
$\tilde{t}_1\tilde{t}_1(t\bar{t}hh)$	35	11.0%	4.6%	3.6%	1.6%	0.5%	0.5%	0.175
$\tilde{t}_1\tilde{t}_1(t\bar{t}hZ)$	80	8.7%	4.3%	3.4%	1.6%	0.45%	0.45%	0.36
$\tilde{t}_1\tilde{t}_1(t\bar{t}ZZ)$	46	5.7%	3.1%	2.3%	1.3%	0.31%	0.31%	0.14
$t\bar{t}$	261230	1.9%	5.2×10^{-4}	1.6×10^{-4}	8.4×10^{-7}	5×10^{-8}	5×10^{-8}	0.013
$t\bar{t}b\bar{b}$	8305	3.2%	0.17%	9.3×10^{-4}	7.4×10^{-5}	6.6×10^{-6}	6.6×10^{-6}	0.055
$t\bar{t}Z$	1095	2.3%	0.23%	0.12%	2.7×10^{-4}	2.2×10^{-5}	2.2×10^{-5}	0.024
$t\bar{t}W^{\pm}$	747	1.8%	0.18%	0.11%	9.7×10^{-5}	4.8×10^{-6}	4.8×10^{-6}	3.6×10^{-3}
$t\bar{t}h$	572	4.6%	0.34%	0.22%	1.6×10^{-4}	1.4×10^{-5}	1.4×10^{-5}	8.1×10^{-3}
$t\bar{t}hh$	0.83	10.8%	1.1%	0.87%	0.012%	1.7×10^{-4}	1.7×10^{-4}	1.5×10^{-4}
$t\bar{t}hZ$	1.41	7.4%	1.2%	0.85%	0.022%	3.3×10^{-4}	3.3×10^{-4}	4.6×10^{-4}
$t\bar{t}ZZ$	1.73	4.1%	0.74%	0.51%	0.016%	2.0×10^{-4}	2.0×10^{-4}	3.5×10^{-4}

Table 5.13: Cut efficiencies and cross sections before and after advanced selection cuts for the signal $\tilde{t}_1\tilde{t}_1^* \to bbWWhh\ \not{E}_T$, $bbWWhZ\ \not{E}_T$ and $bbWWZZ\ \not{E}_T$ with one lepton in the final states as well as SM backgrounds at the 14 TeV LHC. Here the cross section of $t\bar{t}$ is that of semileptonic decay, the cross sections of other backgrounds are the production cross sections at $\sqrt{s} = 14$ TeV LHC.

- $m_{\ell\ell}$, the invariant mass of two OS leptons which survive from the basic selection cuts.
- N_j, the number of all the jets which meet the basic selection cuts.
- N_b, the number of all the b jets which meet the basic selection cuts.

Results of the one lepton signal region

In this section and the following, we focus on the discovery/exclusion reach of the light stop at the 14 TeV LHC with an integrated luminosity of 300 fb^{-1}. In the one lepton signal region, the advanced selection cuts H_T, $\not{E}_T$, m_T, N_j and N_{bj} are used to cut down the huge SM backgrounds. Table 5.13 shows the cut efficiencies and cross sections before and after one set of advanced cuts for the signals as well as the SM backgrounds. As expected, the signal process has larger m_T as well as extra $\not{E}_T$ contributions from the missing LSP than the background processes, which is typically bounded at m_W because of the primary process $W \to \ell\nu$. $t\bar{t}$, $t\bar{t}b\bar{b}$ and $t\bar{t}Z$ are the dominant backgrounds after strong m_T, H_T and $\not{E}_T$ cuts. While the irreducible SM backgrounds $t\bar{t}hh$, $t\bar{t}hZ$ and $t\bar{t}ZZ$ are almost negligible due to the very low cross sections.

In Figure 5.11, the 95% C.L. upper limits (black curve) and 5σ discovery (red curve) reach are shown in the plane of the MSSM parameter space $m_{\tilde{t}_1}$ vs $m_{\chi_1^0}$ for the stop pair production pp $\rightarrow \tilde{t}_1\tilde{t}_1 \rightarrow t\bar{t}\chi_2^0/\chi_3^0 \rightarrow t\bar{t}hh\not{E}_T$ (top left), $t\bar{t}hZ\not{E}_T$ (top right) and $t\bar{t}ZZ\not{E}_T$ (bottom) at 14 TeV LHC with 300 fb^{-1} integrated luminosity. μ is fixed to be M_1 + 150 GeV and 10% (20%) systematic uncertainties are assumed for solid (dotted) curves. For each mass point of $(m_{\tilde{t}_1}, m_{\chi_1^0})$, given the mass dependence of the production cross section and decay branching fractions shown in Figure 5.8, the signal $\sigma \times$ BR for each individual point has been used. All combinations of the advanced selection cuts, $\not{E}_T$, H_T, m_T, N_j and N_{bj} are examined. The optimized combination that gives the best significance is used for that particular mass point. The channel $t\bar{t}hh\not{E}_T$ has no sensitivity in the low χ_1^0 mass region because of the very low branching fraction of the $t\bar{t}hh\not{E}_T$ channel in the low χ_1^0 mass region, on the contrary, the channel $t\bar{t}ZZ\not{E}_T$ has the largest reach in the low χ_1^0 mass region, due to the large branching fraction in the low χ_1^0 mass region. The $t\bar{t}hZ\not{E}_T$ has the best reach in the whole mass parameter region because of the comparably large branching fraction. For the channel $t\bar{t}hh\not{E}_T$, stop masses up to 750 GeV can be discovered at the 5 σ significance level for $m_{\chi_1^0}$ = 220 GeV, and the 95% C.L. exclusion limits are about 950 GeV for $m_{\chi_1^0}$ = 250 GeV, assuming 10% systematic uncertainties. The 5 σ discovery reach can go up to 920 GeV (840 GeV), or the stop masses up to 1050 GeV (1000 GeV) can be excluded at the 95% C.L for the channel $t\bar{t}hZ\not{E}_T$ ($t\bar{t}ZZ\not{E}_T$). Limits with 20% systematic uncertainties are about 100 GeV worse.

Results of the two OS leptons signal region

In the two OS leptons signal region, advanced selection cuts including H_T, $\not{E}_T$, M_{T2}, N_j and N_{bj} are used for the channel $t\bar{t}hh\not{E}_T$; one more cut besides the above mentioned cuts, $m_{\ell\ell}$, is used for the channels $t\bar{t}hZ\not{E}_T$ and $t\bar{t}ZZ\not{E}_T$. The normalized distributions of M_{T2} and $m_{\ell\ell}$ for the signal processes and SM backgrounds are shown in Figure 5.12. The M_{T2} distribution for the signal extends to larger values, while the M_{T2} distributions for the SM backgrounds are cut off at m_W mass given that the two leptons of the SM backgrounds come from leptonic W Decay. The $m_{\ell\ell}$ distributions for the signal and $t\bar{t}Z$ has a sharp peak at about the Z boson mass, contrarily, the $m_{\ell\ell}$ distributions for the other SM backgrounds

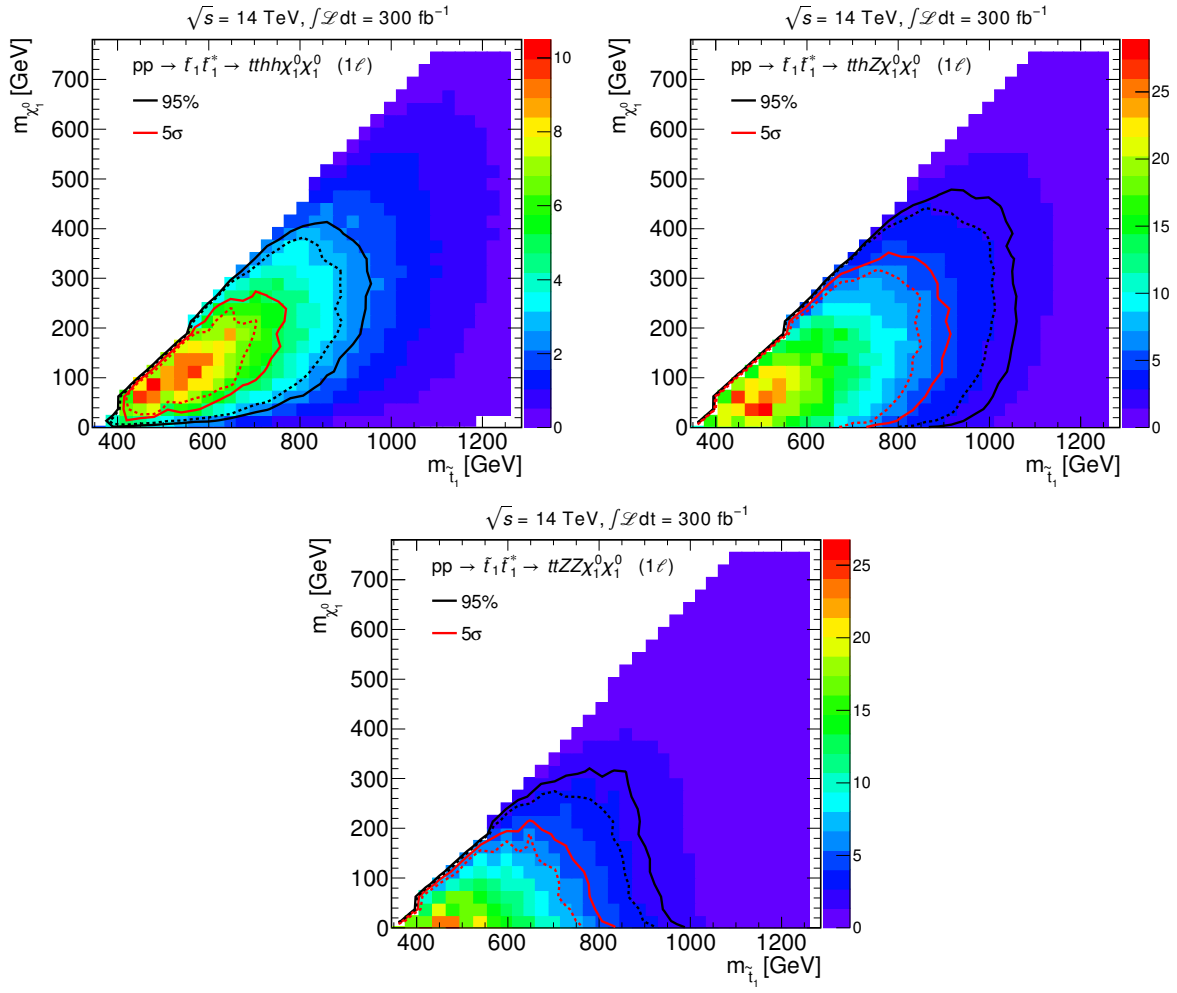

Figure 5.11: The 95% C.L. upper limits (black) and 5σ discovery reach (red) are shown in the plane of MSSM parameter space $m_{\tilde{t}_1}$ vs $m_{\chi_1^0}$ for the stop pair production pp $\to \tilde{t}_1\tilde{t}_1 \to t\bar{t}\chi_2^0/\chi_3^0 \to t\bar{t}hh\,\not{E}_T$ (top left), $t\bar{t}hZ\,\not{E}_T$ (top right) and $t\bar{t}ZZ\,\not{E}_T$ (bottom) with exact one lepton in the final states at 14 TeV LHC with 300 fb^{-1} integrated luminosity. μ is fixed to be M_1 + 150 GeV and 10% (20%) systematic uncertainties are assumed for solid (dotted) curves. The color coding on the right indicates the signal significance defined simply as $S/\sqrt{B}$ to guide the eye.

are flat because the two leptons are not from the Z boson decay.

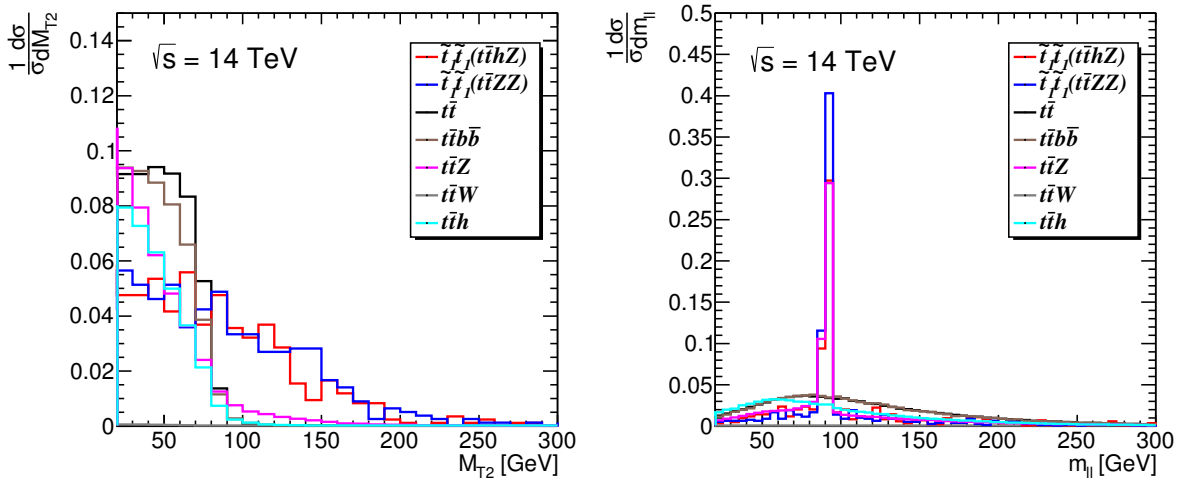

Figure 5.12: Normalized distributions of M_{T2} (left) and $m_{\ell\ell}$ (right) for the signal channel $t\bar{t}hZ$ and $t\bar{t}ZZ$ at the benchmark point with $m_{\tilde{t}_1} = 625$ GeV and the SM backgrounds after basic selection cuts.

Table 5.14 illustrates the cumulative cut efficiencies and cross sections before and after one set of advanced selection cuts for the signals and SM backgrounds. The dominant background for the two OS leptons signal region is $t\bar{t}Z$, given its relatively large cross section and similar final states to the signal process. $t\bar{t}$ is the second dominant background due to its large cross section. A significance of about 12σ (7.7σ) can be reached for signal channel $t\bar{t}hZ\ \not{E}_T$ ($t\bar{t}ZZ\ \not{E}_T$) for the benchmark point at the 14 TeV LHC with 300 fb^{-1} integrated luminosity, including 10% systematic error.

Signal significance contours are shown in Figure 5.13 with 5σ discovery reach (red curve) and 95% C.L. exclusion limit (black curve) in the plane of $m_{\tilde{t}_1}$ versus $m_{\chi_1^0}$ for the 14 TeV LHC with 300 fb^{-1} integrated luminosity, including 10% (solid curve) and 20% (dashed curve) systematic uncertainties, for the stop pair production pp $\rightarrow \tilde{t}_1\tilde{t}_1 \rightarrow t\bar{t}\chi_2^0/\chi_3^0 \rightarrow t\bar{t}hZ\,\not{E}_T$ (left) and $t\bar{t}ZZ\,\not{E}_T$ (right). μ is fixed to be $M_1 + 150$ GeV. The same procedure to pick the exact combination of cuts, $\not{E}_T$, H_T, M_{T2}, $m_{\ell\ell}$, N_j and N_{bj} is applied here as the previous section. The channel $t\bar{t}hh\,\not{E}_T$ has no reach sensitivity, in that the branching fraction of the dilepton channel is very low and its final states are similar to the large SM

Process	σ (fb)	Basic cuts	$\not{E}_T >$ 100 GeV	$H_T >$ 400 GeV	$M_{T2} >$ 80 GeV	$\lvert m_{\ell\ell} - m_Z \rvert <$ 5 GeV	$N_j \geq$ 6	$N_b \geq$ 2	σ (fb) after cuts
$\tilde{t}_1\tilde{t}_1(t\bar{t}hZ)$	80	1.7%	1.3%	1.1%	0.34%	0.2%	0.1%	0.1	0.08
$\tilde{t}_1\tilde{t}_1(t\bar{t}ZZ)$	46	1.6%	1.2%	1.1%	0.35%	0.24%	0.11%	0.11%	0.051
$t\bar{t}$	33330	0.4%	0.14	5×10^{-4}	2×10^{-5}	1×10^{-6}	9×10^{-8}	9×10^{-8}	0.003
$t\bar{t}b\bar{b}$	8305	0.18%	6×10^{-4}	3×10^{-4}	1×10^{-5}	4×10^{-7}	1.2×10^{-7}	1.2×10^{-7}	0.001
$t\bar{t}Z$	1095	0.4%	9×10^{-4}	5.3×10^{-4}	5×10^{-5}	2.7×10^{-5}	5.4×10^{-6}	5.4×10^{-6}	0.0056
$t\bar{t}W^{\pm}$	747	0.2%	9.3×10^{-4}	5.1×10^{-4}	1.1×10^{-5}	3.2×10^{-7}	1.2×10^{-7}	1.2×10^{-7}	-
$t\bar{t}h$	572	0.6%	0.2%	0.1%	2.9×10^{-5}	1.2×10^{-6}	3.5×10^{-7}	3.5×10^{-7}	-
$t\bar{t}hh$	0.83	3.1%	1.2%	1.0%	3.5×10^{-4}	1.9×10^{-5}	4.8×10^{-6}	2.5×10^{-6}	-
$t\bar{t}hZ$	1.41	2.2%	0.8%	0.7%	6×10^{-4}	2.4×10^{-4}	5.9×10^{-5}	5.9×10^{-5}	-
$t\bar{t}ZZ$	1.73	1.2%	0.4%	0.3%	6×10^{-4}	3×10^{-4}	9×10^{-5}	9×10^{-5}	-

Table 5.14: Cut efficiencies and cross sections before and after advanced selection cuts for the signal $\tilde{t}_1\tilde{t}_1^* \to bbWWhZ\not{E}_T$ and $bbWWZZ\not{E}_T$ with two OS leptons in the final states as well as SM backgrounds at the 14 TeV LHC. We do not list the information for the channel $bbWWhh\not{E}_T$ in that there is no reach for this channel. Here the cross section of $t\bar{t}$ is that of dileptonic decay, the cross sections of other backgrounds are the production cross section at $\sqrt{s} = 14$ TeV LHC.

backgrounds. Stop masses up to 800 GeV (920 GeV) can be discovered at 5σ significance, or stop masses up to 900 GeV (1000 GeV) can be excluded at 95% C.L. for the channels $t\bar{t}hZ\not{E}_T$ ($t\bar{t}ZZ\not{E}_T$) if there is no SUSY signal found over SM backgrounds. Limits with 20% systematic uncertainties are very close to that of 10% case.

Results of the at-least-three leptons signal region

The at-least-three leptons signal region is further divided into two signal regions: the "off-Z" and "on-Z" signal region as defined in Section 5.4.2. The "off-Z" signal region is applied to the $t\bar{t}hh\not{E}_T$ channel, the "on-Z" signal region is applied to the $t\bar{t}hZ\not{E}_T$ and $t\bar{t}ZZ\not{E}_T$ channels. The cut efficiencies and cross sections before and after one set of advanced selection cuts for the "on-Z" signal region are shown in Table 5.15. We do not list the tables of cut efficiencies and cross sections for the "off-Z" signal region because the reach is very small for all the three channels. As can be seen from Table 5.15, the $t\bar{t}Z$ is the dominant background, followed by the $t\bar{t}h$ process. The at least three leptons channel are highly suppressed for the $t\bar{t}$ and $t\bar{t}b\bar{b}$ processes such that they are always cut to be 0.

In Figure 5.14, the 95% C.L. upper limits (black curve) and 5σ discovery reach (red

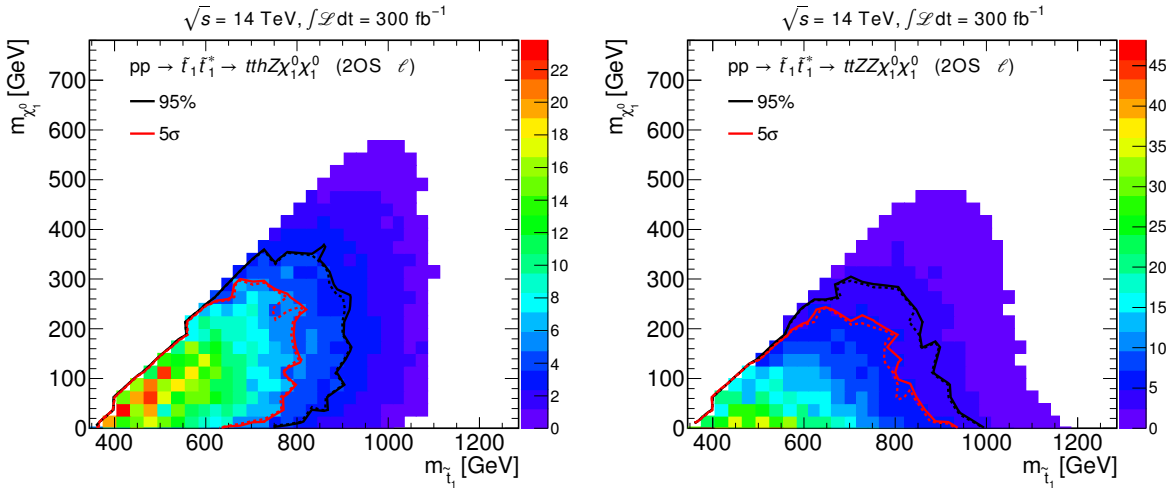

Figure 5.13: The 95% C.L. upper limits (black) and 5σ discovery reach (red) are shown in the plane of MSSM parameter space $m_{\tilde{t}_1}$ vs $m_{\chi_1^0}$ for the stop pair production pp $\to \tilde{t}_1\tilde{t}_1 \to t\bar{t}\chi_2^0/\chi_3^0 \to t\bar{t}hZ\,\not{E}_T$ (left) and $t\bar{t}ZZ\,\not{E}_T$ (right) with two OS leptons in the final states at 14 TeV LHC with 300 fb^{-1} integrated luminosity. The channel $t\bar{t}hh\,\not{E}_T$ has no reach due to the very low branching fraction and large SM backgrounds. μ is fixed to be $M_1 + 150$ GeV and 10% (20%) systematic uncertainties are assumed for solid (dotted) curves. The color coding on the right indicates the signal significance defined simply as $S/\sqrt{B}$ to guide the eye.

on-Z

Process	σ (fb)	Basic cuts	$\not{E}_T >$ 175 GeV	$H_T >$ 400 GeV	$\lvert m_{\ell\ell} - m_Z \rvert <$ 5	$N_j \geq$ 4	$N_b \geq$ 1	σ (fb) after cuts
$\tilde{t}_1\tilde{t}_1(t\bar{t}hZ)$	80	1%	0.4%	0.3%	0.27%	0.23%	0.23%	0.19
$\tilde{t}_1\tilde{t}_1(t\bar{t}ZZ)$	46	1.5%	0.7%	0.5%	0.46%	0.35%	0.35%	0.16
$t\bar{t}Z$	1095	0.8%	5×10^{-4}	2×10^{-4}	1.7×10^{-4}	8.1×10^{-5}	8.1×10^{-5}	0.09
$t\bar{t}W^{\pm}$	747	7×10^{-4}	6.6×10^{-5}	1.8×10^{-5}	6.4×10^{-6}	2.4×10^{-6}	2.4×10^{-6}	0.002
$t\bar{t}h$	572	0.1%	1.1×10^{-4}	4.4×10^{-5}	1.6×10^{-5}	9.4×10^{-6}	9.4×10^{-6}	0.005
$t\bar{t}hh$	0.83	0.7%	9×10^{-4}	5×10^{-4}	2×10^{-4}	1.4×10^{-4}	1.4×10^{-4}	-
$t\bar{t}hZ$	1.41	1.8%	0.21%	0.1%	9×10^{-4}	5.7×10^{-4}	5.7×10^{-4}	-
$t\bar{t}ZZ$	1.73	2.2%	0.32%	0.17%	0.14%	8.3×10^{-4}	8.3×10^{-4}	-

Table 5.15: Cut efficiencies and cross sections before and after cuts for the signal $\tilde{t}_1\tilde{t}_1^* \to bbWWhZ\not{E}_T$ and $bbWWZZ\not{E}_T$ with at least three leptons in the final states as well as SM backgrounds for the "on-Z" signal region at the 14 TeV LHC. The $bbWWhh$ has no reach, so we will not consider it here. The $t\bar{t}$ and $t\bar{t}b\bar{b}$ can only have dileptonic decay channel, so the at least three leptons channel are extremely suppressed such that they can be ignored.

curve) are shown in the plane of MSSM parameter space $m_{\tilde{t}_1}$ vs $m_{\chi_1^0}$ for the stop pair production pp $\to \tilde{t}_1\tilde{t}_1 \to t\bar{t}\chi_2^0/\chi_3^0 \to t\bar{t}hZ\ \not{E}_T$ and $t\bar{t}ZZ\ \not{E}_T$ at 14 TeV LHC with 300 fb^{-1} integrated luminosity. μ is fixed to be M_1 + 150 GeV and 10% (20%) systematic uncertainties are assumed for solid (dotted) curves. The same procedure used to pick the exact combination of cuts, $\not{E}_T$, H_T, $m_{\ell\ell}$, N_j and N_{bj} is applied here as the previous section. Again there is no reach for the $t\bar{t}hh\not{E}_T$ channel due to the very low branching fraction of at least three leptons final states and large SM backgrounds. In the "on-Z" signal region, stop masses up to 800 GeV (850 GeV) for the channel $t\bar{t}hZ\not{E}_T$ ($t\bar{t}ZZ\not{E}_T$) can be discovered at the 5σ significance, assuming 10% systematic uncertainties. The 95% C.L. exclusion limits can reach about 880 GeV (1000 GeV) for the channel $t\bar{t}hZ\ \not{E}_T$ ($t\bar{t}ZZ\ \not{E}_T$) if there is no SUSY signal found over SM backgrounds. Limits with 20% systematic uncertainties are almost the same as that of 10% systematic uncertainties. The reach for the "off-Z" signa region is much smaller than that of "on-Z" signal region.

Results of combined channels

In this section, we perform two different combination approaches: 1) combine the three channels $t\bar{t}hh\not{E}_T$, $t\bar{t}hZ\not{E}_T$ and $t\bar{t}ZZ\not{E}_T$ to obtain the 5σ and 95% C.L. reach for the three primary signal regions. 2) combine the three primary signal regions to obtain the 5σ and

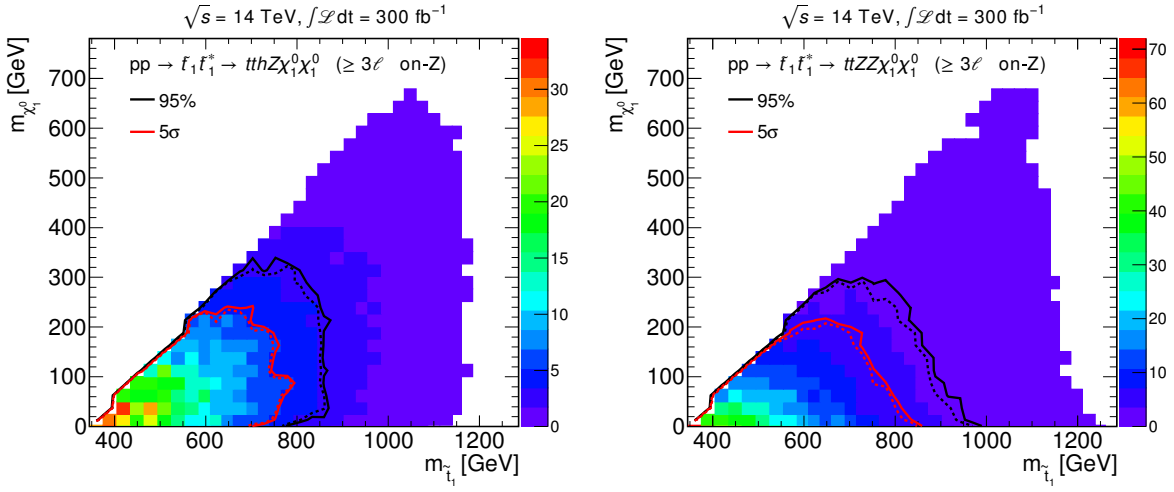

Figure 5.14: The 95% CL upper limits (black curve) and 5σ discovery reach (red curve) are shown in the plane of MSSM parameter space $m_{\tilde{t}_1}$ vs $m_{\chi_1^0}$ for the stop pair production $pp \to \tilde{t}_1\tilde{t}_1 \to t\bar{t}\chi_2^0/\chi_3^0 \to t\bar{t}hZ\not{E}_T$ (left) and $t\bar{t}ZZ\not{E}_T$ (right) with at least three leptons in the final states at 14 TeV LHC with 300 fb^{-1} integrated luminosity. μ is fixed to be M_1 + 150 GeV and 10% (20%) systematic uncertainties are assumed for solid (dotted) curves. The two panels are for the "on-Z" signal region, the reach plots for the "off-Z" signal region are not shown here because of the very low reach. The color coding on the right indicates the signal significance defined simply as $S/\sqrt{B}$ to guide the eye.

95% C.L. reach for the three channels $t\bar{t}hh\not{E}_T$, $t\bar{t}hZ\not{E}_T$ and $t\bar{t}ZZ\not{E}_T$. We take one specific set of advanced selection cuts to do the combinations, which are listed in Table 5.16.

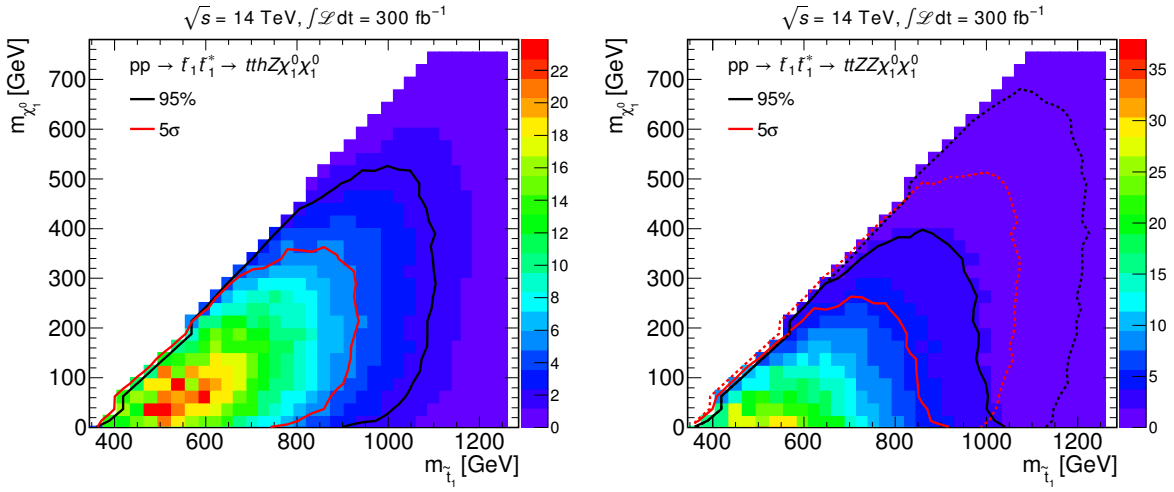

Figure 5.15: The 95% CL upper limits (black curve) and 5σ discovery reach (red curve) are shown in the plane of MSSM parameter space $m_{\tilde{t}_1}$ vs $m_{\chi_1^0}$ for the combined signal regions in the two channels $t\bar{t}hZ$ and $t\bar{t}ZZ$ at 14 TeV LHC with 300 fb^{-1} integrated luminosity. μ is fixed to be M_1 + 150 GeV and 10% systematic uncertainties are assumed. Because the reaches of the two OS leptons signal region and at-least-three leptons signal region are much smaller than that of the one lepton signal region, therefore the combined reach is very close to that of the one lepton signal region. The dotted line in right panel represents the case of 100% decay branching fraction assumption. The color coding on the right indicates the signal significance defined simply as $S/\sqrt{B}$ to guide the eye.

We again use the root package TLimit [189] to calculate the 95% C.L. upper limits and use $S/\sqrt{B}$ to calculate the 5 σ significance. Combined signal significance contours of 5σ discovery reach (red curve) and 95% C.L. exclusion limit (black curve) are shown in Figure 5.15 and Figure 5.16 in the plane of $m_{\tilde{t}_1}$ versus $m_{\chi_1^0}$ for the 14 TeV LHC with 300 fb^{-1} integrated luminosity, including 10% systematic error. Because $t\bar{t}hh\not{E}_T$ has no reach in either the two OS signal region or the at least three leptons signal region, it is not considered for the combinations for the the two signal regions. As can be seen in Figure 5.15, the one lepton signal region contributes most to both $t\bar{t}hZ\not{E}_T$ and $t\bar{t}ZZ\not{E}_T$ channels. The 5σ reach can go up to 920 GeV, and the 95% exclusion limits can extend to 1100 GeV for the channel $t\bar{t}hZ\not{E}_T$.

In the combined reach of the three channels $t\bar{t}hh\not{E}_T$, $t\bar{t}hZ\not{E}_T$ and $t\bar{t}ZZ\not{E}_T$ shown in Figure 5.16, the one lepton signal region has the best reach sensitivity, in which the channel $t\bar{t}hZ\not{E}_T$ has the largest contribution. The top mass can be discovered up to 1030 GeV, or excluded up to 1200 GeV for the one lepton signal region. For the 2OS ℓ signal region and at least 3ℓ signal region, the combined reach is almost the average of the two channels $t\bar{t}hZ\not{E}_T$ and $t\bar{t}ZZ\not{E}_T$, leading to an almost vertical right boundary. A stop mass up to 930 GeV for $m_{\chi_1^0} \sim 120$ GeV can be discovered, or a stop mass between 370 GeV and 1060 GeV is excluded at the 95% C.L. for the 2OS ℓ signal region. For the at-least-three lepton "on-Z" signal region, the 5σ reach of a stop mass can go to 880 GeV for a small LSP mass, and the 95% C.L. exclusion limit can reach 1000 GeV for a broad LSP mass region.

Signal region	$\not{E}_T >$	$H_T >$	m_T	$\lvert m_{\ell\ell} - m_Z \rvert <$	$M_{T2} >$	$N_j \geq$	$N_b \geq$
One lepton	200 GeV	550 GeV	200 GeV	-	-	7	2
Two OS leptons	150 GeV	500 GeV	-	5 GeV	80 GeV	5	2
At least three leptons	200 GeV	500 GeV	-	5 GeV	-	5	1

Table 5.16: The set of advanced selection cuts for the three primary signal regions. There are total 11.57±0.82 background events for the one lepton signal region, 2.66±0.57 background events for the two OS leptons signal region, and 6.55±0.28 background events for the at least three leptons signal region.

5.4.3 Collider analysis at $\sqrt{s} = 100$ TeV

We focus on the $\sqrt{s} = 100$ TeV collider phenomenology under the same assumption: Higgsino NLSP and Bino LSP with mass hierarchies of $M_1 < \mu < M_{3SQ} \ll M_2$, other irrelevant SUSY particles are decoupled to be 20 TeV. We fix μ to be M_1 + 500 GeV because we believe the low mass particles are not degenerate. Under this assumption, the branching fractions of $\chi_2^0/\chi_3^0 \to \chi_1^0 h \approx \chi_2^0/\chi_3^0 \to \chi_1^0 Z \approx 50\%$ as discussed in Ref[122], so the decay branching fractions of $t\bar{t}hh\not{E}_T$, $t\bar{t}hZ\not{E}_T$, $t\bar{t}ZZ\not{E}_T$ are roughly 25%, 50%, 25% for the entire mass region. We perform a broad scan over the high mass parameter regions:

- M_{3SQ} from 1000 to 8000 GeV in steps of 250 GeV, corresponding to $m_{\tilde{t}_1}$ from about 1009 GeV to about 8001 GeV.

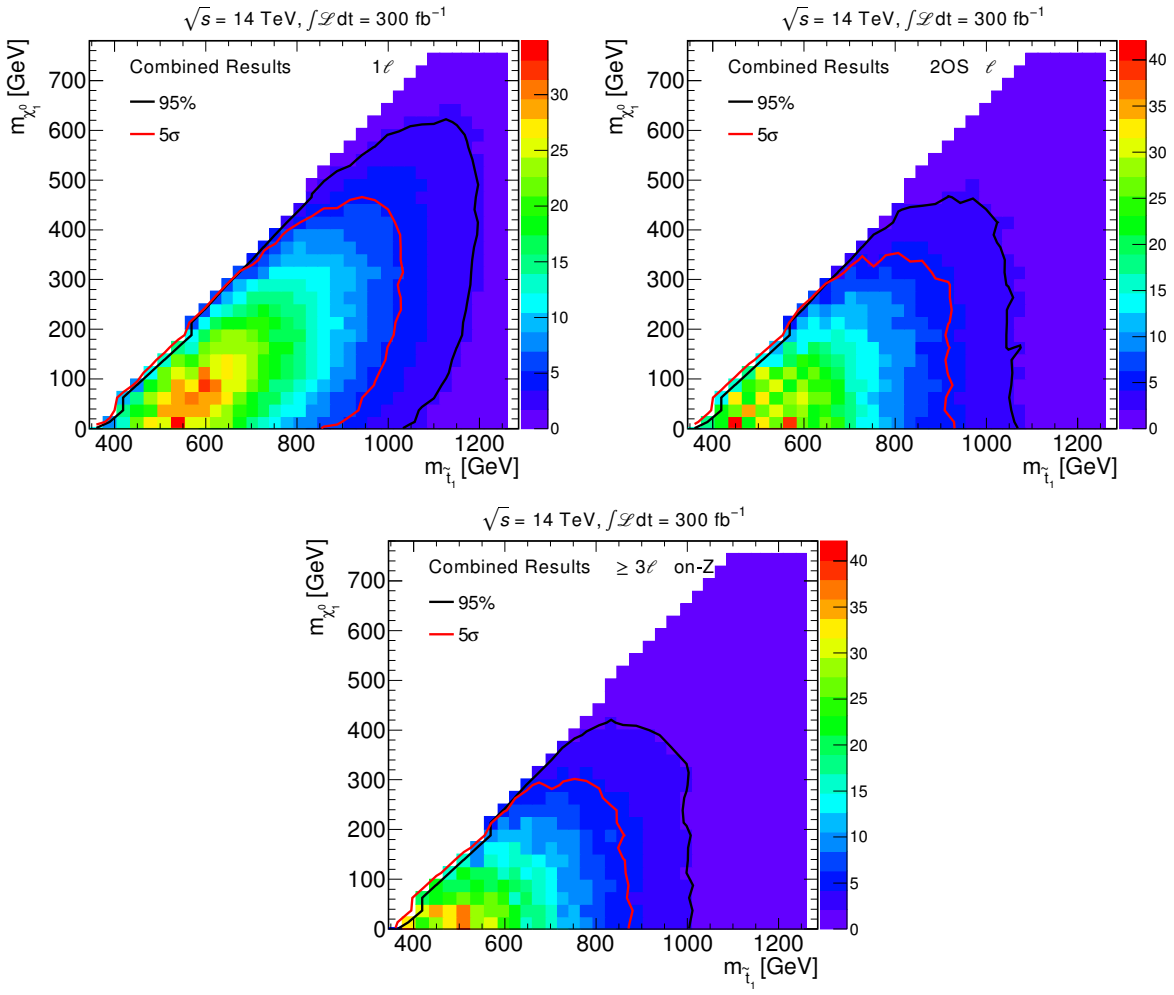

Figure 5.16: The 95% CL upper limits (black curve) and 5σ discovery reach (red curve) are shown in the plane of MSSM parameter space $m_{\tilde{t}_1}$ vs $m_{\chi_1^0}$ for the combined decay channels of $t\bar{t}hh$, $t\bar{t}hZ$ and $t\bar{t}ZZ$ in the three primary signal regions at 14 TeV LHC with 300 fb^{-1} integrated luminosity. μ is fixed to be M_1 + 150 GeV and 10% systematic uncertainties are assumed. The color coding on the right indicates the signal significance defined simply as $S/\sqrt{B}$ to guide the eye.

- M_1 is scanned from 5 GeV to 5000 GeV, in steps of 250 GeV.
- μ is fixed to be $\mu = M_1 + 500$ GeV.
- We further require $m_{\tilde{t}_1} > m_{\chi_2^0}/m_{\chi_3^0} + m_t$ such that $\tilde{t}_1 \to t\chi_2^0/\chi_3^0$ is kinematically open.

The top quark from the large mass stop is highly boosted as discussed in Ref. [190], which leads to the leptons collinear with the high p_T jets. So at the event generation, we do not require the separation ΔR between jets and leptons to be larger than 0.5. Event samples including all SM backgrounds and signals are generated using Madgraph 5 [131], processed through Pythia 6 [132] for the fragmentation and hadronization and then through Delphes 3 [134] with the Snowmass combined LHC No-Pile-up detector card [172] for the detector simulation. We allow up to one additional parton in the final state, and adopt the MLM matching scheme [191] with xqcut = 80 GeV for $t\bar{t}j$ background. Both the SM backgrounds and the stop pair production signal are normalized to theoretical cross sections, calculated including higher-order QCD corrections [121, 188]. For the event generation, the top quark mass m_t is set to be 175 GeV, and the Higgs mass m_h to be 125 GeV. At the generator level, we apply the S_T cut (p_T scalar sum of all partons) as follows: $S_T \geq 3$ TeV for the $t\bar{t}j$ background and $S_T \geq 1$ TeV for the $t\bar{t}B$ background, where B stands for bosons including W, Z and h.

For the signal events of the whole parameter space and all SM backgrounds, we have the following requirements:

- All jets reconstructed using the anti-k_t algorithm [192] with a cone radius $R = 0.4$, are required to have $p_T > 50$ GeV and $|\eta| < 2.5$, and include at least two jets with $p_T > 500$ (1000) GeV.

- All leptons (e or μ) are required to have $p_T > 30$ GeV and $|\eta| < 2.5$, and include at lest one lepton with $p_T > 100$ (200) GeV contained within a $\Delta R = 0.5$ cone centered around one of the leading two jets.

- The missing transverse momentum is separated from any jet with $p_T > 100$ (200) GeV and $|\eta| < 2.5$, $\Delta\Phi(\mathbf{p}_T^{miss}, j) > 1.0$.

- m_T, defined as the invariant mass of the leading lepton and the missing transpose momentum, to be greater than 500, 750, 1000, 1250, 1500 GeV.
- $\not{E}_T$ to be greater than 1, 1.5, 2, 2.5, 3, 3.5, 4 TeV.
- H_T to be greater than 2, 3, 4, 5, 6 TeV.
- N_j to be at least 4, 5, 6, 7; N_{bj} to be at least 2, 3 ,4 ,5.

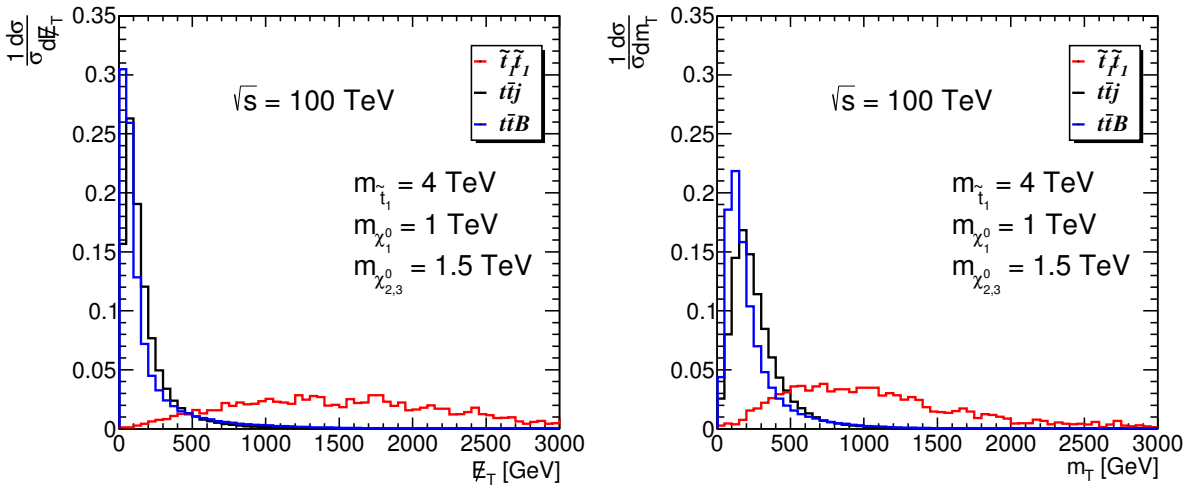

Figure 5.17: Normalized distributions of $\not{E}_T$ (left) and m_T (right) for the signal channel $t\bar{t}hZ\not{E}_T$ with $m_{\tilde{t}_1} = 4000$ GeV and $m_{\chi^0_1} = 1000$ GeV as well as SM backgrounds after the N_j, N_ℓ and $\Delta\Phi(j,\not{E}_T)$ cuts.

After imposing the requirement that leptons are collinear to the two leading jets on the SM backgrounds, the selected samples mainly contain the boosted heavy quarks. The neutrinos in the form of $\not{E}_T$ from the W's decays are highly aligned with the jet momenta, while $\not{E}_T$ of signals mainly come from the LSP, which is not usually aligned with the jet momenta. Therefore it is useful to impose the angle separation $\Delta\Phi$ cut between $\not{E}_T$ and the jets with $p_T > 100$ (200) GeV and $|\eta| < 2.5$. The normalized distributions after the above cuts of $\not{E}_T$ and m_T are displayed in Figure 5.17. The $\not{E}_T$ and m_T distribution of SM backgrounds are typically bounded by m_W because $\not{E}_T$ and m_T mainly come from the decay $W \to \ell\nu$, while the signal has much broader distribution because of the LSP contribution, as expected.

Description	$\tilde{t}_1\tilde{t}_1$ ($t\bar{t}hh$)	$\tilde{t}_1\tilde{t}_1$ ($t\bar{t}hZ$)	$\tilde{t}_1\tilde{t}_1$ ($t\bar{t}ZZ$)	$t\bar{t}j$	$t\bar{t}B$
CS (fb) before cuts	0.66	1.32	0.67	2670	2003
$N_j \geq 2$	94%	93%	92%	93%	40%
$N_\ell \geq 1$	37%	37%	35%	40.6%	8.6%
$\Delta\Phi(j,\not{E}_T)$	5.5%	6.6%	7.5%	1.7%	7.3×10^{-3}
$\not{E}_T > 1500$ GeV	2.5%	3.3%	4.1%	2.9×10^{-5}	6.6×10^{-5}
$H_T > 4000$ GeV	1.2%	1.6%	1.9%	1.0×10^{-5}	8.5×10^{-6}
$m_T > 1000$ GeV	7.4×10^{-3}	1.1%	1.4%	3.2×10^{-6}	5.4×10^{-6}
$N_j \geq 5$	5.8×10^{-3}	8.3×10^{-3}	8.7×10^{-3}	1.8×10^{-6}	2.4×10^{-6}
$N_{bj} \geq 2$	4.9×10^{-3}	6.0×10^{-3}	5.5×10^{-3}	3.1×10^{-7}	1.3×10^{-6}
CS (fb) after cuts	3.2×10^{-3}	8.0×10^{-3}	3.7×10^{-3}	8.3×10^{-4}	2.6×10^{-3}
Yields	9.6	24	11.1	2.5	7.8

Table 5.17: The cumulative cut efficiencies, cross sections and yields for the signal with $m_{\tilde{t}_1} = 4000$ GeV and $m_{\chi_1^0} = 1000$ GeV as well as SM backgrounds. The B in $t\bar{t}B$ stands for bosons including W, Z and h.

Table 5.17 shows the cross sections, yields and cut efficiencies after each level of one set of cuts for the signals as well as the SM backgrounds. The $t\bar{t}B$ ($B = W, Z, h$) is the dominant background after all strong cuts, other SM backgrounds are typically small after strong H_T and $\not{E}_T$ cuts, therefore they are not considered in this analysis. The discovery significance of 7σ for channel $t\bar{t}hZ\not{E}_T$ can be reached after the strong cuts.

In Figure 5.18, the 95% C.L. upper limits (black curve) and 5σ discovery reach (red curve) are shown in the plane of the MSSM parameter space $m_{\tilde{t}_1}$ vs $m_{\chi_1^0}$ for the stop pair production pp $\to \tilde{t}_1\tilde{t}_1 \to t\bar{t}\chi_2^0/\chi_3^0 \to t\bar{t}hh\ \not{E}_T$ (top left), $t\bar{t}hZ\ \not{E}_T$ (top right), $t\bar{t}ZZ\ \not{E}_T$ (bottom left) and combined channels (bottom right) at 100 TeV LHC with 3000 fb^{-1} integrated luminosity. μ is fixed to be $M_1 + 500$ GeV and 10% systematic uncertainties are assumed. For each mass point of $(m_{\tilde{t}_1}, m_{\chi_1^0})$, given the mass dependence of the production cross section and decay branching fractions shown in Figure 5.8, the signal $\sigma \times$ BR for each individual point has been used. All combinations of the advanced selection cuts of $\not{E}_T$, H_T, m_T, N_j and N_{bj} are examined. The optimized combination that gives the best significance is used for each particular mass point. The channel $t\bar{t}hZ\not{E}_T$ has the best reach sensitivity due to the large branching fractions. The stop masses up to 5 TeV for the channel $t\bar{t}hZ\not{E}_T$ can be discovered at the 5σ significance, assuming 10% systematic uncertainties. The 95%

C.L. exclusion limits can reach about 6 TeV for the channel $t\bar{t}hZ\not{E}_T$ if there is no SUSY signal found over SM backgrounds. In the simplified model, assuming the stop pair 100% decaying to $t\bar{t}hh\not{E}_T$ or $t\bar{t}ZZ\not{E}_T$, the stop mass up to 6.2 TeV can be discovered at 5σ significance, or can be excluded up to 6.8 TeV. The combined reach of all three channels can also push the discovery limit to 6 TeV just as that of the simplified model. This greatly improves our understanding of the TeV scale SUSY and the nature of electroweak breaking.

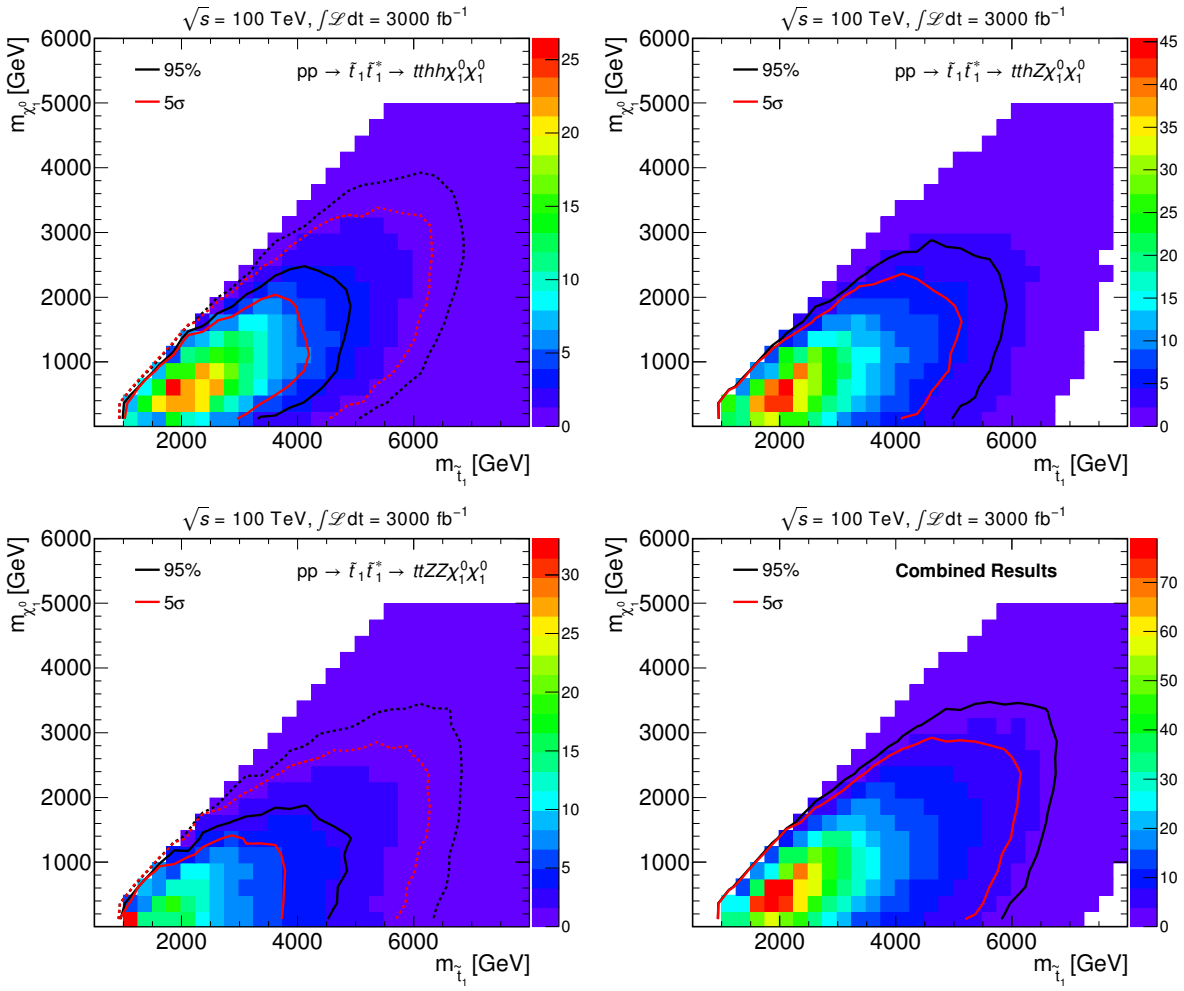

Figure 5.18: The 95% CL upper limits (black curve) and 5σ discovery reach (red curve) are shown in the plane of MSSM parameter space $m_{\tilde{t}_1}$ vs $m_{\chi_1^0}$ for the stop pair production $pp \to \tilde{t}_1\tilde{t}_1 \to t\bar{t}\chi_2^0/\chi_3^0 \to t\bar{t}hh\not{E}_T$ (top left), $t\bar{t}hZ\not{E}_T$ (top right), $t\bar{t}ZZ\not{E}_T$ (bottom left) and combined channels (bottom right) at 100 TeV LHC with 3000 fb^{-1} integrated luminosity. μ is fixed to be $M_1 + 500$ GeV and 10% systematic uncertainties are assumed. Solid line stands for the real situation in the scenario and dotted line represents the case of 100% decay branching fraction assumption. The color coding on the right indicates the signal significance defined simply as $S/\sqrt{B}$ to guide the eye.

CHAPTER 6

Precision Measurements

Precision measurements have been essential in establishing the theory of the Standard Model, furthermore, they provide a complimentary approach to probe new physics in addition to the direct collider searches. Although the LHC is entering the TeV scale era, the Higgs couplings to fermions and vector bosons (W, Z) can only be measured approximately at a $5 \sim 10$ % precision level [193–195] at the $\sqrt{s} = 14$ TeV LHC with 300 fb^{-1} integrated luminosity due to the huge QCD backgrounds in the proton proton collision. Therefore, future e^+ e^- colliders like the Circular Electron Positron Collider (CEPC) [196] are critical to both the Z-pole and the Higgs precision measurements. One of the greatest advantages of a lepton collider Higgs factory like CEPC is the capability to determine the Higgs coupling constants model independently. In this chapter, we aim to study the implementation of Higgs and Z-pole precision measurements on the constraints of the Two-Higgs-Doublet-Model (2HDM) parameter space for current and future colliders.

6.1 NLO radiative corrections to Higgs couplings

The Higgs boson couplings to quarks (except top quark) and τ lepton can be measured through the Higgs decay branching fractions to the corresponding fermions. In the same way, the Higgs boson couplings to vector bosons and photons can also be determined by measuring the Higgs decay branching fractions to them. Furthermore, the tri-linear coupling of the Higgs boson hhh [89, 197–202] is essential to understand the structure of the Higgs potential. Studying possible deviations of the Higgs couplings in the new physics models is useful in understanding discriminative phenomenological properties. In this section, we will study the theoretical prediction of Higgs couplings in the framework

of the 2HDM at the NLO level.

6.1.1 hff couplings

The tree level scale factor of Higgs for hff and hVV ($V = W, Z$) coupling constants compared to the Standard Model values are listed in Table 3.3. In the alignment limit, namely $\sin(\beta - \alpha) = 1$, all scale factors become unity, which means all the tree level hVV and hff couplings are the same as the Standard Model values. In the non-alignment limit, the tree level deviations of hVV and hff couplings can be significant. The on-shell renormalization scheme of the one-loop corrected Yukawa couplings hff is discussed in Ref. [203]. The renormalized hff vertex can be expressed as:

$$\hat{\Gamma}_{hff}(p_1^2, p_2^2, q^2) = \Gamma^0_{hff} + \delta\Gamma_{hff} + \Gamma^{1\text{PI}}_{hff}(p_1^2, p_2^2, q^2) \tag{6.1}$$

where Γ^0_{hff} is the tree level vertex, p_1 and p_2 are the incoming momenta for the fermion and anti-fermion, and $q = p_1 + p_2$ is the outgoing momentum for h. The counter term contribution is given by:

$$\delta\Gamma_{hff} = -i\frac{m_f}{v}\xi^f_h\left[\frac{\delta m_f}{m_f} + \delta Z^f_V + \frac{1}{2}\delta Z_h + \frac{\delta\xi^f_h}{\xi^f_h} + \frac{\delta\xi^f_h}{\xi^f_h}(\delta C_h + \delta\alpha) - \frac{\delta v}{v}\right] \tag{6.2}$$

where $\delta\xi^f_h$ is the counter term of the Yukawa coupling scale factor, depending on the type of Yukawa interaction. δZ_h is the counter term for h wave function renormalization. δC_h is the counter term for the off-diagonal term in the CP-even Higgs matrix. $\delta\alpha$ and δv are the counter terms for the rotation angle α and VEV, respectively. The counter terms for the fermion mass and the left-handed and right-handed fermion wave function renormalization are given as:

$$m_f \to m_f + \delta m_f, \quad \psi_L \to \left(1 + \frac{1}{2}\delta Z^f_L\right)\psi_L, \quad \psi_R \to \left(1 + \frac{1}{2}\delta Z^f_R\right)\psi_R \tag{6.3}$$

The renormalized fermion two point Green function can be split into the vector, axial vector parts:

$$\hat{\Pi}_{ff}(p^2) = \hat{\Pi}_{ff,V}(p^2) + \hat{\Pi}_{ff,A}(p^2) \tag{6.4}$$

where the two parts can be expressed in terms of the 1PI diagram contributions and the counter terms:

$$\begin{aligned}\hat{\Pi}_{ff,V}(p^2) &= \not{p}\left[\Pi^{\rm 1PI}_{ff,V}(p^2) + \delta Z^f_V\right] + m_f\left[\Pi^{\rm 1PI}_{ff,S}(p^2) - \delta Z^f_V - \frac{\delta m_f}{m_f}\right] \\ \hat{\Pi}_{ff,A}(p^2) &= \not{p}\gamma_5\left[\Pi^{\rm 1PI}_{ff,A}(p^2) + \delta Z^f_A\right]\end{aligned} \tag{6.5}$$

where $\Pi^{\rm 1PI}_{ff,V}$, $\Pi^{\rm 1PI}_{ff,A}$ and $\Pi^{\rm 1PI}_{ff,S}$ are the vector, axial vector and scalar parts of the 1PI diagram contributions at one-loop level, respectively. The wave function renormalization counter term can be expressed as:

$$\delta Z^f_V = \frac{\delta Z^f_L + \delta Z^f_R}{2}, \quad \delta Z^f_A = \frac{\delta Z^f_L - \delta Z^f_R}{2} \tag{6.6}$$

The counter terms δm_f, δZ^f_V and δZ^f_A can be obtained from the three renormalization conditions:

$$\begin{aligned}&\hat{\Pi}_{ff,V}(m_f^2) = 0 \\ &\frac{d}{d\not{p}}\hat{\Pi}_{ff,V}(p^2)\Big|_{p^2=m_f^2} = 0, \quad \frac{d}{d\not{p}}\hat{\Pi}_{ff,A}(p^2)\Big|_{p^2=m_f^2} = 0\end{aligned} \tag{6.7}$$

with

$$\begin{aligned}\frac{\delta m_f}{m_f} &= \Pi^{\rm 1PI}_{ff,V}(m_f^2) + \Pi^{\rm 1PI}_{ff,S}(m_f^2) \\ \delta Z^f_V &= -\Pi^{\rm 1PI}_{ff,V}(m_f^2) - 2m_f^2\left[\ \frac{d}{dp^2}\hat{\Pi}^{\rm 1PI}_{ff,V}(p^2)\Big|_{p^2=m_f^2} + \frac{d}{dp^2}\hat{\Pi}^{\rm 1PI}_{ff,S}(p^2)\Big|_{p^2=m_f^2}\ \right] \\ \delta Z^f_A &= -\Pi^{\rm 1PI}_{ff,A}(m_f^2) + 2m_f^2\frac{d}{dp^2}\hat{\Pi}^{\rm 1PI}_{ff,A}(p^2)\Big|_{p^2=m_f^2}\end{aligned} \tag{6.8}$$

The same strategy applies to the derivation of the other counter terms δZ_h, δC_h and $\delta\alpha$, which are absorbed in the CP even Higgs sectors, from the on-shell conditions for the scalar two point functions:

$$\frac{d}{dp^2}\hat{\Pi}_{hh}(p^2)\Big|_{p^2=m_h^2} = 0, \quad \hat{\Pi}_{Hh}(p^2 = m_H^2) = \quad \hat{\Pi}_{Hh}(p^2 = m_h^2) = 0 \tag{6.9}$$

The counter term for the VEV δv is determined from the renormalization of the electroweak sectors: the masses of the W and Z bosons and the fine structure constant. The 1PI diagram contributions to hff couplings can be obtained from the one loop level shown in Figure 6.1 using hbb as an example.

$h \to b\,b$

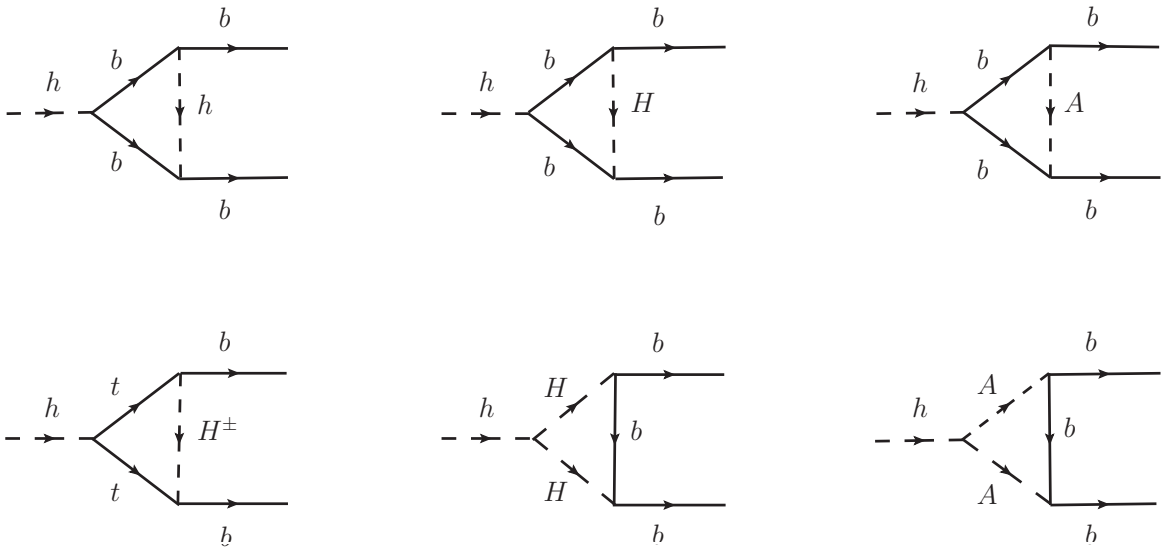

Figure 6.1: The one loop radiative corrections to hbb coupling constant from the extra Higgs bosons in the framework of the 2HDM.

6.1.2 hVV $(V = W, Z)$ couplings

In the future e^+e^- collider, the Higgs boson is produced mainly via the Higgsstrahlung process $e^+e^- \to Zh$ and $e^+e^- \to \nu\bar{\nu}h$ for a relative low center of mass energy. The hZZ coupling is expected to be measured at a sub-percent level at CEPC [196]. Therefore, the thorough calculations the hVV couplings including the NLO radiative corrections are becoming essential in preparation for the future colliders.

The tree level hZZ coupling can be read out:

$$M_1^{hZZ\ (\text{tree})} = \frac{m_Z^2}{v}\sin(\beta - \alpha) \tag{6.10}$$

The same renormalization scheme as that of the hff couplings can be applied here [204]. All the counter terms can be obtained from the (on-shell) renormalization conditions. The

counter terms for the hZZ vertex are:

$$\begin{aligned}\mathcal{L}_{hZZ} &= -\frac{m_Z^2}{v}\sin(\beta-\alpha)g_{\mu\nu}Z^\mu Z^\nu h \\ &\to -\frac{m_Z^2}{v}\Big\{\sin(\beta-\alpha)\Big(1+\frac{\delta m_Z^2}{m_Z^2}-\frac{\delta v}{v}+\delta Z_Z+\frac{1}{2}\delta Z_h\Big) \\ &\quad +\cos(\beta-\alpha)(\delta\beta-\delta C_h)\Big\}g_{\mu\nu}Z^\mu Z^\nu h+...\end{aligned} \tag{6.11}$$

Finally, the renormalized hZZ vertex can be expressed as:

$$M^{hZZ}(p_1^2,p_2^2,q^2) = M^{hZZ\ (\text{tree})} + M^{hZZ\ (1\text{PI})}(p_1^2,p_2^2,q^2) + \delta M^{hZZ} \tag{6.12}$$

The hZZ coupling constant deviation from the SM predictions occurs due to two sources: the tree level scale factor $\sin(\beta-\alpha)$ and the radiative corrections at loop level from the extra Higgs bosons which is shown in Figure 6.2. In the alignment limit, $\sin(\beta-\alpha)\simeq 1$, let $x=\beta-\alpha-\pi/2$, the one loop corrected hZZ coupling can be obtained in the limit of $x\ll 1$:

$$\begin{aligned}M^{hZZ} = \frac{2m_Z^2}{v}\Big\{1-\frac{1}{2}x^2+\frac{1}{64\pi^2v^2}(m_H^2+m_A^2+2m_{H^\pm}^2)-\frac{m_H^2}{96\pi^2v^2}\Big(1-\frac{M^2}{m_H^2}\Big) \\ -\frac{m_A^2}{96\pi^2v^2}\Big(1-\frac{M^2}{m_A^2}\Big)-\frac{m_{H^\pm}^2}{96\pi^2v^2}\Big(1-\frac{M^2}{m_{H^\pm}^2}\Big)-\frac{5N_{ct}m_t^2}{96\pi^2v^2}+...\Big\}\end{aligned} \tag{6.13}$$

where M is defined to be $M=m_{12}^2/\sin\beta\cos\beta$.

6.2 Current constraints

The theoretical constraints in the case of an exact Z_2 symmetry ($m_{12}^2=0$) based on the potential stability, perturbativity and unitarity lead to upper limits on the four Higgs masses of $m_H\lesssim 870$ GeV, $m_A\lesssim 870$ GeV, $m_{H^\pm}\lesssim 780$ GeV [205]. If we allow soft Z_2 symmetry breaking ($m_{12}^2\neq 0$), the upper bounds on the Higgs masses can be relaxed. The current limits from Z-pole precision measurements set strong constraints on the mass difference between charged Higgs and neutral Higgs bosons. The flavor physics of BR($B\to X_s\gamma$) require a charged Higgs mass larger than 480 GeV at 95% C.L level [115]. The search from the current ATLAS and CMS groups [114, 206–209] shows null results at 95% C.L. level in the $H^\pm$ mass range of 200 - 300 GeV for a small $\tan\beta$ $0.5\lesssim\tan\beta\lesssim 0.6$, and in the H^+ mass range of 350 - 400 GeV for $\tan\beta\approx 0.5$.

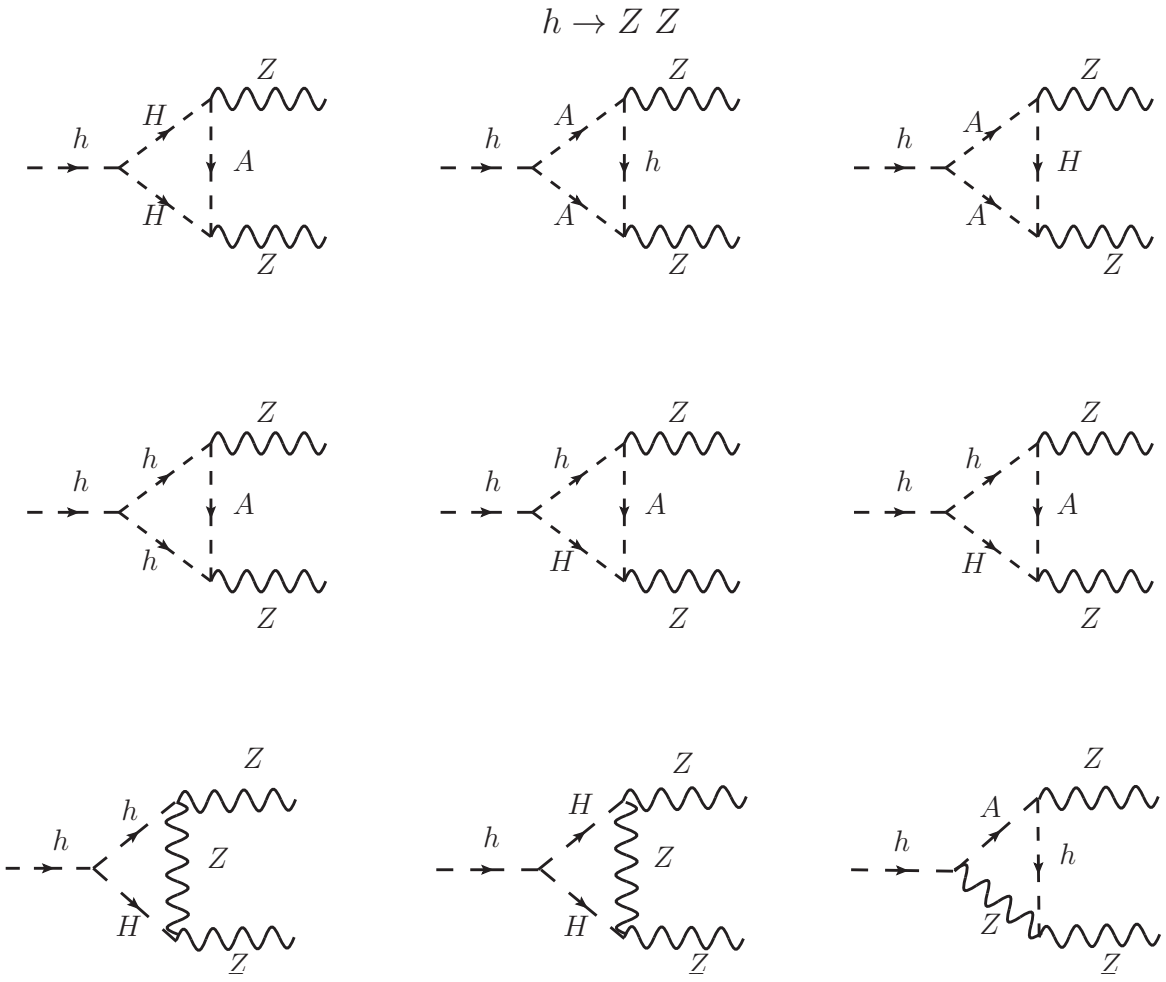

Figure 6.2: The one loop radiative corrections to the hZZ coupling constant from the extra Higgs bosons in the framework of the 2HDM.

6.2.1 Z-pole precision measurements

The Z-pole precision measurements S, T, U in the framework of 2HDM are discussed in detail in Chapter 3. The global fitting of the Standard Model observables and S, T, U can be accomplished by the GFitter package [210–213]. The Standard Model observables can be expressed in terms of $S/T/U$ and three other Z-pole precision observables $X/Y/W$ which are defined in Ref. [214]. The more precise measurements of the Standard Model observables can lead to better constraints on the $S/T/U$ using the global fitting of all the Standard Model observables, as stated in Eq. 6.14. The current experimental observables, their values and uncertainties used in the fit, is given in the first two columns of Table 6.1. We then use the experimental observables as well as the uncertainties to do a global fitting using the Gfitter package. The global fitting results of all Standard Model observables from the GFitter group and ours are listed in the last two columns of Table 6.1. The fit results and correlation matrix of S, T, U are listed in Table 6.2 and Table 6.3, in which the GFitter results are listed for reference. The non-zero S, T, U parameters represent an unambiguous indication of new physics beyond the Standard Model.

$$\begin{aligned} \Gamma_Z &= (\Gamma_Z)_{\rm SM} - 0.00961S + 0.0263T + 0.0194V - 0.0207X \\ m_W^2 &= (m_W^2)_{\rm SM}\ (1 - 0.00723S + 0.0111T + 0.00849U) \\ \Gamma_W &= (\Gamma_W)_{\rm SM}\ (10.00723S + 0.0111T + 0.00849U + 0.00781W) \end{aligned} \tag{6.14}$$

The constraints on the S, T, U parameters for the current experimental measurements are shown in Figure 6.3. The large parameter space of the S, T, U parameters still survives, about -0.2 (-0.25) $< S,\ T <$ 0.3 (0.35) for the 95% (99%) C.L.

In the framework of 2HDM, we require the contributions from the extra Higgs bosons to S and T to fall within the 68%, 95% and 99% C.L. S-T contour shown in Figure 6.3 for a SM Higgs reference mass of 125 GeV. Then we can obtain the constraints on the Higgs masses of 2HDM. Here we show the constraints in the mass plane m_H vs m_A in the left panel of Figure 6.4 and m_H vs $m_{H^\pm}$ in the right panel of Figure 6.4 for three representative Higgs masses.

As can be seen from Figure 6.4, the allowed mass regions behave the same for different $m_{H^\pm}$ or m_A values in the alignment limit ($\beta - \alpha = \pi/2$): the charged Higgs mass tend to

Parameter	Input value	GFitter Fit Result	Our Fit Result
M_H [GeV]	125.14 ± 0.24	125.14±0.24	125.14 ± 0.24
$\Delta\alpha_{had}(M_Z^2)$	0.02757 ± 0.00010	0.02756±0.00010	0.02756 ± 0.00010
M_Z [GeV]	91.1875 ± 0.0021	91.1880 ± 0.0021	91.1879 ± 0.0021
m_t [GeV]	173.34 ± 0.76	173.81±0.85	173.79 ± 0.85
$\alpha_s(M_Z^2)$	–	0.1196 ± 0.0030	0.1196 ± 0.0021
M_W [GeV]	80.385 ± 0.015	80.364±0.007	80.364 ± 0.007
Γ_W [GeV]	2.085 ± 0.042	2.091±0.001	2.09142 ± 0.00096
Γ_Z [GeV]	2.4952 ± 0.0023	2.4950±0.0014	2.4951 ± 0.0011
$\sin^2\theta^l_{eff}$	0.2324 ± 0.0012	0.23150±0.00006	0.231450 ± 0.00006

Table 6.1: The current experimental precision measurements extracted from Ref [210] and global fit results of all Standard Model observables.

Parameter	GFitter Fit Result	Our Fit Result
S	0.05 ± 0.11	0.05 ± 0.10
T	0.09 ± 0.13	0.078 ± 0.114
U	0.01 ± 0.11	0.018 ± 0.094

Table 6.2: The fitting results of $S/T/U$ from electroweak precision measurement.

align to either the CP-odd Higgs mass or CP-even Higgs mass. As the angle $\beta-\alpha$ deviates from the alignment limit, the charged Higgs mass can deviate away from the two neutral Higgs masses and the mass region is split into two parts for large Higgs masses. Imagine that $m_{H^\pm}$ is continuous instead of being fixed to some certain values in the plane of m_A vs m_H, then the survived mass region after $S/T/U$ cut is still very large.

Ours (GFitter)	S	T	U
S	1	0.89 (0.90)	-0.50 (-0.59)
T	–	1	-0.78 (-0.83)
U	–	–	1

Table 6.3: The Correlation matrix of $S/T/U$ from the electroweak precision measurement.

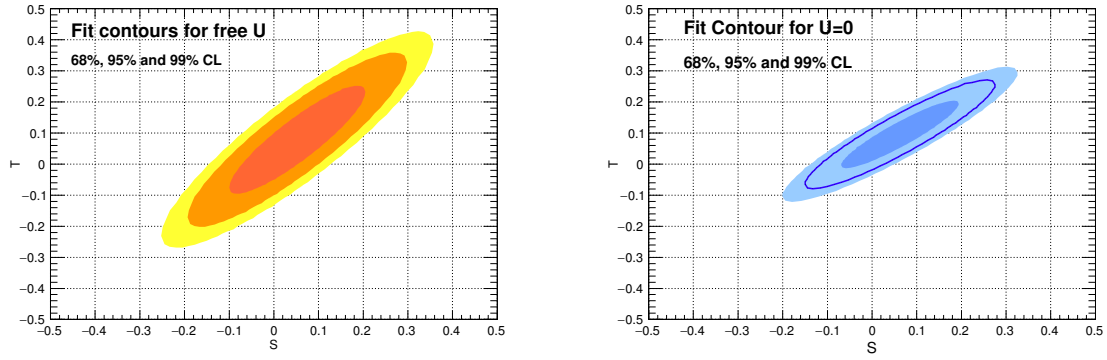

Figure 6.3: The $T - S$ contour constraints for free U parameter (left) and fixed $U = 0$ (right). The color codes from the innermost to outmost represent the 68%, 95%, 99% C.L. exclusion upper limits.

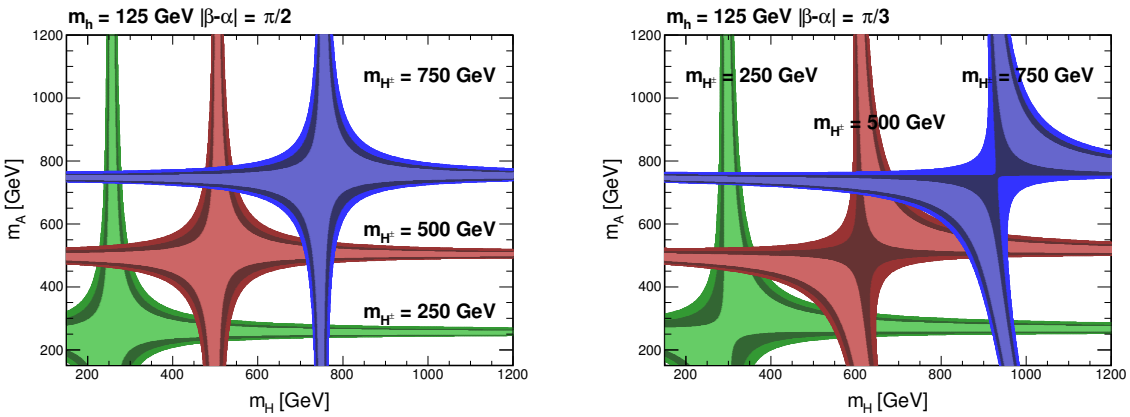

Figure 6.4: The allowed mass regions in the plane of m_H vs m_A for three fixed $m_{H^\pm}$ values in the alignment limit $\alpha - \beta = \pi/2$ (left) and away from the alignment limit $\alpha - \beta = \pi/3$ (right). The color codes from the innermost to outmost represent the 68%, 95%, 99% C.L. exclusion upper limit.

6.2.2 Higgs precision measurements

The breakthrough discovery of the Higgs boson by both the ATLAS and CMS groups on one hand completes the last missing piece of the Standard Model, on the other hand it provides us an extra window to look for new physics beyond the Standard Model. The properties of the Higgs boson including its mass and its decay channels are studied in detail by the ATLAS and CMS groups subsequently. In this work, we use the package called "2HDMC" [215] to calculate the mass spectra of the 2HDM, the Higgs couplings, the decay branching fractions of the Higgs bosons, and implement all the theoretical constraints. We use two other packages HiggsBounds [216] and HiggsSignals [217] to set constraints using experimental searches of the Higgs boson signal rates, masses and cross section limits from LEP, the Tevatron and the LHC. The degrees of freedom include the five Higgs masses m_h, m_H, m_A, and $m_{H^\pm}$, the ratio of the two VEVs $\tan\beta$, the mixing angle of the two CP-even Higgs $\cos(\beta-\alpha)$, and m_{12}^2 since we allow soft breaking of the discrete symmetry. Incorporating all the current experimental Higgs precision measurements, the constraints on the 2HDM parameter space can be obtained. Due to the comparably low precision measurements of Higgs decay branching fractions, the constraints from current experimental direct searches are not strong.

6.2.3 Complementary constraints

In this section, we combine all the constraints to do a complementary probe in the 2HDM parameter space. In order to perform as broad a scan of the parameter space as possible, we randomly throw ten million points in the plane of m_H, m_A, $m_{H^\pm}$, $\tan\beta$ and m_{12}^2. The surviving parameter space can be obtained after each level of constraints. We project the results in the two-parameter plane, as shown in Figure 6.12 and Figure 6.13. The parameter space we scan over are:

- $150\ \text{GeV} < m_H, m_A, m_{H^\pm} < 1000\ \text{GeV}$
- $0\ \text{GeV} < m_{12} < 300\ \text{GeV}$
- $0 < \tan\beta < 20$

As can be clearly seen, the theoretical constraints from the potential stability, pertur-

bativity, and unitarity lead to upper limits on the Higgs masses of $m_H \lesssim 900$ GeV, $m_A \lesssim 900$ GeV, $m_{H^\pm} \lesssim 800$ GeV except for a few points in the high mass region, matching the limits in the case of exact Z_2 symmetry ($m_{12}^2 = 0$) from Ref. [205] well. The Oblique Parameters S, T, U set strong constraints on the mass differences of Higgs bosons: the charged Higgs mass either align with the mass of the CP-even Higgs mass or the CP-odd Higgs mass. The experimental search does not set strong constraints on the Higgs masses. In the plane of m_A vs m_H, the region of $m_H > 350$ GeV and $m_A < 300$ GeV are excluded at 95% C.L. level. In the plane of $m_{H^\pm}$ vs m_A, the mass region within $m_{H^\pm} > 250$ GeV and $m_A < 300$ GeV are excluded at 95% C.L. level.

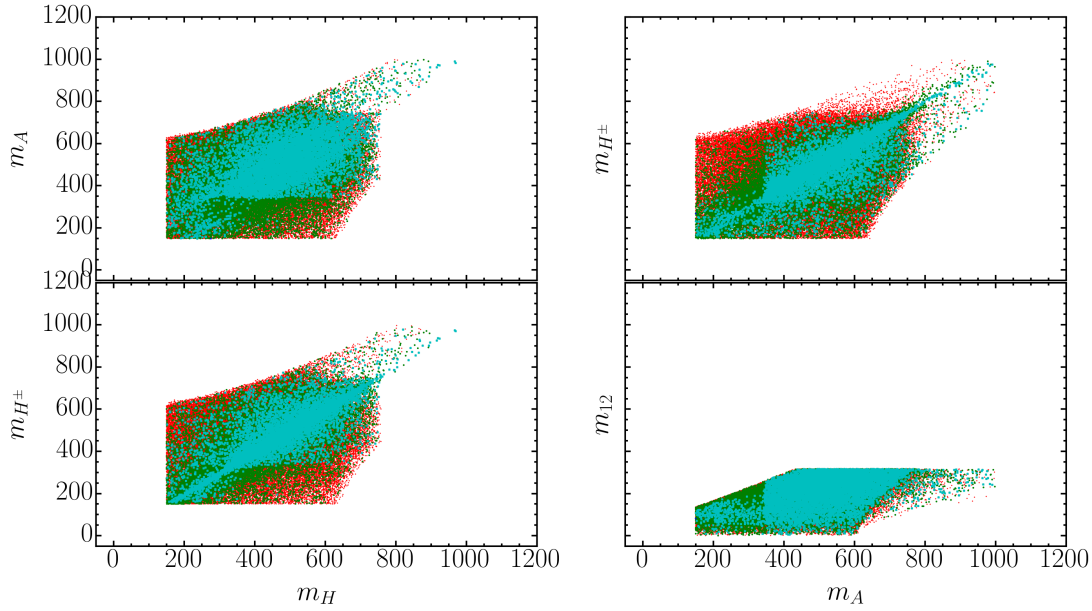

Figure 6.5: The surviving mass regions in the projected mass planes. The red region corresponds to the surviving region after the theoretical constraints, the green region to the Oblique Parameters S, T, U constraints and the blue region to the experimental constraints.

The constraints on the angle $\tan\beta$ are much stronger. There are only very sparse points for $\tan\beta > 5$, indicating that the parameter space for $\tan\beta > 5$ is highly constrained. The

masses of Higgs bosons are required from the direct experimental search to be larger than ~ 350 GeV in the small $\tan\beta \lesssim 1$ region.

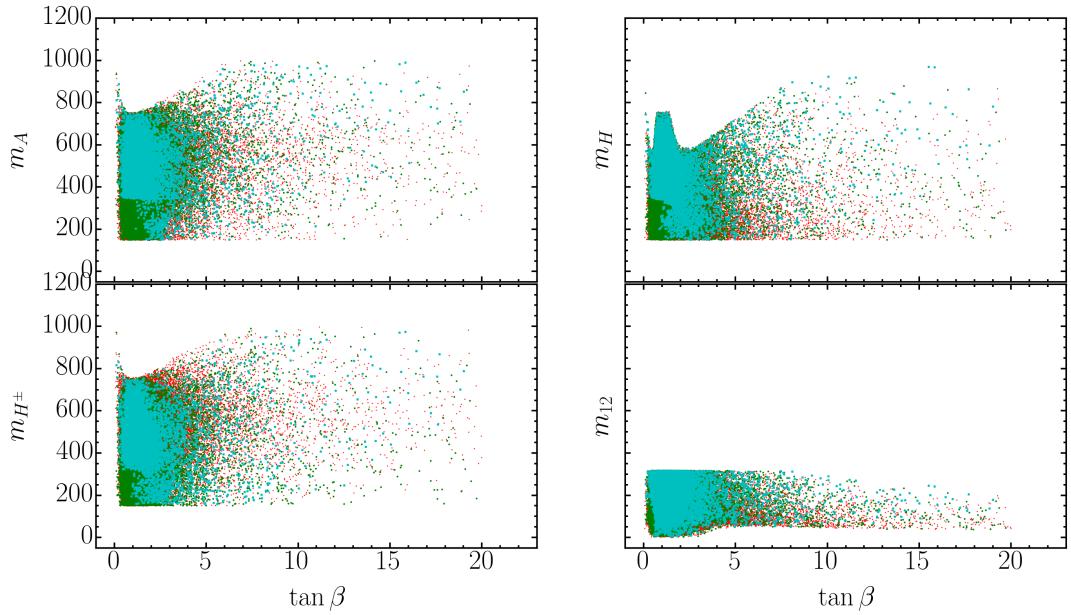

Figure 6.6: The surviving $\tan\beta$-mass regions in the projected mass planes. The color coding is the same as in Figure 6.12.

6.3 Constraints in the future collider

The Circular Electron Positron Collider (CEPC) is designed to have e^+e^- collision at $\sqrt{s} = 250$ GeV, which can produce 1 million h events with 5 ab^{-1} integrated luminosity. It can also run at Z-pole, which is expected to collect 10^{10} Z events for an integrated luminosity of 500 fb^{-1}. With this wealth of statistics, the precision of most of the observables here can be improved by at least an order of magnitude, presented in Table 6.4.

Parameter	CEPC Precision
M_H [GeV]	$< \pm 0.1$
M_Z [GeV]	$\pm$(0.0005 - 0.001)
$\Delta\alpha_{had}(M_Z^2)$	$\pm 4.7 \times 10^{-5}$
m_t [GeV]	$\pm 0.6_{exp} \pm 0.25_{th}$
$\alpha_s(M_Z^2)$	$\pm 1.0 \times 10^{-4}$
M_W [GeV]	$(\pm(3-5)_{exp} \pm 1_{th}) \times 10^{-3}$
$\sin^2\theta^l_{eff}$	$(\pm(4.6-5.1)_{exp} \pm 1.5_{th}) \times 10^{-5}$
Γ_Z [GeV]	$(\pm(5-10)_{exp} \pm 0.8_{th}) \times 10^{-4}$

Table 6.4: The precisions of the Standard Model observables in the simplified electroweak fit at the CEPC.

6.3.1 Z-pole precision measurements

In the $S/T/U$ fitting, the $S-T$ contour is not at the center of the SM-point (0,0) when fixing U=0. If we take the precision in Table 6.4 into account without changing the center values of all the observables, then we might end up excluding the Standard Model, which is not our purpose. Thus, our strategy is using the center value of each observable listed in the fourth column of Table 6.1 with the uncertainties listed in Table 6.4. For those observables that we lack predictions of their precision measurements in CEPC, we still use current precision (the second column of Table 6.1). Then, using these inputs for $S/T/U$ fitting in the case of CEPC, leads to the center values of $S/T/U$ as being around zero. The fitting result of the Oblique Parameters is given in Figure 6.7 in terms of the confidence level contour in $T-S$ plane, with both U free and U fixed at 0. The new precision measurements can greatly improve the constraints on the new physics. In the framework of 2HMD, we require the contributions from theextra Higgs bosons to S and T to fall within the 68%, 95% and 99% C.L. S-T contour for a SM Higgs reference mass of 125 GeV. Then the constraints on the parameters of 2HMD are shown in Figure 6.8.

As can be seen from Figure 6.8, the allowed mass regions behave the same as the current constraints except for having a much smaller parameter space region in the alignment limit, which is because the $S/T/U$ parameter space is much smaller at the CEPC than the current limits. As the angle $\beta-\alpha$ deviates from the alignment limit, the allowed mass regions are split into two parts for large Higgs masses. And the region of which the three Higgs masses

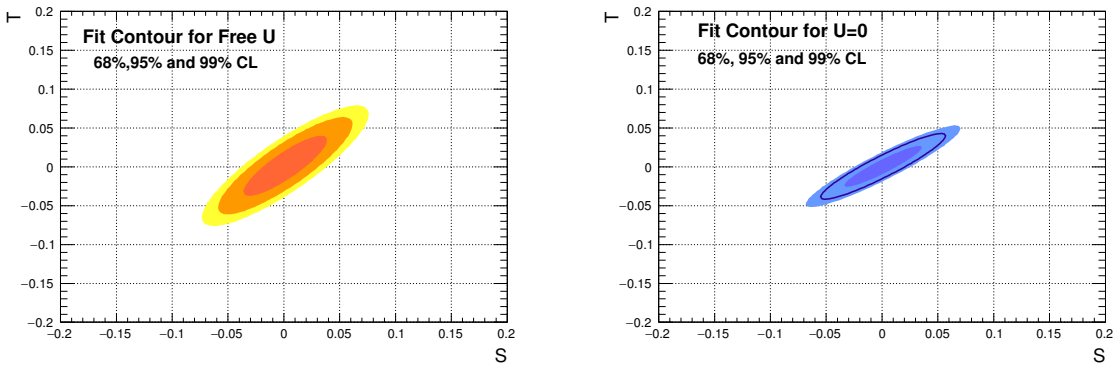

Figure 6.7: The T-S contour at precision level of the CEPC.

are decoupled ($m_A = m_H = m_{H^\pm}$) is excluded.

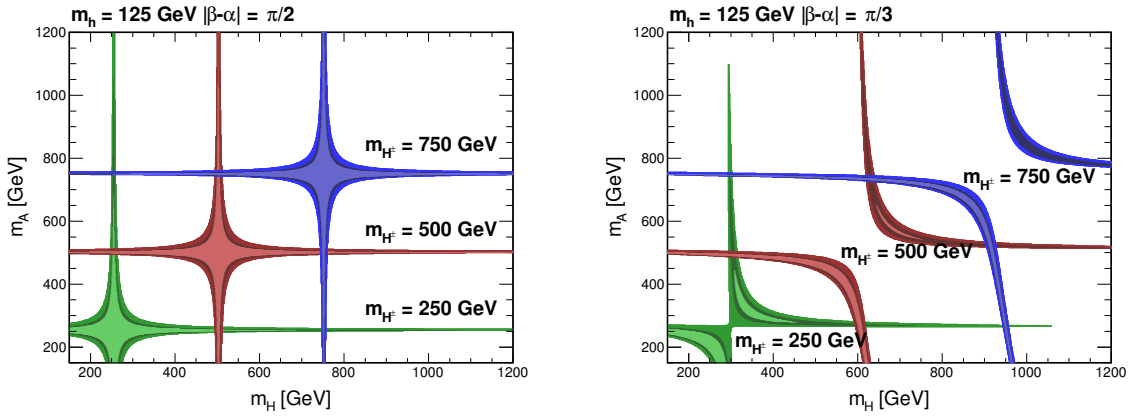

Figure 6.8: The allowed mass regions in the plane of m_H vs m_A for three fixed $m_{H^\pm}$ values in the alignment limit $\alpha - \beta = \pi/2$ (left) and away from the alignment limit $\alpha - \beta = \pi/3$ (right) at the future e^+e^- CEPC collider. The color codes from the innermost to outmost represent the 68%, 95%, 99% C.L. exclusion upper limit.

6.3.2 Higgs precision measurements

The precision of Higgs decay branching fractions can be greatly improved at the CEPC. With the measurements of inclusive cross section $\sigma(Zh)$ and the cross sections of the individual Higgs boson decay mode $\sigma(Zh) \times$ BR, the Higgs boson individual branching fraction can be extracted, as shown in Table 6.5. A relative precision of 0.51% on $\sigma(Zh)$ can be achieved at the CEPC by combining all three channels of the Z boson decay for

an integrated luminosity of 5 ab^{-1}. The best achievable precision at the CEPC is 0.28% for $\sigma(e^+e^- \to Zh) \times \mathrm{BR}(h \to bb)$ due to the very clean backgrounds for b jets. The other two measurements $\sigma(e^+e^- \to Zh) \times \mathrm{BR}(h \to cc, gg)$ can also achieve high precision level since the flavour tagging algorithms and vertex/inner tracking system design can be greatly improved at the CEPC. We work in the alighment limit ($\sin(\beta-\alpha) = 1$), otherwised mentioned.

Figure 6.9 presents the NLO correction of $\sigma(Zh)$ in the framework of the 2HDM in the plane of m_H vs $m_{H^\pm}$ or m_A vs $m_{H^\pm}$. The NLO correction of $\sigma(Zh)$ for both Type I and Type II 2HDM are comparable except for the high mass region, where the program of HiggsBounds crashed. In the limit of $m_{H^\pm} > m_H$ or $m_{H^\pm} < m_A$, the larger correction happens and can reach as high as $\sim 1\%$.

Decay mode	$\sigma(Zh) \times$ BR	BR
$h \to bb$	0.28%	0.57%
$h \to cc$	2.2%	2.3%
$h \to gg$	1.6%	1.7%
$h \to \tau\tau$	1.2%	1.3%
$h \to WW$	1.5%	1.6%
$h \to ZZ$	4.3%	4.3%
$h \to \gamma\gamma$	9.0%	9.0%
$h \to \mu\mu$	17%	17%
$h \to$ inv	-	0.28%

Table 6.5: Estimated precision measurements of Higgs boson branching fractions with 5 ab^{-1} integrated luminosity at the CEPC [196].

The deviation (denoted by κ) from the Standard Model Higgs coupling constants can be derived from Table 6.5, as shown in Table 6.6. The κ_Z can reach the sub-percent precision level, which can be used to greatly constrain the parameter space of the 2HDM.

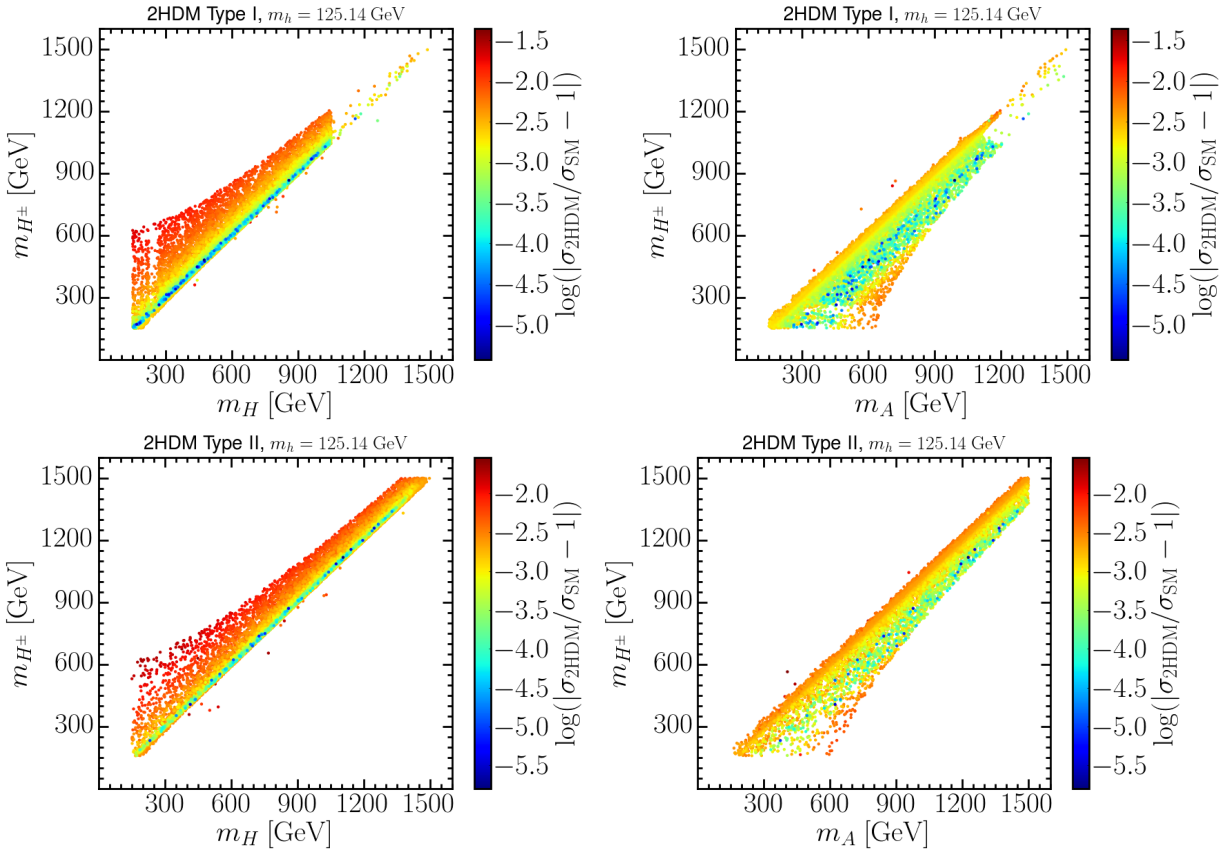

Figure 6.9: The NLO correction of $\sigma(Zh)$ in the framework of the 2HDM for Type I (top two) and Type II (bottom two) in the plane of m_H vs $m_{H^\pm}$ or m_A vs $m_{H^\pm}$. The color coding is the precision of $\sigma(Zh)$. The data points already survived from the theoretical and CEPC $S/T/U$ constraints.

The deviations are denoted as:

$$\kappa_f = \frac{g(hff)}{g(hff;\mathrm{SM})}, \qquad \kappa_V = \frac{g(hVV)}{g(hVV;\mathrm{SM})} \tag{6.15}$$

The Higgs boson coupling deviations κ are shown in Figure 6.10 for Type I 2HDM and in Figure 6.11 for Type II 2HDM. The scattering of data points in Type II 2HDM is much wider than that in Type I 2HDM due to the different couplings constants. As can be seen, κ_γ has very large deviation, which can reach as high as 5%. κ_b, κ_Z and κ_τ have relatively small deviation, most of which are around or within 0.5%, because of the small couplings of SM particles and the extra Higgs bosons in the 2HDM. If we apply the precision measurements of the CEPC, we can set very strong constraints on the parameter space

Luminosity (ab^{-1})	0.5	2	5	10
κ_b	3.7	1.9	1.2	0.83
κ_c	5.1	3.2	1.6	1.2
κ_g	4.7	2.3	1.5	1.0
κ_τ	4.2	2.1	1.3	0.94
κ_W	3.8	1.9	1.2	0.84
κ_Z	0.51	0.25	0.16	0.11
κ_γ	15	7.4	4.7	3.3

Table 6.6: Estimated precision measurements in percentage of Higgs boson coupling constant deviations for several benchmark integrated luminosity of the CEPC [196].

of the 2HDM. The color coding in Figure 6.10 is the charged Higgs mass. The deviation decreases as the Higgs mass increases. The NLO corrections from the extra Higgs bosons of the 2HDM tend to decrease the coupling instead of increasing it. We obtain similar results if we replace the charged Higgs mass with CP-odd neutral Higgs masses.

6.3.3 Complementary constraints

In this section, we combine all the constraints to do a complementary probe in the 2HDM parameter space as in Sec. 6.2.3. The same parameter space is scanned with the implementation of CEPC $S/T/U$ precision measurements. We use current Higgs precision measurements here because the future Higgs precision measurements are still under construction.

The $S/T/U$ precision measurements at the CEPC can greatly help to constrain the parameter space of the 2HDM. Specifically, in the mass plane $m_{H^\pm}$ vs m_H or m_A, the off-diagonal region are highly discarded. Since the Higgs precision measurements can be improved by an order of magnitude at the CEPC over the current measurements, we can imagine how strong it will be to constrain the parameter space of the 2HDM.

The constraints on the angle $\tan\beta$ are much stronger than those in Sec. 6.2.3. The parameter space at the CEPC has more space than the current one for $\tan\beta > 5$. The

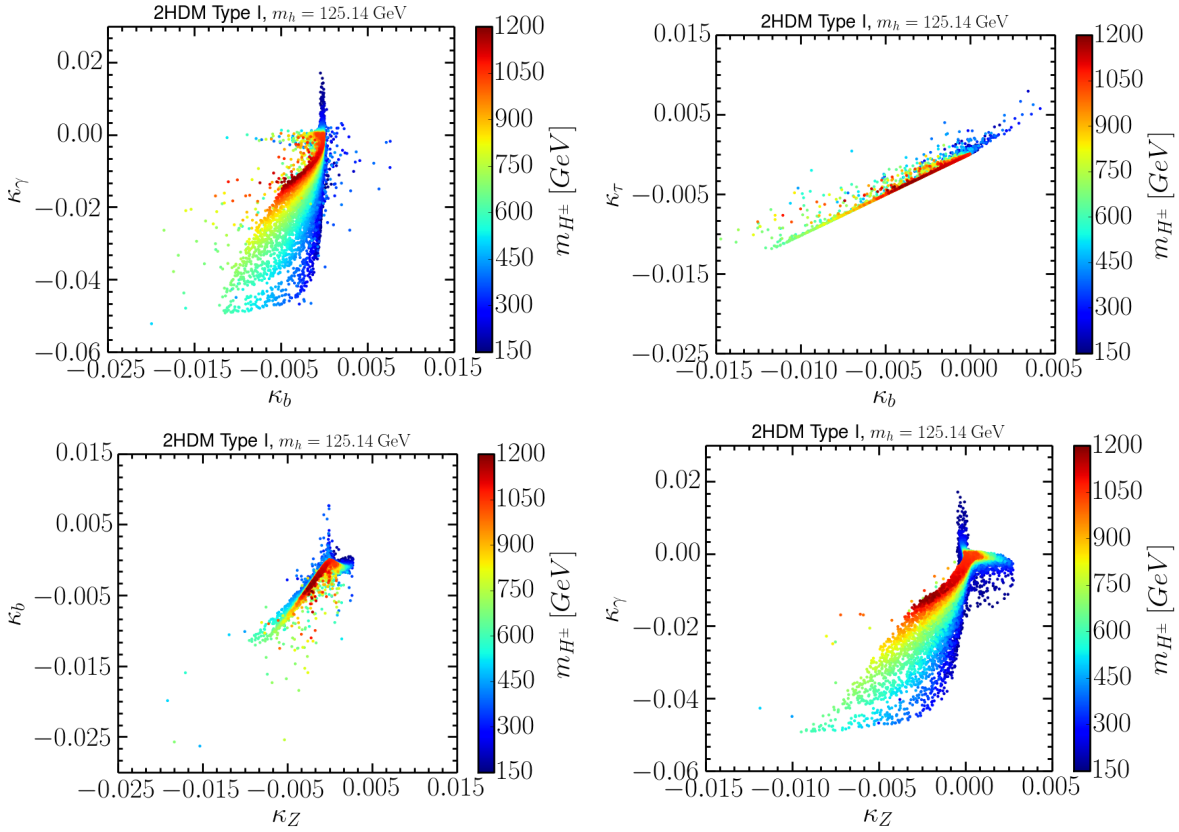

Figure 6.10: The Higgs boson coupling constant deviations κ for hbb, $h\tau\tau$, $h\gamma\gamma$ and hZZ in Type I 2HDM. The color coding is the charged Higgs mass. The data points already survived from the theoretical and CEPC $S/T/U$ constraints.

$\tan\beta$ is even constrained to be less than 3.5 at the CEPC instead of 5 as in the current experiment. The masses of Higgs bosons are required to be larger than ~ 350 GeV in the small $\tan\beta \lesssim 1$ region from the direct experimental search.

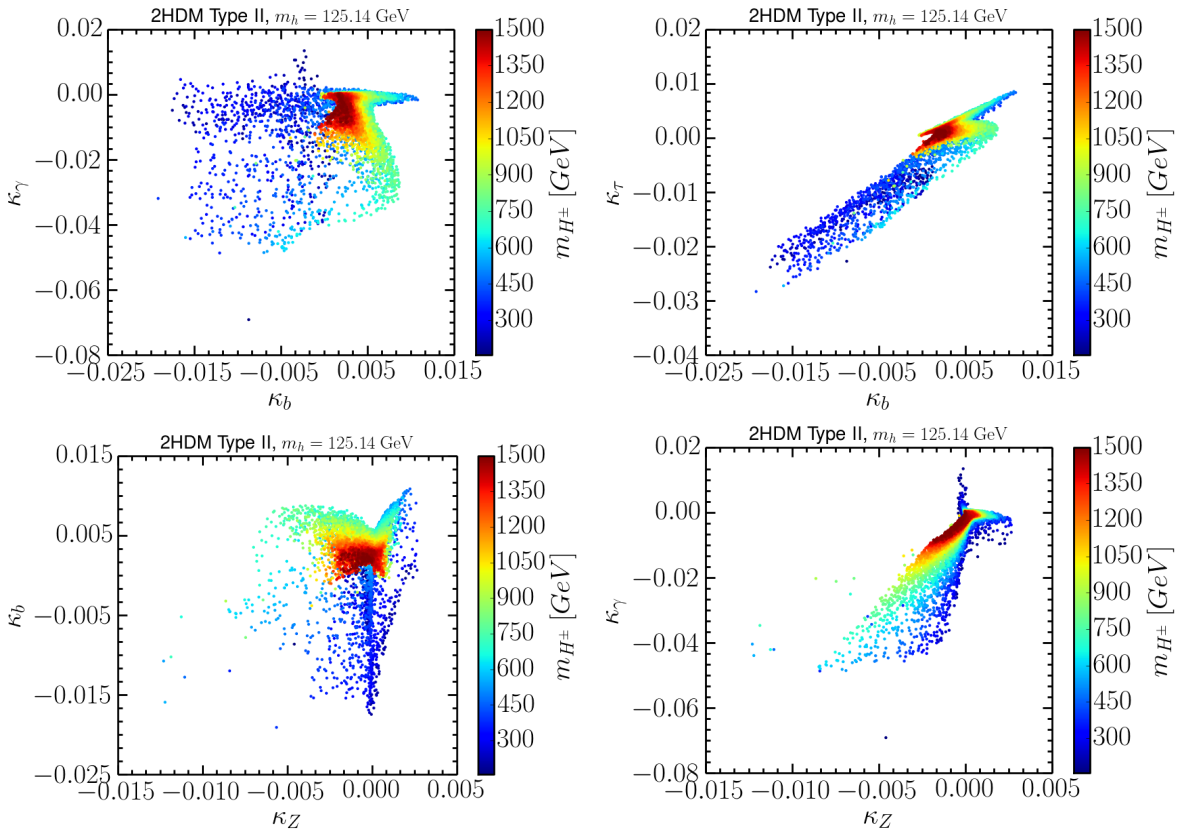

Figure 6.11: The Higgs boson coupling constant deviations κ for hbb, $h\tau\tau$, $h\gamma\gamma$ and hZZ in Type II 2HDM. The color coding is the charged Higgs mass. The data points already survived from the theoretical and CEPC $S/T/U$ constraints.

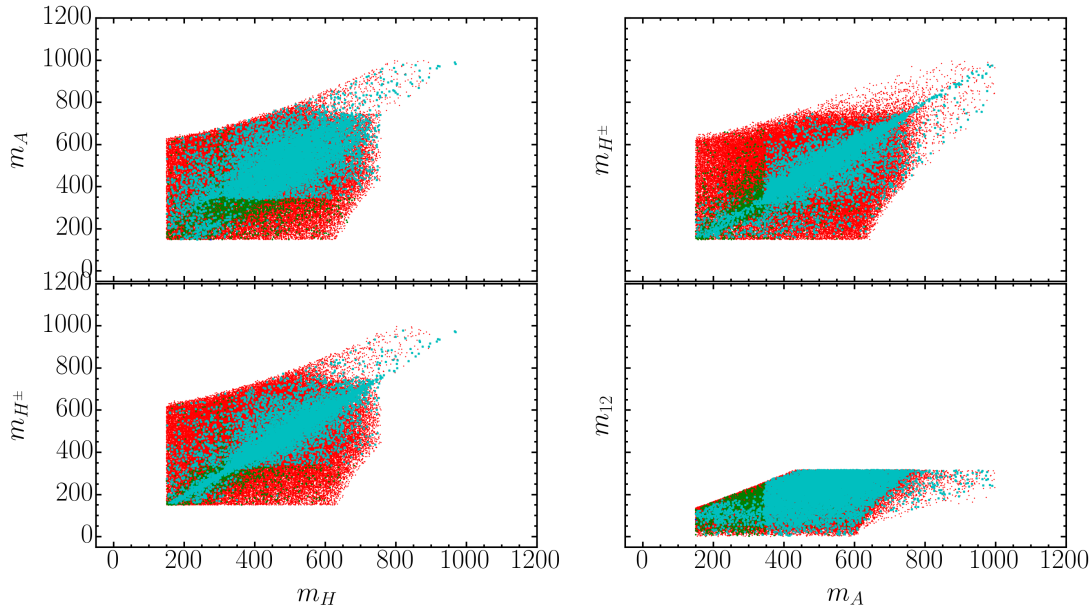

Figure 6.12: The surviving mass regions in the projected mass planes at the CEPC. The red region corresponds to the surviving region after the theoretical constraints. The green region for the Oblique Parameters S, T, U constraints and the blue region for the experimental constraints.

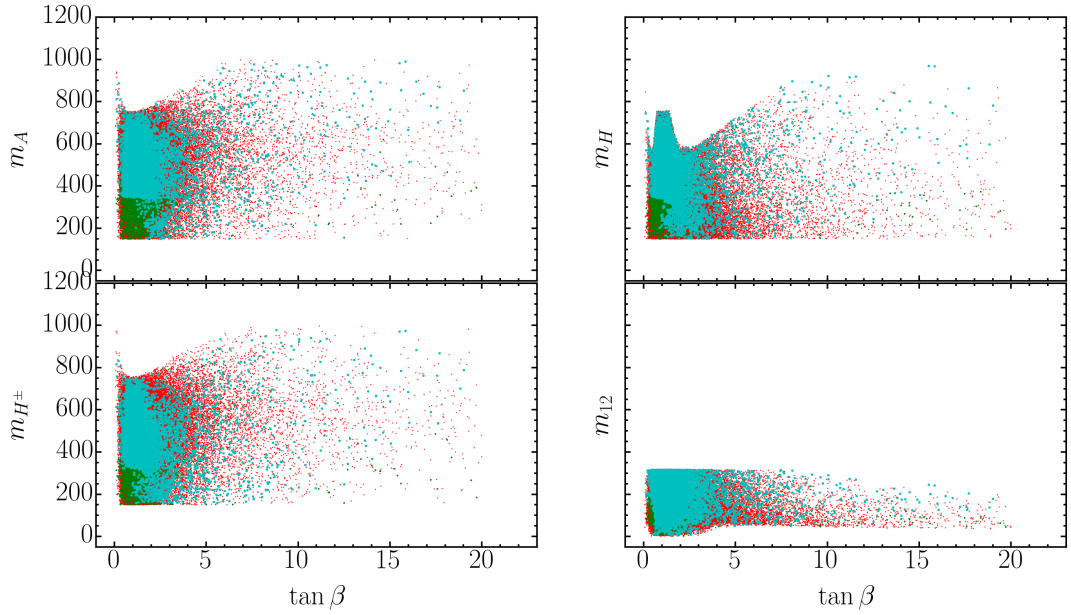

Figure 6.13: The surviving $\tan\beta$-mass regions in the projected mass planes at the CEPC. The color coding is the same as in Figure 6.12.

CHAPTER 7

Conclusion

In this dissertation, we stress that in a realistic situation in a generic MSSM, the stop/sbottom decay can be far from 100% to a specific channel, as assumed in most of the current studies and all the LHC stop/sbottom searches. It is only true for the Bino-LSP and with either the left-handed stop/sbottom being the NLSP, or the right-handed stop/sbottom (or Wino) being the NLSP. On a more general ground, stop/sbottom decays lead to a much richer pattern. The inclusion of the ignored decay channels will significantly weaken the current stop/sbottom search limits and also open new decay modes for alternative discovery channels for stop/sbottom searches.

We studied in detail the stop/sbottom decay patterns and dominant collider signatures in a few representative SUSY mass scenarios. For the left-handed stop/sbottom, we found that:

(1) in the Bino LSP and Wino NLSP case with minimal mixing between the stop sector, $\tilde{t}_1 \to b\chi_1^\pm \sim 70\%$ dominates, with $\tilde{t}_1 \to t\chi_2^0 \sim 30\%$ subdominant for the stop, the sbottom has $\tilde{b}_1 \to t\chi_1^\pm \sim 70\%$ and $\tilde{b}_1 \to b\chi_2^0 \sim 30\%$. The stop/sbottom pair production to the above decay channels lead to final states $bbWWh$ for the parameter $\mu > 0$ and $bbWWZ$ for the parameter $\mu < 0$.

(2) in the Bino LSP and Wino NLSP case with maximal mixing between the stop sector, the $\tilde{t}_1 \to b\chi_1^\pm \sim 63\%$ still dominates, with $\tilde{t}_1 \to t\chi_2^0 \sim 27\%$ subdominant for the stop, while the branching fraction of conventional decay $\tilde{t}_1 \to t\chi_1^0$ increases to about 10%. The maximal mixing leads to the sbottom mass being larger than the stop mass, then the sbottom directly decaying to stop opens and dominates, while the $\tilde{b}_1 \to t\chi_1^\pm$ and $\tilde{b}_1 \to b\chi_2^0$ are suppressed. The stop pair production to the decay channels still lead

to feasible final states $bbWWh/Z$ for a positive/negative μ as in case 1, however, the dominant final states for the sbottom becomes $bbWWWW$.

(3) in the Bino LSP and Higgsino NLSP case with minimal mixing between the stop sector, the stop dominantly decays to $t\chi^0_{2,3}$ at about 50% each, while channels $\tilde{t}_1 \to b\chi^\pm_1$ and $\tilde{t}_1 \to t\chi^0_1$ are highly suppressed, due to the large $SU(2)$ coupling constant over the small $U(1)$ coupling constant. However, the decay channel of sbottom $\tilde{b}_1 \to b\chi^0_{2,3}$ is highly suppressed, and $\tilde{b}_1 \to t\chi^\pm_1 \sim 100\%$ dominates, due to the large top Yukawa coupling constant compared to the bottom Yukawa coupling constant. Then the stop pair production to the decay channels leads to very interesting $bbWWZ/h\ Z/h$ final states and the sbottom pair production to the decay channels lead to $bbWWWW$.

(4) in the Bino LSP and Higgsino NLSP case with maxmal mixing between the stop sector, the decay channel of $\tilde{t}_1 \to b\chi^\pm_1$ increases to be as dominant as $\tilde{t}_1 \to t\chi^0_3 \sim 35\%$ with $\tilde{t}_1 \to t\chi^0_2 \sim 30\%$ being subdominant. For sbottom decay, the channel of $\tilde{b}_1 \to W\tilde{t}_1$ still dominates as in case 3, while $\tilde{b}_1 \to t\chi^\pm_1$ also has an increasing large branching fraction as the sbottom mass increases. The stop pair production to the decay channels lead to two almost equal final states $bbWWZ/h$ and $bbWWZ/h\ Z/h$, while the sbottom pair production gives rise to the dominant final states $bbWWWW$ and $bbWWWWZ/h$.

(5) in mixed NLSP cases for the sbottom case, $\mathrm{BR}(\tilde{b}_1 \to b\chi^0_2) \sim \mathrm{BR}(\tilde{b}_1 \to t\chi^\pm_1) \sim \mathrm{BR}(\tilde{b}_1 \to t\chi^\pm_2) \sim 30\%$ and $\mathrm{BR}(\tilde{b}_1 \to b\chi^0_1) \sim 3\%$ when $|\mu| > M_2$; while $\mathrm{BR}(\tilde{b}_1 \to t\chi^\pm_1) \sim \mathrm{BR}(\tilde{b}_1 \to t\chi^\pm_2) \sim 30\%$ and $\mathrm{BR}(\tilde{b}_1 \to b\chi^0_1) < 10\%$ when $M_2 > |\mu|$.

For the right-handed sbottom case, decays of $\tilde{b}_1 \to b\chi^0_1$ dominate for the case of Bino-LSP with Wino-NLSP. In the case of Bino-LSP with Higgsino-NLSP, however, the branching fraction of $\tilde{b}_1 \to b\chi^0_1$ is reduced to about 40%−60%, while $\tilde{b}_1 \to t\chi^\pm_1$ is about 20−30%, followed by $\tilde{b}_1 \to b\chi^0_{2,3}$ of about 10% each.

We analyzed in detail the stop/sbottom pair production signals with the mixed decay channels. We focused on the search sensitivity at the 14 TeV LHC with a 300 fb^{-1} integrated luminosity. We scanned over a large SUSY mass parameter region and performed

semi-realisc detector simulations. For the left-handed stop/sbottom pair production, we focused on the scenario of Bino LSP with Wino NLSP and Bino LSP with Higgsino NLSP. For the scenario of Bino LSP with Wino NLSP, with one stop (sbottom) decaying via $\tilde{t} \to t\chi_2^0$ ($\tilde{b} \to b\chi_2^0$) and the other stop (sbottom) decaying via $\tilde{t} \to b\chi_1^\pm$ ($\tilde{b} \to t\chi_1^\pm$), we found that

- With $\chi_2^0 \to h\chi_2^0$ ($\mu > 0$) and $\chi_1^\pm \to W^\pm\chi_1^0$, the leading signal is the $bbbb\ jj\ \ell + \not{E}_T$ final state. From Fig. 5.4(a), we see that a 5σ discovery can be made up to 920 GeV, and the 95% C.L exclusion limit can reach 1050 GeV for this Higgs channel. The reach of the combined sbottom and stop signals of the same final states is about 120 GeV higher, as shown in Fig. 5.4(b).

- With $\chi_2^0 \to Z\chi_2^0$ ($\mu < 0$) and $\chi_1^\pm \to W^\pm\chi_1^0$, we studied the reach of the $bb\ jjjj\ \ell\ell + \not{E}_T$ final state. As seen from Fig. 5.6, a 5σ discovery can be made up to 840 GeV, and the 95% C.L exclusion limit can reach up to 900 GeV for the Z channel. The 5σ discovery potential of the combined sbottom and stop signals can reach up to 980 GeV, and the 95% exclusion limit is about 1025 GeV.

In the case of the Bino LSP with Higgsino NLSP, we focused on the stop search sensitivity for the three decay channels of stop pair production in three primary signal regions based on lepton multiplicities. We found that

- In the one lepton signal region, for the channel $t\bar{t}hh\not{E}_T$, stop masses up to 750 GeV can be discovered at the 5σ significance level for $m_{\chi_1^0} = 220$ GeV, and the 95% C.L. exclusion limits are about 950 GeV for $m_{\chi_1^0} = 250$ GeV, assuming 10% systematic uncertainties. The 5σ discovery reach can go up to 900 GeV (840 GeV), or the stop masses up to 1050 GeV (1000 GeV) can be excluded at the 95% C.L for the channel $t\bar{t}hZ\ \not{E}_T$ ($t\bar{t}ZZ\ \not{E}_T$). Limits with 20% systematic uncertainties are about 100 GeV worse. The combined results of the one lepton signal region achieves the best reach sensitivity, a stop mass up to 1030 GeV can be discovered at 5σ significance, or excluded up to 1200 GeV at 95% C.L. if there is no SUSY signal found over the SM backgrounds.

- In the two OS leptons signal region, there is no reach for the $t\bar{t}hh\not{E}_T$ channel due to the very low branching fraction and the large SM backgrounds. Stop masses up to 800 GeV (920 GeV) can be discovered at 5σ significance, or stop masses up to 900 GeV (1000 GeV) can be excluded at 95% C.L. if there is no SUSY signal found over SM backgrounds for the channel $t\bar{t}hZ\not{E}_T$ ($t\bar{t}ZZ\not{E}_T$). Limits with 20% systematic uncertainties are very similar to that of 10% case. The combined results of channels $t\bar{t}hZ\not{E}_T$ and $t\bar{t}ZZ\not{E}_T$ show that a stop mass up to 930 GeV for $m_{\chi_1^0} \sim 120$ GeV can be discovered, or a stop mass between 370 GeV and 1060 GeV is excluded at the 95% C.L. for the two OS leptons signal region.

- In the at-least-three leptons signal region, again there is no reach for the $t\bar{t}hh\not{E}_T$ channel due to the very low branching fraction of at least three leptons and large SM backgrounds. In the "on-Z" signal region, stop masses up to 800 GeV (850 GeV) for the channel $t\bar{t}hZ\not{E}_T$ ($t\bar{t}ZZ\not{E}_T$) can be discovered at the 5σ significance, assuming 10% systematic uncertainties. The 95% C.L. exclusion limits reach about 880 GeV (1000 GeV) for the channel $t\bar{t}hZ\not{E}_T$ ($t\bar{t}ZZ\not{E}_T$) if there is no SUSY signal over SM backgrounds. Limits with 20% systematic uncertainties are pretty much the same. The reach for the "off-Z" signa region is much much smaller than that of the "on-Z" signal region because both channels $t\bar{t}hZ\not{E}_T$ and $t\bar{t}ZZ\not{E}_T$ have small branching fractions for the off-Z signal region. The combined results of channels $t\bar{t}hZ\not{E}_T$ and $t\bar{t}ZZ\not{E}_T$ show that the 5σ reach of a stop mass can go to 880 GeV for the small LSP mass, and the 95% C.L. exclusion limit can reach to 1000 GeV for a broad LSP mass region, for the at-least-three leptons "on-Z" signal region.

We also performed a compact collider analysis of the future $\sqrt{s} = 100$ TeV machine with 3000 fb^{-1} integrated luminosity. The large parameter space of the SUSY model is covered, which is critical to understand the TeV scale SUSY and the origin of electroweak breaking. We find that the stop can be discovered up to 6 TeV at 5σ significance level, or excluded up to 6.8 TeV at 95% C.L. if there is still no SUSY signal over SM backgrounds being found for the combined reach of all three channels.

Although we only consider one very interesting scenario of the MSSM parameter space,

it is important to identify all the leading decay channels in various regions of the parameter space to fully explore the reach of the LHC for the third generation squarks. It has important implications for the stabilization of the electroweak scale in supersymmetric models. The strategy developed in our analysis can be applied to the study of the top partners in other new physics scenarios as well.

In this work, we also study the indirect probe for new physics through Z-pole and Higgs precision measurements. The Higgs couplings are calculated in detail including radiative corrections at the one loop level for the future collider. The Higgs couplings deviation from the SM predictions occurs due to two sources: the tree level scale factor shown in Table 3.3, and the radiative corrections at loop level from the extra Higgs bosons which is shown in Figures 6.2 and 6.1.

The S, T, U is not that sensitive to the rotation angle $\beta - \alpha$, while the Higgs precision measurements set strong constrains on the angle $\beta - \alpha$. Therefore, we mainly focus on the alignment limit ($\beta - \alpha = \pi/2$), in which the Higgs couplings recover the Standard Model predictions. Applying the $S/T/U$, the allowed mass regions behave the same for different $m_{H^\pm}$ or m_A values in the alignment limit ($\beta - \alpha = \pi/2$): the charged Higgs mass tend to align to either the CP-odd Higgs mass or the CP-even Higgs mass. As the angle $\beta - \alpha$ deviates from the alignment limit, the charged Higgs mass can deviate away from the two neutral Higgs masses and the mass region is split into two parts for large Higgs masses. Imagine that $m_{H^\pm}$ is continuous instead of being fixed to some certain values in the plane of m_A vs m_H, then the surviving mass region after the $S/T/U$ cut is still very large. The constraints from current experimental direct search is not strong due to the comparably low precision measurements of the Higgs decay branching fractions.

The combination of the Z-pole and Higgs precision measurements complementarily set constraints on the 2HDM parameter space. The experimental search does not set strong constraints on the Higgs masses. In the plane of m_A vs m_H, the region of $m_H > 350$ GeV and $m_A < 300$ GeV are excluded at 95% C.L. level. In the plane of $m_{H^\pm}$ vs m_A, the mass region within $m_{H^\pm} > 250$ GeV and $m_A < 300$ GeV are excluded at 95% C.L. level. The constraints on the angle $\tan\beta$ are much stronger. There are only very sparse points for $\tan\beta > 5$, indicating that the parameter space for $\tan\beta > 5$ is highly constrained. The

masses of Higgs bosons are required to be larger than ~ 350 GeV in the small $\tan\beta \lesssim 1$ region from the direct experimental search.

The Higgs coupling constants can only be measured at $\sim 10\%$ precision level at the $\sqrt{s} = 14$ TeV LHC with 300 fb^{-1} integrated luminosity, therefore the future circular e^+e^- colliders are critical to study Higgs physics and probe new physics beyond the Standard Model. The Higgs decay branching fractions can be precisely measured at the CEPC. The deviation of $g(hZZ)$ from the Standard Model Higgs coupling constant can achieve sub-percent precision level. The Z-pole precision measurements can also be greatly improved.

REFERENCES

[1] G. Aad et al. (ATLAS Collaboration), Phys.Lett. **B716**, 1 (2012), 1207.7214.

[2] S. Chatrchyan et al. (CMS Collaboration), Phys.Lett. **B716**, 30 (2012), 1207.7235.

[3] The LEP Collaborations: (ALEPH Collaboration, DELPHI Collaboration, L3 Collaboration, OPAL Collaboration, LEP Electroweak Working Group) (2005), hep-ex/0511027.

[4] S. Schael et al. (ALEPH Collaboration, DELPHI Collaboration, L3 Collaboration, OPAL Collaboration, SLD Collaboration, LEP Electroweak Working Group, SLD Electroweak Group, SLD Heavy Flavour Group), Phys.Rept. **427**, 257 (2006), hep-ex/0509008.

[5] G. Aad et al. (ATLAS, CDF, CMS, D0) (2014), 1403.4427.

[6] D. Hanneke, S. Fogwell Hoogerheide, and G. Gabrielse, Phys.Rev. **A83** (2011), 1009.4831.

[7] G. Aad et al. (ATLAS), Phys. Rev. **D90**, 052004 (2014), 1406.3827.

[8] G. Aad et al. (ATLAS), Eur. Phys. J. **C76**, 6 (2016), 1507.04548.

[9] V. Khachatryan et al. (CMS), Eur. Phys. J. **C75**, 212 (2015), 1412.8662.

[10] S. Weinberg, Phys.Rev. **D13**, 974 (1976).

[11] B. T. Cleveland, T. Daily, R. Davis, Jr., J. R. Distel, K. Lande, C. K. Lee, P. S. Wildenhain, and J. Ullman, Astrophys. J. **496**, 505 (1998).

[12] Y. Fukuda et al. (Kamiokande), Phys. Rev. Lett. **77**, 1683 (1996).

[13] J. N. Abdurashitov et al. (SAGE), Phys. Rev. **C80**, 015807 (2009), 0901.2200.

[14] P. Anselmann et al. (GALLEX), Phys. Lett. **B285**, 376 (1992).

[15] W. Hampel et al. (GALLEX), Phys. Lett. **B447**, 127 (1999).

[16] M. Altmann et al. (GNO), Phys. Lett. **B616**, 174 (2005), hep-ex/0504037.

[17] S. Fukuda et al. (Super-Kamiokande), Phys. Lett. **B539**, 179 (2002), hep-ex/0205075.

[18] Q. R. Ahmad et al. (SNO), Phys. Rev. Lett. **87**, 071301 (2001), nucl-ex/0106015.

[19] Q. R. Ahmad et al. (SNO), Phys. Rev. Lett. **89**, 011301 (2002), nucl-ex/0204008.

[20] K. Eguchi et al. (KamLAND), Phys. Rev. Lett. **90**, 021802 (2003), hep-ex/0212021.

[21] T. Araki et al. (KamLAND), Phys. Rev. Lett. **94**, 081801 (2005), hep-ex/0406035.

[22] Y. Fukuda et al. (Super-Kamiokande), Phys. Rev. Lett. **81**, 1562 (1998), hep-ex/9807003.

[23] Y. Ashie et al. (Super-Kamiokande), Phys. Rev. Lett. **93**, 101801 (2004), hep-ex/0404034.

[24] V. Barger, P. Huang, M. Ishida, and W.-Y. Keung, Phys.Lett. **B718**, 1024 (2013), 1206.1777.

[25] S. P. Martin, Adv.Ser.Direct.High Energy Phys. **21**, 1 (2010), hep-ph/9709356.

[26] D. J. H. Chung, L. L. Everett, G. L. Kane, S. F. King, J. D. Lykken, and L.-T. Wang, Phys. Rept. **407**, 1 (2005), hep-ph/0312378.

[27] M. Carena, S. Heinemeyer, C. E. M. Wagner, and G. Weiglein, Eur. Phys. J. **C45**, 797 (2006), hep-ph/0511023.

[28] M. E. Peskin and T. Takeuchi, Phys. Rev. Lett. **65**, 964 (1990).

[29] M. E. Peskin and T. Takeuchi, Phys. Rev. **D46**, 381 (1992).

[30] W. J. Marciano and J. L. Rosner, Phys. Rev. Lett. **65**, 2963 (1990), URL http://link.aps.org/doi/10.1103/PhysRevLett.65.2963.

[31] D. C. Kennedy and P. Langacker, Phys. Rev. Lett. **65**, 2967 (1990), URL http://link.aps.org/doi/10.1103/PhysRevLett.65.2967.

[32] D. C. Kennedy and P. Langacker, Phys. Rev. D **44**, 1591 (1991), URL http://link.aps.org/doi/10.1103/PhysRevD.44.1591.

[33] K. A. Olive et al. (Particle Data Group), Chin. Phys. **C38**, 090001 (2014).

[34] P. W. Higgs, Phys.Lett. **12**, 132 (1964).

[35] P. W. Higgs, Phys.Rev.Lett. **13**, 508 (1964).

[36] F. Englert and R. Brout, Phys.Rev.Lett. **13**, 321 (1964).

[37] T. Kibble, Phys.Rev. **155**, 1554 (1967).

[38] S. Glashow, Nucl.Phys. **22**, 579 (1961).

[39] S. Weinberg, Phys.Rev.Lett. **19**, 1264 (1967).

[40] A. Salam, Conf.Proc. **C680519**, 367 (1968).

[41] J. Goldstone, Nuovo Cim. **19**, 154 (1961).

[42] N. Cabibbo, Phys. Rev. Lett. **10**, 531 (1963), URL `http://link.aps.org/doi/10.1103/PhysRevLett.10.531`.

[43] M. Kobayashi and T. Maskawa, Progress of Theoretical Physics **49**, 652 (1973).

[44] F. J. Hasert et al. (Gargamelle Neutrino), Phys. Lett. **B46**, 138 (1973).

[45] G. Arnison et al. (UA1), Phys. Lett. **B122**, 103 (1983), [,611(1983)].

[46] M. Banner et al. (UA2), Phys. Lett. **B122**, 476 (1983).

[47] F. Abe et al. (CDF), Phys. Rev. Lett. **74**, 2626 (1995), `hep-ex/9503002`.

[48] B. P. Schmidt, N. B. Suntzeff, M. M. Phillips, R. A. Schommer, A. Clocchiatti, R. P. Kirshner, P. Garnavich, P. Challis, B. Leibundgut, J. Spyromilio, et al., APJ **507**, 46 (1998), `astro-ph/9805200`.

[49] S. Perlmutter, S. Gabi, G. Goldhaber, A. Goobar, D. E. Groom, I. M. Hook, A. G. Kim, M. Y. Kim, J. C. Lee, R. Pain, et al., APJ **483**, 565 (1997), `astro-ph/9608192`.

[50] K. G. Begeman, A. H. Broeils, and R. H. Sanders, MNRAS **249**, 523 (1991).

[51] H. Hoekstra, H. Yee, and M. Gladders, New Astron. Rev. **46**, 767 (2002), `astro-ph/0205205`.

[52] M. Mateo, Ann. Rev. Astron. Astrophys. **36**, 435 (1998), `astro-ph/9810070`.

[53] J. Beringer et al. (Particle Data Group), Phys.Rev. **D86**, 010001 (2012).

[54] G. Bertone, D. Hooper, and J. Silk, Phys.Rept. **405**, 279 (2005), `hep-ph/0404175`.

[55] N. Arkani-Hamed, A. G. Cohen, and H. Georgi, Phys. Lett. **B513**, 232 (2001), `hep-ph/0105239`.

[56] N. Arkani-Hamed, A. G. Cohen, T. Gregoire, and J. G. Wacker, JHEP **08**, 020 (2002), `hep-ph/0202089`.

[57] N. Arkani-Hamed, A. G. Cohen, E. Katz, and A. E. Nelson, JHEP **07**, 034 (2002), `hep-ph/0206021`.

[58] N. Arkani-Hamed, A. G. Cohen, E. Katz, A. E. Nelson, T. Gregoire, and J. G. Wacker, JHEP **08**, 021 (2002), hep-ph/0206020.

[59] A. Birkedal-Hansen and J. G. Wacker, Phys. Rev. **D69**, 065022 (2004), hep-ph/0306161.

[60] K. Agashe and G. Servant, Phys. Rev. Lett. **93**, 231805 (2004), hep-ph/0403143.

[61] C. Boehm, T. A. Ensslin, and J. Silk, J. Phys. **G30**, 279 (2004), astro-ph/0208458.

[62] C. Boehm and P. Fayet, Nucl. Phys. **B683**, 219 (2004), hep-ph/0305261.

[63] D. J. Gross and F. Wilczek, Phys. Rev. Lett. **30**, 1343 (1973), URL http://link.aps.org/doi/10.1103/PhysRevLett.30.1343.

[64] H. D. Politzer, Phys. Rev. Lett. **30**, 1346 (1973), URL http://link.aps.org/doi/10.1103/PhysRevLett.30.1346.

[65] M. E. Machacek and M. T. Vaughn, Nucl. Phys. **B249**, 70 (1985).

[66] D. J. Castano, E. J. Piard, and P. Ramond, Phys. Rev. **D49**, 4882 (1994), hep-ph/9308335.

[67] G. C. Branco, P. M. Ferreira, L. Lavoura, M. N. Rebelo, M. Sher, and J. P. Silva, Phys. Rept. **516**, 1 (2012), 1106.0034.

[68] G. F. Giudice and R. Rattazzi, Phys. Rept. **322**, 419 (1999), hep-ph/9801271.

[69] L. Randall and R. Sundrum, Nucl. Phys. **B557**, 79 (1999), hep-th/9810155.

[70] G. F. Giudice, M. A. Luty, H. Murayama, and R. Rattazzi, JHEP **12**, 027 (1998), hep-ph/9810442.

[71] T. Gherghetta, G. F. Giudice, and J. D. Wells, Nucl. Phys. **B559**, 27 (1999), hep-ph/9904378.

[72] A. B. Lahanas and D. V. Nanopoulos, Phys. Rept. **145**, 1 (1987).

[73] S. Dimopoulos and D. W. Sutter, Nucl. Phys. **B452**, 496 (1995), hep-ph/9504415.

[74] H. Nishino et al. (Super-Kamiokande Collaboration), Phys.Rev.Lett. **102**, 141801 (2009), 0903.0676.

[75] G. R. Farrar and P. Fayet, Phys.Lett. **B76**, 575 (1978).

[76] I. J. R. Aitchison (2005), hep-ph/0505105.

[77] D. Pierce and A. Papadopoulos, Phys. Rev. **D50**, 565 (1994), hep-ph/9312248.

[78] D. Pierce and A. Papadopoulos, Nucl. Phys. **B430**, 278 (1994), hep-ph/9403240.

[79] D. M. Pierce, J. A. Bagger, K. T. Matchev, and R.-j. Zhang, Nucl. Phys. **B491**, 3 (1997), hep-ph/9606211.

[80] M. S. Carena, J. Espinosa, M. Quiros, and C. Wagner, Phys.Lett. **B355**, 209 (1995), hep-ph/9504316.

[81] M. Carena, M. Quiros, and C. E. M. Wagner, Nucl. Phys. **B461**, 407 (1996), hep-ph/9508343.

[82] A. Zee, Phys. Lett. **B93**, 389 (1980), [Erratum: Phys. Lett.B95,461(1980)].

[83] E. Ma, Phys. Rev. Lett. **86**, 2502 (2001), hep-ph/0011121.

[84] E. Ma, Phys. Rev. **D73**, 077301 (2006), hep-ph/0601225.

[85] M. Aoki, S. Kanemura, and O. Seto, Phys. Rev. Lett. **102**, 051805 (2009), 0807.0361.

[86] Y. Kajiyama, H. Okada, and K. Yagyu, JHEP **10**, 196 (2013), 1307.0480.

[87] M. Hashimoto and S. Kanemura, Phys. Rev. **D70**, 055006 (2004), [Erratum: Phys. Rev.D70,119901(2004)], hep-ph/0403005.

[88] H. E. Haber and R. Hempfling, Phys. Rev. **D48**, 4280 (1993), hep-ph/9307201.

[89] J. F. Gunion and H. E. Haber, Phys. Rev. **D67**, 075019 (2003), hep-ph/0207010.

[90] I. F. Ginzburg and M. Krawczyk, Phys. Rev. **D72**, 115013 (2005), hep-ph/0408011.

[91] B. McWilliams and L.-F. Li, Nucl. Phys. **B179**, 62 (1981).

[92] O. U. Shanker, Nucl. Phys. **B206**, 253 (1982).

[93] S. L. Glashow and S. Weinberg, Phys. Rev. **D15**, 1958 (1977).

[94] E. A. Paschos, Phys. Rev. D **15**, 1966 (1977), URL http://link.aps.org/doi/10.1103/PhysRevD.15.1966.

[95] H. E. Haber, in *Theoretical Advanced Study Institute (TASI 92): From Black Holes and Strings to Particles Boulder, Colorado, June 3-28, 1992* (1993), hep-ph/9306207.

[96] N. G. Deshpande and E. Ma, Phys. Rev. **D18**, 2574 (1978).

[97] M. Sher, Phys. Rept. **179**, 273 (1989).

[98] H. Huffel and G. Pocsik, Z. Phys. **C8**, 13 (1981).

[99] J. Maalampi, J. Sirkka, and I. Vilja, Phys. Lett. **B265**, 371 (1991).

[100] S. Kanemura, T. Kubota, and E. Takasugi, Phys. Lett. **B313**, 155 (1993), hep-ph/9303263.

[101] A. G. Akeroyd, A. Arhrib, and E.-M. Naimi, Phys. Lett. **B490**, 119 (2000), hep-ph/0006035.

[102] I. F. Ginzburg and I. P. Ivanov, Phys. Rev. **D72**, 115010 (2005), hep-ph/0508020.

[103] G. Abbiendi et al. (LEP, DELPHI, OPAL, ALEPH, L3), Eur. Phys. J. **C73**, 2463 (2013), 1301.6065.

[104] S. Schael et al. (DELPHI, OPAL, ALEPH, LEP Working Group for Higgs Boson Searches, L3), Eur. Phys. J. **C47**, 547 (2006), hep-ex/0602042.

[105] G. A. et al (ATLAS Collaboration), Tech. Rep. ATLAS-CONF-2013-013, CERN, Geneva (2013), URL http://cds.cern.ch/record/1523699.

[106] G. Aad et al. (ATLAS), Phys. Rev. **D92**, 012006 (2015), 1412.2641.

[107] V. Khachatryan et al. (CMS), JHEP **10**, 144 (2015), 1504.00936.

[108] G. Aad et al. (ATLAS), Phys. Rev. Lett. **114**, 081802 (2015), 1406.5053.

[109] V. Khachatryan et al. (CMS Collaboration), Tech. Rep. CMS-PAS-HIG-13-032, CERN, Geneva (2014), URL https://cds.cern.ch/record/1697512.

[110] V. Khachatryan et al. (CMS), Phys. Lett. **B749**, 560 (2015), 1503.04114.

[111] G. Aad et al. (ATLAS), Phys. Lett. **B744**, 163 (2015), 1502.04478.

[112] V. Khachatryan et al. (CMS), Phys. Lett. **B748**, 221 (2015), 1504.04710.

[113] G. Aad et al. (ATLAS), JHEP **03**, 088 (2015), 1412.6663.

[114] V. Khachatryan et al. (CMS), JHEP **11**, 018 (2015), 1508.07774.

[115] M. Misiak et al., Phys. Rev. Lett. **114**, 221801 (2015), 1503.01789.

[116] H.-J. He, N. Polonsky, and S.-f. Su, Phys. Rev. **D64**, 053004 (2001), hep-ph/0102144.

[117] M. Papucci, J. T. Ruderman, and A. Weiler, JHEP **1209**, 035 (2012), 1110.6926.

[118] A. Djouadi, M. Muhlleitner, and M. Spira, Acta Phys.Polon. **B38**, 635 (2007), hep-ph/0609292.

[119] W. Beenakker, S. Brensing, M. Kramer, A. Kulesza, E. Laenen, et al., JHEP **1008**, 098 (2010), 1006.4771.

[120] A. Broggio, A. Ferroglia, M. Neubert, L. Vernazza, and L. L. Yang, JHEP **1307**, 042 (2013), 1304.2411.

[121] C. Borschensky, M. Krmer, A. Kulesza, M. Mangano, S. Padhi, T. Plehn, and X. Portell, Eur. Phys. J. **C74**, 3174 (2014), 1407.5066.

[122] T. Han, S. Padhi, and S. Su, Phys.Rev. **D88**, 115010 (2013), 1309.5966.

[123] D. Ghosh, Phys.Rev. **D88**, 115013 (2013), 1308.0320.

[124] J. Eckel, S. Su, and H. Zhang, JHEP **07**, 075 (2015), 1411.1061.

[125] J. Callan, Curtis G., Phys.Rev. **D2**, 1541 (1970).

[126] K. Symanzik, Communications in Mathematical Physics **18**, 227 (1970), ISSN 1432-0916, URL http://dx.doi.org/10.1007/BF01649434.

[127] G. Aad et al., Tech. Rep. CERN-LHCC-2011-012. LHCC-I-020, CERN, Geneva (2011).

[128] G. Aad et al. (ATLAS Collaboration), JINST **3**, S08003 (2008).

[129] S. Chatrchyan et al. (CMS Collaboration), JINST **3**, S08004 (2008).

[130] A. Belyaev, N. D. Christensen, and A. Pukhov, Comput.Phys.Commun. **184**, 1729 (2013), 1207.6082.

[131] J. Alwall, R. Frederix, S. Frixione, V. Hirschi, F. Maltoni, et al., JHEP **1407**, 079 (2014), 1405.0301.

[132] T. Sjostrand, S. Mrenna, and P. Z. Skands, JHEP **0605**, 026 (2006), hep-ph/0603175.

[133] *PGS – Pretty Good Simulator*, http://www.physics.ucdavis.edu/~conway/research/software/pgs/pgs4-general.htm .

[134] J. de Favereau et al. (DELPHES 3), JHEP **1402**, 057 (2014), 1307.6346.

[135] G. Aad et al. (ATLAS Collaboration), JHEP **1409**, 015 (2014), 1406.1122.

[136] G. Aad et al. (ATLAS Collaboration), Tech. Rep. CERN-PH-EP-2014-143, CERN, Geneva (2014), 1407.0583.

[137] G. Aad et al. (ATLAS Collaboration), JHEP **1406**, 124 (2014), 1403.4853.

[138] V. Khachatryan et al. (CMS Collaboration), Tech. Rep. CMS-PAS-SUS-13-015, CERN, Geneva (2013).

[139] V. Khachatryan et al. (CMS Collaboration), Tech. Rep. CMS-PAS-SUS-14-011, CERN, Geneva (2014).

[140] S. Chatrchyan et al. (CMS Collaboration), Eur.Phys.J. **C73**, 2677 (2013), 1308.1586.

[141] G. Aad et al. (ATLAS), Phys.Rev. **D90**, 052008 (2014), 1407.0608.

[142] V. Khachatryan et al. (CMS Collaboration), Tech. Rep. CMS-PAS-SUS-13-009, CERN, Geneva (2014).

[143] G. Aad et al. (ATLAS Collaboration), Eur.Phys.J. **C74**, 2883 (2014), 1403.5222.

[144] V. Khachatryan et al. (CMS Collaboration), Phys.Lett. **B736**, 371 (2014), 1405.3886.

[145] V. Khachatryan et al. (CMS Collaboration), Tech. Rep. CMS-PAS-SUS-13-021, CERN, Geneva (2013).

[146] S. Chatrchyan et al. (CMS Collaboration), Phys.Rev.Lett. **112**, 161802 (2014), 1312.3310.

[147] G. Aad et al. (ATLAS), JHEP **1310**, 189 (2013), 1308.2631.

[148] C. Collaboration (CMS Collaboration), Tech. Rep. CMS-PAS-SUS-13-018, CERN, Geneva (2014).

[149] G. Aad et al. (ATLAS), JHEP **1410**, 24 (2014), 1407.0600.

[150] S. Chatrchyan et al. (CMS Collaboration), Tech. Rep. CMS-PAS-SUS-13-008, CERN, Geneva (2013).

[151] G. Aad et al. (ATLAS Collaboration), JHEP **1406**, 035 (2014), 1404.2500.

[152] S. Chatrchyan et al. (CMS), JHEP **1401**, 163 (2014), 1311.6736.

[153] S. Chatrchyan et al. (CMS), Phys.Rev. **D90**, 032006 (2014), 1404.5801.

[154] G. Aad et al., Tech. Rep. ATL-PHYS-PUB-2013-011, CERN, Geneva (2013).

[155] G. Aad et al., Tech. Rep. ATL-PHYS-PUB-2014-010, CERN, Geneva (2014).

[156] C. Collaboration (CMS Collaboration), Tech. Rep. CMS-PAS-SUS-14-012, CERN, Geneva (2015).

[157] R. Grober, M. Muhlleitner, E. Popenda, and A. Wlotzka (2014), 1408.4662.

[158] P. Agrawal and C. Frugiuele, JHEP **1401**, 115 (2014), 1304.3068.

[159] M. Muhlleitner and E. Popenda, JHEP **1104**, 095 (2011), 1102.5712.

[160] J. Aebischer, A. Crivellin, and C. Greub (2014), 1410.8459.

[161] C. Boehm, A. Djouadi, and Y. Mambrini, Phys.Rev. **D61**, 095006 (2000), hep-ph/9907428.

[162] A. Delgado, G. F. Giudice, G. Isidori, M. Pierini, and A. Strumia, Eur.Phys.J. **C73**, 2370 (2013), 1212.6847.

[163] K. Rolbiecki and K. Sakurai, JHEP **1309**, 004 (2013), 1303.5696.

[164] D. Curtin, P. Meade, and P.-J. Tien (2014), 1406.0848.

[165] J. S. Kim, K. Rolbiecki, K. Sakurai, and J. Tattersall (2014), 1406.0858.

[166] M. Czakon, A. Mitov, M. Papucci, J. T. Ruderman, and A. Weiler (2014), 1407.1043.

[167] D. Berenstein, T. Liu, and E. Perkins, Phys.Rev. **D87**, 115004 (2013), 1211.4288.

[168] E. Alvarez and Y. Bai, JHEP **1208**, 003 (2012), 1204.5182.

[169] M. L. Graesser and J. Shelton, Phys. Rev. Lett. **111**, 121802 (2013), 1212.4495.

[170] J. F. Gunion and H. E. Haber, Physical Review D **37**, 2515 (1988).

[171] S. Jung, JHEP **06**, 111 (2014), 1404.2691.

[172] J. Anderson, A. Avetisyan, R. Brock, S. Chekanov, T. Cohen, et al. (2013), 1309.1057.

[173] M. Cacciari, S. Frixione, M. L. Mangano, P. Nason, and G. Ridolfi, JHEP **0809**, 127 (2008), 0804.2800.

[174] A. Bredenstein, A. Denner, S. Dittmaier, and S. Pozzorini, Phys.Rev.Lett. **103**, 012002 (2009), 0905.0110.

[175] W. Beenakker, S. Dittmaier, M. Kramer, B. Plumper, M. Spira, et al., Nucl.Phys. **B653**, 151 (2003), hep-ph/0211352.

[176] J. M. Campbell and R. K. Ellis, JHEP **1207**, 052 (2012), 1204.5678.

[177] A. Lazopoulos, T. McElmurry, K. Melnikov, and F. Petriello, Phys.Lett. **B666**, 62 (2008), 0804.2220.

[178] A. Broggio, A. Ferroglia, M. Neubert, L. Vernazza, and L. L. Yang, JHEP **1307**, 042 (2013), 1304.2411.

[179] W. Beenakker, S. Brensing, M. Kramer, A. Kulesza, E. Laenen, et al., JHEP **1008**, 098 (2010), 1006.4771.

[180] M. Cacciari, S. Frixione, M. L. Mangano, P. Nason, and G. Ridolfi, JHEP **0809**, 127 (2008), 0804.2800.

[181] A. Bredenstein, A. Denner, S. Dittmaier, and S. Pozzorini, Phys.Rev.Lett. **103**, 012002 (2009), 0905.0110.

[182] A. Lazopoulos, T. McElmurry, K. Melnikov, and F. Petriello, Phys.Lett. **B666**, 62 (2008), 0804.2220.

[183] W. Beenakker, S. Dittmaier, M. Kramer, B. Plumper, M. Spira, et al., Nucl.Phys. **B653**, 151 (2003), hep-ph/0211352.

[184] J. M. Campbell and R. K. Ellis, JHEP **1207**, 052 (2012), 1204.5678.

[185] C. Lester and D. Summers, Phys.Lett. **B463**, 99 (1999), hep-ph/9906349.

[186] A. Barr, C. Lester, and P. Stephens, J.Phys. **G29**, 2343 (2003), hep-ph/0304226.

[187] H.-C. Cheng and Z. Han, JHEP **0812**, 063 (2008), 0810.5178.

[188] A. Avetisyan, J. M. Campbell, T. Cohen, N. Dhingra, J. Hirschauer, et al. (2013), 1308.1636.

[189] T. Junk, Nucl. Instrum. Meth. **A434**, 435 (1999), hep-ex/9902006.

[190] T. Cohen, R. T. D'Agnolo, M. Hance, H. K. Lou, and J. G. Wacker, JHEP **11**, 021 (2014), 1406.4512.

[191] M. L. Mangano, M. Moretti, F. Piccinini, and M. Treccani, JHEP **01**, 013 (2007), hep-ph/0611129.

[192] M. Cacciari, G. P. Salam, and G. Soyez, JHEP **04**, 063 (2008), 0802.1189.

[193] M. E. Peskin (2012), 1207.2516.

[194] D. M. Asner et al., in *Community Summer Study 2013: Snowmass on the Mississippi (CSS2013) Minneapolis, MN, USA, July 29-August 6, 2013* (2013), 1310.0763, URL https://inspirehep.net/record/1256491/files/arXiv:1310.0763.pdf.

[195] H. Baer, T. Barklow, K. Fujii, Y. Gao, A. Hoang, S. Kanemura, J. List, H. E. Logan, A. Nomerotski, M. Perelstein, et al. (2013), 1306.6352.

[196] C.-S. S. Group (2015).

[197] U. Baur, T. Plehn, and D. L. Rainwater, Phys. Rev. Lett. **89**, 151801 (2002), hep-ph/0206024.

[198] U. Baur, T. Plehn, and D. L. Rainwater, Phys. Rev. **D68**, 033001 (2003), hep-ph/0304015.

[199] F. Boudjema and A. Semenov, Phys. Rev. **D66**, 095007 (2002), hep-ph/0201219.

[200] M. N. Dubinin and A. V. Semenov, Eur. Phys. J. **C28**, 223 (2003), hep-ph/0206205.

[201] A. Dobado, M. J. Herrero, W. Hollik, and S. Penaranda, Phys. Rev. **D66**, 095016 (2002), hep-ph/0208014.

[202] V. Barger, T. Han, P. Langacker, B. McElrath, and P. Zerwas, Phys. Rev. **D67**, 115001 (2003), hep-ph/0301097.

[203] S. Kanemura, M. Kikuchi, and K. Yagyu, Phys. Lett. **B731**, 27 (2014), 1401.0515.

[204] S. Kanemura, Y. Okada, E. Senaha, and C. P. Yuan, Phys. Rev. **D70**, 115002 (2004), hep-ph/0408364.

[205] F. Mahmoudi and O. Stal, Phys. Rev. **D81**, 035016 (2010), 0907.1791.

[206] G. Aad et al. (ATLAS) (2015), 1512.03704.

[207] G. Aad et al. (ATLAS), JHEP **01**, 032 (2016), 1509.00389.

[208] V. Khachatryan et al. (CMS) (2015), 1510.01181.

[209] V. Khachatryan et al. (CMS), JHEP **12**, 178 (2015), 1510.04252.

[210] M. Baak, J. Cth, J. Haller, A. Hoecker, R. Kogler, K. Mnig, M. Schott, and J. Stelzer (Gfitter Group), Eur. Phys. J. **C74**, 3046 (2014), 1407.3792.

[211] M. Baak, M. Goebel, J. Haller, A. Hoecker, D. Kennedy, R. Kogler, K. Moenig, M. Schott, and J. Stelzer, Eur. Phys. J. **C72**, 2205 (2012), 1209.2716.

[212] M. Baak, M. Goebel, J. Haller, A. Hoecker, D. Ludwig, K. Moenig, M. Schott, and J. Stelzer, Eur. Phys. J. **C72**, 2003 (2012), 1107.0975.

[213] H. Flacher, M. Goebel, J. Haller, A. Hocker, K. Monig, and J. Stelzer, Eur. Phys. J. **C60**, 543 (2009), [Erratum: Eur. Phys. J.C71,1718(2011)], 0811.0009.

[214] C. P. Burgess, Pramana **45**, S47 (1995), hep-ph/9411257.

[215] D. Eriksson, J. Rathsman, and O. Stal, Comput. Phys. Commun. **181**, 189 (2010), 0902.0851.

[216] P. Bechtle, S. Heinemeyer, O. Stal, T. Stefaniak, and G. Weiglein, Eur. Phys. J. **C75**, 421 (2015), 1507.06706.

[217] P. Bechtle, S. Heinemeyer, O. Stl, T. Stefaniak, and G. Weiglein, Eur. Phys. J. **C74**, 2711 (2014), 1305.1933.